MICROGALVANIC ASPECTS OF THE SEAWATER CORROSION OF MARINE MATERIALS IN THE PRESENCE OF HYPOCHLORITE ION FOULING INHIBITOR

Kenneth Judson Graham

NAVAL POSTGRADUATE SCHOOL
Monterey, California

THESIS

MICROGALVANIC ASPECTS OF THE SEAWATER
CORROSION OF MARINE MATERIALS
IN THE PRESENCE OF HYPOCHLORITE ION
FOULING INHIBITOR

by

Kenneth Judson Graham
December 1979

Thesis advisors: R. Reinhardt and M. Miles

Unclassified

SECURITY CLASSIFICATION OF THIS PAGE (When Data Entered)

REPORT DOCUMENTATION PAGE		READ INSTRUCTIONS BEFORE COMPLETING FORM
1. REPORT NUMBER	2. GOVT ACCESSION NO.	3. RECIPIENT'S CATALOG NUMBER
4. TITLE (and Subtitle) Microgalvanic Aspects of the Seawater Corrosion of Marine Materials in the Presence of Hypochlorite Ion Fouling Inhibitor.		5. TYPE OF REPORT & PERIOD COVERED Master's Thesis; December 1979
		6. PERFORMING ORG. REPORT NUMBER
7. AUTHOR(s) Kenneth Jusdon Graham		8. CONTRACT OR GRANT NUMBER(s)
9. PERFORMING ORGANIZATION NAME AND ADDRESS Naval Postgraduate School Monterey, California 93940		10. PROGRAM ELEMENT, PROJECT, TASK AREA & WORK UNIT NUMBERS
11. CONTROLLING OFFICE NAME AND ADDRESS Naval Postgraduate School Monterey, California 93940		12. REPORT DATE December 1979
		13. NUMBER OF PAGES 286
14. MONITORING AGENCY NAME & ADDRESS(if different from Controlling Office) Naval Postgraduate School Monterey, California 93940		15. SECURITY CLASS. (of this report) Unclassified
		15a. DECLASSIFICATION/DOWNGRADING SCHEDULE

16. DISTRIBUTION STATEMENT (of this Report)

Approved for public release; distribution unlimited

17. DISTRIBUTION STATEMENT (of the abstract entered in Block 20, if different from Report)

18. SUPPLEMENTARY NOTES

19. KEY WORDS (Continue on reverse side if necessary and identify by block number)

Copper Alloys CDA 101, CDA 260, CDA 280, CDA 706, CDA 715
Corrosion Products Analysis
X-Ray Fluorescence Analysis
Marine corrosion
Sodium Hypochlorite
Chloropac Electrolytic Chlorinator
Anti-fouling Agents
Scanning Electron Microscopy
Intergranular Corrosion

20. ABSTRACT (Continue on reverse side if necessary and identify by block number)

This corrosion research has been conducted in two ways: microscopically and electrochemically. In the microscopic portion has been studied the mode and distribution of attack on metal coupons immersed in corrosive fluids. Here could be observed the effects of alloying, the corrosion product morphology, selective phase corrosion, and base metal microstructure. Both optical and scanning electron microscopy were used.

DD FORM 1 JAN 73 1473 (Page 1) EDITION OF 1 NOV 65 IS OBSOLETE S/N 0102-014-6601

Unclassified

SECURITY CLASSIFICATION OF THIS PAGE (When Data Entered)

20. (continued)

In the electrochemical portion has been examined the effects of varying the corrosive electrolyte from synthetic seawater alone to one containing a marine fouling inhibitor, sodium hypochlorite. Here, corrosion rates were obtained for the specimens in the various corrosive media by a variety of methods. These ranged from rather simple controlled immersion tests to the more sophisticated electrochemical measurements such as linear polarization and potentiodynamic polarization. Chemical and x-ray analyses were performed on the corrosion products.

The information gained from these two parts was integrated to provide predictions as to the suitability, probable rate and failure mode for each of the materials studied.

Approved for public release; distribution unlimited.

Microgalvanic Aspects of the Seawater Corrosion of Marine Materials in the Presence of Hypochlorite Ion Fouling Inhibitor

by

Kenneth Judson Graham
Research Chemist, Naval Weapons Center
A.B., University of California, 1968

Submitted in partial fulfillment of the requirements for the degree of

MASTER OF SCIENCE IN APPLIED SCIENCE

from the

NAVAL POSTGRADUATE SCHOOL
December 1979

ABSTRACT

This corrosion research has been conducted in two ways: microscopically and electrochemically. In the microscopic portion has been studied the mode and distribution of attack on metal coupons immersed in corrosive fluids. Here could be observed the effects of alloying, the corrosion product morphology, selective phase corrosion and base metal microstructure. Both optical and scanning electron microscopy were used.

In the electrochemical portion has been examined the effects of varying the corrosive electrolyte from synthetic seawater alone to one containing a marine fouling inhibitor, sodium hypochlorite. Here, corrosion rates were obtained for the specimens in the various corrosive media by a variety of methods. These ranged from rather simple controlled immersion tests to the more sophisticated electrochemical measurements such as linear polarization and potentiodynamic polarization. Chemical and x-ray analyses were performed on the corrosion products.

The information gained from these two parts was integrated to provide predictions as to the suitability, probable rate and failure mode for each of the materials studied.

TABLE OF CONTENTS

LIST OF TABLES

LIST OF FIGURES

ACKNOWLEDGEMENT

This thesis research was made possible by the encouragement of friends and colleagues at the Naval Postgraduate School and the Naval Weapons Center, and the loving support of my family -- Betty, Kenneth, and Jonathan. Thank you all!

I. INTRODUCTION

The adverse effects of marine biofouling on ship performance have long been recognized by the navies of the world. The physical effects of fouling range from increased hydrodynamic resistance on the hull and loss of condenser vacuum to the actual plugging of the pipes and other seawater distribution equipment aboard ship. For example, see Figure 1. In addition to the physical effects, the economic impact is huge. In a shipyard repair facility, these adverse effects are especially noted because the vessels spend their time in port, where the seawater flow through the piping is low or stagnant and the biofouling is most severe.

For the purposes of this paper, marine fouling refers to the growth of plant and animal organisms in a seawater environment and attachment of these organisms on or in submerged surfaces.

Universally, marine biofouling increases in intensity as a ship nears land masses or enters the warmer waters of the tropics [1]. Of the large number of species classified as biofoulers, mussels and barnacles are considered to be especially troublesome because of their hardiness and widespread distribution. For example, over 100 of the more than 600 species of barnacles distributed throughout the waters of the world are known biofoulers. These, and the more than 2000 other species of marine organisms associated with barnacles, initiate or compound the impediment of ocean-borne cargos, the proper functioning of buoys, navigational aids, mines,

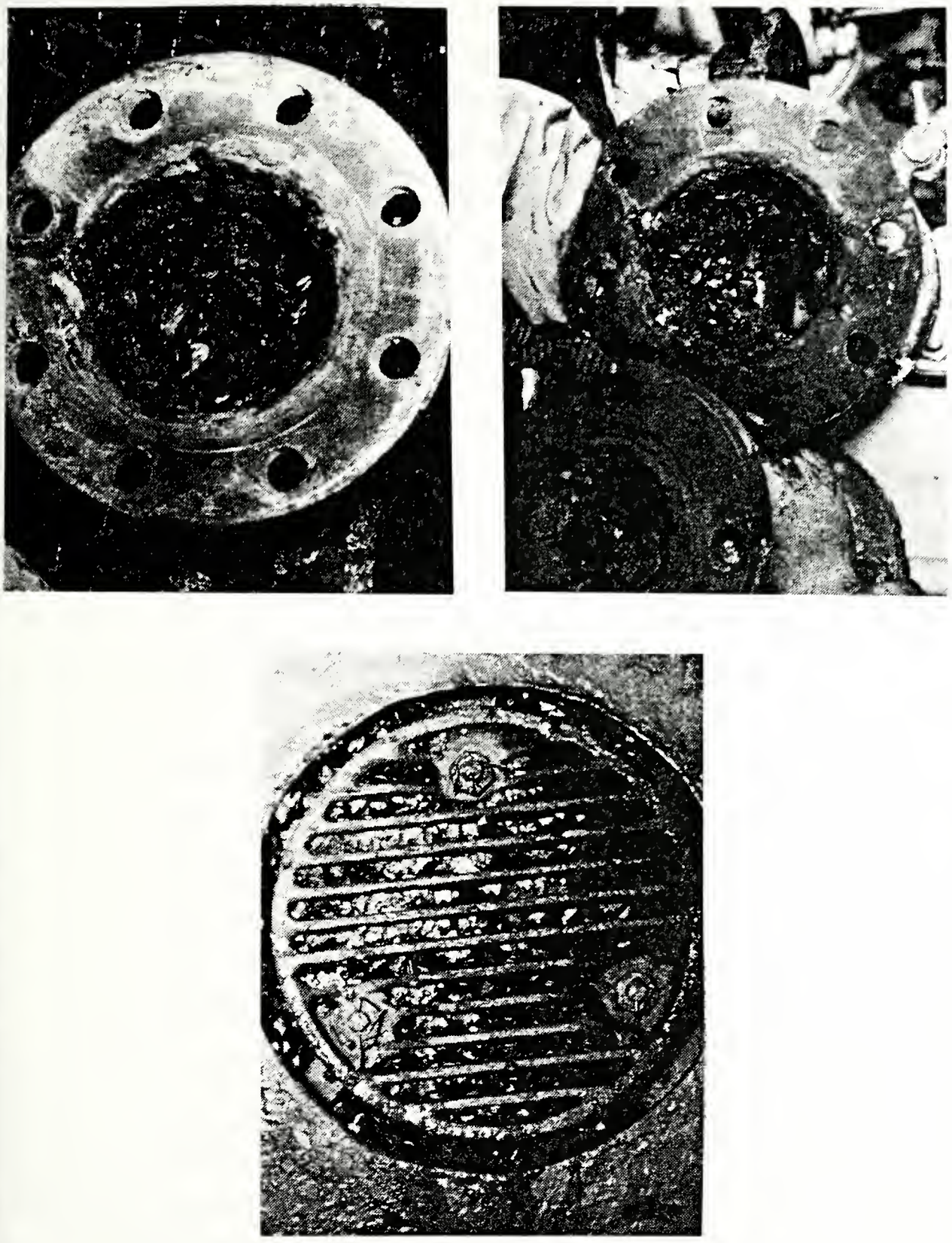

Figure 1. Examples of biofouled marine water pipes [18].

marine heat exchangers and seawater piping [2]. Consequently, extensive studies have been conducted on these organisms; methods for their effective control have generally been found also to control other fouling organisms.

A. FOULING-CONTROL TECHNIQUES

There are several techniques used in controlling marine fouling, some of which are at least partially effective. These include mechanical cleaning, coatings, heating of the seawater or the surface to be protected, maintaining high seawater velocities in the system, or adding toxic substances such as metal ions or chlorine to the water. However, mechanical cleaning is very time-consuming and difficult to accomplish in large heat exchangers. Seawater heating is impractical from an energy consumption standpoint since the water on the surface must be heated to about 52°C (125°F) to ensure complete protection [1]. Even high velocity pumping to control fouling can be of limited utility due to points of stagnation or low velocity that develop at changes in the cross-sectional area of the flow path.

The application of chlorine gas to seawater has been previously shown [3] to be an effective method for controlling biofouling in land-based, seawater-cooled power plants and desalinization plants. Such chlorination has also been applied to shipboard seawater piping and waterchests in the merchant marine. However, the direct injection of chlorine gas in most cases is not suitable for naval applications for reasons of safety and logistics. Therefore, electrolytic generators have

been developed that produce the biocidal chlorinating species directly by the electrolysis of seawater. Low concentrations of "chlorine" from electrolytic generators (ca. 1-10 ppm) are known to cause shell closing of mussels in a short time, a process that soon asphixiates them. The mussel larvae are killed at slightly higher concentrations, but their attachment to substrates is inhibited at steady state concentrations greater than ca. 0.5 ppm [3].

Attempts to use "electricity" to prevent marine fouling appear to date back to the 19th century, where in 1863, a patent [4] claimed the use of electricity "however obtained or applied for protecting ships' bottoms from corrosion, fouling, sea monsters and other evil things." Later patents suggested the use of a battery [5], an electrical generator [6], a chain of zinc anodes [7], electrolysis of hull sections to form gases that remove fouling [8], alternate anodic and cathodic currents [9], as well as high voltage alternating currents, in 1911 [10], and intermittent direct currents one year later [11].

The common fiber running throughout all of these seemingly magic antifouling measures was the electrolytic generation of the biocide chlorine. Chemically, there is no difference between chlorine gas injection and electrolytic generation of chlorine. In the gaseous method, chlorine gas is directly introduced into the water. But since chlorine is unstable with respect to the formation of hypochlorous acid (HOCl) and hypochlorite ion (OCl^-) in weakly acid to alkaline media [12], and the seawater is about pH 8-9, no chlorine gas remains

after the instant of injection. In the electrolytic method, a current is passed between two electrodes immersed in seawater. A mixture of hypochlorous acid and hypochlorite ion collects at the anode, as a result of the oxidation of chloride ion. The ratio of ClO^- to HClO at room temperature is governed by the relationship

$$\log_{10} \frac{(ClO^-)}{(HClO)} = -7.49 + pH, \qquad (1)$$

which is shown schematically in Figure 2.

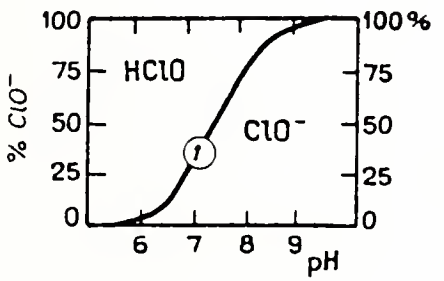

Figure 2. Influence of pH on the dissociation of hypochlorous acid. [12]

Below pH 6, the dissociation of hypochlorous acid is negligible. At higher pH levels, (6-8.5), dissociation takes place by the chemical reaction (2).

$$HOCl = H^+ + OCl^- \qquad (2)$$

Beyond pH 8.5 there is very little HOCl left in the solution. At pH 8.2 and 15°C, which are typical of surface seawater, the ratio of OCl^- to HOCl is calculated to be about 3.5:1 [13].

It has been reported [14] that there is an apparent difference in the biocidal efficiency of HOCl and OCl^-. This effect varies with pH. Since the pH of the seawater is effectively fixed, one cannot control the proportion of HOCl to OCl^- to obtain optimum killing efficiency.

Nevertheless, the level of total chlorine needed to prevent fouling is really quite small, typically less than 5 ppm. Therefore, the aforementioned "electric" methods of preventing marine fouling were still quite effective and, in principle, simple. Many chemical plants, electrical generating plants, oil rigs, and ships applied the techniques to their marine water streams, all with fairly good results. However, due to the buildup of alkaline salt materials on the cathodic surfaces of the electrolytic generators (primarily hydroxides of magnesium and calcium formed by the reaction of the aqueous metal ions with the high concentrations of hydroxide formed at the cathodes) and, because the anodes were frequently rapidly eroded, much research in the 1960's and 1970's was involved with solving these problems. (For example, see [15].)

Englehard Industries Division, Englehard Minerals and Chemicals Corporation, took the information provided in the scientific literature and developed a commercial chlorinator called the Chloropac® electrolytic generator. It consists of a series of bipolar noble metal electrodes in which the chloride ion of the seawater is oxidized at the anodes and hydrogen gas and hydroxide ions are formed at the cathodes. By resorting to turbulent flow through the generator, the buildup of cathodic deposits is minimized and the production of hypochlorite ion is assured. The rate of production is coarsely controlled by a constant-current power supply. A problem for a high-production unit is that the hydrogen gas developed at

the cathode must be vented to prevent possible explosion. Figure 3 shows a cutaway diagram of the electrolysis cell.

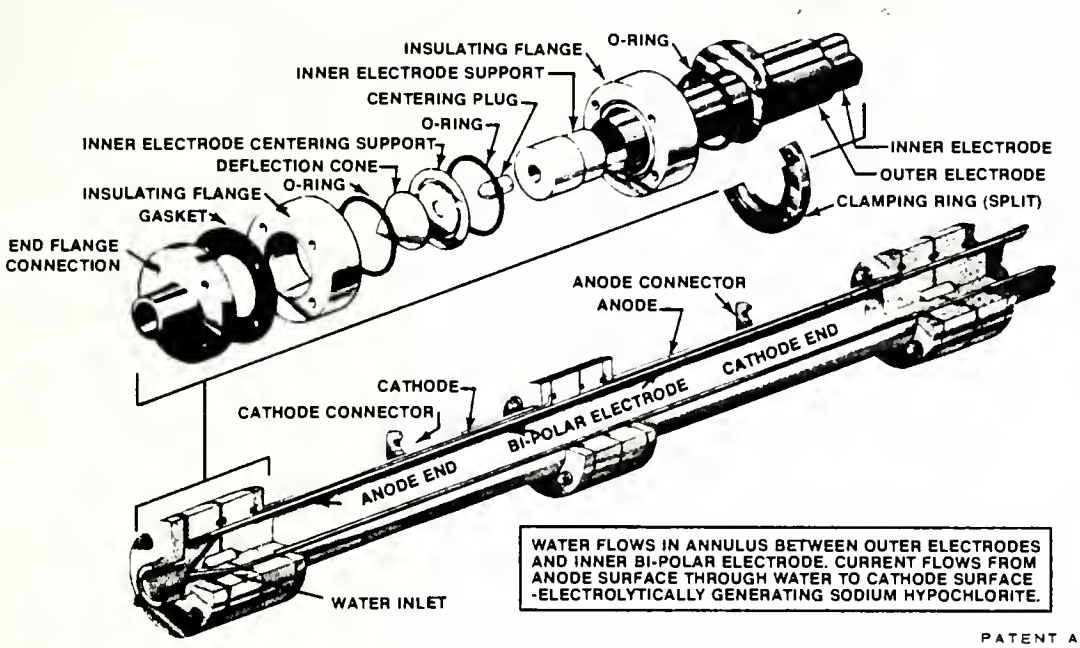

Figure 3. Chloropac® Electrolytic Generator (courtesy Englehard Minerals and Chemicals Corporation)

Since marine fouling is greatly increased in still water, the Navy has made the decision to install several of the units at Naval shipyards [16]. In particular, there is a unit being installed at Pearl Harbor Naval Shipyard for dockside attachment to the seawater piping of a ship while under repair [17].

B. CORROSION RATE STUDIES

While there has been a great deal of research accomplished regarding the anti-fouling capabilities of hypochlorite ion and hypochlorous acid, substantially less work has been done on the corrosion resistance of materials immersed in salt water solutions of hypochlorite ion. For those studies that

have included the corrosive effects of hypochlorite ion, the results range from a minimum increase in corrosion rate to an increase by as much as several orders of magnitude for some materials. For example, Yoshii reported that adding 0.2 ppm "residual chlorine" generated by the electrolysis of seawater increased the corrosion rates for several materials by 10 to 20% [18]. Price [19] found that for a 100-ppm addition of hypochlorite ion to synthetic seawater (an amount likely to be present near the mouth of the electrolytic generator [20]), the potentiokinetically determined corrosion rates increase noticeably. Some of his results are presented in Table I.

TABLE I. Corrosion Rates for Naval Materials That Were Exposed to Hypochlorite Ion. (Determined by Price [19])

Material	Concentration of hypochlorite ion	
	0 ppm	100 ppm
Copper	2.63 mpy	110 mpy
Nickel	3.31	13.5
Naval brass	3.89	33.1
70/30 Copper nickel	1.37	45.4
HY-80 Steel	37.8	161

The present work was undertaken to increase the general body of knowledge regarding the hypochlorite-assisted seawater corrosion of structural materials. If the trend in previously observed corrosion rate increases is indeed true, the marine engineer can be provided with data relative to corrosion rates of piping materials, the type and distribution

of corrosion products, and the ultimate mode of failure. With this knowledge, a catastrophic piping failure due to the corrosion of the piping by the applied anti-fouling agent may be prevented.

II. EXPERIMENTAL METHODS

A. SURVEY OF THE CORROSION EXPERIMENTS

In order to correlate corrosion rates with electrochemical observations, it was decided to determine the corrosion rate by several methods. These are described below.

1. The Coupon Immersion Mass-Loss Method (IML)

Machined, accurately weighed metal coupons were immersed in the corrosive fluid of choice. In these experiments, either synthetic seawater (see Appendix E, Table E-2 for composition of seawater) or synthetic seawater plus 200 ppm sodium hypochlorite was used, while other variables such as the temperature and dissolved oxygen content were kept constant. Following immersion for a fixed length of time, the specimens were photographed and rinsed, the corrosion products were removed (by one or more methods), and after drying, the coupons were accurately reweighed. The information obtained from these experiments was the mass-loss per unit time, as well as the mode and distribution of corrosive attack.

2. The Linear Polarization Method (LPM)

Samples were immersed in the corrodent as in the IML method. (The same specimen serves for both purposes.) However, with this electrochemical technique, the instantaneous corrosion rate was measured during corrosion of the specimen. LPM involves determination of the corrosion potential relative to a reference electrode; this potential is designated E_{corr}. Then, a very small polarizing voltage ($E_{corr} \pm 20$ mV) is applied between the specimen and a third electrode, while the

voltage (E) and current (I) are recorded. The slope of the $\Delta E/\Delta I$ curve was then translated to the instantaneous corrosion rate. Further details of this technique are given in Appendix C.

3. The Potentiodynamic Polarization Method (PDP)

Specially machined test coupons of known geometry were placed in a well-characterized corrosive medium. The corrosion potential, E_{corr}, was measured after the specimen had begun to corrode freely. Then, starting at E_{corr}, the potential of the specimen was forced at some slow linear rate to either more positive reduction potentials (anodic polarization) or more negative reduction potentials (cathodic polarization). This was accomplished using a potentiostat especially equipped with a programmer to scan potential slowly in the anodic or cathodic directions, respectively. The potentiostat functions as a potentiometer in that it measures the potential between the specimen and a reference electrode (such as the saturated calomel electrode, SCE). It also functions as a precision power supply in that it is capable of controlling the potential between the specimen and the reference electrode to any desired level by passing current between a third (set of) electrode(s) and the specimen. When the specimen potential relative to SCE (E vs. SCE) was scanned, a plot of E vs. $\log_{10} I$ was obtained. (For a typical plot, see Figure C-1.) The resulting plot was then used to determine the corrosion current density at E_{corr}. This value is related to the corrosion rate (see Appendix C). The plot also served to show how the material behaves at various potentials (e.g., does the material protect itself by

forming a passivating dielectric film on its surface when polarized anodically?, etc.).

Each of the techniques mentioned above was used to determine the corrosion rate and the relative corrosivity of the environment on the various specimens.

4. The Potentiostatic Polarization Method (PSP)

It was also necessary to carry out accelerated corrosion of coupons in the various media of interest for subsequent microscopic examination. There are two commonly accepted methods for accelerated corrosion testing--galvanostatic polarization (GSP) and potentiostatic polarization (PSP). In GSP, the current flowing is set constant; in PSP, the potential relative to some reference electrode is fixed. In the PSP method, current (I) vs. elapsed time must also be recorded. By either of these techniques, knowledge of the current-time integral will allow calculation of the amount of material oxidized from Faraday's Law:

$$\text{mass lost} = (e/F)\int I\, dt \qquad (3)$$

where e is the equivalent weight of the metal in grams per equivalent (atomic weight divided by number of electrons participating in the redox reaction), $\int I\, dt$ is the current-time integral in ampere-seconds (coulombs), and F is the Faraday constant, 96484.6 coulombs/equivalent. The result of the calculation is the mass lost in grams, assuming soluble reaction products or exact scraping off of insoluble products.

By exposing coupons in known environments for a known passage of charge, microscopic information was obtained as to

the method of initiation and dissolution in the corrosion process. Also obtained were the qualitative electrochemical relationships between the phases in polyphase alloys and sometimes the composition of the corrosion products as well.

In this set of controlled potential tests, the specimens were forced to oxidize by PSP at 100 mV more positive than their previously determined corrosion potentials. While this required the added effort of recording the current-time relationship, it was felt that this might more nearly represent real conditions in which a metal component might be accidently coupled to one more noble than itself, with a resulting change in its potential as it polarized anodically. The specimens were exposed for varying times and then slightly rinsed with water and dried in vacuuo until observation by light microscopy (LM), scanning electron microscopy (SEM), or microanalytical beam techniques could be accomplished.

B. SURVEY OF THE MICROSCOPIC AND MACROSCOPIC ANALYSES

Two types of specimens were studied--those from the IML experiments and those from the PSP tests. The information sought included the corrosion mode (such as intergranular corrosion, pitting, cracking, etc.) and the distribution of corrosion (localized or overall). It was also of interest to try to hypothesize as to the mechanism of corrosion (e.g., was the zinc-rich phase of a two-phase brass preferentially corroded?). Microanalytical beam techniques were used to examine for dealloying (e.g., dezincification in the brasses) and sometimes to aid in determining the composition of the

corrosion products. Observations were presented as photographs from the various instruments. These photographs were then analyzed by standard micrographic methods for the size, shape, and if possible, the elemental composition in the displayed image. For further details, see Sections II,F and II,G.

C. IMMERSION MASS-LOSS (IML) EXPERIMENTS

1. Test Coupons

There were five metals considered in this study. They are described in detail in Appendices B and E, but are briefly identified below in Table II.

TABLE II. Identification of the Metals Used.

Common name	Identification	Specimen designation
70/30 Copper zinc (cartridge brass)	[a]CDA 260	#1
60/40 Copper zinc (Muntz metal)	CDA 280	#2
Copper, oxygen-free electronic grade	CDA 101	#3
70/30 Copper nickel	CDA 715	#4
90/10 Copper nickel	CDA 706	#5

[a] Copper Development Agency

The five metals considered represent a cross section of the types commonly used for marine applications. Numbers 1, 4, and 5 are solid solution alloys and along with #3, share the face-centered cubic (FCC) crystal lattice. Number 2 was selected to examine the effects of a two-phase material. Its major phase is face-centered cubic (FCC); the minor one is the zinc-rich body-centered cubic (BCC) crystal lattice.

Metallurgical information is contained in Appendix E, and the microstructures are shown in section III,B. (See Figures 19 through 23.)

Each of the sample materials was machined into rectangular test coupons with an exposed surface area of ca. 14 cm^2. This geometry is shown in Figure 4. After machining, the specimens were hand ground to a 3/0 surface with metallurgical paper and identification numbers were stamped on each.[1] They were then cleaned ultrasonically, measured, accurately weighed, degreased, and finally immersed in the electrolyte of choice.

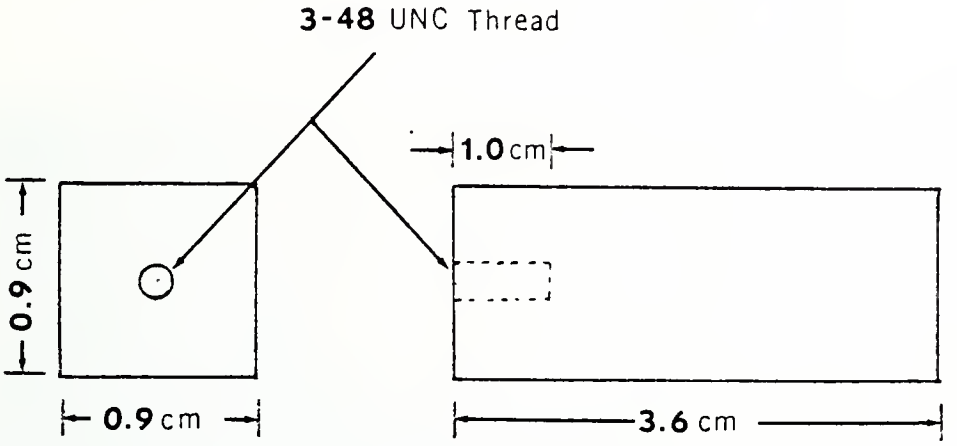

Figure 4. Detail of immersion mass-loss metal coupon.

[1] Those specimens corroding in synthetic seawater alone were given the suffix "-O" to their specimen numbers. Those specimens corroding in synthetic seawater with added hypochlorite were designated by the suffix "-H." For example, the 70/30 copper nickel specimen corroding in electrolyte with added hypochlorite was designated "4-H."

2. Test Fixture

A specially designed fixture (Figure 5) was built to hold twelve 1000-cm^3 round-bottomed, three-necked flasks in the 25 ± 0.1°C constant temperature bath. Each flask was fitted with a gas sparger, a Graham condenser, and the center neck was reserved for emplacement of the specimen and its holder. Figure 6 shows the corrosion cell, and Figure 7 shows a specimen attached to its holder. The holder was designed such that with the specimen attached to the center rod and immersed in the electrolyte, linear polarization measurements (LPM) could still be made via the internal electrical circuit.

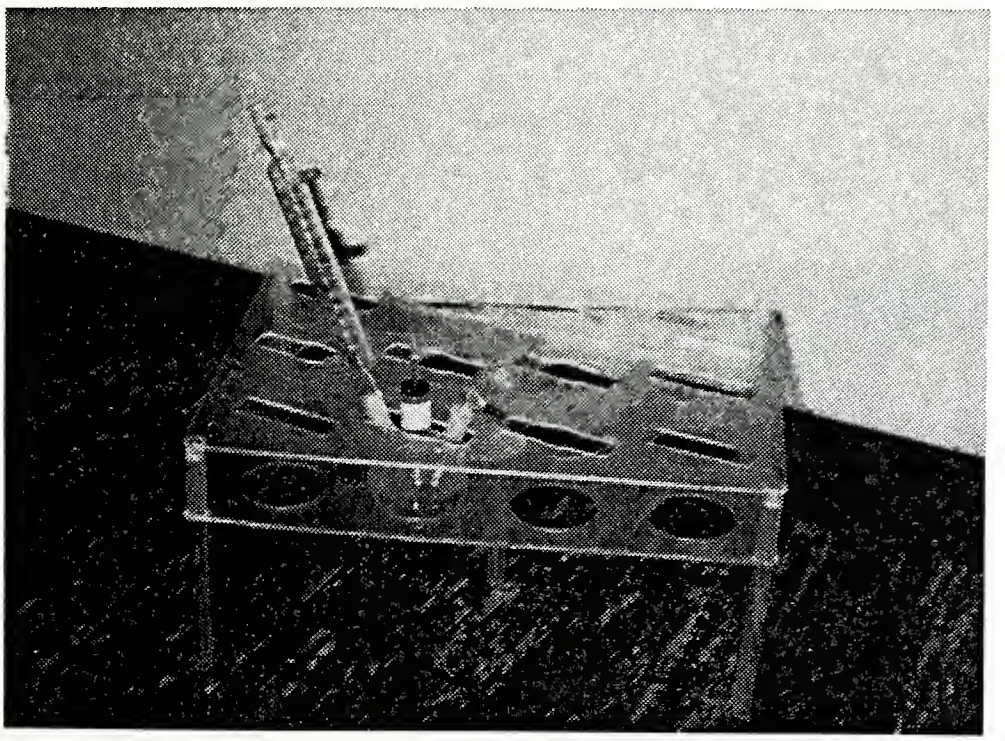

Figure 5. Acrylic fixture designed to hold twelve corrosion cells in a constant temperature water bath.

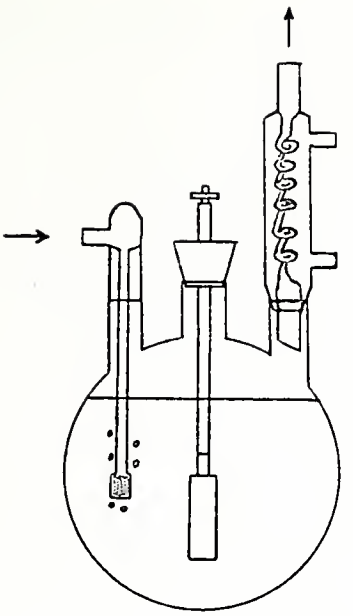

Figure 6. A typical IML corrosion cell including from left to right a gas sparger, the test coupon holder, and the Graham condenser.

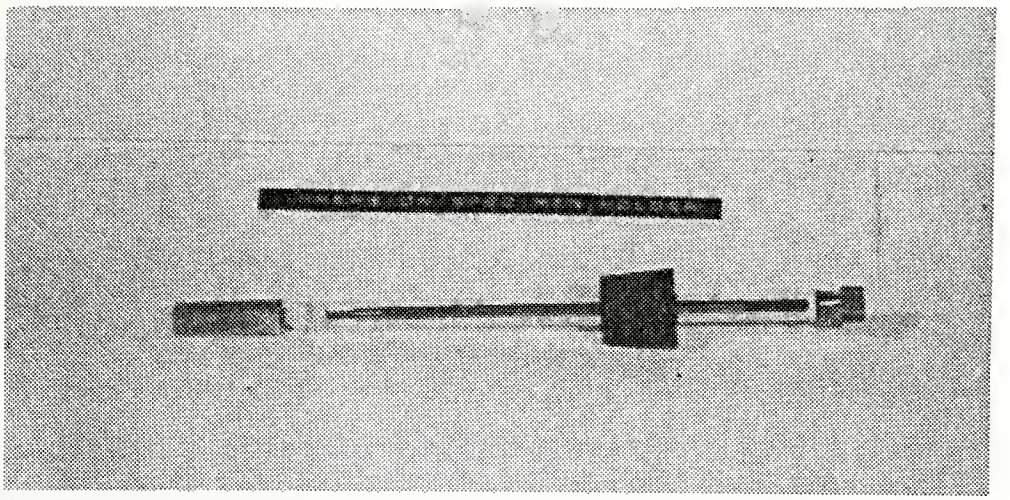

Figure 7. An IML test specimen holder with attached specimen.

The Teflon compression seal excluded the electrolyte in order that a bimetallic couple might not be established between the specimen and the internal metal holder. The gas spargers were attached to a cylinder of compressed air of known composition (see Appendix E for composition of purge gas), which flowed through each flask at a rate of 47 cm^3/min. The condensers maintained the electrolyte levels by preventing evaporation.

3. Electrolytes

Each of the five metals considered in this study was subjected to a 34-day immersion test in synthetic seawater of known composition and under reproducible conditions. Half of the specimens were immersed in synthetic seawater alone; the others were placed in synthetic seawater containing 200 ppm sodium hypochlorite solution (138 ppm hypochlorite ion concentration). The pH of the hypochlorite-containing medium was not adjusted to that of the one containing synthetic seawater only, since in the operation of the Chloropac® unit this would not normally be done. However, it is of note that the pH was typically about 0.3 units more alkaline in the flasks with added hypochlorite.

4. The Experiment

After addition of the appropriate electrolyte to each of the flasks, they were placed in the special test fixture in the constant temperature bath. The corrosion cells were fitted with the sparger and the condenser and the center hole was stoppered in each. Air flow was started through the sparger and allowed to purge through the electrolyte overnight.

For those flasks containing added hypochlorite ion, 200 ppm of sodium hypochlorite solution were added before the overnight purge. In this way, any chlorine demand by the solution could be accomplished. The next day, just prior to immersion of the specimens, those flasks containing hypochlorite were refreshed with any needed amount of sodium hypochlorite, as determined by titration (see Appendix E for titration methodology). The specimens were then placed on their holders and inserted into the center necks of their respective flasks. The starting time was noted, and a record sheet was started for each specimen.

All corrosion cells were monitored periodically for electrolyte pH, conductivity, and dissolved oxygen content. These variables were recorded to demonstrate the constancy of test conditions in these immersion experiments. Each cell was also monitored for E_{corr} whenever LPM's were made. Through the use of LPM, repeated measurements of corrosion rates could be performed, in situ, without disturbing the immersion test in progress. In this way, a correlation was developed between the instantaneous corrosion rates (from LPM) and those calculated from the IML tests. Figures 8, 9, and 10 show the equipment used in making these measurements. (Further details of the LPM method are given in Appendix C).

For those corrosion cells containing added hypochlorite, the electrolyte was monitored every few days for the concentration of hypohalite ions. For each measurement, a 25-cm^3 aliquot of the electrolyte was taken and added to a solution of 4 grams of potassium iodide in 35 cm^3 of distilled

Figure 8. Combination pH, conductivity, and millivolt meter.

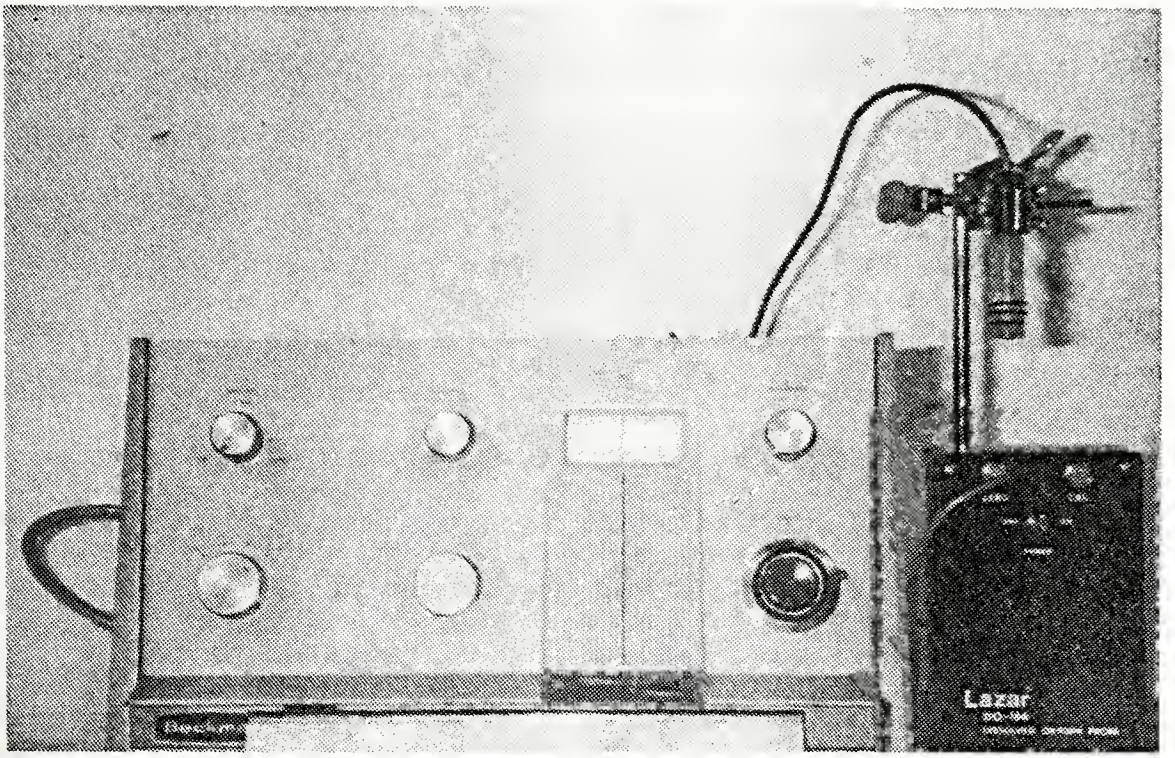

Figure 9. Dissolved oxygen electrode and interface coupled to millivoltmeter.

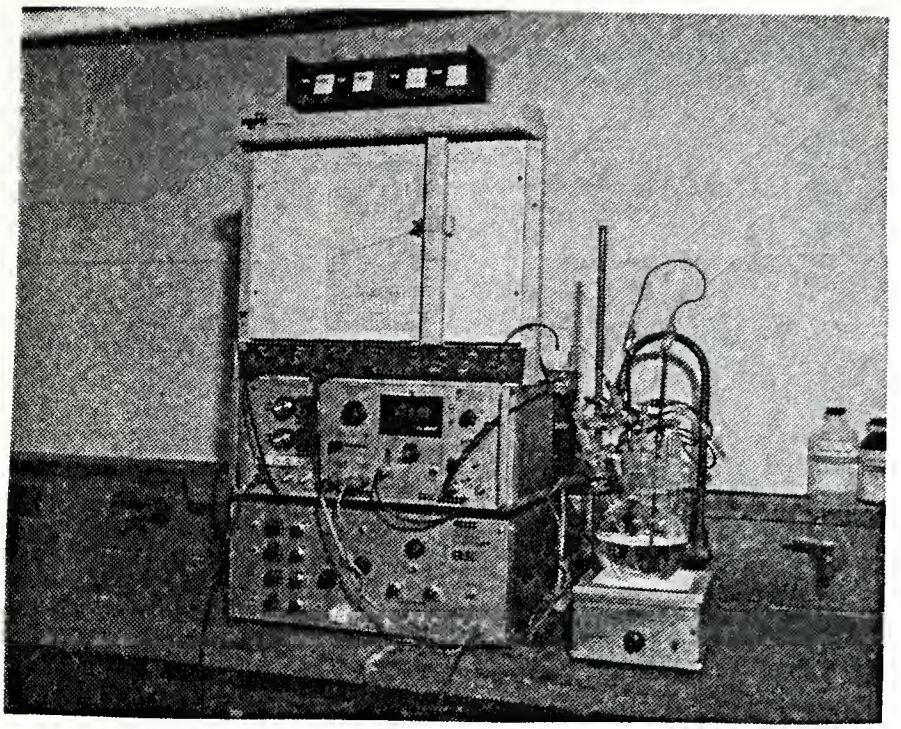

Figure 10. Linear polarization measurement apparatus.

water. Then 0.25 cm^3 of 1M hydrochloric acid was added followed by four drops of starch indicator. The solution was stirred briefly to liberate iodine, and then was buffered by the addition of 15 cm^3 of pH 8.0 phosphate buffer. A previously standardized sodium arsenite solution was then added automatically by a Sargent Automatic Titrator, Model SE (see Figure 11) and was titrated to a colorless endpoint. The volume of arsenite used was then employed to calculate the amount of hypohalite present in the aliquot. From this calculation, it could be determined how much sodium hypochlorite solution should be added to return the concentration of hypohalite to the 200 ppm level in the cell. A discussion of the chemistry of the standardization and titration reactions is given in Section III,M and Appendix E. Plots of the monitored

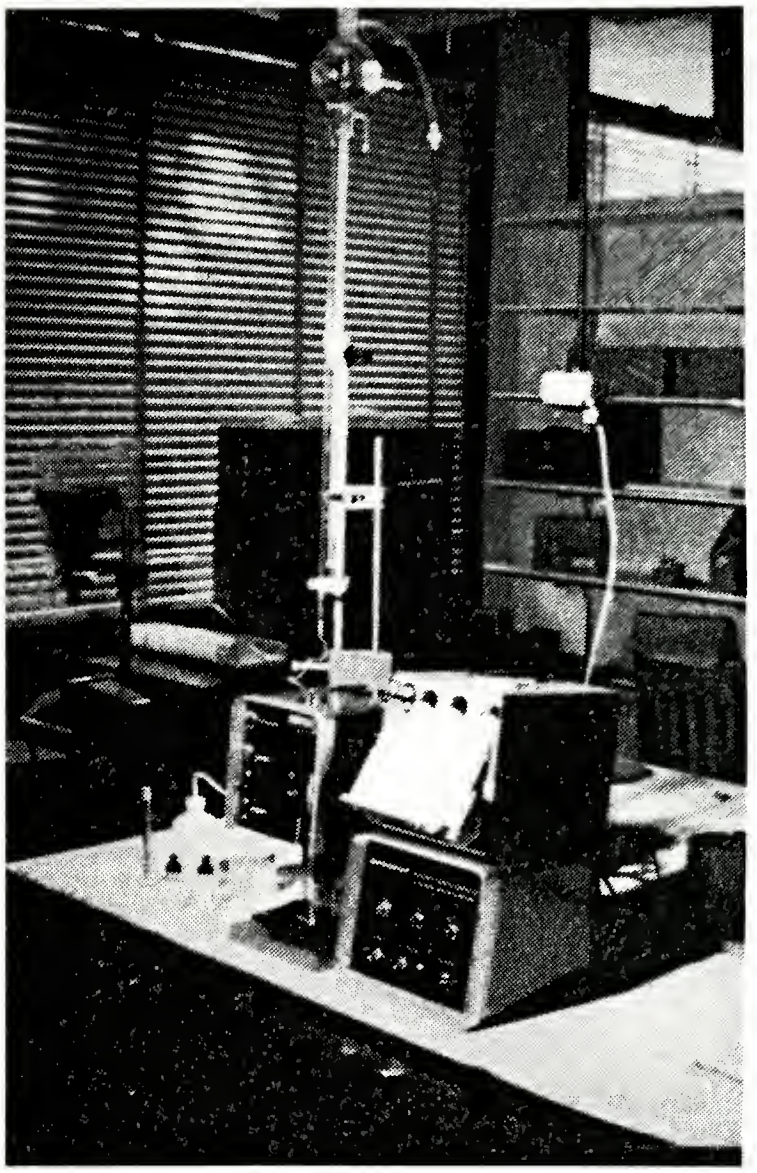

Figure 11. Automatic titrator used in performing the hypohalite quantitations.

variables vs. time as well as instantaneous corrosion rates are given in Appendix B, Figures B-3 through B-12.

At the end of the IML experiment (34 days), specimens were removed from the corrosion cells and photographed in color on 35-mm transparencies, with the aid of a close-up lens. Samples were then gently rinsed with water and allowed to dry with their corrosion products intact. Light micrographs were

then taken at low magnifications and, afterwards, SEM and X-ray fluorescence analyses were performed, again with the corrosion products still adhering to the IML specimens. Finally, the corrosion products were carefully scraped off the specimens for further analysis. The metal coupons were scrubbed with a stiff brush in running water to remove most of the remaining corrosion products. Residual amounts of the precipitate were removed ultrasonically. Each specimen was then dipped in cold acid solution for 2-10 seconds, following ASTM standard G1-72 [21]. Samples were rinsed in distilled water, followed by an acetone wash, and then dried *in vacuuo* for ten minutes before weighing them on an analytical balance. Mass losses were recorded for each specimen and were converted to mass-loss rates (mg/dm^2-da) and penetration rates (mm/yr). A comparison of the corrosion rates as determined by IML and as determined by LPM is given in Appendix B, Table B-III. See also Section III.

Following the removal of the corrosion products, the test coupons were once again examined by SEM and LM, in an effort to determine the mode of corrosion operating when the electrolyte either did or did not contain added hypochlorite ion. In many cases it was necessary to cut the specimens transversely and examine them by LM end-on for determination of pit depth and depth of dealloying. Methods used in these studies are given in Section II-F. Results are given in Section III-B.

D. POTENTIODYNAMIC POLARIZATION MEASUREMENTS (PDP)

1. Test Coupons

Test coupons of the same materials used in the IML tests were machined from the same stock but with considerably different geometry. The chosen form of coupon was a right circular cylinder with 9.5 mm diameter, 9.5 mm in height with a 3-48 UNC thread tapped into one end. This geometry is shown in Figure 12 below.

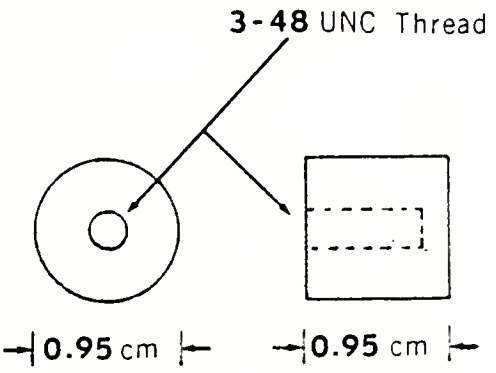

Figure 12. Detail of potentiodynamic polarization test coupon.

The exposed surface area of the test coupons (which was later used to determine the corrosion current density) was essentially the same from run to run, this being about 4.2 cm^2. Coupons were cleaned and then finished to a 3/0 surface with metallurgical polishing paper just before a PDP run. Specimens were cleaned ultrasonically in ethanol, dried with warm air blower, attached to the specimen holder, and placed in the electrolyte of choice.

2. Corrosion Cell

The test cell used was the one recommended by ASTM Standard G5-72 [22]. It consisted of a 1000-cm^3 round-bottomed flask with five necks. Through two of these, the high density graphite auxiliary electrodes were placed. The gas sparger was placed through the third and the Luggin probe-salt bridge was fitted in the fourth. The specimen holder was very similar to the one used in the IML experiments and was placed through the center neck in the flask. The corrosion cell is shown schematically in Figure 13, and a detail of the specimen holder is given in Figure 14.

3. Corrosion Measurement System

The corrosion measurement system used for the PDP runs was the Princeton Applied Research Deluxe Corrosion Measurement System, Model 331-3. This consists of four modules in addition to the corrosion cell: a precision potentiostat capable of applying a potential difference of ±5 V between the specimen and the auxiliary electrodes; a waveform programmer that allows the progressive scanning of potential in one direction or another at fixed rates; a logarithmic current converter that measures the current flowing through the auxiliary electrode and the specimen and reports it logarithmically as an analog voltage; and an X-Y plotter that gives a hard copy record of the whole potential-log current scan. Details of the system are given in Appendix C.

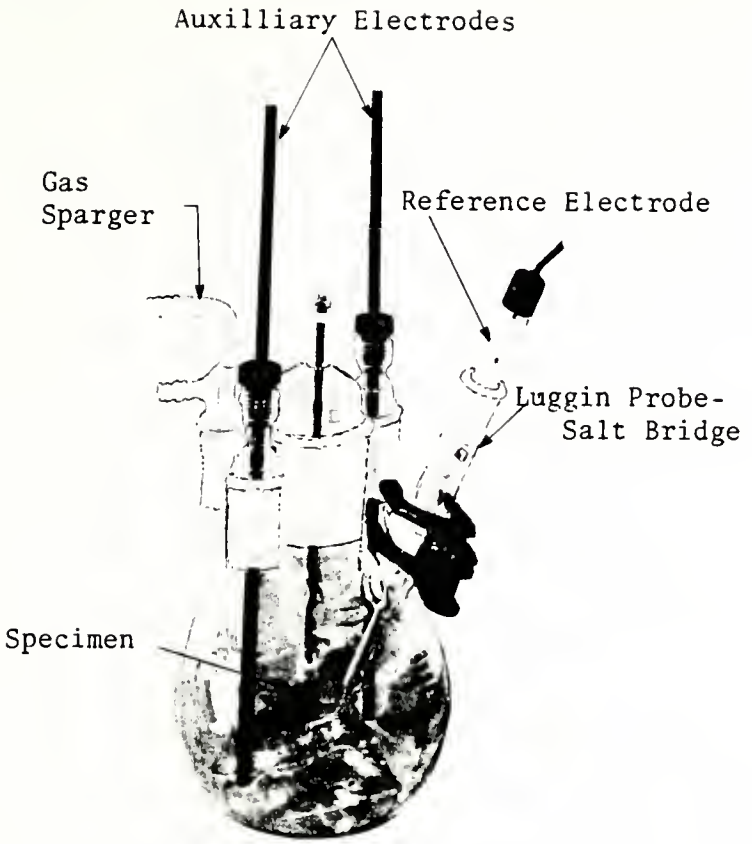

Figure 13. PDP corrosion cell (courtesy Princeton Applied Research, Inc).

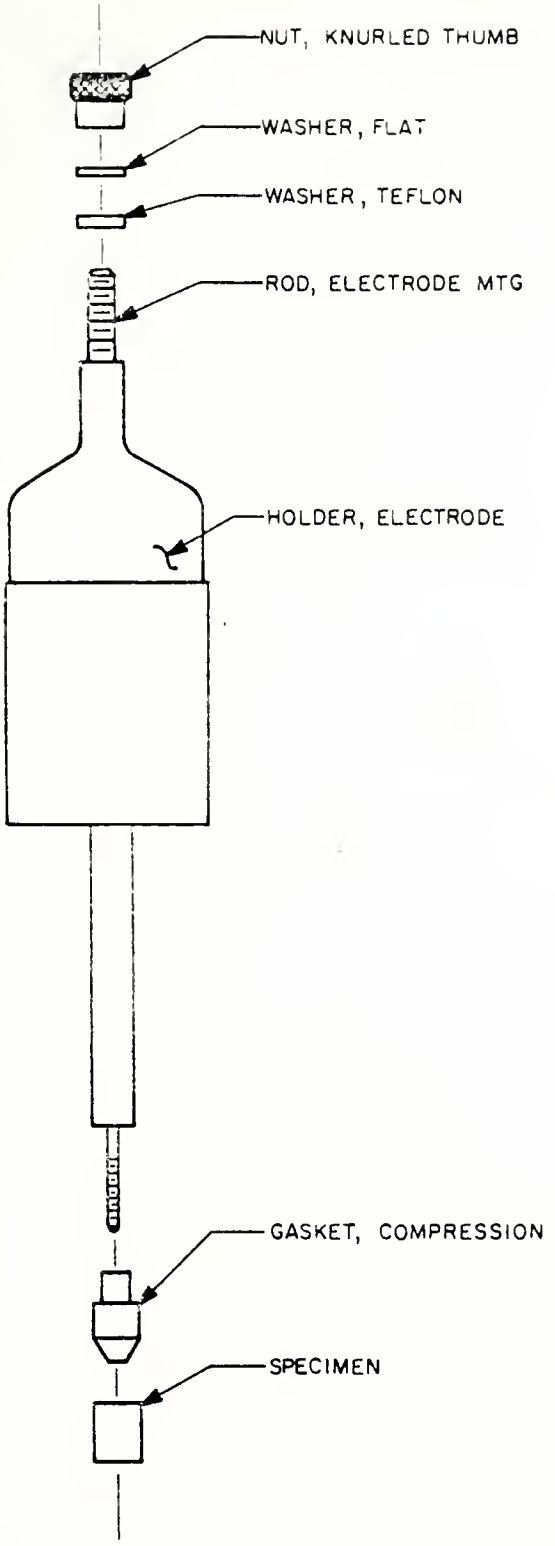

Figure 14. Detail of PDP specimen holder (courtesy Princeton Applied Research, Inc.)

4. Electrolytes

There were two major electrolytes used in this part of the study. One was aerated synthetic seawater of known composition (see Appendix E) with 50 ppm sodium thiosulfate ($Na_2S_2O_3$) added to react with any hypohalite that might be formed in the polarization process. Price showed previously [19] that this level of thiosulfate addition had no effect on the observed corrosion rates of copper and its alloys as determined by PDP. The other electrolyte used was aerated synthetic seawater of known composition, but the added thiosulfate ion was replaced with various hypochlorite ion concentrations, up to 138 ppm ClO^- inclusive. The hypohalite concentration was determined as in the IML tests, by reacting an aliquot of the solution with iodide ion and then titrating the resulting iodine with standardized sodium arsenite solution in the automatic titrator, using starch as the indicator.

Both electrolyte solutions were aerated with the same compressed air as in the IML tests (see Appendix E for composition of the air). However, in a limited number of tests without hypochlorite ion, deoxygenated nitrogen gas was used to purge the solution to test for the effects of dissolved oxygen on the corroding system. See Section III,D for further discussion of these experiments.

5. The Experiment

A test coupon was placed in the electrolyte of choice, after the solution had been saturated with air for at least 10 minutes. The air flow was reduced after insertion of the

specimen and any adhering bubbles were shaken loose from the coupon. The electrode leads were attached appropriately (see Appendix C for standard methodology of PDP), and the corrosion potential, E_{corr}, was measured. When the specimen was freely corroding in the electrolyte (as shown by attainment of a stable E_{corr}), the corrosion potential was recorded. Starting at this potential, the potential was scanned at 0.5 mV/sec in the anodic direction (toward more positive reduction potentials). Potential applied vs. log current flowing in the circuit was recorded by the X-Y recorder. The run was terminated at some preset level by the programmer. Next, fresh electrolyte was placed in the corrosion cell and the aeration procedure was repeated. A freshly polished and cleaned specimen was placed on the specimen holder into the electrolyte and E_{corr} was measured as above. Then, starting at the corrosion potential, the potential was scanned at the same rate, but this time in the cathodic direction (toward more negative reduction potentials). The resulting potential vs. log current relationship was plotted on the same paper as the anodic scan and together, the pair of curves comprised one complete potentiodynamic polarization curve. The features of this curve were noted and later compared to those of the other specimens. The traces of applied potential vs. logarithm of current were analyzed by standard methods (see Appendix C to give the corrosion current density at the corrosion potential and, from this, the corrosion rate (in mg/dm^2-da) and the penetration rate (in mm/yr).

E. POTENTIOSTATIC POLARIZATION

1. Test Coupons

Coupons used for these experiments were of the same materials and shape as those for the PDP experiments--namely, a right circular cylinder. Specimen preparation followed exactly the same procedure as for PDP.

2. Corrosion Cell

The corrosion cell used in these experiments was the same as the one for PDP. All electrical hookups were identical to those for the dynamic runs. See Figure 13.

3. Electrolytes

Two electrolytes were chosen for these runs. One was aerated synthetic seawater. The other one had 200 ppm sodium hypochlorite added to the seawater. On a few long-term runs, the hypochlorite ion concentration was refreshed at intermediate times, but in the majority of cases, the concentration of hypohalite ion was measured before and after the constant potential runs, since it was of interest to note how much hypochlorite ion was used up in an experiment. As in the previous tests, the air used was well characterized (see Appendix E).

4. The Experiments

As in the PDP runs, the electrolyte of choice was placed in the corrosion cell and well aerated with stirring. Air flow was then reduced and the stirring stopped. The test specimen of choice was then immersed in the electrolyte, any attached bubbles of air on it were removed, and the E_{corr}

monitored either until it stabilized (runs without added hypochlorite) or for a fixed length of time if constant potential was not readily achieved (some runs with added hypochlorite). After this initial equilibration, a potential 100 mV more positive (in reduction potential) than E_{corr} was applied for a fixed length of time. This forced the specimen to act as an anode and therefore to oxidize. Standard run times were 12, 60, 240, and 720 minutes and occasionally a longer time was also used. Current was recorded as a function of elapsed time on a strip chart recorder, using the current-output jack on the current-to-voltage module of the potentiostat. Following the potentiostatic polarization, the sample was carefully removed from the corrosion cell and rinsed slightly with distilled water to remove seawater salts. Sample coupons were then lightly rinsed in ethanol and dried with an air drier. Coupons were placed in protective plastic boxes and stored in a vacuum chamber until they could be examined by microscopic means. The amount of material oxidized was calculated from the area under the current-time plot by graphical integration and then applying Faraday's Law as was stated in equation (3) earlier. Hypohalite was measured both before and after each run to determine how much was used up in the corrosion process.

F. MICROSCOPIC EXAMINATIONS

1. Metallography of the Test Specimens

Standard metallographic procedures were employed in the preparation and etching of the sample materials. Coupons about 10 x 10 x 40 mm were ground on silicon carbide belts to

progressively finer finishes. Then the work was transferred to plate glass flats with grinding papers of emery (aluminum and iron oxide combination) laid on the glass. Finally, after hand grinding on the glass flats, the work was transferred to horizontal rotary polishing wheels covered with napped cloth. These cloths were wet with water and filled with a slurry of aluminum oxide particles suspended in water. Each wheel had a different particle size of aluminum oxide on it. Each specimen was finished through a grit size of 50 nm. Specimens were then etched chemically with one of three etching solutions listed in Table III below.

TABLE III. Chemical Etchants Used on Corrosion Coupon Materials [23].

Etch No.	Material to be etched	Composition of etchant	Page No., Ref. [23]
1	Copper and brasses	NH_4OH (ρ=.88)..5 cm^3 H_2O.....5 cm^3 H_2O_2(3%).....2-5 cm^3	419
2	Copper, nickel, and zinc alloys	$FeCl_3$.....5 g Ethanol(96%)..96 cm^3 HCl(ρ=1.19)....2 cm^3	420
3	Copper-nickel alloys	Acetic acid....5 cm^3 (glacial) HNO_3(ρ=1.42)..10 cm^3 H_2O.....30 cm^3	433

The polished and etched coupons were examined by optical microscopy, using a Bausch & Lomb Balplan® Conference Research Microscope. Microstructures were characterized as to the

identification of the alloy; the location, size, shape, and distribution of inclusions and second phases. For the two-phase Muntz metal (CDA 280), a stereometric analysis was performed to verify the composition obtained from the Cu-Zn phase diagram. See Appendix E for phase diagrams and detailed compositions of the materials used in this thesis.

2. Post-Immersion Examination

a. Corrosion Products Attached to Test Coupon

Following the IML experiments, the specimens were examined very soon after removal from the test electrolyte (ca. 1 hour). They were first photographically recorded on color film using a macro lens. Then low magnification micrographs were taken on the slightly water-rinsed, dried specimens, to get an idea of the distribution of the corrosion products on the surface of the coupons. In this examination, colors of precipitates and crystal shapes and sizes were noted. Also of interest was the relative stratum occupied by each layer of corrosion product. Next, the specimens were placed in a vacuum oven at room temperature for several days, after being mounted with conductive silver paste on SEM stubs. Specimens were not coated with metal. Each was then examined by SEM, using the Cambridge S4-10 Stereoscan scanning electron microscope (see Figure 15). The utility of this examination lay in the extreme depth of field attainable in the SEM; one can see the whole corrosion product layer in focus at high magnification, whereas with light microscopy one is limited to a very narrow plane of focus. Particular attention was

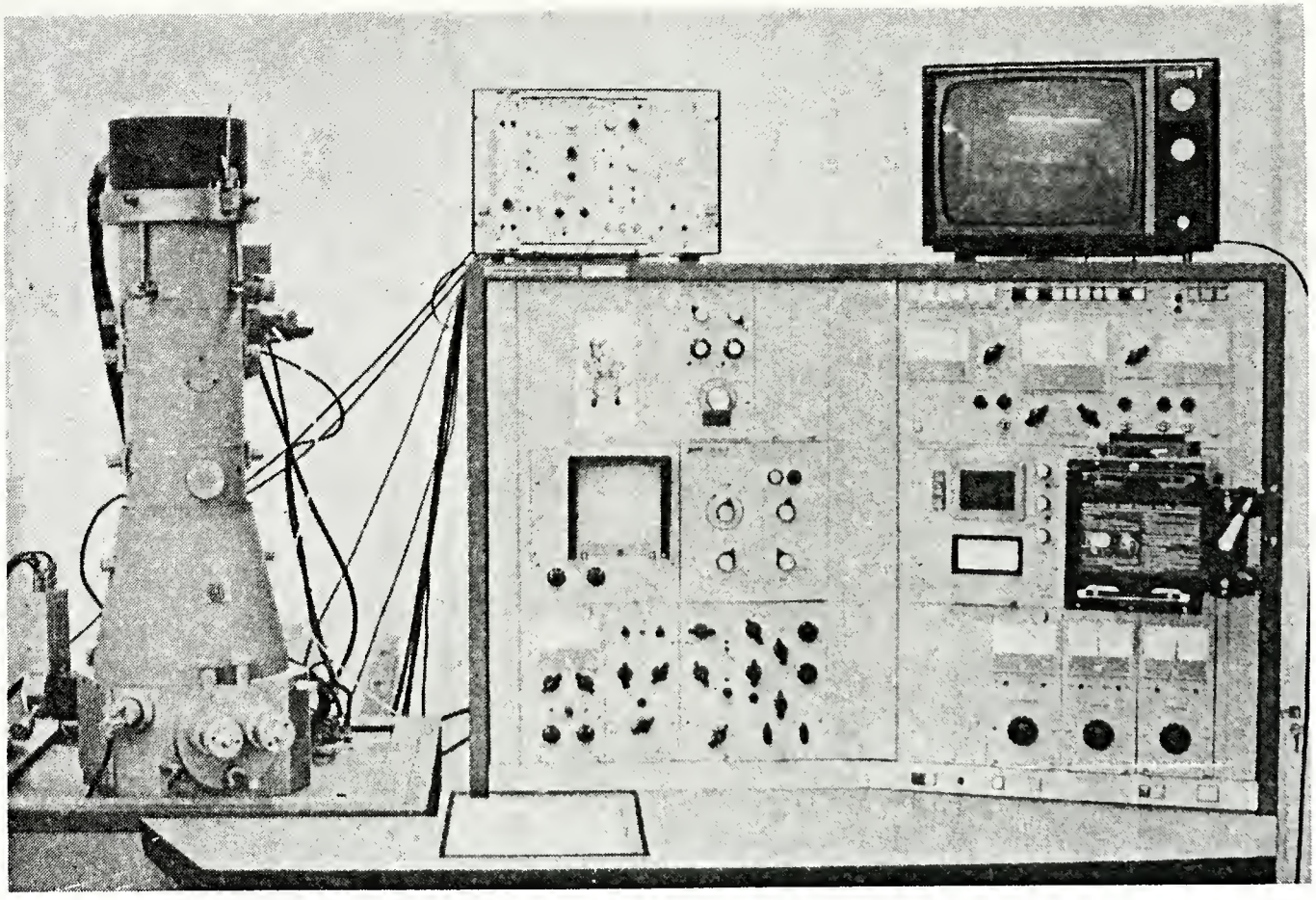

Figure 15. Cambridge Stereoscan S4-10 scanning electron microscope.

paid to crystal shapes as well as any evidence of pitting. In addition, while the uncoated specimens were in the SEM, energy dispersive X-ray fluorescence analysis could be performed on the corrosion products, providing some clue as to the composition. Selective leaching of one phase (in two-phase systems) or of one component (of the single-phase alloys) could sometimes be determined in this way. (See Section II-G).

b. After Removal of Corrosion Products

After the removal of the corrosion products (as in Section II,C,4), the specimens were once again examined by light microscopy and scanning electron microscopy. Here the metal surface could be examined and the damage beneath the corrosion product film ascertained. Again, the high resolution and large depth of field of the SEM proved to be of great value. With the corrosion products removed, examination centered upon obtaining crystallographic information such as the preferential etching of certain crystal planes, the attack at the grain boundaries, etc. Specimens were again uncoated. Finally, the long, rectangular specimens were removed from SEM stubs, cleaned, and cut transversely through highly corroded areas on the samples using a metallographic cutoff wheel. They were then cold-mounted in epoxy and polished as in Section II,F,1, above. Examination by light microscopy on a Bausch & Lomb bench metallograph permitted the determination of pit depth and depth of dealloying.

3. Post-Potentiostatic Polarization Examination

Following PSP runs, specimens were put in protective plastic boxes and placed in a vacuum chamber at room temperature. The specimen geometry had been chosen such that the test coupon was also capable of being placed directly in the SEM after attachment of a small, threaded, metal rod. SEM observations were always confined to the flat bottom of the specimen, although macroscopic observations included the sides of the cylindrical coupons. Since these specimens were run in time series, it was possible to watch the growth and change of the corrosion products on successive specimens. Again, the specimens were not coated with metal so that X-ray fluorescence analysis could be performed simultaneously.

G. X-RAY ANALYSIS

Energy dispersive X-ray fluorescence analysis was performed using the Princeton Gamma-Tech PGT-1000 X-ray fluorescence analyzer (see Figure 166). Simply stated, when an energetic beam of electrons impinges on the surface of a material, one of the ways the energy is dissipated is by the emission of X-rays. The energy associated with these emitted X-rays is characteristic of the elements composing the specimen. The PGT detector is attached to one port of the scanning electron microscope. This detector has a special window of lithium-drifted silicon that can be biased to allow only a very small energy distribution through it. When the bias-voltage is scanned, a series of energy distributions successively pass through the window to the detector and on to a multichannel

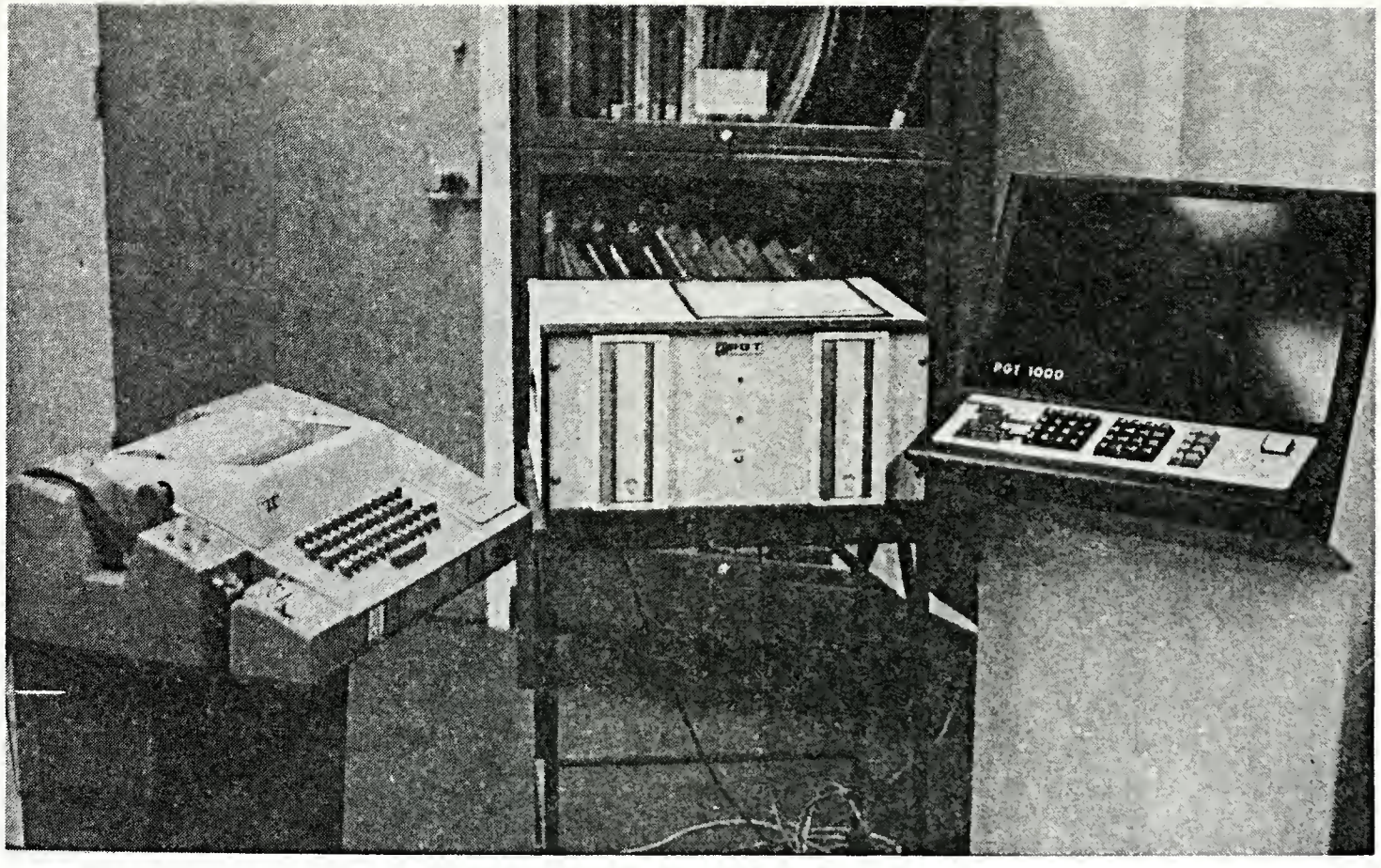

Figure 16. Princeton Gamma-Tech (PGT-1000) X-ray fluorescence analyzer.

analyzer. Here the intensity and energy are digitized and stored in the core of a minicomputer. The accumulated data can then be manipulated in various ways, using the keyboard of the PGT console, and run information as well as plots of energy vs. intensity can be displayed on the large, attached CRT monitor. Whatever area is being examined on the SEM can be analyzed by the device; i.e., the analyzer is coupled to the raster width of the SEM CRT. In this way, X-ray fluorescence analysis can be performed on very small portions of a specimen. The display on the PGT-1000 shows increasing energy (in eV) on the abscissa and intensity (number of X-ray counts) on the ordinate. A typical display is shown in Figure 17. The display shows a series of X-ray "lines" that are characteristic of the elements in the specimen.

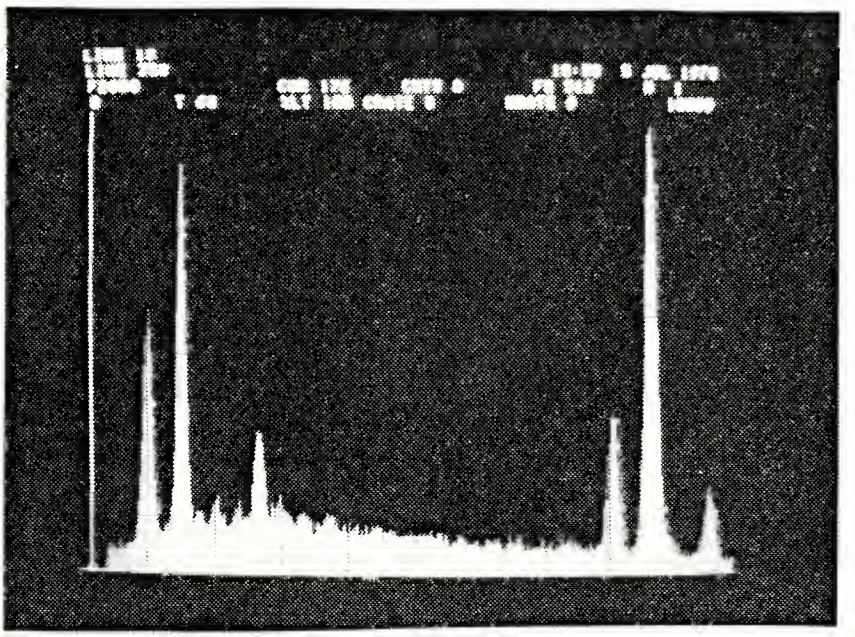

Figure 17. Typical CRT display from the PGT-1000 X-ray Fluorescence Analyzer.

The analyzer is capable of providing quantitative analysis of carefully prepared specimens when the proper corrections are applied (for example, the ZAF program, available from PGT). However, the quantitative feature is practically useless with the rough-textured specimens that are obtained as a result of corrosion experiments. The system is still of great utility, though, since it does allow for rapid (a few seconds) identification of the elements present (for atomic numbers greater than 9). Since it does not provide data on the amount of hydrogen and oxygen present, one can only make educated guesses as to the compositions of the corrosion products present. For a complete description of the theory and applications of X-ray fluorescence, the reader is referred to Ref. [24].

In some cases, the corrosion products were carefully scraped from the coupons and examined by X-ray diffraction techniques. Here, a sample was finely ground and spread in a thin layer on a special sample holder. This was placed in the X-ray beam from a copper tube operating at 35 kV and 18 mA. The detector was a special crystal monochromator manufactured by Advanced Metals Research Corporation and provided by the Naval Weapons Center, China Lake, California. The intensity vs. 2θ was plotted on a strip chart recorder and later analyzed by the standard Hanawalt method [25]. This gives crystallographic information (inter-atomic spacing in the lattice, etc.) and the pattern obtained is unique for each chemical compound. This then allowed for relatively easy identification of the corrosion product materials if the compounds contained had been previously indexed [26].

H. CHEMICAL ANALYSIS

There were no wet chemical analyses of the corrosion products. However, an analytical method for the determination of hypohalite in seawater was developed. This involved the oxidation of iodide ion by the hypohalite in moderately acidic solution, followed by reduction of the iodine formed with arsenite ion in a buffered pH 8 solution, using starch as the endpoint indicator. The reason for having to adjust the pH twice is based on the equilibria involved. The iodide-iodine half-reaction does not depend on the hydrogen ion concentration (rxn 1). If this oxidation is performed in basic solution, however, some of the iodine will react with the hydroxide ion present to form hypoiodite ion (rxn 2) and this further disproportionates to iodate and iodide ions (rxn 3). These side reactions may cause serious errors in iodine titrations if the pH is not controlled.

$$2I^- = I_2 + 2e^- \qquad \text{(rxn 1)}$$

$$I_2 + OH^- = HOI + I^- \qquad \text{(rxn 2)}$$

$$3HOI + 3OH^- = IO_3^- + 2I^- + 3H_2O \qquad \text{(rxn 3)}$$

The other part of the quantitation scheme has the following stoichiometry:

$$H_3AsO_3 + I_2 + H_2O = HAsO_4^{-2} + 4H^+ + 2I^- \qquad \text{(rxn 4)}$$

The equilibrium constant for this reaction is about 6×10^{-2} [27], meaning that in acid solution, the equilibrium lies to the left. However, if one can reduce the hydrogen sufficiently,

the reaction is forced to the right. Calculations show that at a pH of 4.5 to 5, the reaction will go as written, but the rate of reaction is very slow. From kinetic considerations, a pH of 8 was chosen, since here the rate of reaction is rapid [28]. Note, at greater pH, the reaction is even more rapid, but serious hydrolysis problems again occur with the iodine formed from the first reaction forming iodate ion which is very slow to react.

The arsenite solution was standardized prior to quantitating the hypohalite ion by standard methods [29] using standard potassium acid iodate, $KIO_3 \cdot HIO_3$ as in reaction 5 below.

$$2IO_3^- + 10I^- + 12H^+ = 6I_2 + 6H_2O \qquad \text{(rxn 5)}$$

The actual operating procedure was to take 10 cm^3 of 0.01 N standard acid iodate solution in 50 cm^3 of distilled water. Potassium iodide (4 grams) was added followed by 0.25 cm^3 of 1.0 M HCl. Iodine was formed almost immediately. After 15 seconds of stirring on the automatic titrator, 15 cm^3 of pH 8.0 ($H_2PO_4^-$-HPO_4^{2-}) buffer was added. This buffer consisted of 50 cm^3 0.1 M KH_2PO_4 + 46.7 cm^3 0.1 M NaOH [30]. The buffered solution was then stirred for ca. 5 seconds, after which the titration with the arsenite solution of unknown normality was begun. Starch indicator was added (4 drops) prior to the buffer addition, and the titration was continued automatically to the colorless endpoint.

For the actual determination of hypohalite[2] in seawater, a 25 cm^3 aliquot was taken from the flask of interest, and placed in a solution of 4 grams of potassium iodide in 35 cm^3 of distilled water. The same amounts of hydrochloric acid, starch indicator, and pH 8.0 buffer were added as above. The previously standardized arsenite solution was then used to titrate automatically to the colorless endpoint.

---

[2] This analysis also includes any hypobromite (OBr^-) and any chlorite (ClO_2^-) which might be present.

III. RESULTS

A. COMPARATIVE CORROSION RATE DATA

Raw data for each of the corrosion measurements are in Appendices B (IML and LPM) and C (PDP). A comparison of the averaged results for each of the three corrosion rate measuring techniques used is presented in Table IV. These numerical data were then converted into histograms for a graphic presentation as Figure 18. The ordinate in this figure is the corrosion rate in μmpy. For each material studied, there are three histograms that correspond to the three different corrosion measurement methods used. The histogram for each method is further divided to show the average corrosion rate obtained in each medium tested. In this way, one may compare the corrosion rates of materials tested, the various methods used for a single material, and the change in corrosion rate of a material by changing the electrolyte. (See the key to Figure 18 for further details.)

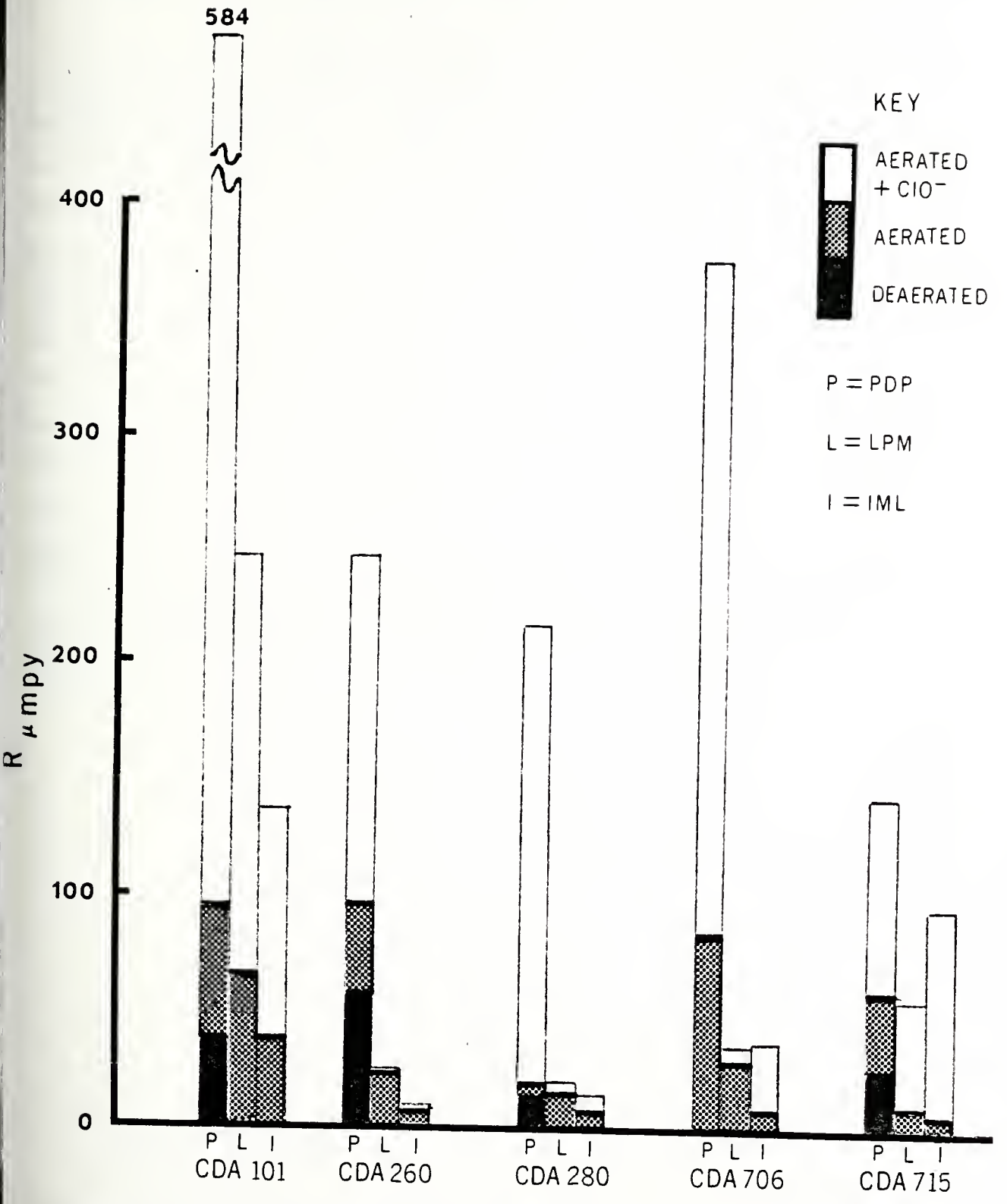

Figure 18. Comparison of the average corrosion rates obtained by the various test methods.

TABLE IV. Comparison of Corrosion Rates Obtained by the Various Test Methods.

Corrosion rate in μmpy.[a]

CDA-ID Number	PDP (aerated)	PDP (deaerated)	LPM (aerated)	IML (aerated)
101-O	94.0	38.1	66.0	37.6
101-H	584	...	249	138
260-O	96.5	58.4	22.6	9.1
260-H	248.9	...	22.9	8.6
280-O	18.3	13.5	14.5	6.9
280-H	211	...	19.8	15
706-O	83.8	...	27.9	5.8
706-H	379	...	35.6	37.6
715-O	58.4	25.4	9.1	4.1
715-H	145	...	55.9	96.3

[a] To convert penetration rates from micrometers per year (μmpy) to mils per year (mpy ≡ 10^{-3} inch per year), divide by 25.4.

B. CORROSION PRODUCT AND SUBSTRATE SURFACE MORPHOLOGY

1. Base Metal Microstructures of the Materials Used

Figure 19 shows an optical micrograph of CDA 101, oxygen-free, high-conductivity copper, prepared from eighth hard rod stock, after polishing to 0.05 μm with alumina and then etching with ferric chloride solution (see Table III, page 32). The grains are of medium to large size, with the average grain size about 150 μm. Grains are generally equi-axed but with irregular borders. A few grains contain twinned areas. Notably absent are the black round or elongate dots of cuprous oxide generally appearing in coppers that have not been specially treated to remove oxygen. The copper-oxygen phase diagram is given in Appendix E, Figure E-2.

Figure 19. Optical micrograph of CDA 101 (100% copper). Specimen polished and then etched in ferric chloride solution. 100X.

Figure 20 shows an optical micrograph of alloy CDA 260, commonly referred to as "cartridge brass." This material received the same polishing treatment as the CDA 101 specimen, but was etched with ammoniacal hydrogen peroxide (see Table III.) This specimen was prepared from annealed rod stock. Here, the grains are well equiaxed, with quite regular borders. Only a very few grains show twinned areas. The average grain size is 120 μm, suggesting that the final annealing temperature was of the order of 630-650°C [31]. There appear to be no inclusions in the crystalling structure.

Figure 21 shows an optical micrograph of CDA 280, known also as "Muntz metal." This specimen was prepared from soft, annealed, half-inch plate stock. This material is a two-phased copper-zinc alloy with dendrites of the alpha phase composition surrounded by a zinc-rich beta matrix. In this micrograph of a polsihed and etched specimen, the zinc-rich beta phase is the dark material; the alpha is the lighter colored one. Here the grains are not equiaxed, but are highly elongated when compressed in the rolling operation. Grains are roughly 100 μm x 20 μm. Stereometric volume fraction analysis confirms the composition of each phase and suggests a final annealing temperature of about 400°C. For details of the stereometric analysis, see Ref. [32]. The copper-zinc phase diagram is shown in Appendix E, Figure E-1.

Figure 22 shows the optical micrograph of 90/10 copper-nickel, CDA 706. The test coupons were prepared from flat stock, and appear to be in the "as-hot-rolled" condition.

Figure 20. Optical micrograph of CDA 260 (70/30 copper-zinc). Specimen polished and then etched in ammoniacal hydrogen peroxide. 100X.

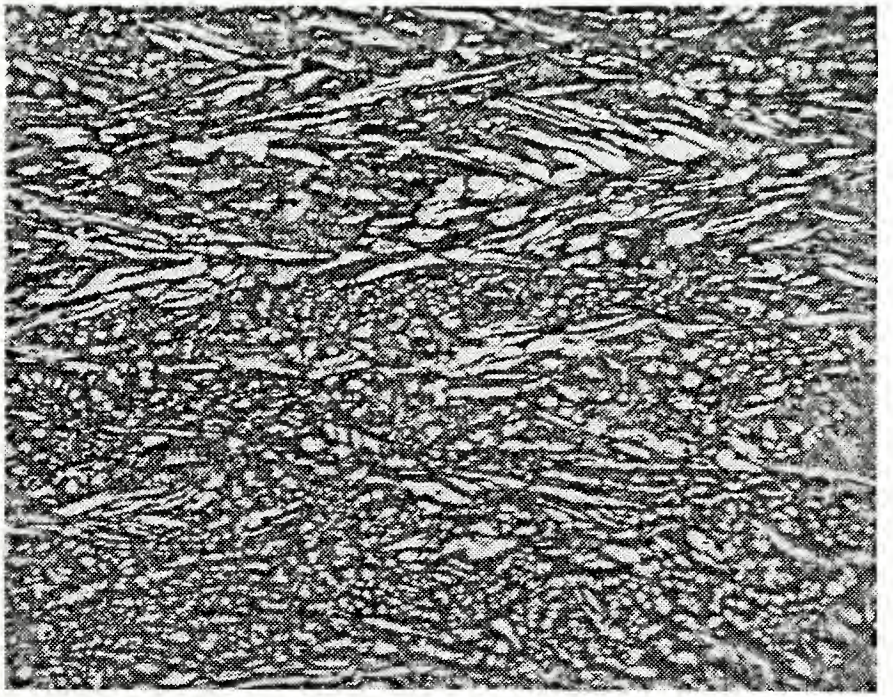

Figure 21. Optical micrograph of CDA 280 (60/40 copper-zinc). Specimen polished and then etched in ferric chloride solution. 100X.

Specimens were polished as above, and etched in ferric chloride. There is some evidence (parallel dark lines) of working of the material. The grains are very large, with their average dimensions being about 300 μm. In general the grain boundaries are sharply distinct, but occasionally there appear particles of impurities segregated to the grain boundaries. This particular alloy contains about 1.5% iron added to it to increase its corrosion resistance.

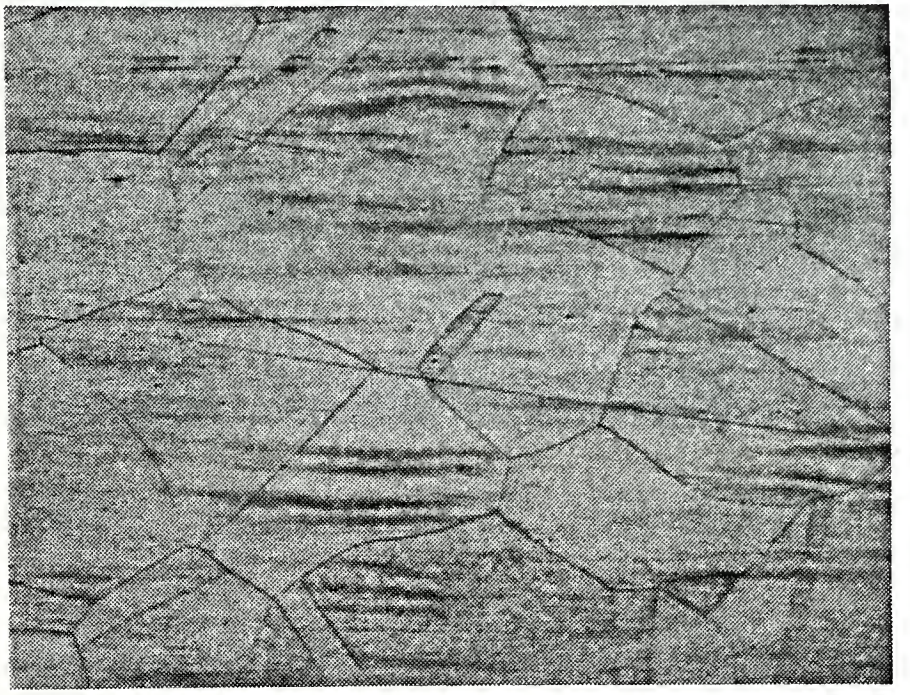

Figure 22. Optical micrograph of CDA 706 (90/10 copper-nickel). Specimen polished and then etched in ferric chloride solution. 100X.

Figure 23 shows alloy CDA 715, 70/30 copper nickel. The specimens were prepared from half-inch plate stock. They also were polished as above and etched in ferric chloride solution. As in the previous photograph, the grains are equiaxed and many contain twinned areas. The material was

used in the "as-hot-rolled" condition. Black spherical inclusions are noted along several of the grain boundaries. The large grains average 200 μm in diameter. The copper-nickel phase diagram is shown in Appendix E, Figure E-3.

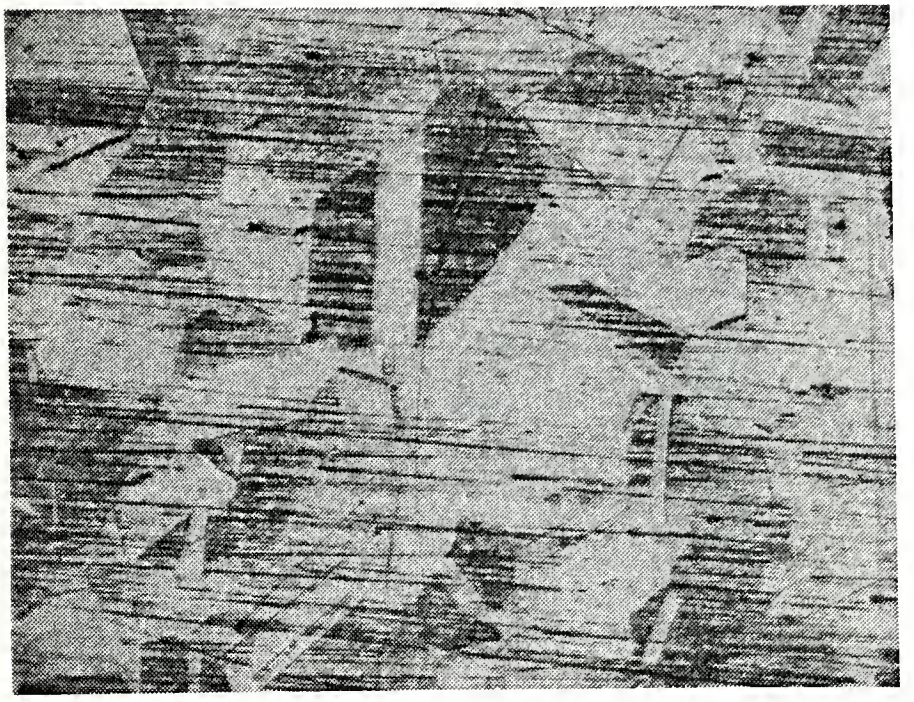

Figure 23. Optical micrograph of CDA 715 (70/30 copper-nickel Specimen polished and then etched in ferric chloride solution. 100X.

It is perhaps most informative to look at the corrosion of the pure copper specimens and then to compare these results with the effects of alloying on corrosion behavior.

2. CDA 101 (OFHC Copper) in Synthetic Seawater

a. Results With No Added Hypochlorite Ion

It was seen in the base metal micrograph (Figure 19) that the copper specimens possessed uniform grain size and shape with virtually no impurities present either within the grains or at the grain boundaries. In the IML

experiments, the CDA 101 test coupon (oxygen-free copper) was bright and shiny and copper-colored when originally immersed in the aerated synthetic seawater. After 34 days, it appeared reddish purple over the whole surface. There did not appear to be any localized corrosion. There were, however, a series of "claw-shaped" crystals spread uniformly over the surface as seen in Figures 24 and 25.

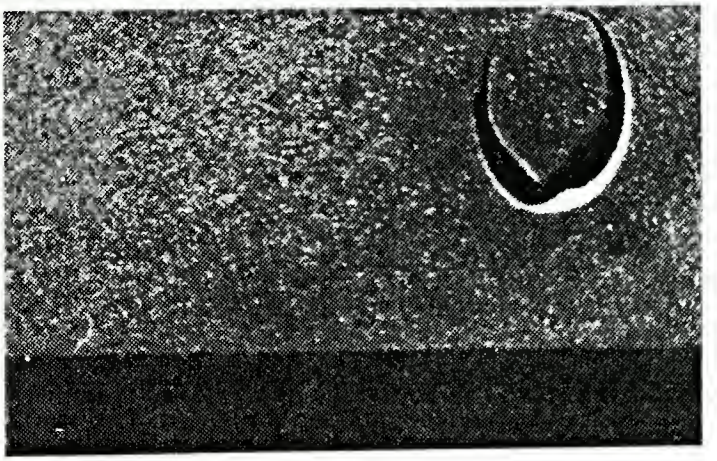

Figure 24. "Claw-shaped" crystals spread over the surface of the CDA 101 IML specimens after 34 days' exposure to aerated synthetic seawater. (7.2X).

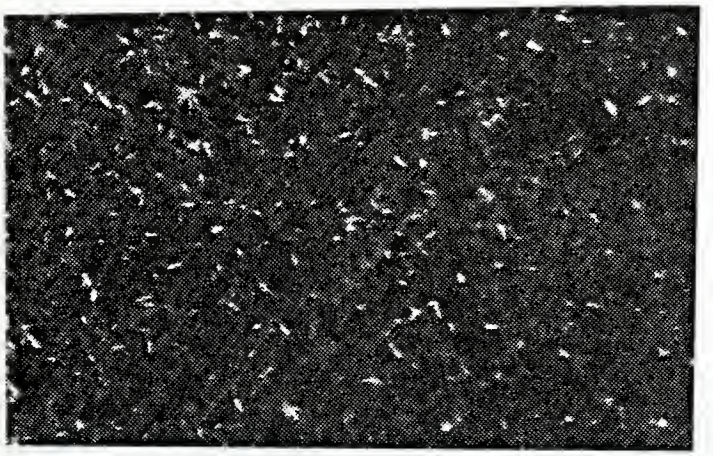

Figure 25. "Claw-shaped" crystals spread over the surface of the CDA 101 IML specimens after 34 days' exposure to aerated synthetic seawater. (52.5X).

Upon examination of the uncleaned surface by scanning electron microscopy, these crystals were shown to be uniformly distributed over the surface (see Figures 26 and 27).

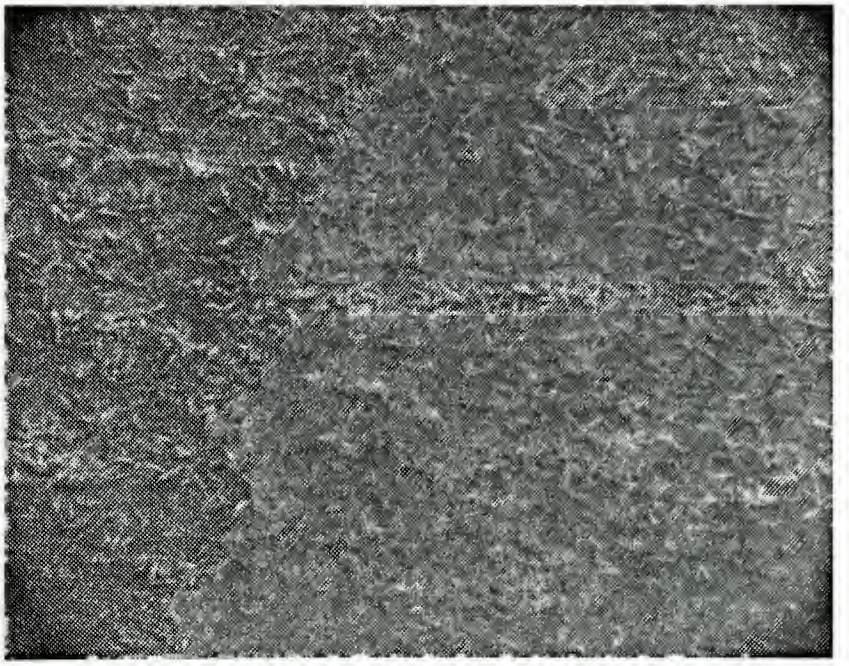

Figure 26. Scanning electron micrograph of "claw-shaped" crystals distributed over surface of CDA 101 IML specimens. (112X).

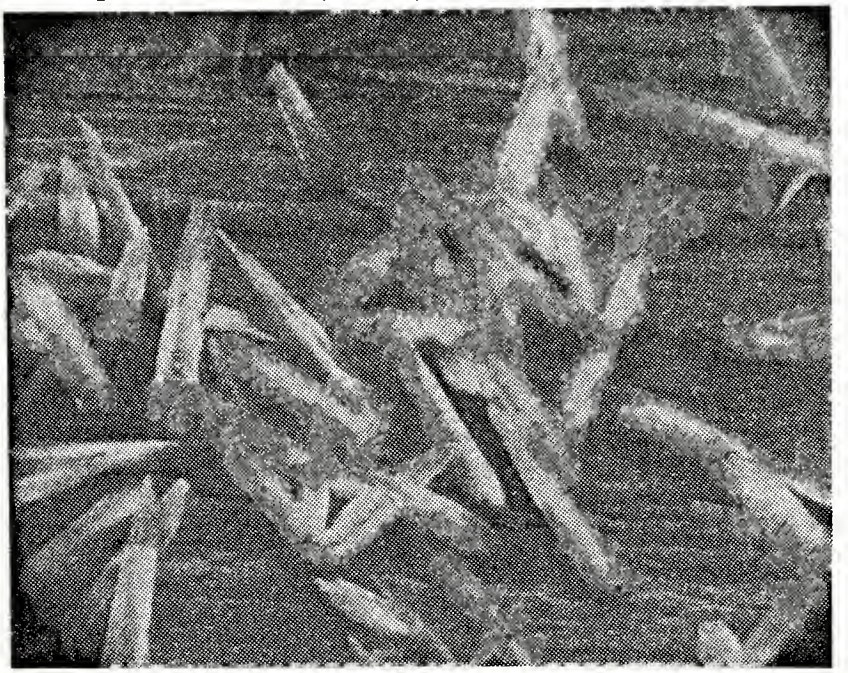

Figure 27. Scanning electron micrograph of "claw-shaped" crystals distributed over surface of CDA 101 IML specimens. (1120X).

An X-ray fluorescence spectrum of the crystals showed the presence of large amounts of calcium, suggesting that they were calcium carbonate formed on the aeration of the synthetic seawater. Figure 28 demonstrates this spectrum.

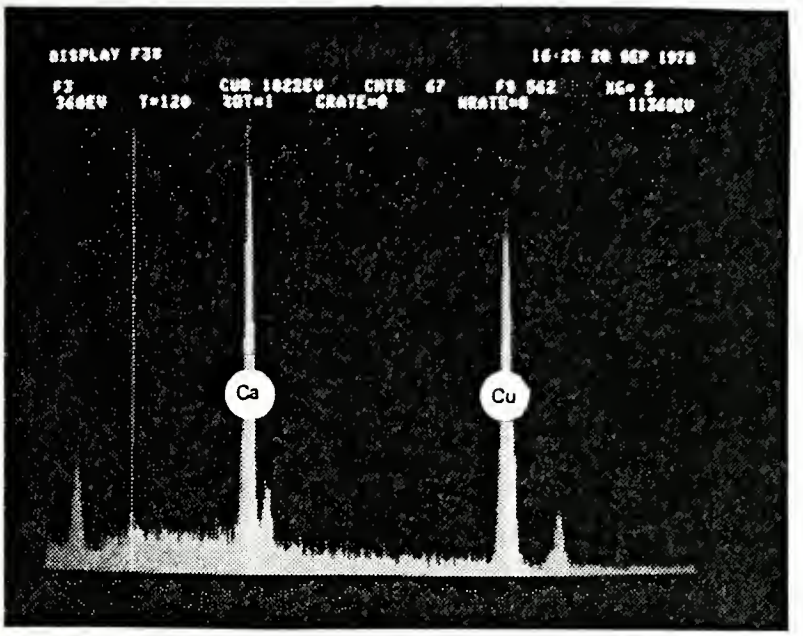

Figure 28. X-ray fluorescence spectrum of "claw-shaped" crystals from CDA 101 IML specimens, showing presence of strong calcium line.

These crystals did not appear to grow out of the surface of the specimen; rather, they looked as if they had simply crystallized on top of the metal.

Examination of the cleaned surface indicated the presence of minute pits, each surrounded by a thin patina of corrosion product, as shown in Figures 29 and 30.

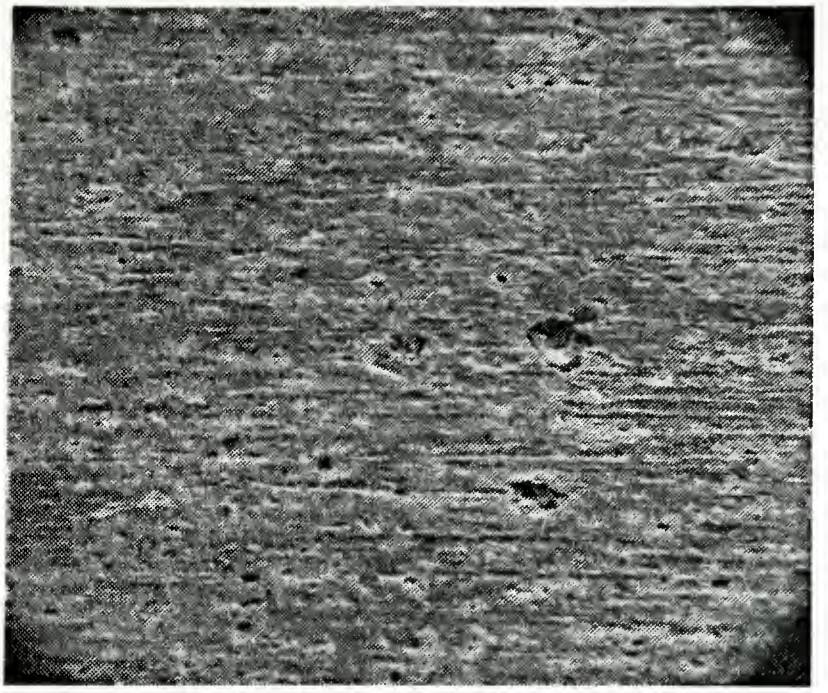

Figure 29. Minute pits observed on the cleaned surfaces of CDA 101 IML specimens. (130X).

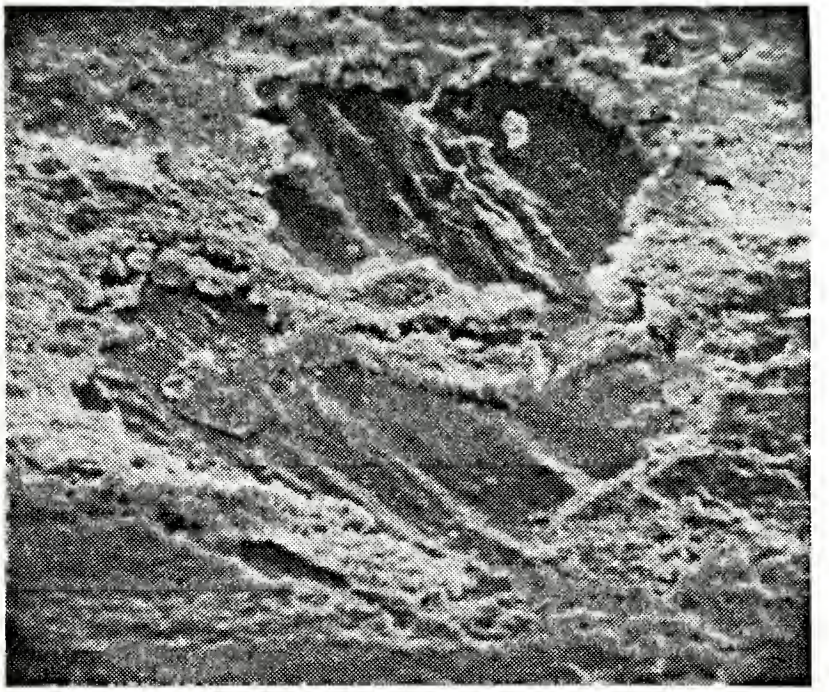

Figure 30. High magnification SEM micrograph of localized corrosion on the cleaned surface of CDA 101 IML specimen. (1300X).

When CDA 101 specimens were corroded in the PSP tests, there was a progressive film-forming activity on the surface. Visually, the specimen developed a deep-brown adherent coating that increased in thickness with the duration of the test. Figure 31 shows a spot where some of the film fell off the coupon.

Figure 31. Defect in corrosion product film covering CDA 101 PSP test coupon. (750X).

Figure 32 shows this area at higher magnification, displaying the formation of a faceted structure by localized corrosion in this area. At longer exposure times, this film becomes thicker and more tightly adherent. This is shown in Figure 33.

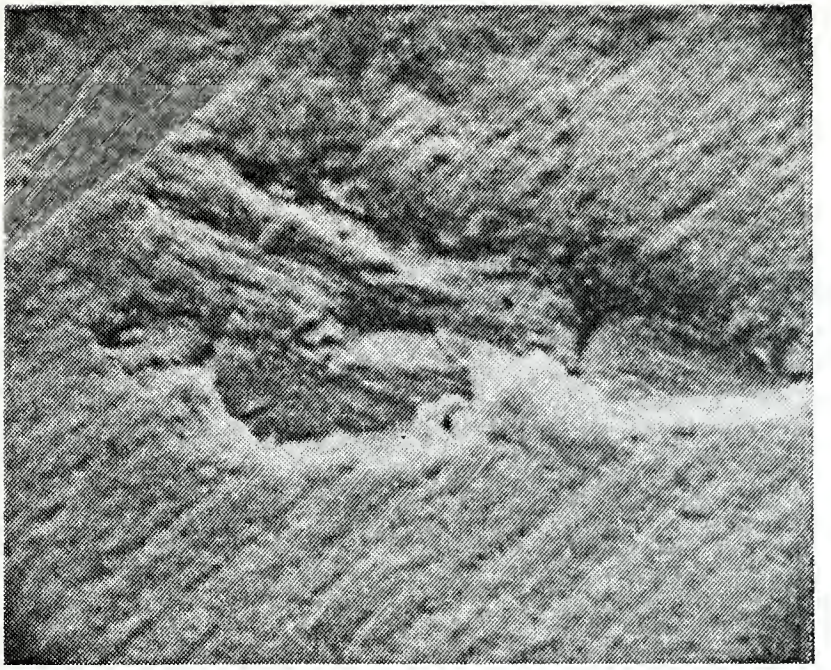

Figure 32. Local defect in corrosion film formed on CDA 101 PSP test coupon, showing formation of a faceted area beneath film. (1500X).

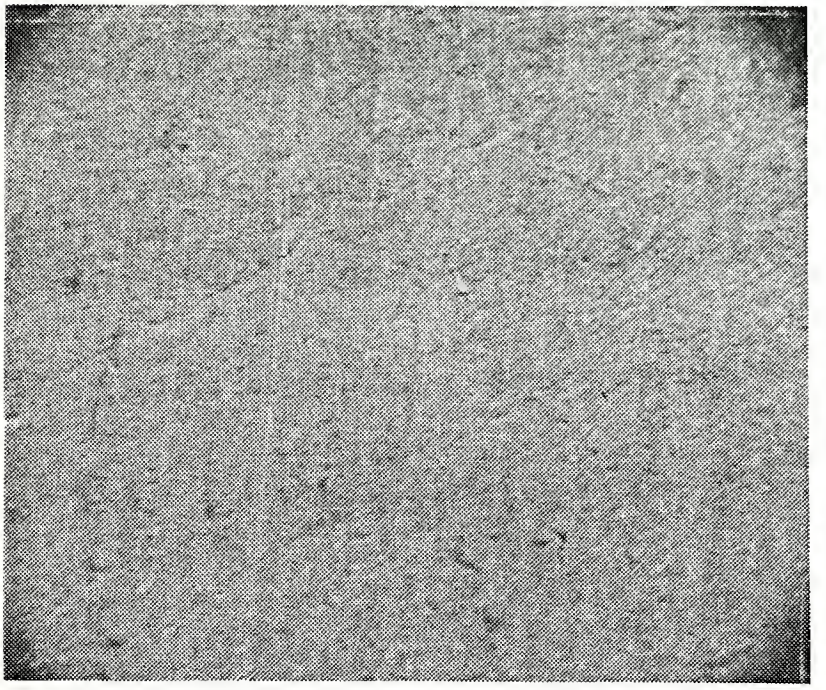

Figure 33. Scanning electron micrograph of the tight, compact film adhering to the surface of CDA 101 PSP test coupon, exposed for four hours to aerated synthetic seawater. (296X).

Figure 34 shows the X-ray fluorescence spectrum delineating the presence of silicon and sulfur in the corrosion product.

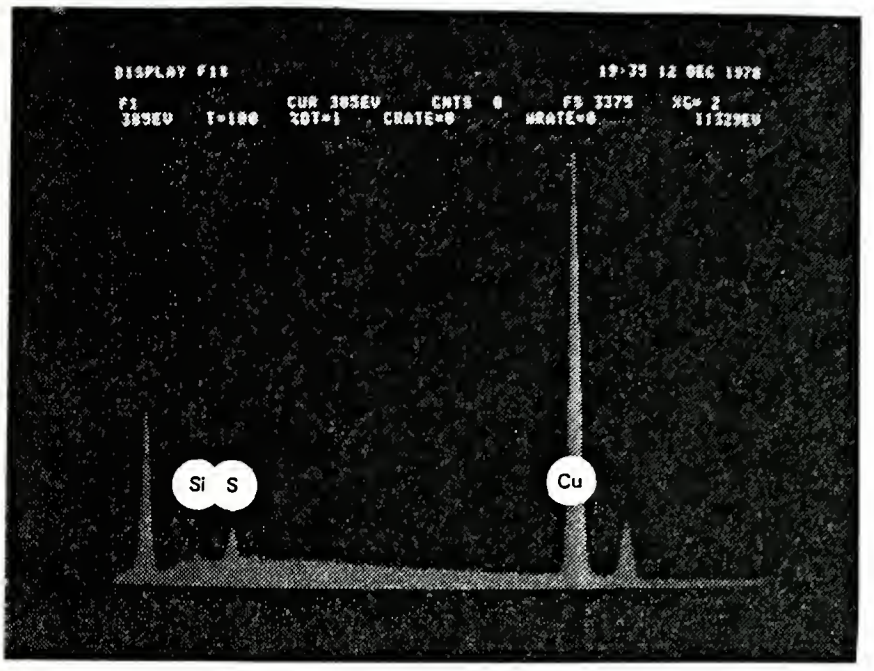

Figure 34. X-ray fluorescence spectrum of the compact adherent film shown in Figure 33. Small amounts of sulfur and silicon are present. in addition to the copper lines.

At still longer exposure times, surface pitting appears to be uniform over the whole surface as shown in Figure 35. Here a piece of the corrosion product film has broken away.

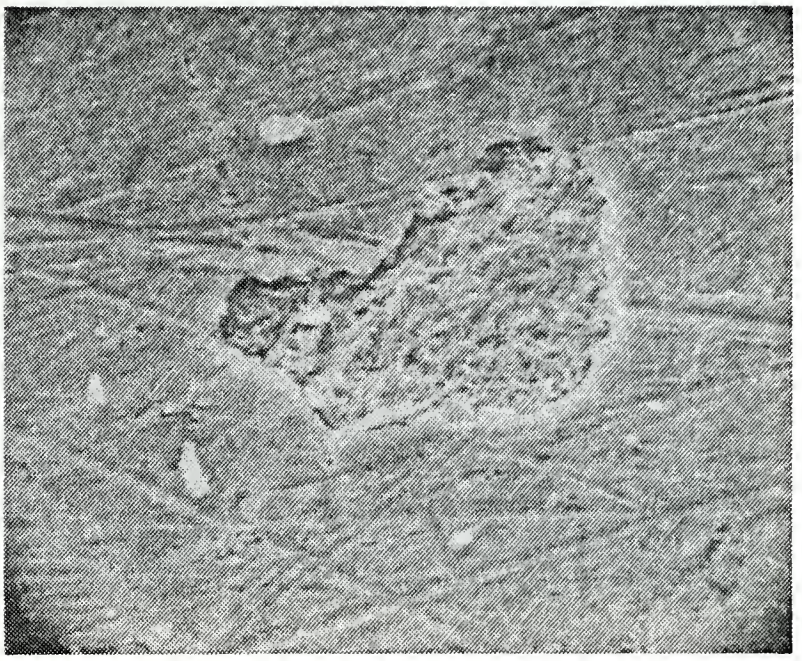

Figure 35. SEM micrograph of pitted area beneath corrosion product film. (1550X).

It is of interest to see that there is preferred etching/pitting in the deeper machine marks while more general corrosion prevails in the shallow ones. This is shown in Figures 36, 37, and 38.

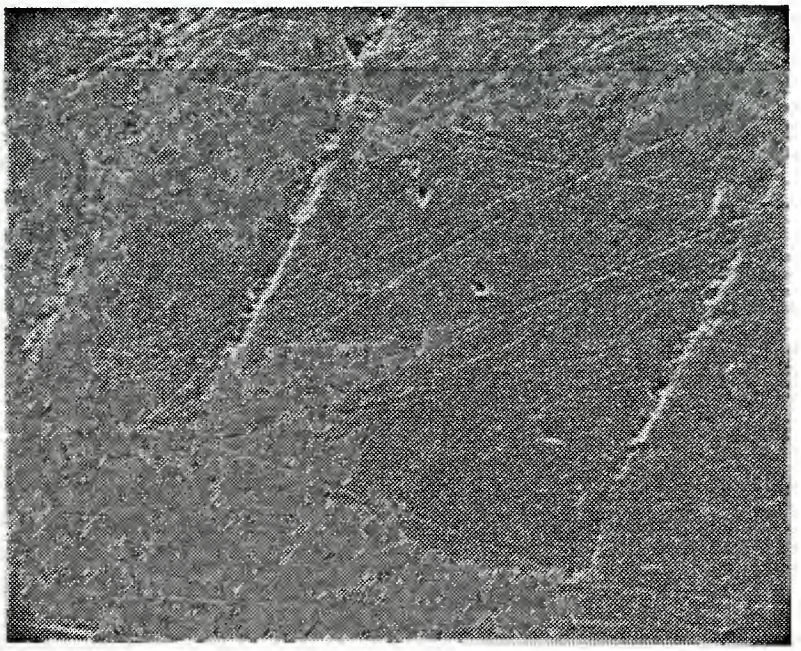

Figure 36. Localized corrosion at deep machine marks on CDA 101 PSP coupon. (394X).

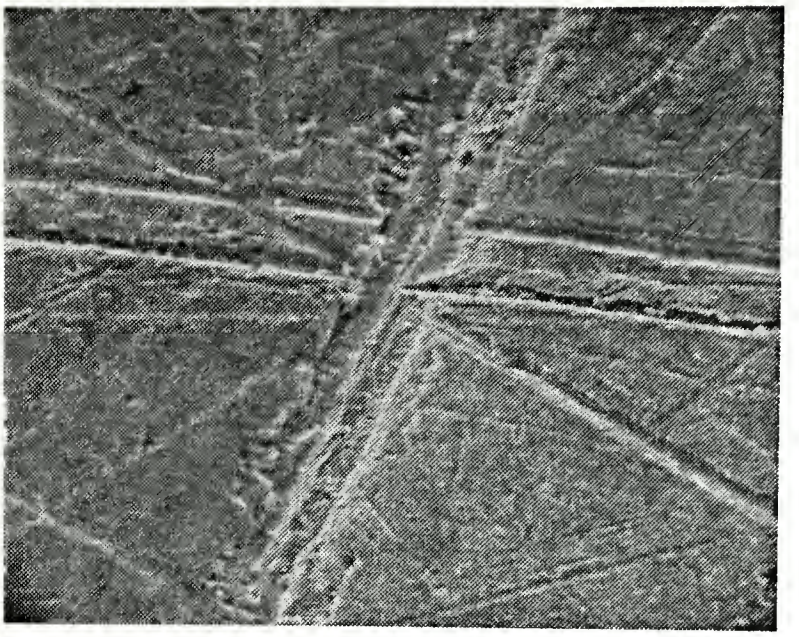

Figure 37. Preferential corrosion about deep machine marks on CDA 101 PSP test specimen. (745X).

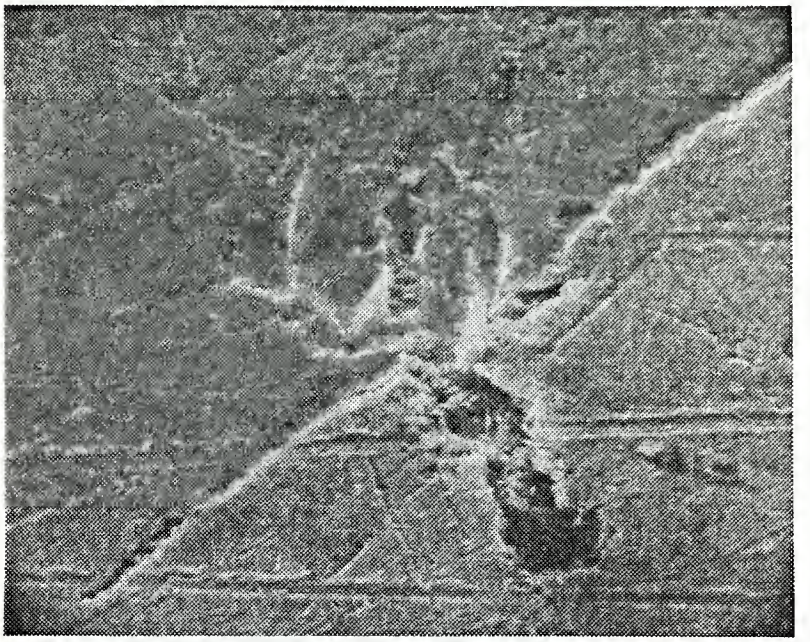

Figure 38. Preferential corrosion at deep machine mark and faceted area of localized corrosion. (130X).

General observations are, then, that copper immersed in aerated synthetic seawater initially corrodes by minute surface pitting and that these minute pits may later merge to give a more generalized corrosion mode. There is also selective corrosion at

deep machine marks. (See also Figures 188 and 194, which are macrophotographs of CDA 101 after immersion in the two different electrolytes).

b. Results With 200 ppm Added Sodium Hypochlorite

The IML tests with CDA 101 immersed in aerated synthetic seawater containing 200 ppm sodium hypochlorite were dramatically different from those without added hypochlorite ion. The base metal (where visible) was greyish-purple, but it was generally covered with a thin layer of whitish rounded crystals. These are shown in Figure 39.

Figure 39. Light macrograph of CDA 101 IML coupon after immersion in aerated synthetic seawater containing 200 ppm sodium hypochlorite. The upper part of the photo shows where the greenish corrosion product appeared to run down the face of the specimen. Rounded, whitish crystals were common on the bottom two-thirds of the specimen. (7.5X).

There was a crystalline material of bright green which was ca. 2-3 mm thick and which appeared to run down from the top of the specimen. A close-up of the green material is shown in Figure 40.

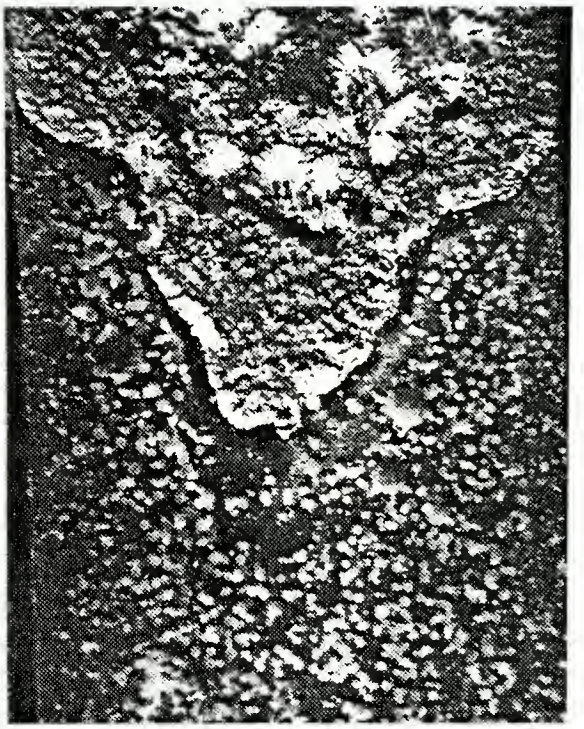

Figure 40. Green crystalline material from upper part of CDA 101 IML coupon. (27X).

At the interface between the green crystalline material and the rounded white crystals was a thin layer of black material. This is shown in Figures 41 and 42.

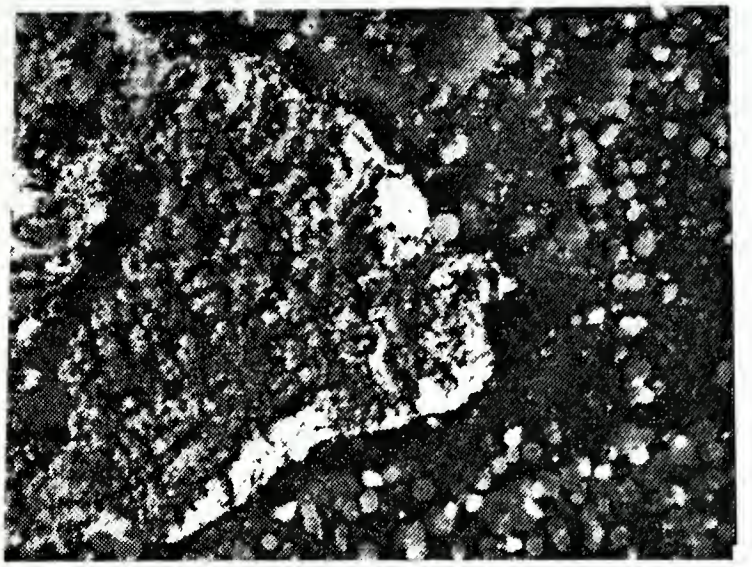

Figure 41. Black demarcation line between green crystalline material and rounded, whitish crystals. (15X).

Figure 42. Enlarged view of black demarcation line shown in Figure 41. (27X).

Observation by SEM was somewhat difficult since the corrosion products tended to become charged (glow brightly) in the electron beam. The rounded nodules seen on the lower part of the specimen of Figure 39 are shown in Figure 43.

Figure 43. SEM photograph of rounded crystals of Figure 39. (50X).

X-ray fluorescence analysis of the rounded crystals showed a high concentration of calcium, with lesser amounts of chlorine and traces of silicon, sulfur, and magnesium present. (No photo taken of the display.) X-ray fluorescence analysis of the greenish, thick crystalline deposit showed moderately strong lines for chlorine and copper and perhaps a bromine line, but no calcium. After rinsing the specimens with deionized water and air drying, re-examination by SEM commenced. It was immediately obvious (see Figure 44) that under the green precipitate preferential etching at the grain boundaries was occuring with no obvious pit formation evident. It appeared that copper was being removed in layers or planes (see Figure 44), and that in many spots tightly adherent crystals were attached to the base metal.

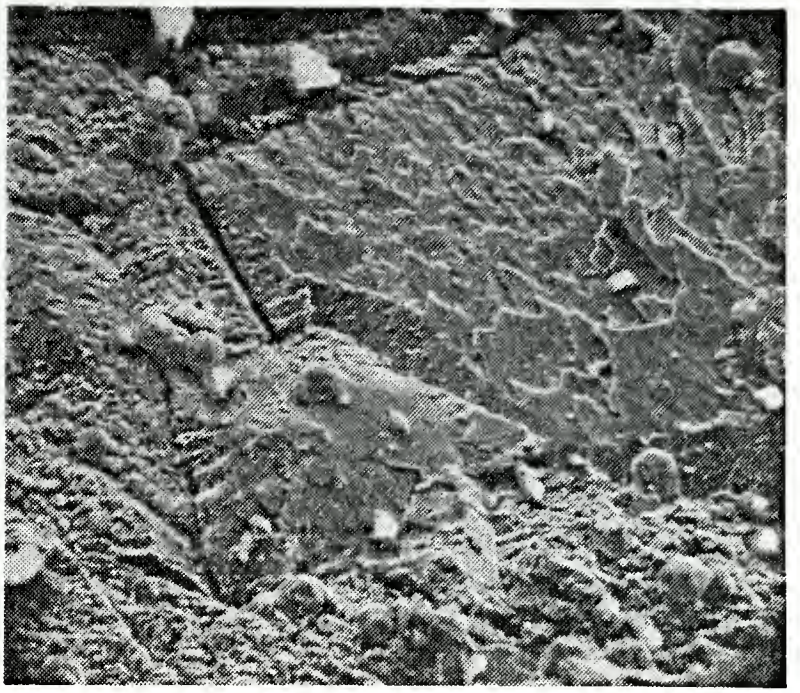

Figure 44. Preferential grain boundary corrosion in CDA 101 IML experiments with added sodium hypochlorite. (630X).

These crystals showed equal development of the cubic (100), octahedral (111), and dodecahedral (110) planes as shown in Figure 45 (see Ref. 33 for a discussion of this phenomenon). X-ray fluorescence analysis shows strong copper lines and a trace of chlorine present (no photograph taken). [Note: Since X-ray fluorescence analysis does not show the presence or absence of oxygen, one cannot be sure of the composition of the species mentioned. However, copper oxides are essentially dielectrics, and should charge up in the electron beam. These crystals do not charge up in general. Also, natural elemental copper deposits near Lake Superior show the same crystal structure as is seen here, indicating that these might indeed be elemental copper crystals (Ref. 34).] High

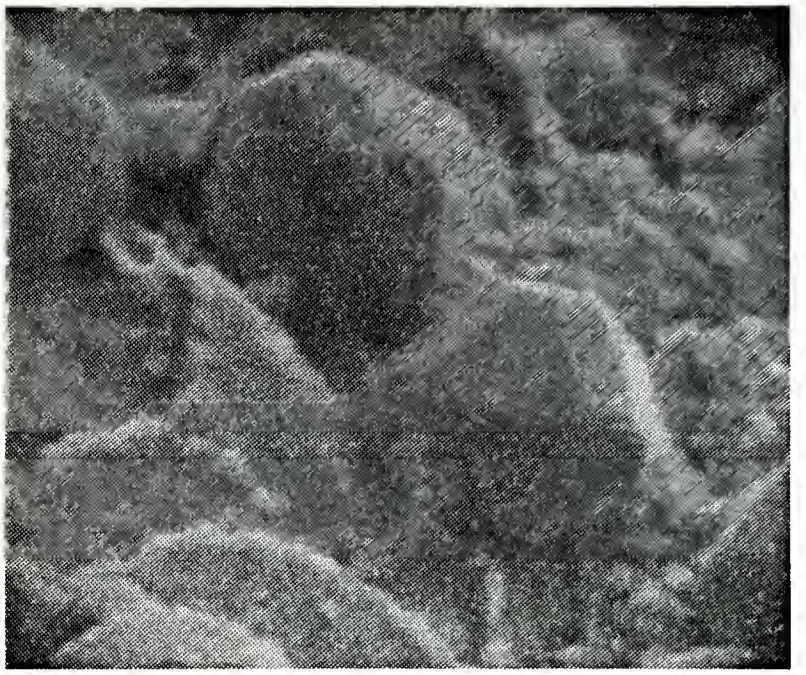

Figure 45. High-magnification SEM micrograph of crystals with mixed cubic, octahedral, and dodecahedral geometries. From CDA 101 IML experiments with added hypochlorite ion. (3750X).

magnification views of the surface continued to show the step-like etching away of planes with a porous matrix virtually all over the specimen where dissolution was actively proceeding. Figures 46 and 47 illustrate this effect.

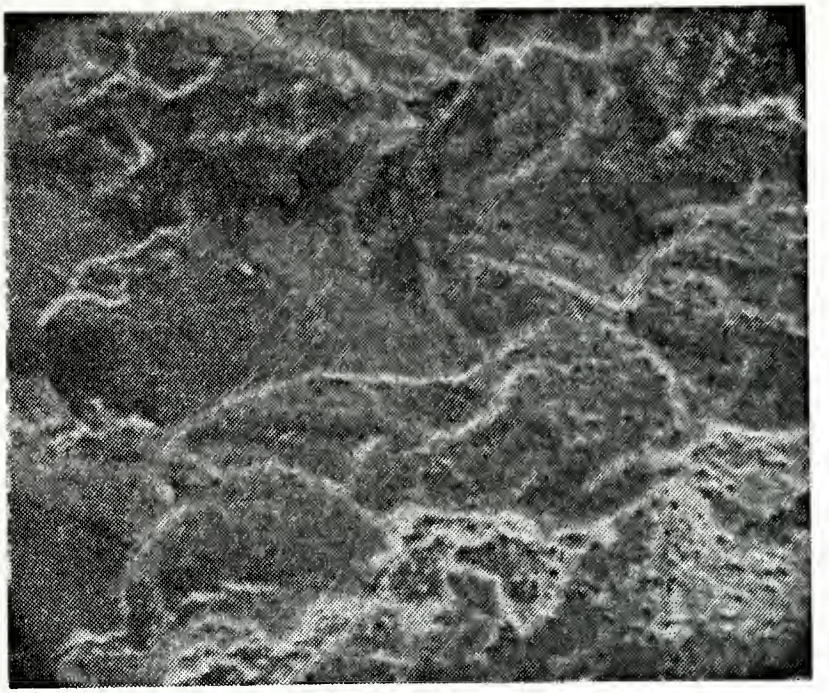

Figure 46. Step-like etching of CDA 101 inside grains. From IML experiments with added sodium hypochlorite. (2200X).

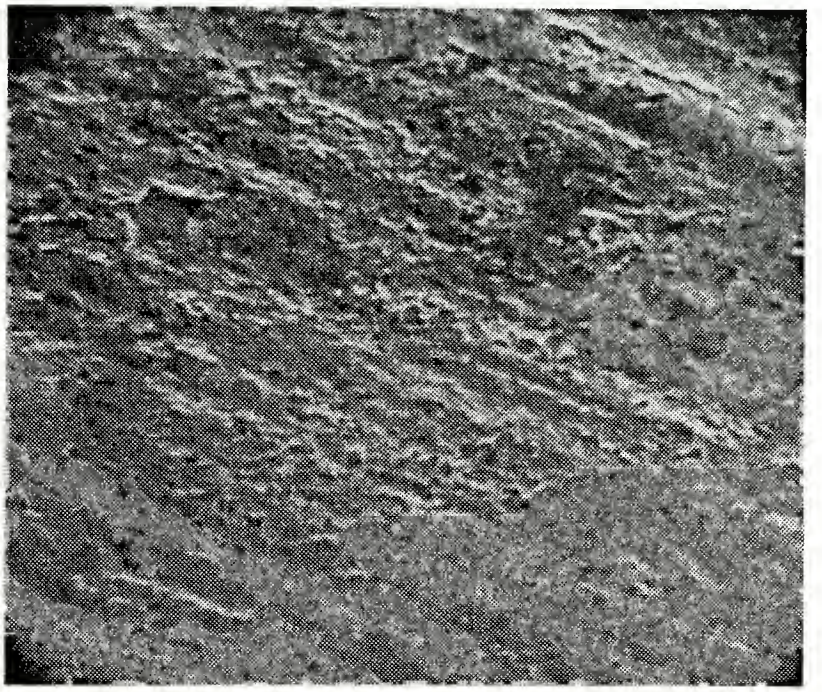

Figure 47. Porous matrix due to the corrosion of CDA 101 in aerated seawater containing 200 ppm sodium hypochlorite. (220X).

Upon chemical cleaning to remove all corrosion products, a network with a distinct granular appearance was evident on the surface, showing complementary crystallinity to the mixed cubic/octahedral/dodecahedral particles that were removed. (See Figure 48.) Grain boundaries are still seen to be preferentially corroded as shown in Figures 48 and 49.

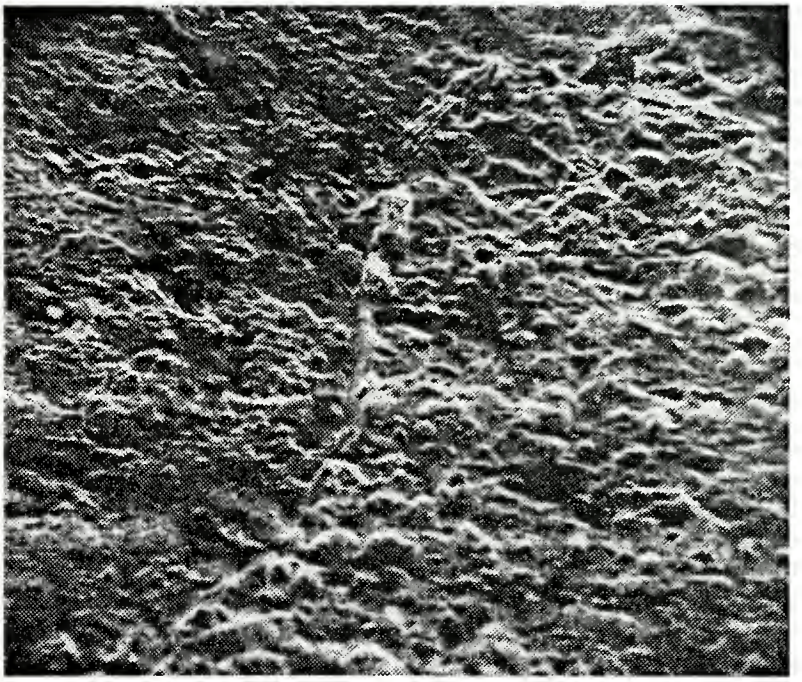

Figure 48. Minutely faceted surface of cleaned CDA 101 IML coupon. Preferentially corroded grain boundary evident in center. (625X).

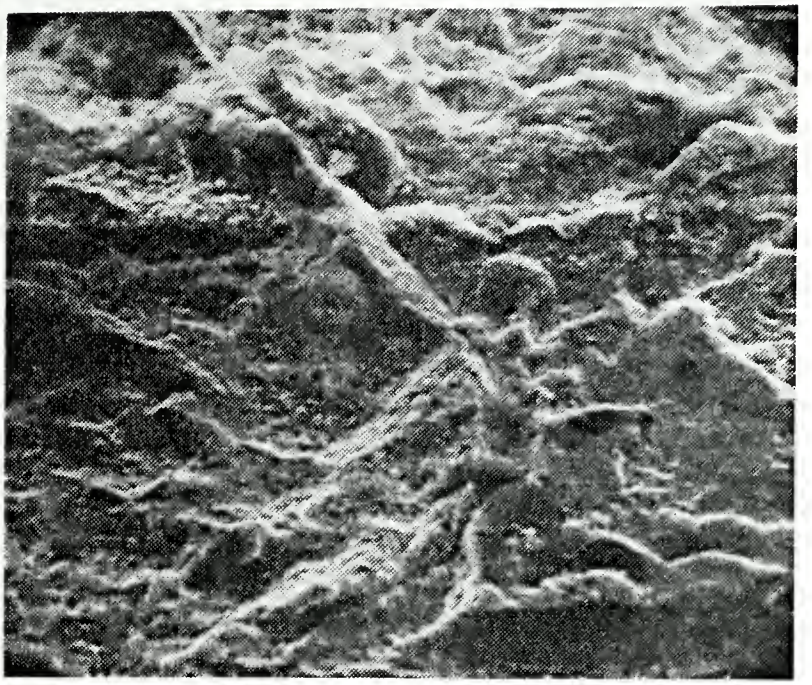

Figure 49. Junction of three grain boundaries, all of which have been preferentially corroded with respect to the grain interior. From the CDA 101 IML experiments with added sodium hypochlorite. (1310X).

Potentiostatic polarization (PSP) runs show a rapid filming of the surface of the specimens with a loosely adherent corrosion product of whitish green, and a thin, compact, dark-brownish film that is more tightly adherent. Scanning electron microscopy examination of coupon surfaces at low magnification (Figure 50) shows the dark film that charges up in the electron beam somewhat. It was anticipated that the dark-brown material might be one of the copper oxides or chlorides. X-ray fluorescence analysis showed the presence of copper and chlorine. See Figure 51. The low magnification photograph also shows the presence of what appear to be mounds on the surface, but when these are magnified as in Figure 52, they are shown to be simply aggregations of particles giving the same X-ray fluorescence analysis as that of the gross surface.

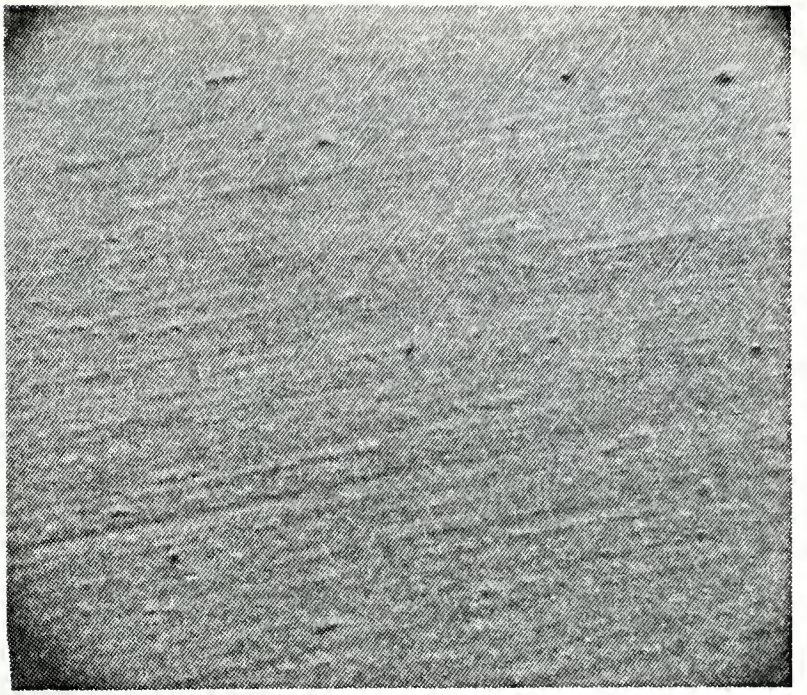

Figure 50. Black dielectric film formed during PSP runs with CDA 101 with added hypochlorite ion. (71X).

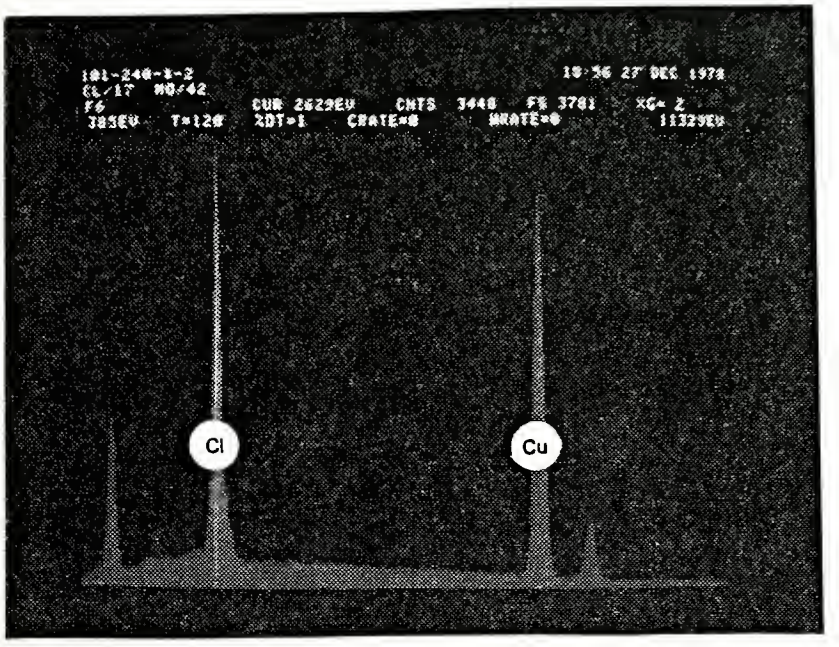

Figure 51. X-ray fluorescence analysis of dark brown-black, thin film formed during PSP runs on CDA 101 with added hypochlorite ion.

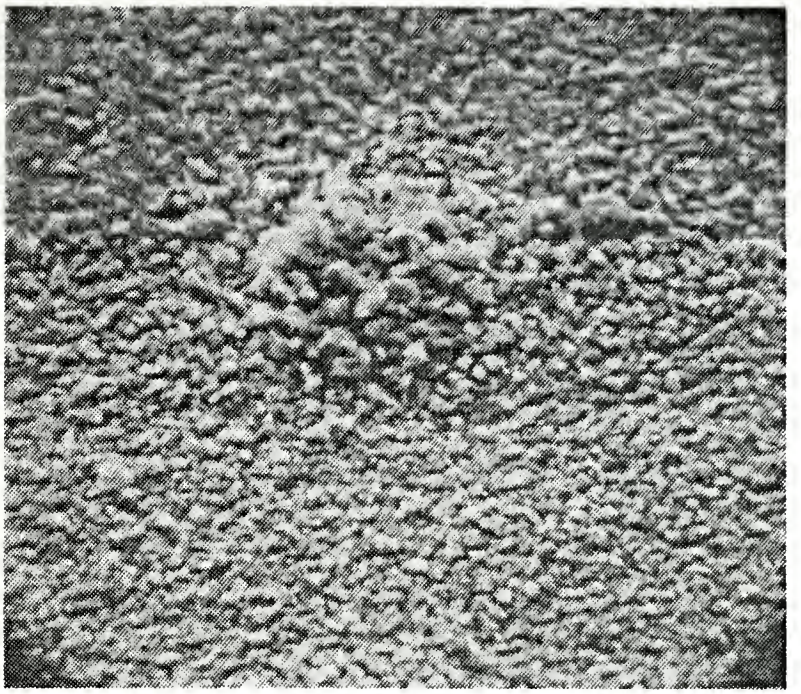

Figure 52. Close-up of aggregation of small particles at intersection of three grain boundaries. Potentiostatic polarization runs of CDA 101 in aerated synthetic seawater with added hypochlorite ion. (1207X).

In summary, hypochlorite ion in aerated synthetic seawater is very corrosive towards copper, with the grain boundaries being attacked preferentially. A complicated dissolution/precipitation process is indicated by the presence of porous pitting over most of the surface and by the complex cubic crystallites of pure copper present. The pitting and dissolution/precipitation appear to be carried out beneath the corrosion product blanket, which contains copper, chlorine, bromine, and, no doubt, oxygen as the oxides or the hydroxides of copper. See also Figures 188 and 194, which are macrographs of CDA 101 after immersion in the two different electrolytes.

3. The Copper-Zinc Alloys (The Brasses)

The brasses were originally developed because they were cheaper than unalloyed copper. In addition, they offer increased cold-formability (up to 30% zinc) and increased static and fatigue strengths [35]. Their resistance to corrosion in various media tends to correlate with the amount of zinc present in the alloy.

a. CDA 260 (70/30 Copper/Zinc--"Cartridge Brass") in Synthetic Seawater

(1) Results Without Added Hypochlorite Ion. Examination of cartridge brass samples corroded in the IML experiments showed a grey-white, patchy deposit over the surface (Figure 53) with small circular areas between the patches as if bubbles had been attached (Figure 54).

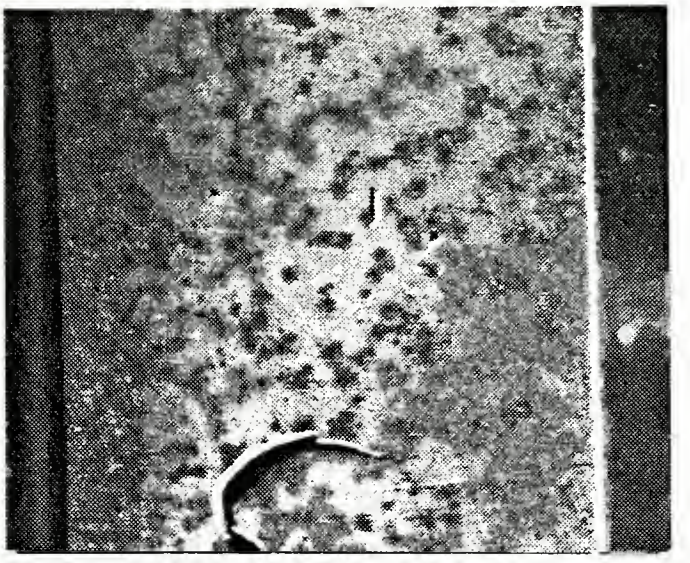

Figure 53. Patchy, grey-white corrosion product distributed over the surface of CDA 260 IML experimental coupon in aerated synthetic seawater. (7.5X).

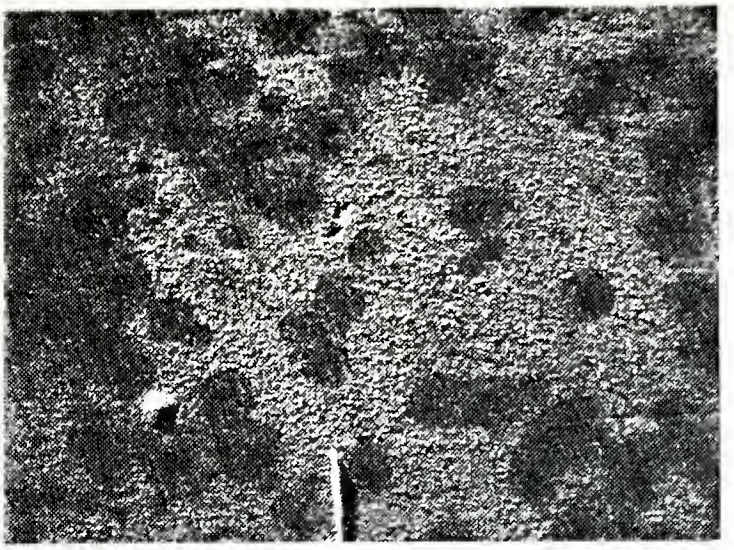

Figure 54. Circular areas interspersed in the white corrosion product observed on CDA 260 IML coupon after immersion for 34 days in aerated synthetic seawater. (22.5X).

On closer examination of the surface by SEM, there appears to be a very thin, whitish film with small particles spread over it except where dark, circular areas occur. This is shown in Figure 55.

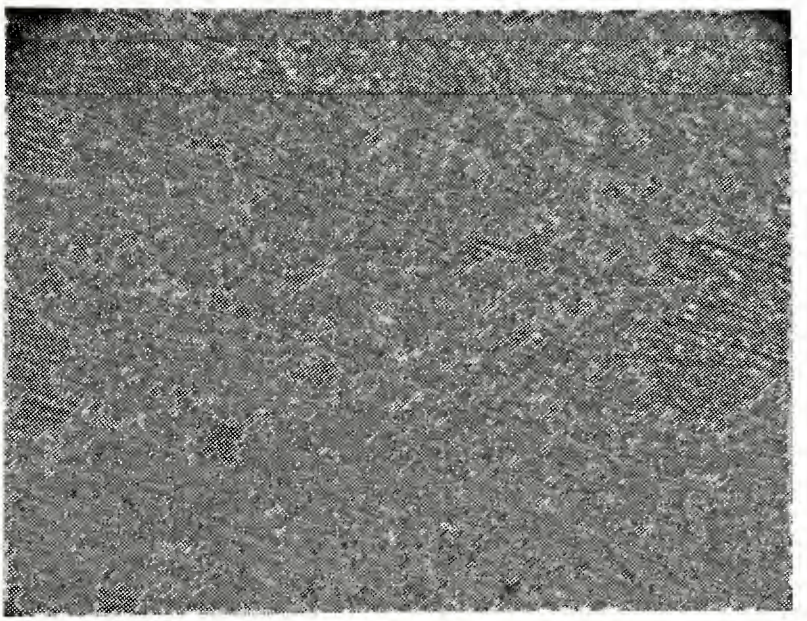

Figure 55. Small particles spread over thin dielectric film produced as the result of 34-day immersion in aerated synthetic seawater. (224X).

These particles were analyzed by X-ray fluorescence methods to show the presence of the copper-zinc base metal as well as smaller amounts of calcium, bromine, chlorine, sulfur, and silicon (Figure 56).

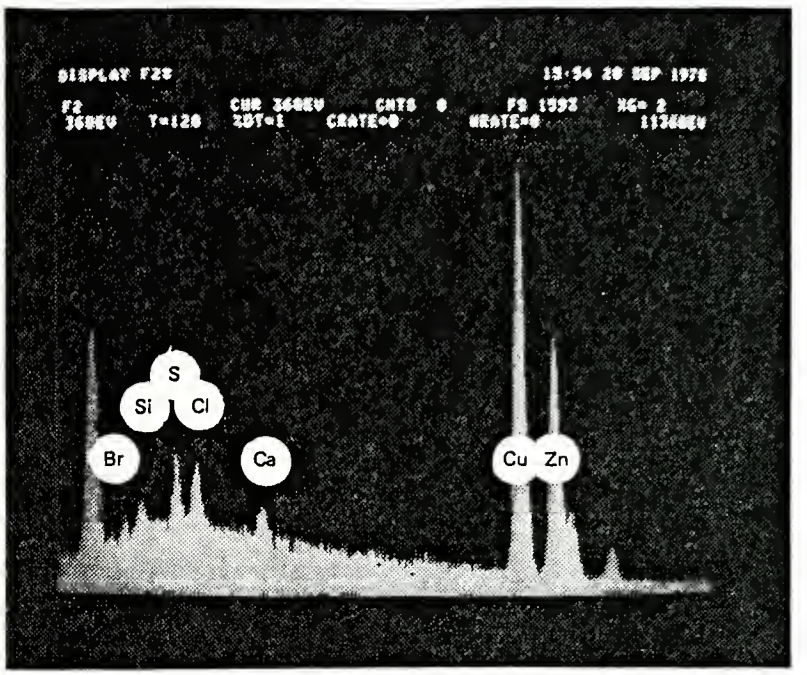

Figure 56. X-ray fluorescence analysis of white particles of Figure 54.

When the IML specimens were cleaned to remove corrosion products, a generally porous structure was shown to exist with no obvious preferential corrosion. Figures 57 and 58 illustrate this porous surface.

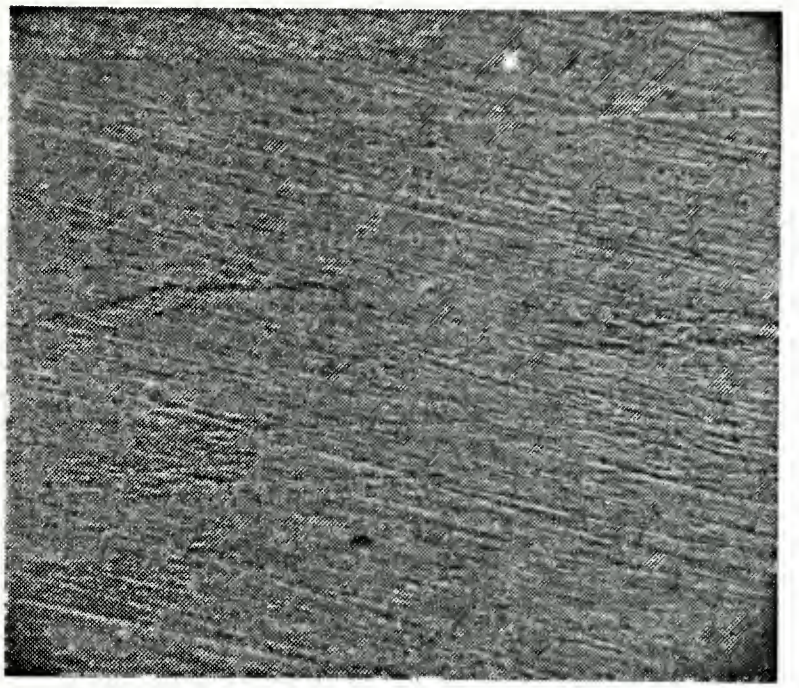

Figure 57. Generally porous nature of the surface of CDA 260 IML coupon after chemical cleaning. (132X).

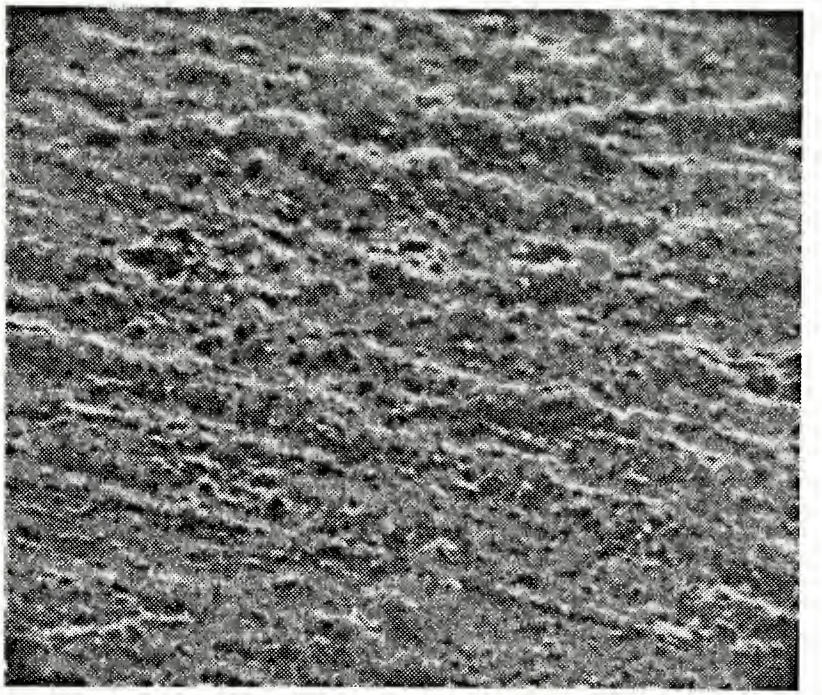

Figure 58. Close-up view of porous surface of CDA 260 IML test coupon exposed to aerated synthetic seawater for 34 days and then cleaned of corrosion products. (1330X).

In the early stages of corrosion, a thin, compact film forms that becomes charged in the electron beam (Figure 59).

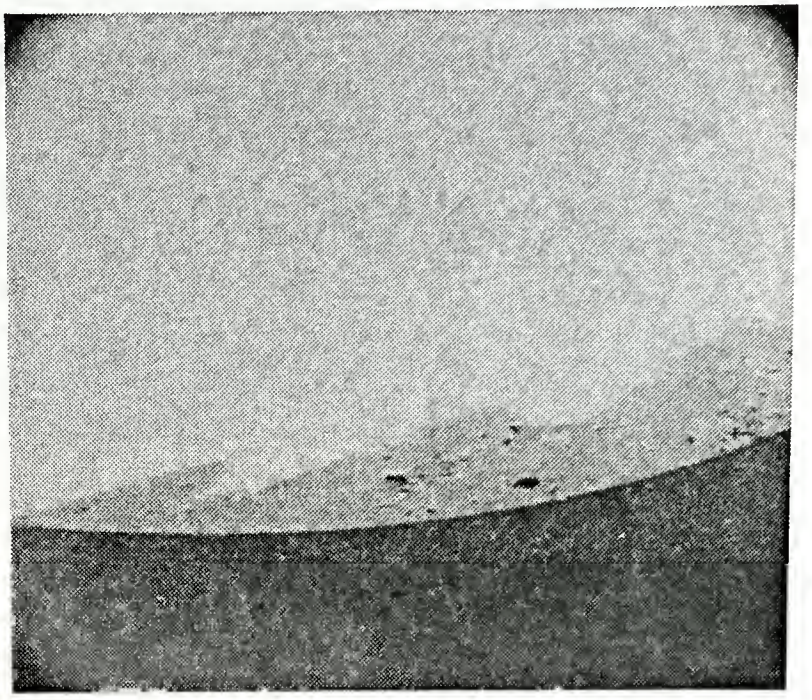

Figure 59. Compact dielectric film (white) forming on short potentiostatic polarization exposure of CDA 260 to aerated synthetic seawater. (32X).

As corrosion progresses, the film thickens and apparently becomes somewhat porous (Figure 60).

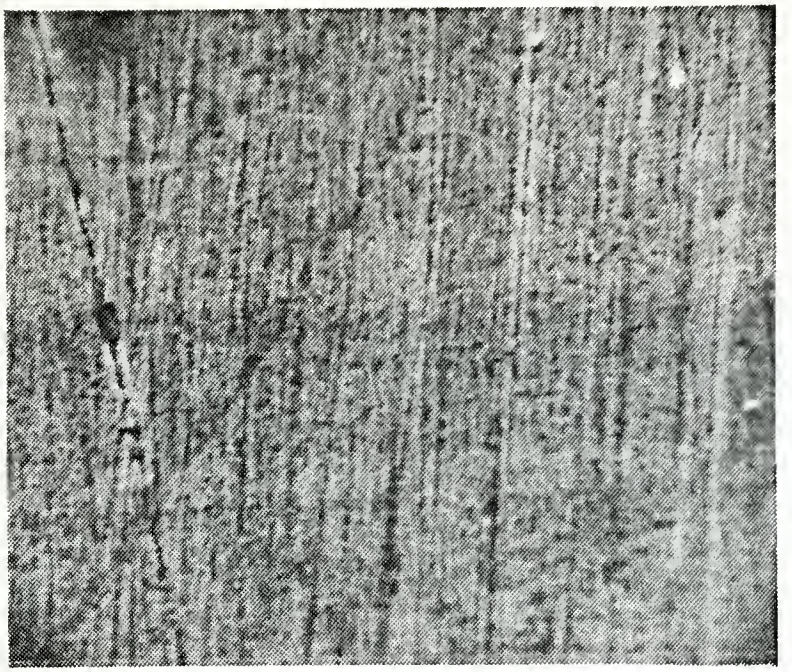

Figure 60. SEM micrograph of the porous nature of film adhering to CDA 260 PSP coupon exposed to aerated synthetic seawater. (910X).

At yet longer times, the film continues to thicken (Figure 61).

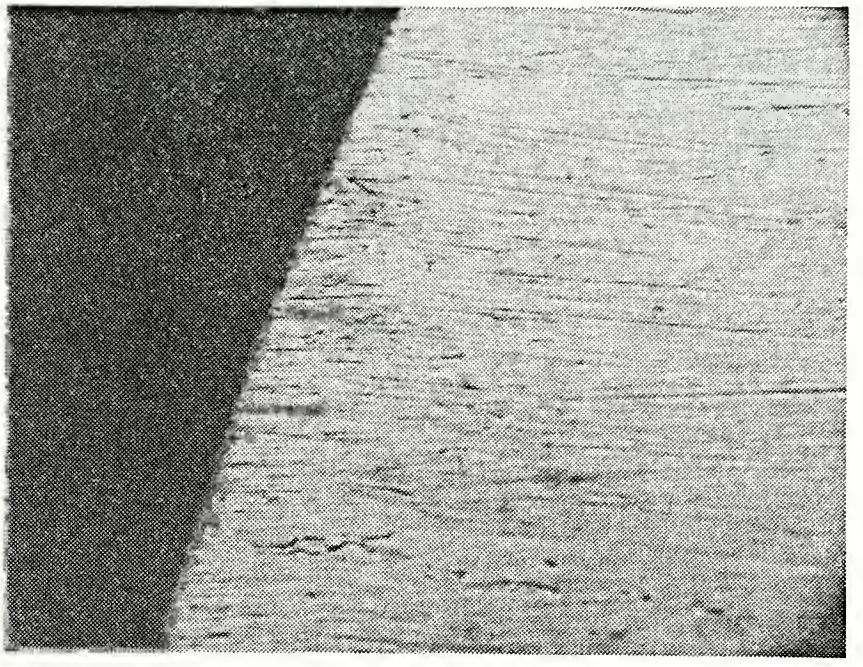

Figure 61. Low magnification SEM micrograph of surface of CDA 260 PSP test exposed to aerated synthetic seawater for 4 hours. Some pinholes through the film are noted. (165X).

X-ray fluorescence analysis of the surface shown in Figure 61 reveals the presence of the base metal (copper plus zinc) along with small amounts of bromine and sulfur. See Figure 62.

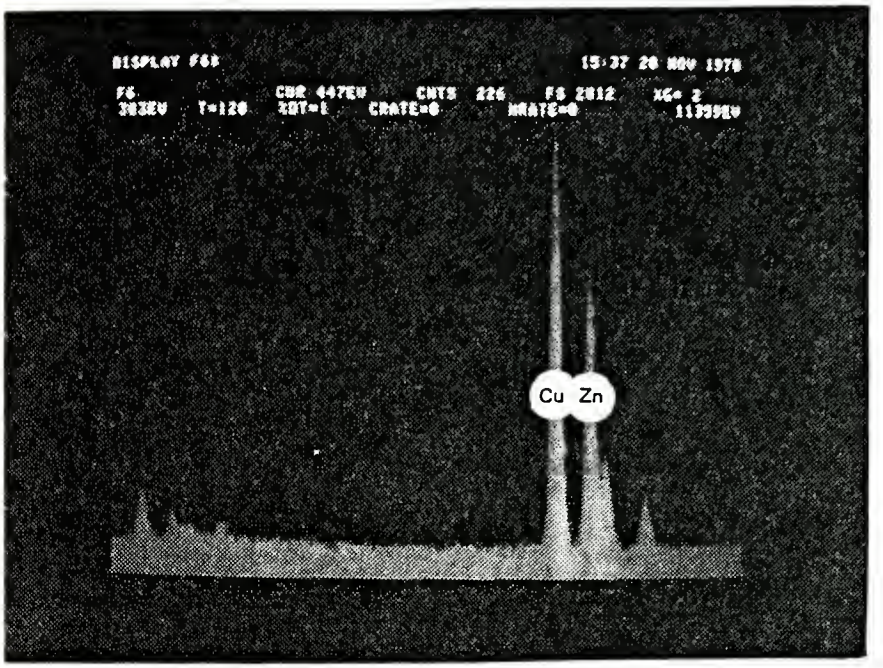

Figure 62. X-ray fluorescence analysis of corrosion film formed on CDA 260 PSP test coupon exposed to aerated synthetic seawater.

Removal of the corrosion products shows definite pitting (Figure 63) as well as initiation of grain boundary attack (Figure 64).

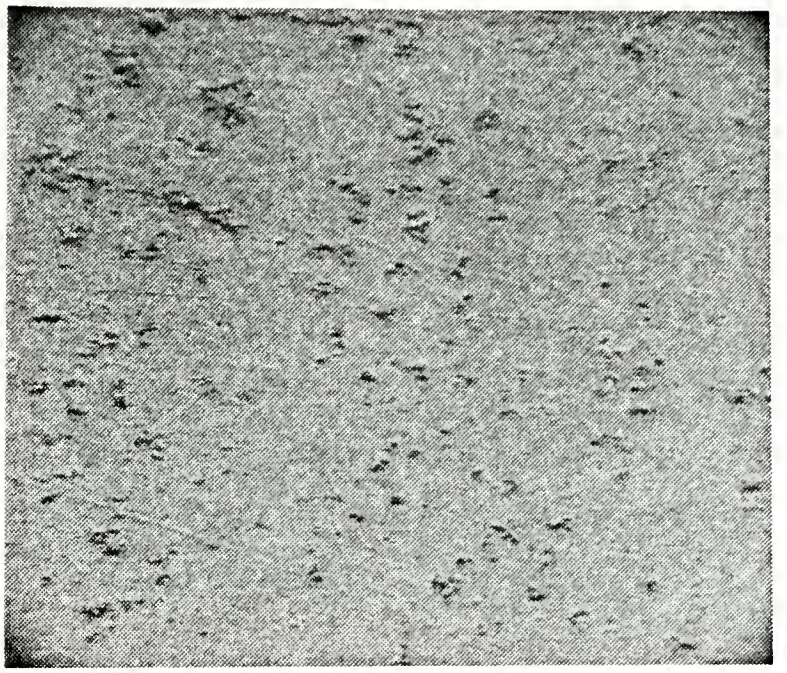

Figure 63. Pitting of the surface of CDA 260 PSP coupon, shown after removal of corrosion products. (324X).

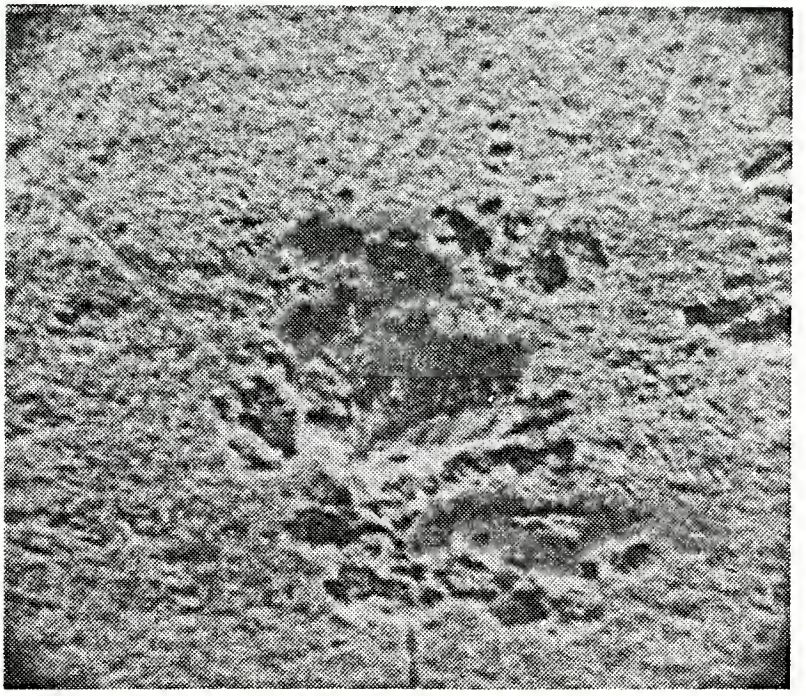

Figure 64. Pitting at the intersection of grain boundaries and preferential corrosion of the grain boundaries in CDA 260 PSP coupon exposed to aerated synthetic seawater for 4 hours and then cleaned of corrosion products. (2100X).

At long PSP exposures in synthetic seawater, a blue-white skirt of loosely adherent precipitate ringed the specimen. Under this was a muddy, red-brown, compact layer which was removed by rinsing the coupon in running water. This left a bright golden surface, with facets visible to the naked eye. Observations by SEM showed classic grain boundary attack (Figures 65 and 66), with the presence of stepped structures etched inside the grains (Figure 67). The steps no doubt correspond to the preferential corrosion of non-close-packed planes as described by Vermilea [36].

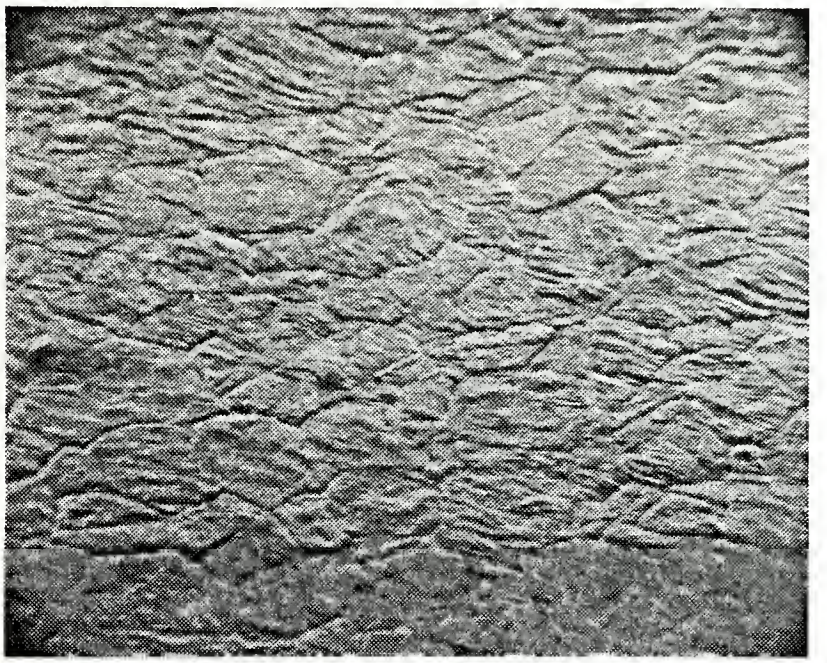

Figure 65. Classic grain boundary attack in CDA 260 PSP long-term exposure to aerated synthetic seawater. Cleaned surface. (147X).

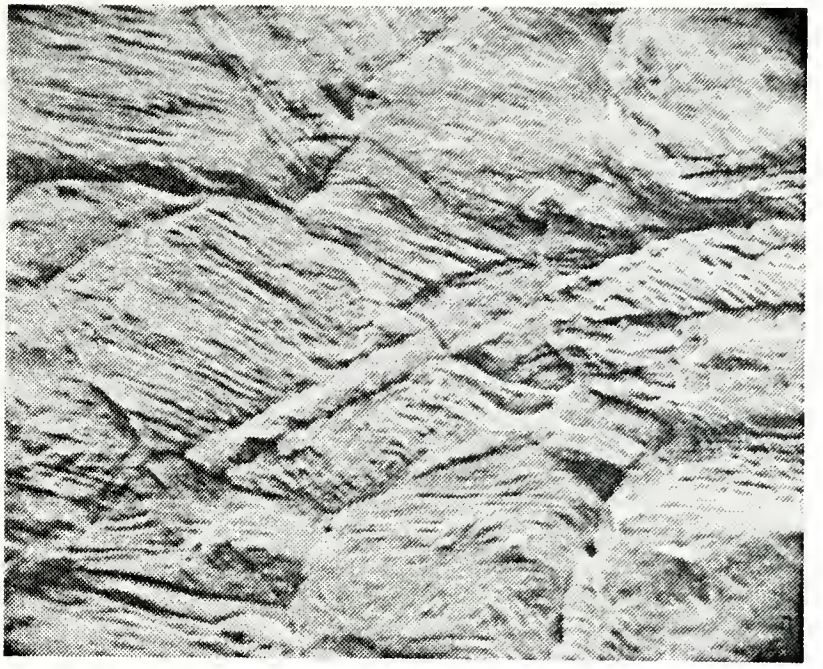

Figure 66. Preferentially etched grain boundaries in long-term PSP exposure of CDA 260 to aerated synthetic seawater. (724X).

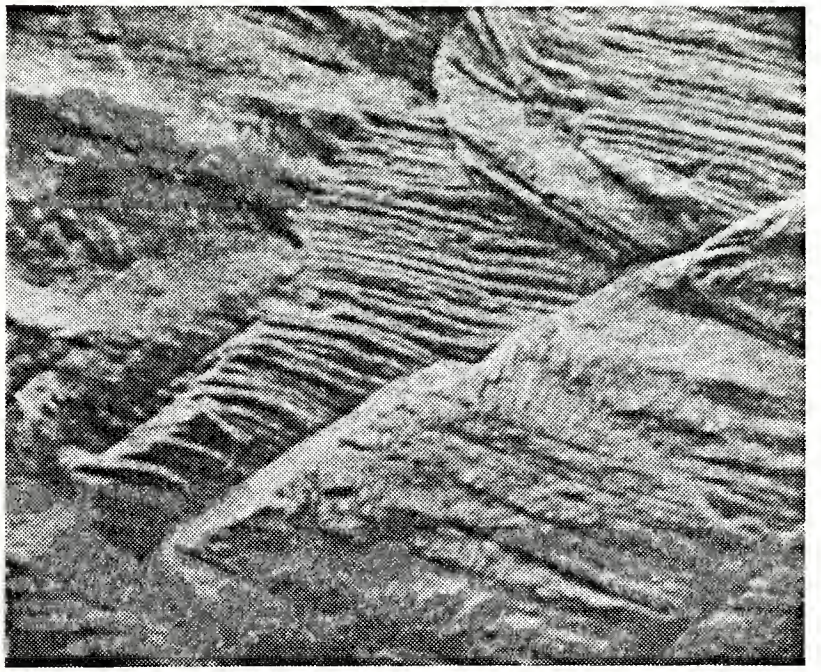

Figure 67. Stepped corrosion within grains of CDA 260 exposed for 12 hours to aerated synthetic seawater in PSP experiment. Also note preferential corrosion of grain boundaries. (147X).

(2) Results With 200 ppm Added Sodium Hypochlorite. As in the case of pure copper, the behavior of the specimen immersed in synthetic seawater containing added hypochlorite ion was dramatically different from that exposed to aerated synthetic seawater alone. The upper third of an IML specimen shows a greenish crystalline deposit (Figure 68), whereas the lower two-thirds shows patches of white material (Figure 69). The base metal appears reddish (copper-colored), and the edges of the specimen appear to be preferentially corroded. The surfaces of two specimens from the IML runs are best compared in the macrophotograph (Figure 186) at the end of this section. The specimen immersed in the hypochlorite containing medium is on the right of that photograph.

Figure 68. Green corrosion product attached to the upper third of CDA 260 IML specimen exposed to aerated synthetic seawater plus added hypochlorite ion. (7.5X).

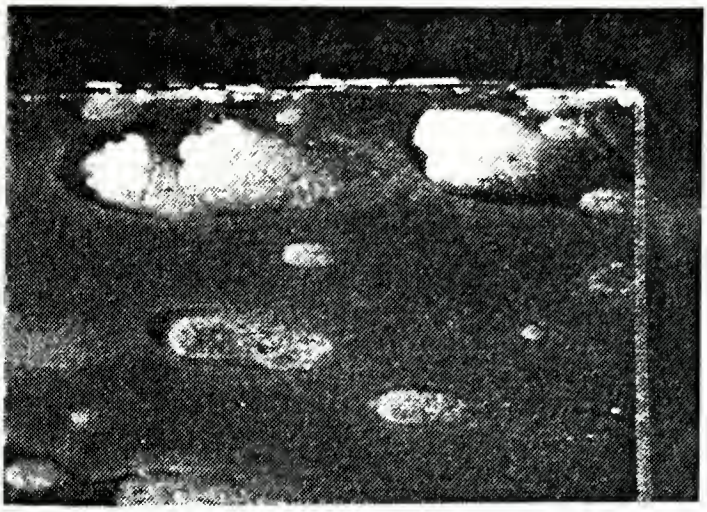

Figure 69. White patchy corrosion products attached to lower two-thirds of CDA 260 IML specimen immersed for 34 days in aerated synthetic seawater·containing 200 ppm sodium hypochlorite. (7.5X).

Examination by SEM showed the white patchy areas as locations of preferential corrosive attack. See Figure 70.

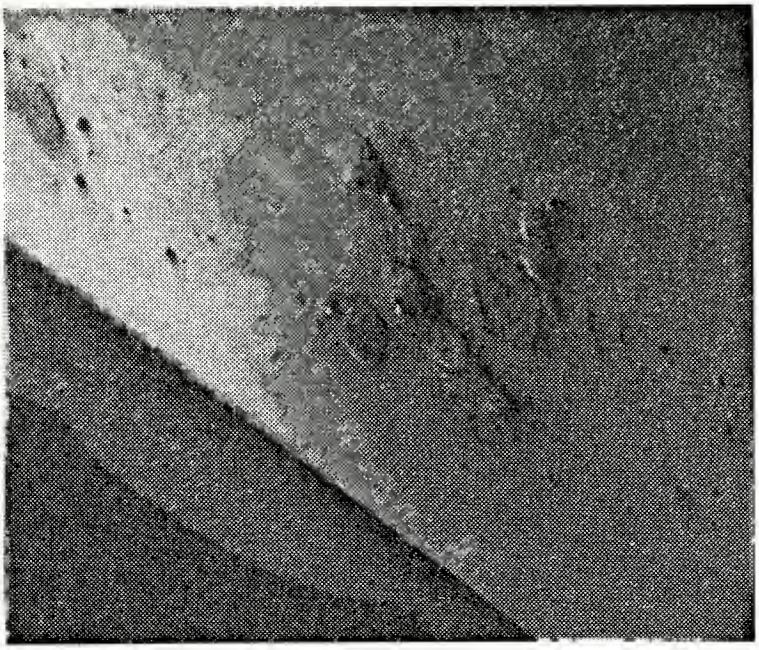

Figure 70. SEM micrograph showing patchy localized corrosion on bottom portion of an IML specimen. CDA 260 immersed in aerated synthetic seawater containing added hypochlorite ion. (24X).

The corrosion products on the white patches were found to be charged excessively in the electron beam, making observation difficult (Figure 71).

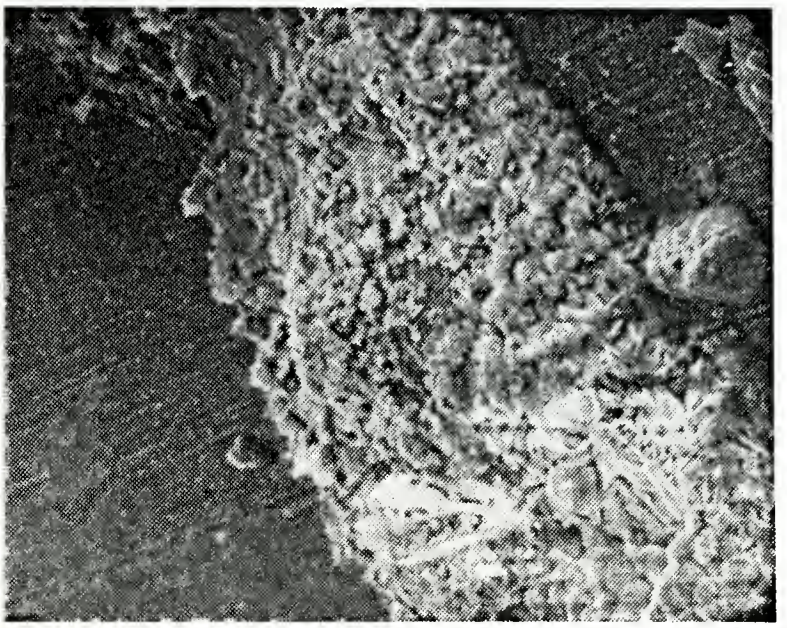

Figure 71. View of white patchy corrosion product shown in Figures 69 and 70. Product charges up in the SEM electron beam. (250X).

The thin, tightly adherent corrosion product film over most of the surface showed sensitivity to the electron beam. In Figure 72, the darker square in the center of the photograph is electron beam damage to the surface at a previously higher magnification. The whitish patches were zinc-rich and also contained a fair concentration of chlorine and bromine as determined by X-ray fluorescence analysis. This is shown in Figure 73. The whitish color of the product and the presence of a chlorine line suggest a zinc chloride or hydroxychloride corrosion product. Near the top of the specimen, the greenish material showed a completely different crystalline structure, as shown in Figure 74.

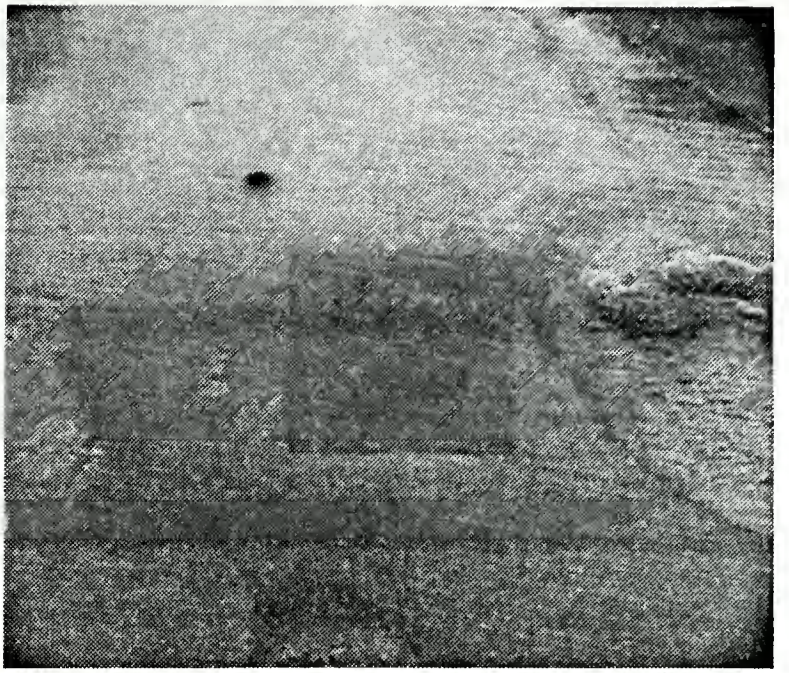

Figure 72. Beam damage to corroded surface of CDA 260 specimen immersed in synthetic seawater with added hypochlorite ion. (34X).

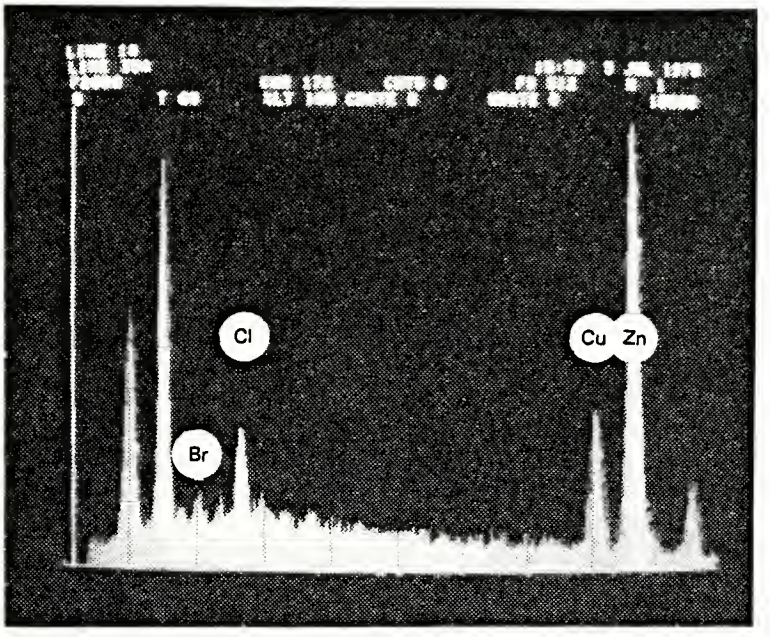

Figure 73. X-ray fluorescence analysis of white corrosion products, showing a high concentration of zinc and chlorine with a lesser amount of bromine.

Figure 74. Unusual structure of green deposit on upper third of IML specimen of CDA 260 exposed to aerated synthetic seawater plus added hypochlorite ion. (47.5X).

After chemical cleaning of the surface, pitting was evident and appeared to be concentrated in the whitish patches on the lower part of the specimen. See Figures 75 and 76 as examples. The pitting did not appear to be correlated with base metal microstructure.

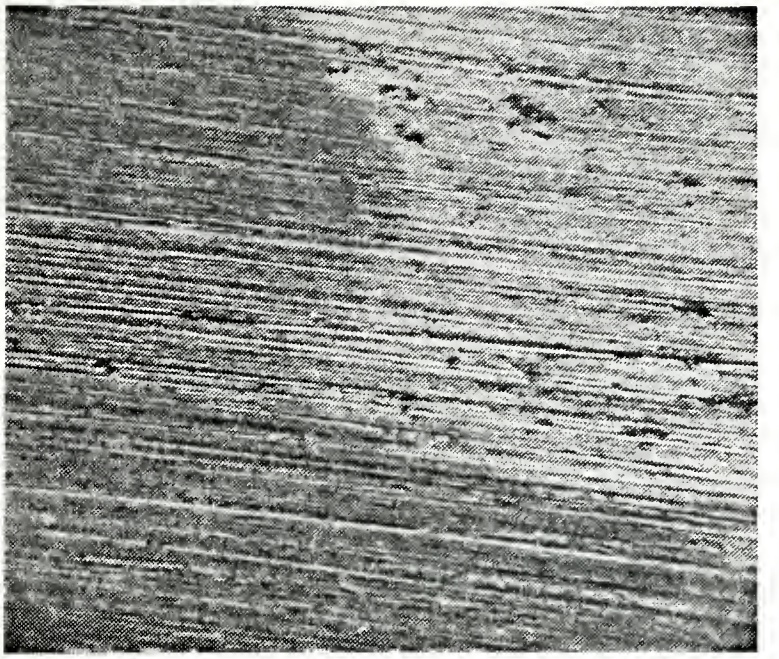

Figure 75. Majority of pitting in cleaned CDA 260 IML specimen exposed to hypochlorite ion is in the lighter zinc-rich area. (129X).

Figure 76. Close-up of pits in zinc-rich area shown in Figure 75. (650X).

When this material was artifically corroded by PSP in a medium containing 200 ppm of sodium hypochlorite in aerated synthetic seawater, the specimens emerged from the corrodent as bright golden and highly faceted with a reddish copper color only at the top. SEM observations confirmed the preferential grain boundary attack (Figure 77) as well as the presence of "steps" within the grains as seen previously in CDA 260 PSP runs without added hypochlorite (Figure 78). Note that this level of attack was attained much more rapidly in hypohalite-containing media than in the synthetic seawater alone. Dezincification was confirmed in both the IML and PSP tests. Figure 79 shows a section through an IML specimen, etched to give contrast between undamaged metal and the copper-rich dezincified areas. Layer-type dealloying was the predominant mode of dezincification.

In summary, CDA 260 corrodes by intergranular corrosion with dezincification prevalent, especially in hypochlorite-containing electrolytes. Macrographs comparing the corroded and cleaned surfaces of CDA 260 in the two media are shown in Figures 186 and 192.

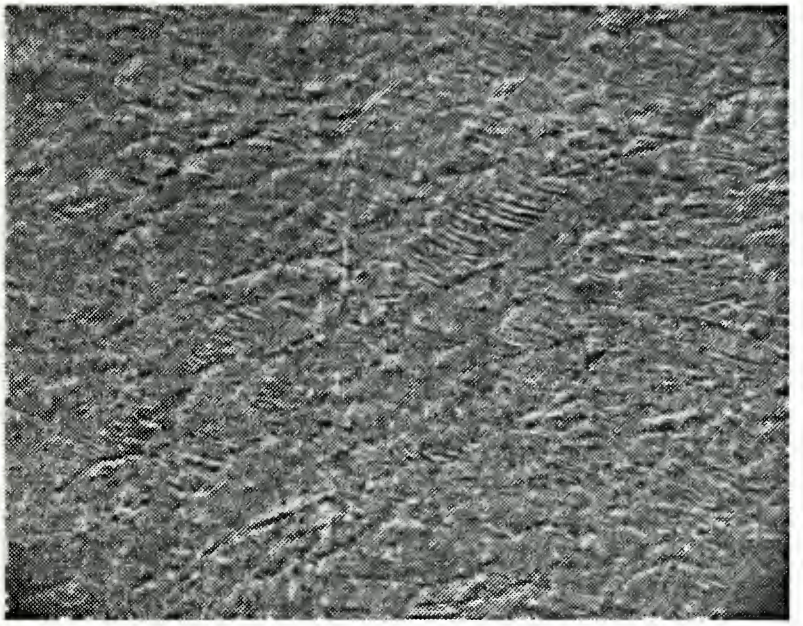

Figure 77. Preferential grain boundary attack in CDA 260 PSP specimen immersed in hypochlorite containing aerated synthetic seawater for 4 hours. (150X).

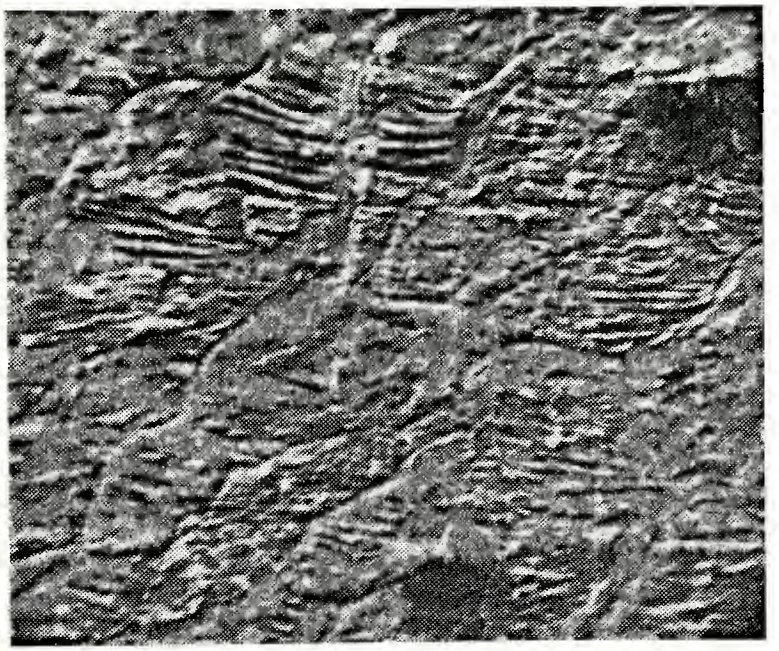

Figure 78. Parallel steps inside grains of corroded CDA 260, as shown in Figure 77. (304X).

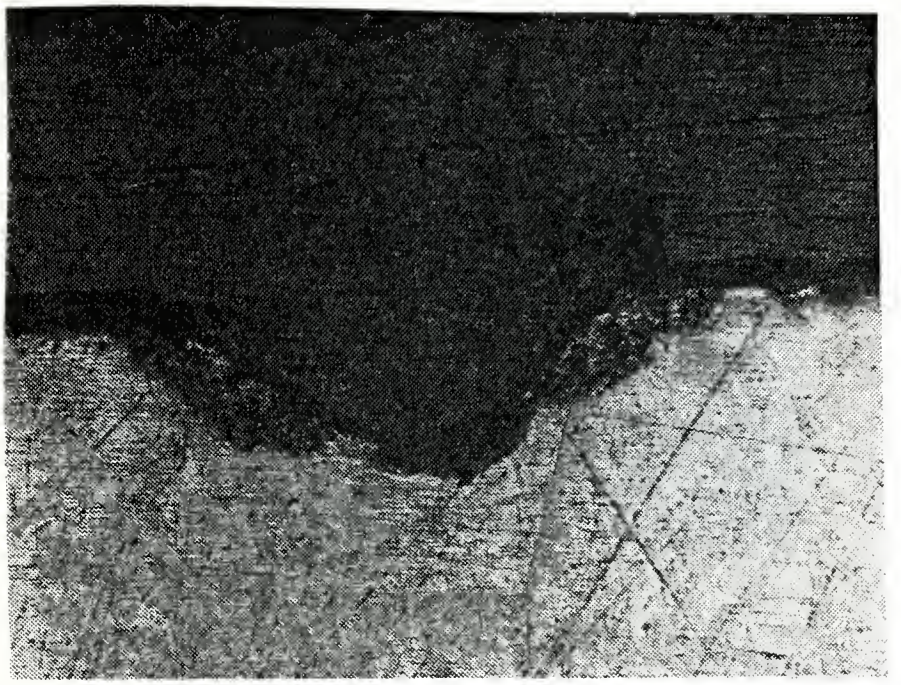

Figure 79. Transverse section through IML coupon after 34 days of exposure to hypochlorite-containing aerated synthetic seawater. Layer type of dezincification (dark areas) is shown around identification mark imprint. (100X).

b. CDA 280 (60/40 Copper/Zinc; "Muntz Metal")

in Synthetic Seawater

(1) Results With No Added Hypochlorite Ion. IML experiments carried out in aerated synthetic seawater alone were decidedly undramatic. Visually, the specimen appeared almost the same before and after the run. (See macrophotographs 187 and 193.) There was a slightly grey-white patina of corrosion product distributed over the surface with a few white salt crystals evenly distributed, as shown in Figure 80.

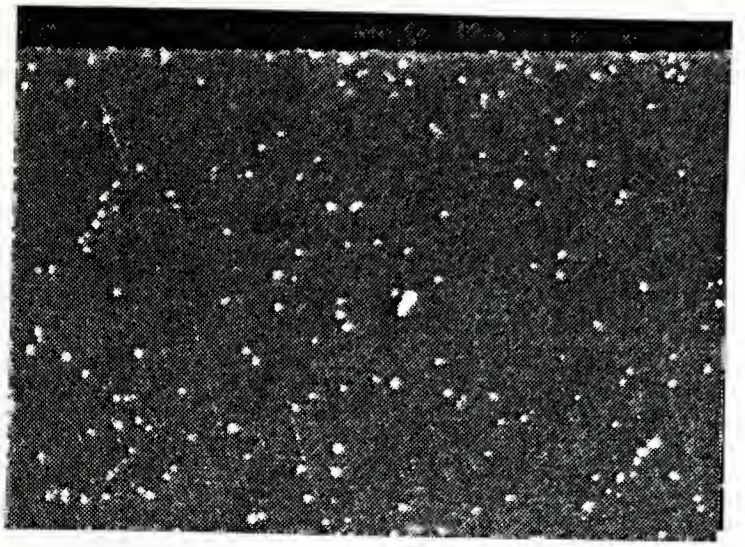

Figure 80. Surface of CDA 280 specimen after 34-day immersion in aerated synthetic seawater. (7.5X).

There was one interesting feature, however. A mass of whitish crystals collected in the identification numbers of an IML specimen as shown in Figure 81 as well as the comparative macrophotograph (Figure 187).

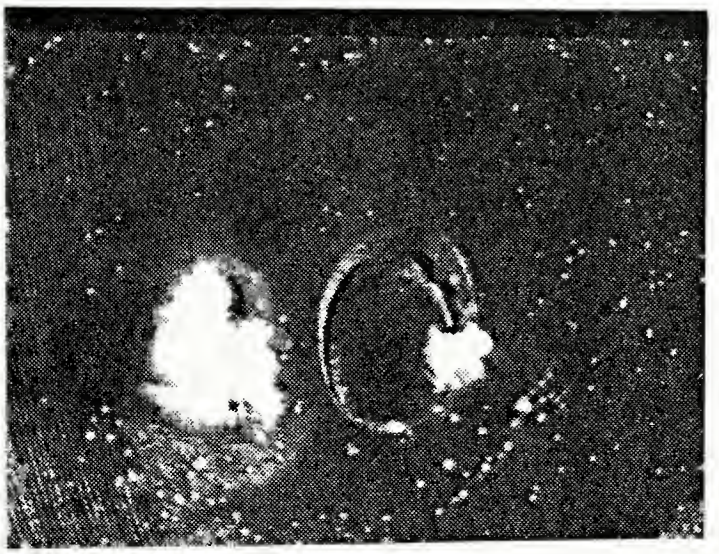

Figure 81. White crystalline material emanating from the stamped identification numbers on CDA 280 immersed in aerated synthetic seawater. (7.5X).

Subsequent examination of this area by scanning electron microscopy showed a strange agglomeration of many crystal types (see Figures 82 and 83).

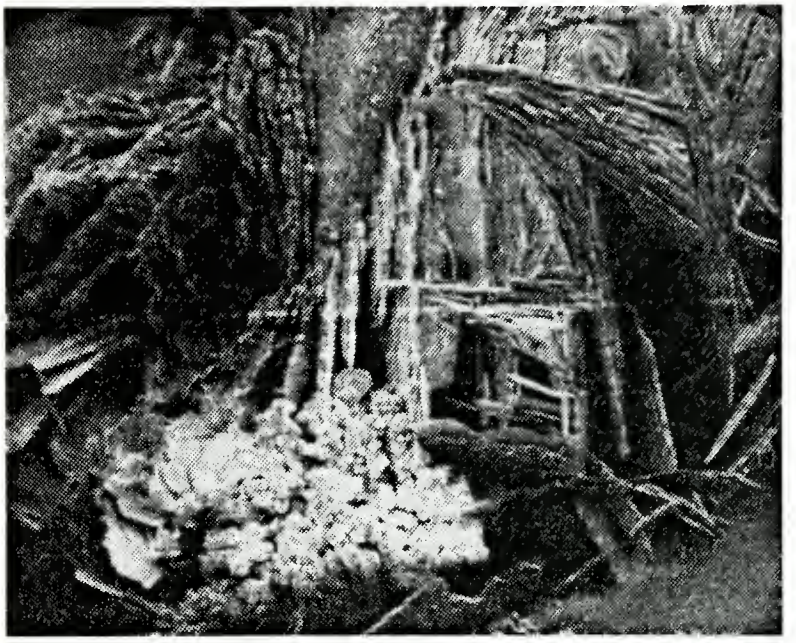

Figure 82. Crystalline mass located in stamped identification number of CDA 280 IML coupon in aerated synthetic seawater. (82X).

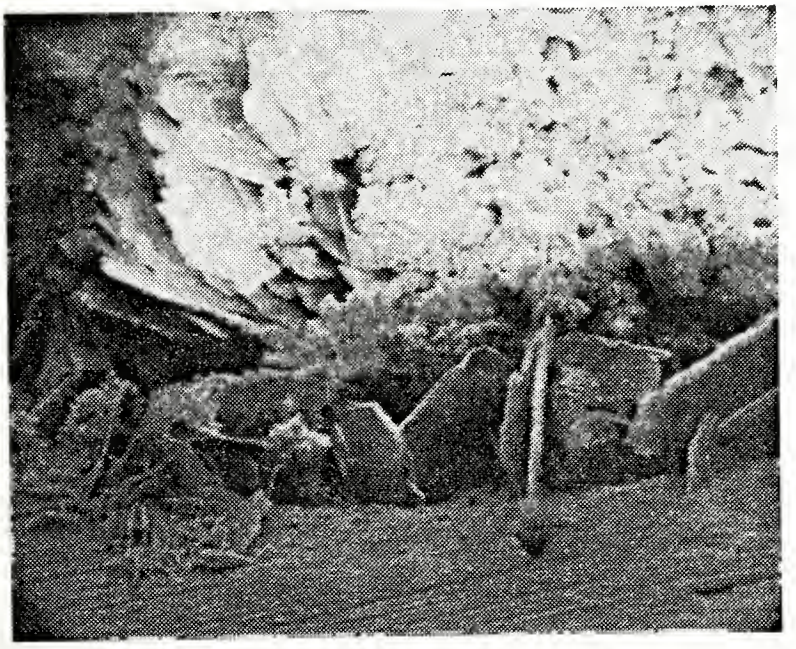

Figure 83. SEM micrograph of agglomeration of crystal types in the stamped identification mark of CDA 280 IML specimen shown in Figure 82.

At first glance, some of the crystalline types might be construed to be hexagonal zinc oxide platelets. (See especially upper left of Figure 83.) X-ray fluorescence analysis of the suspected zinc oxide platelets confirmed the presence of a high concentration of zinc (Figure 84).

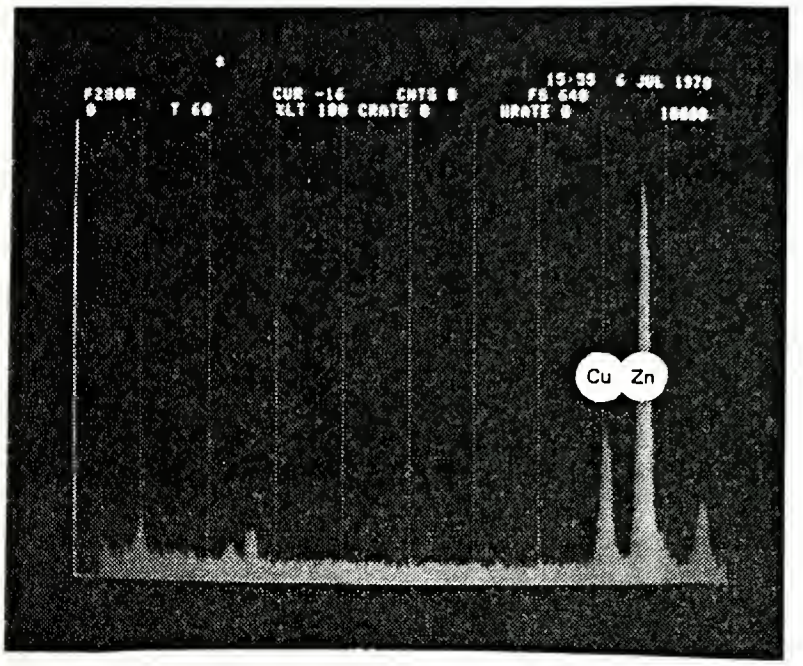

Figure 84. X-ray fluorescence analysis of plate-like crystals on left of Figure 83.

Close examination of the cleaned surface revealed what appeared to be selective beta-phase corrosion, as shown in Figure 85.

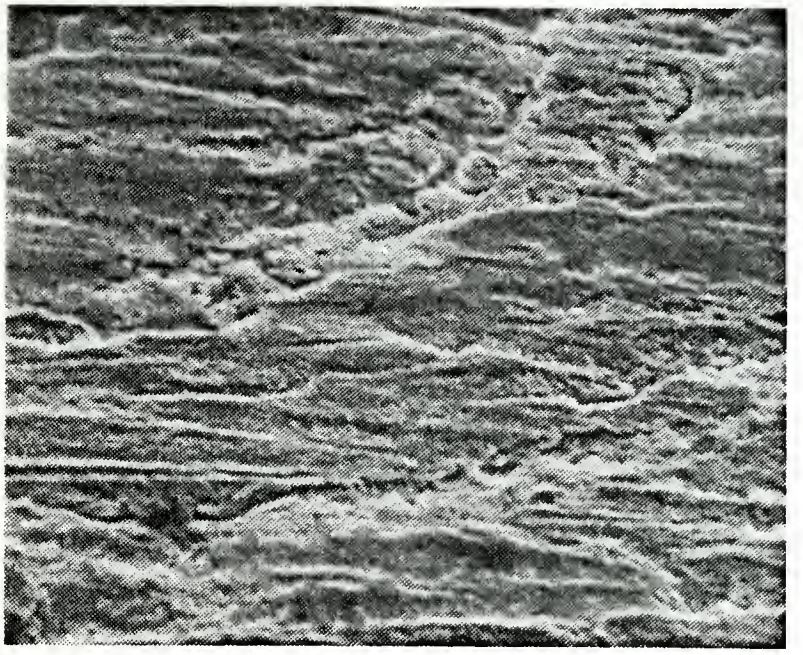

Figure 85. Alternately corroded and non-corroded areas on surface of CDA 280 IML coupon immersed 34 days in aerated synthetic seawater and then cleaned. This is suggestive of beta-phase selective corrosion in this two-phased material. (1300X).

The PSP runs confirmed both the selective corrosion of the beta phase areas and the presence of zinc oxide platelets. The set-by-step mechanism of zinc oxide corrosion product formation is quite similar to that for pure zinc [37] in that a compact basement film is first formed (the white areas in Figure 86). Then, on those areas that have formed this film, an outcropping of small zinc oxide platelets appears (see Figure 87), with an increase in the thickness of the compact film as well as the size and number of platelets with increasing exposure time (Figure 88). Zinc-rich second-phase attack is shown particularly well in Figure 89.

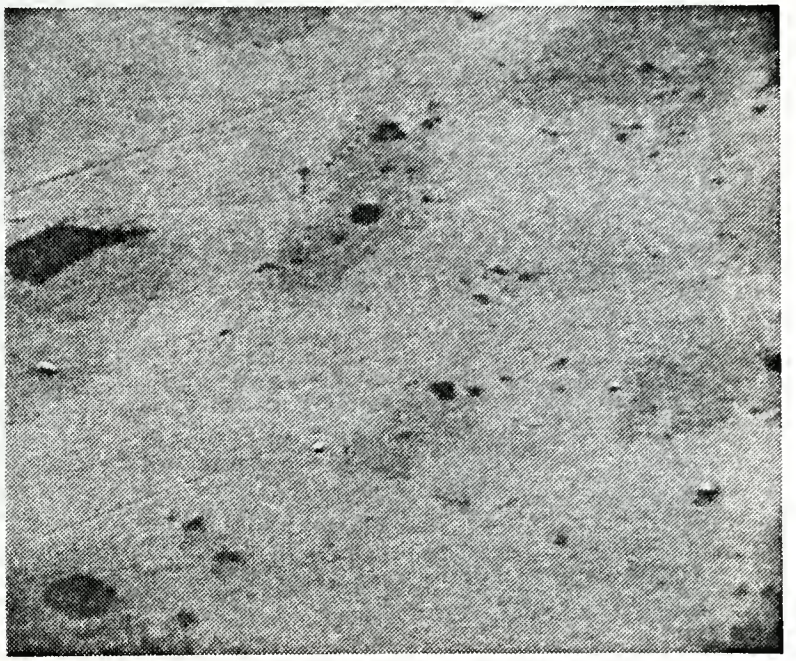

Figure 86. Initiation of a thin compact film on CDA 280 PSP coupon on short exposure to aerated synthetic seawater. (140X).

Figure 87. Formation of small zinc oxide hexagonal platelets on previously filmed areas of CDA 280 PSP specimen. (142X).

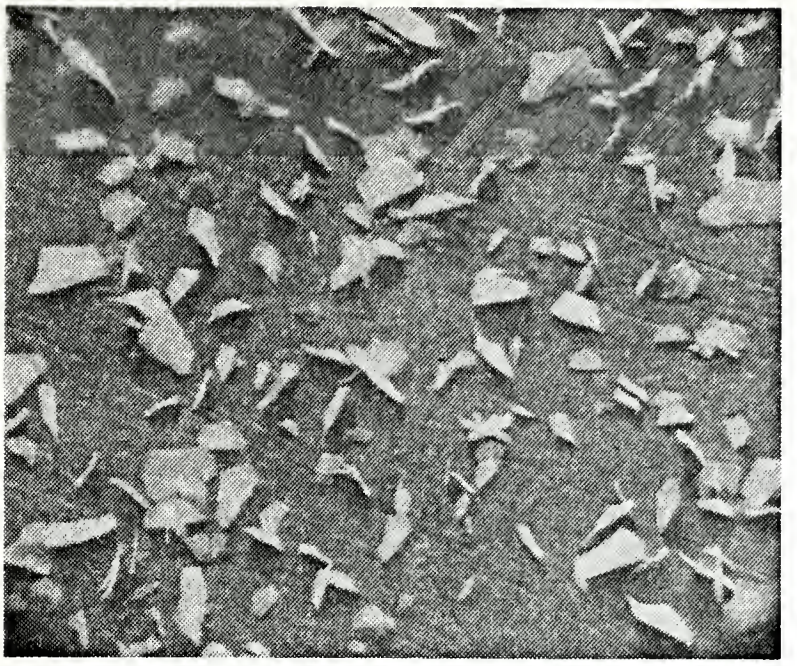

Figure 88. Increased number and size of hexagonal zinc oxide platelets formed as the result of exposure of CDA 280 to aerated synthetic seawater. (137X).

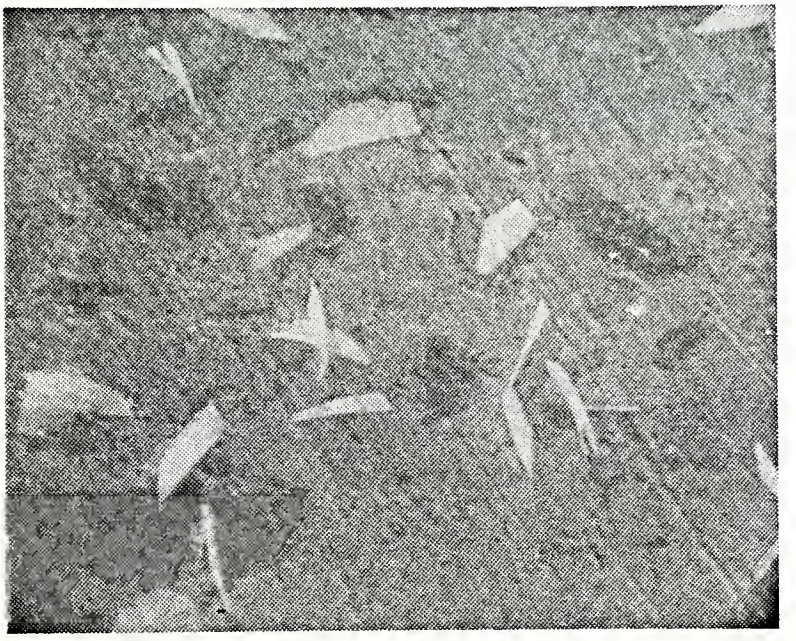

Figure 89. Example of hexagonal zinc oxide platelets growing from preferentially corroded beta phase in CDA 280. (720X).

(2) Results With 200 ppm Added Sodium Hypochlorite. Immersion mass-loss coupons showed large (0.5 cm^2) corroded patches spread over the surface. (See especially the macrophotos comparing corrosion of CDA 280 with and without added hypochlorite, figures 187 and 193). These areas were covered with white or greenish-white thick precipitates, and gave the appearance of having run down the side from top to bottom of the specimen. Figures 90 and 91 show this phenomenon.

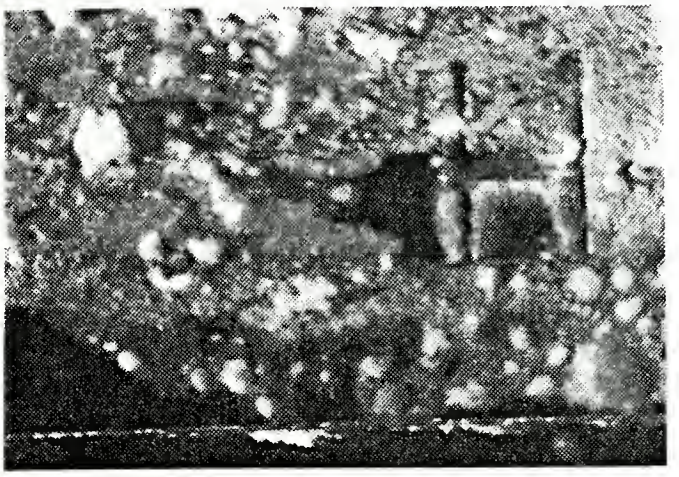

Figure 90. Upper portion of IML test coupon exposed 34 days to aerated synthetic seawater plus 200 ppm sodium hypochlorite. (7.5X).

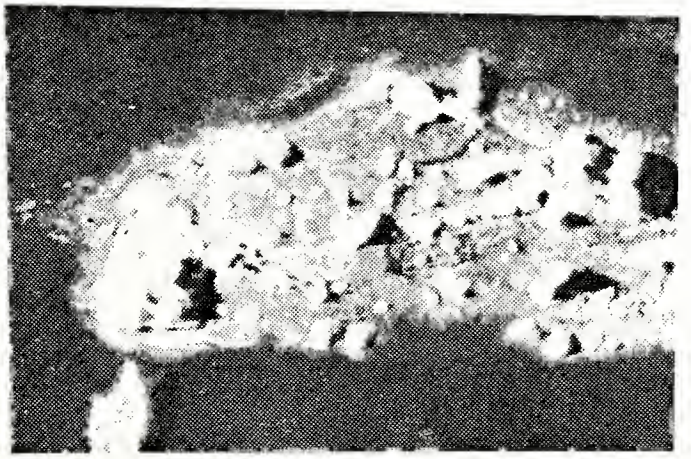

Figure 91. Lower portion of specimen shown in figure 90. (7.5X).

Beneath the corrosion products, the metal is reddish copper colored in sharp contrast to the golden-colored base metal, indicating probable dealloying (dezincification).

Observation of the white patchy area was difficult by SEM since the corrosion products became charged so much in the electron beam (see figure 92).

Figure 92. White patchy corrosion product on CDA 280 IML specimen. (210X).

X-ray fluorescence analysis confirmed the high zinc content of the corrosion product. In contrast, a corroded specimen which was chemically cleaned to reveal preferrential beta-phase corrosion (figure 93) showed almost no zinc present in the metal surface by X-ray fluorescnece analysis (figure 94) indicating that dezincification is not limited to the beta phase alone.

Figure 93. Deep pits into the beta phase of CDA 280 exposed to hypochlorite-containing aerated synthetic seawater. (665X).

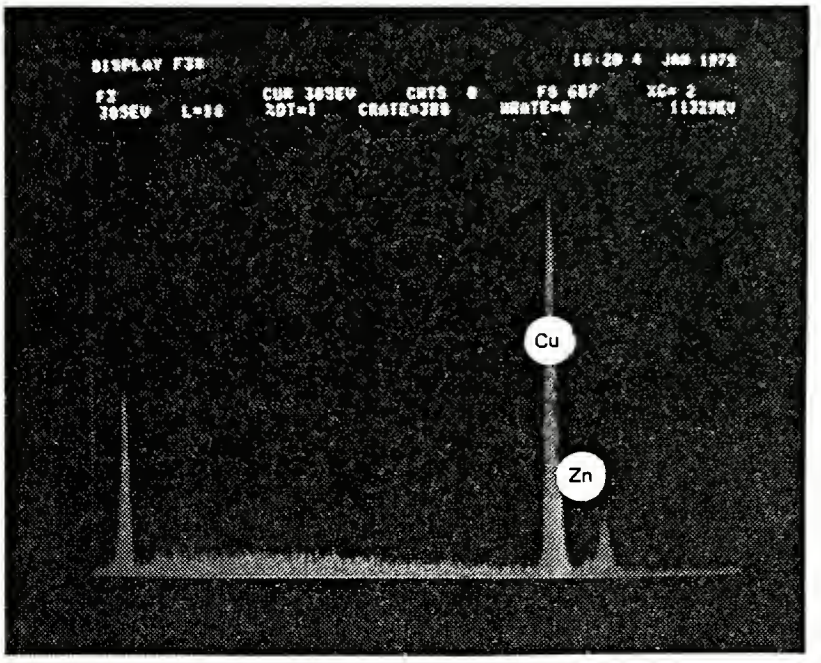

Figure 94. X-ray fluorescence analysis of pitted metal surface shown in figure 93, demonstrating the presence of very little zinc.

The real evidence for beta phase selective dealloying comes from the PSP tests. Visually, even in the shortest (12 minute) run, the specimen became reddish copper color except under the Teflon gasket where no corrosion occured. In figure 95, one sees the white porous corrosion product formed over the zinc-rich beta phase and which surrounds areas of alpha phase which have little or no corrosion prodects on them. Figure 96 shows the porous nature of the surface which would indeed promote the layer type of dezincification.

Figure 95. White corrosion products formed selectively over the zinc-rich beta phase material in CDA 280, upon 12 minute exposure to aerated synthetic seawater containing hypochlorite ion. (195X).

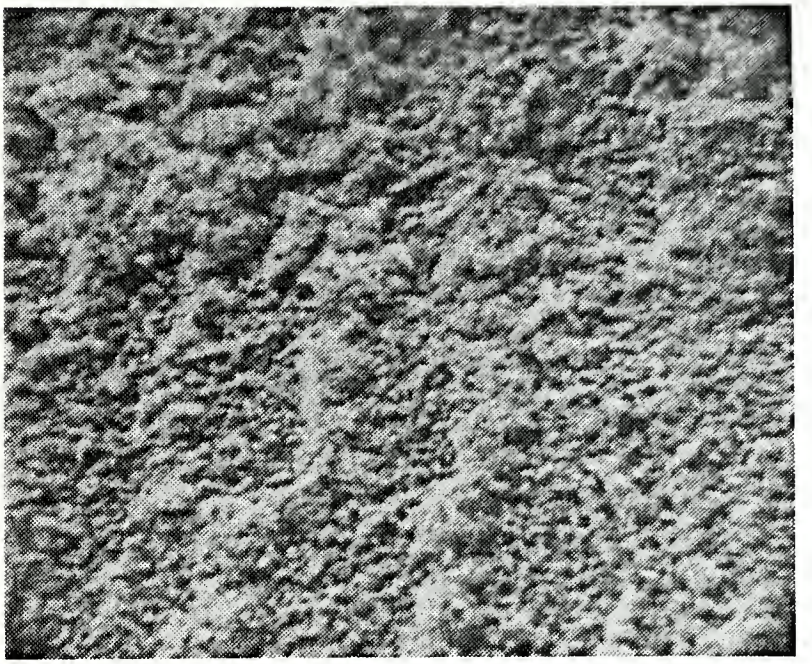

Figure 96. Porous white corrosion product formed on CDA 280 during 12 minute PSP exposure to hypochlorite ion-containing aerated synthetic seawater. White, raised areas are directly above the zinc-rich beta phase. (990X).

In the 60 minute PSP runs, the specimen turns a bronze red with a white precipitate on portions of it. SEM observations show the deep crevice-like areas surrounding the alpha phase material (figure 97). Here the major portion of the white precipitate formerly present on the beta phase is absent and at the edge of most of the deep crevices, small zinc oxide platelets are being formed. This is illustrated in figures 98 and 99.

Figure 99. Another area on PSP specimen shown in Figure 98. (1440X).

X-ray fluorescence analysis of the surface shows copper and zinc base metal with small peaks for sulfur and chlorine. (Figure 100).

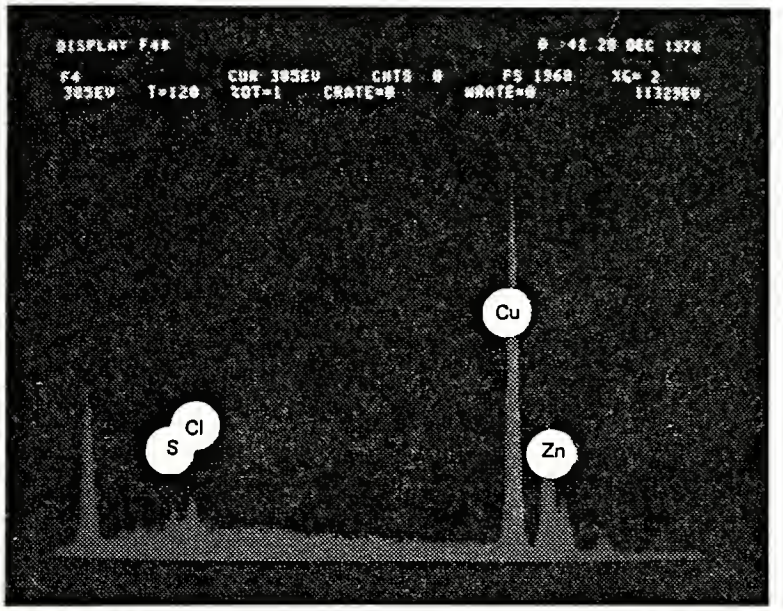

Figure 100. X-ray fluorescence analysis of the surface shown in figure 99, showing the presence of copper/zinc base metal and small sulfur and chlorine peaks.

There were areas on these specimens where no platelet formation had occured (figure 101) but here the beta phase was completely dissolved away.

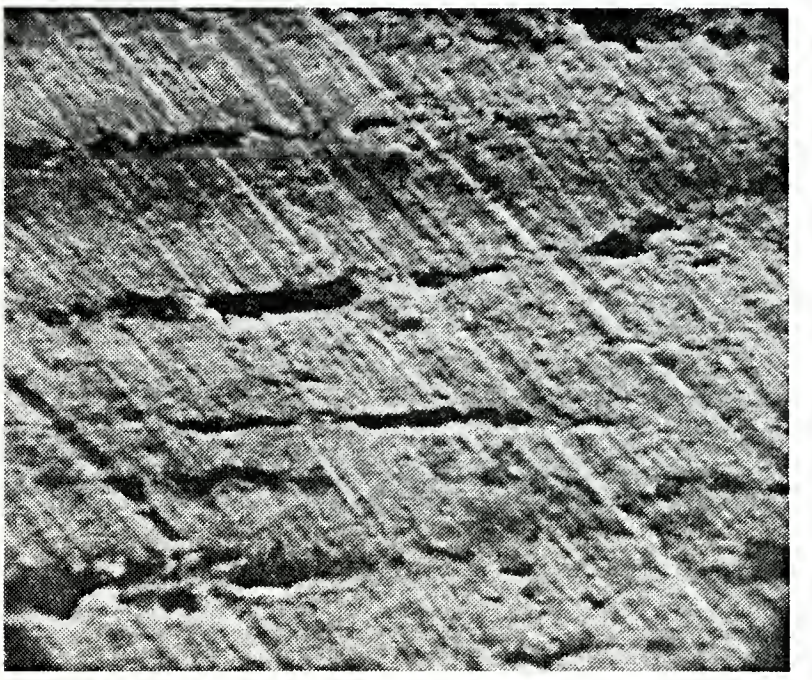

Figure 101. Deeply corroded beta phase of CDA 280 exposed to hypochlorite ion but not exhibiting zinc oxide platelets. (1400X).

This is to be compared with areas on the same specimens where zinc oxide platelets were very thick and rested on a spongy mass in the alpha matrix as in figure 102. A combined X-ray fluorescence analysis for figures 101 and 102, respectively, is shown in figure 103. Here, the dots represent the analysis for the area with the platelets (more zinc present) and the bars represent the analysis for the area without platelets (deficient in zinc).

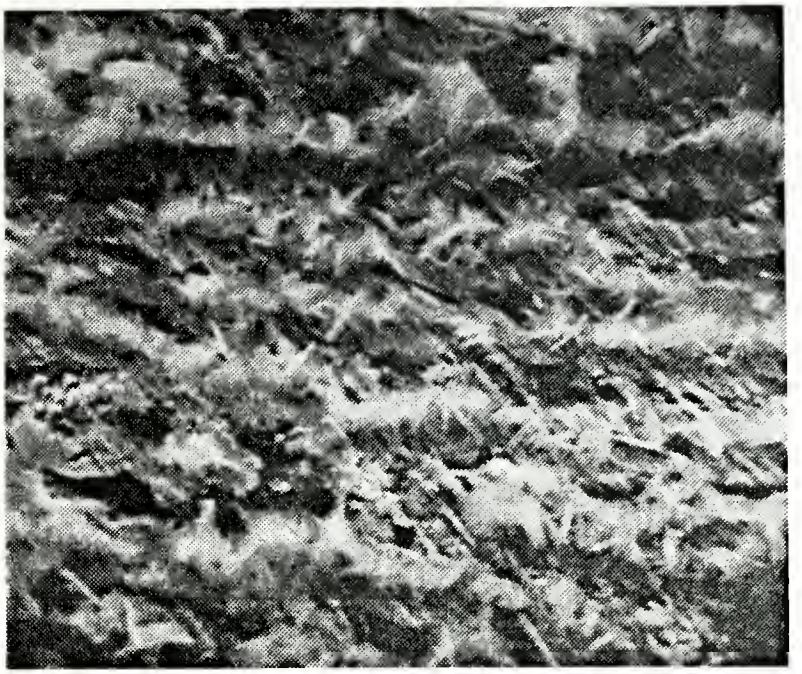

Figure 102. CDA 280 specimen exposed in PSP experiment to aerated synthetic seawater containing hypochlorite ion. Heavy formation of zinc oxide hexagonal platelets. (1400X).

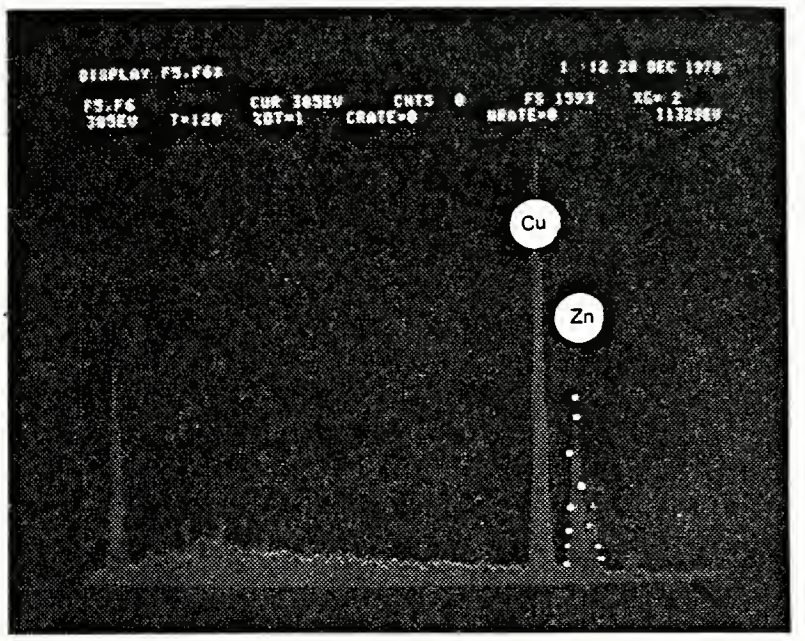

Figure 103. Combined X-ray fluorescence analysis for figures 101 and 102. Lines are for figure 101 and dots are for figure 102. The dotted spectrum shows relatively more zinc for the amount of copper present.

The 4 hour PSP runs showed a growth in the size and number of zinc oxide platelets (figure 104) as well as a thickening and compacting of the layer beneath them (figure 105). The fissures due to the selective corrosion of the beta phase are still present (figure 106). X-ray fluorescence analysis of the surface showed the presence of copper and zinc (base metal) plus sulfur and chlorine (figure 107). The composition of the corrosion products over various parts of the specimen continued to show the same relative stoichiometry (figure 108) and the same mode of corrosion and distribution of corrosion products (figure 109).

Figure 104. Increasing size and number of zinc oxide platelets for longer duration exposure of CDA 280 in PSP experiments. (1470X).

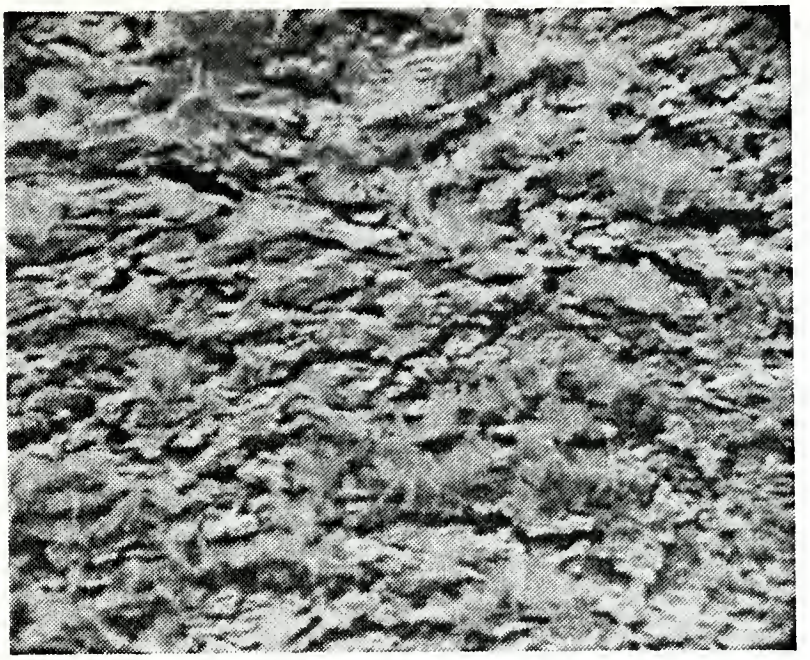

Figure 105. Development of a thickened, compacted layer of corrosion product beneath the hexagonal zinc oxide platelets in CDA 280 PSP experiment with added hypochlorite ion. (710X).

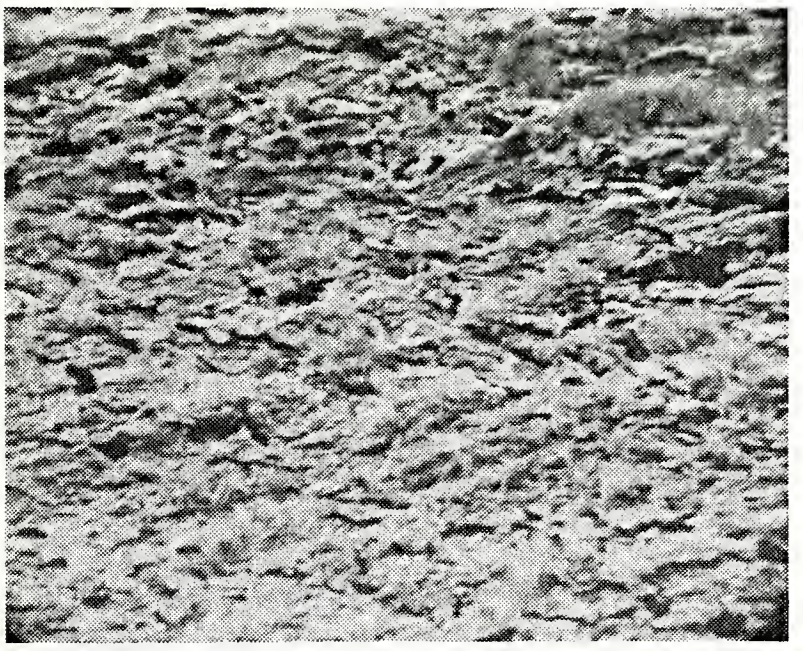

Figure 106. Deep fissures of selectively corroded beta phase surrounded by thick corrosion product film and some hexagonal zinc oxide platelets. (725X).

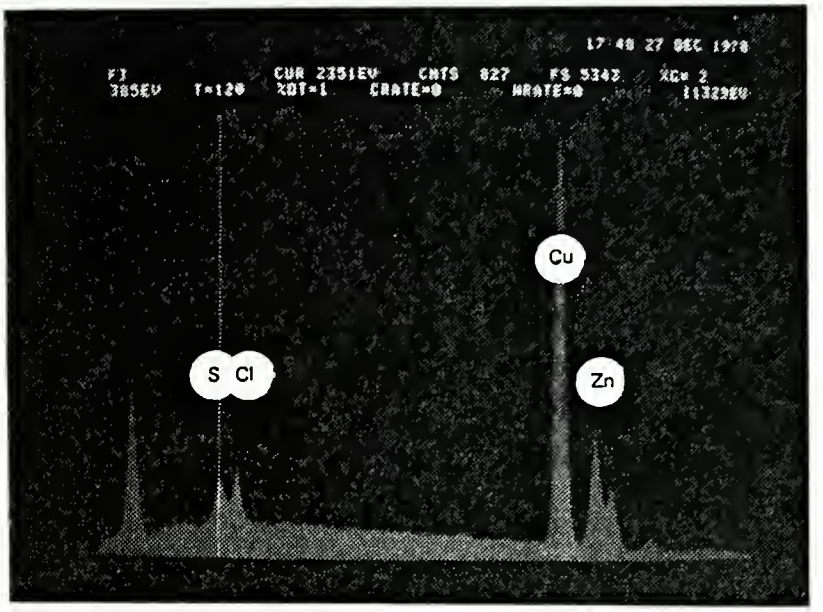

Figure 107. X-ray fluorescence analysis of corroded surface after PSP run of four hours in aerated synthetic seawater containing 200 ppm sodium hypochlorite. Sulfur and chlorine appear as well as the base metal.

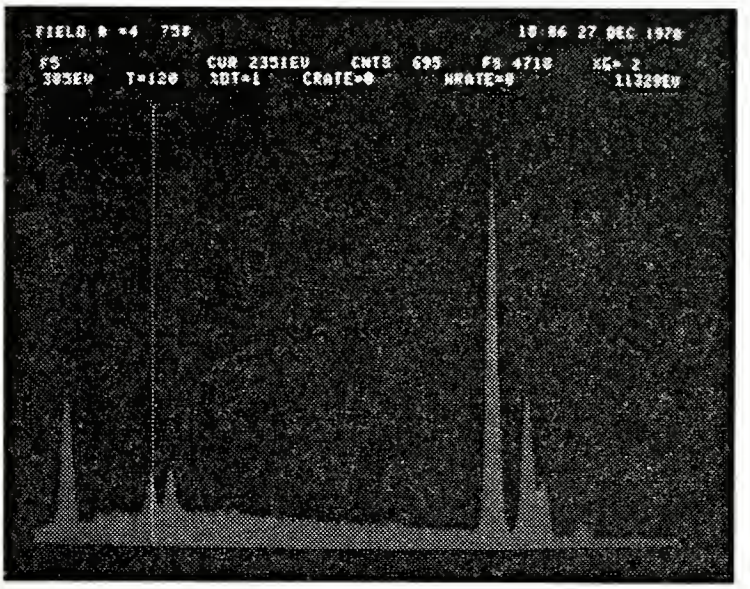

Figure 108. X-ray fluorescence analysis from another part of specimen analyzed in figure 107. Essentially the same stoichiometry prevails.

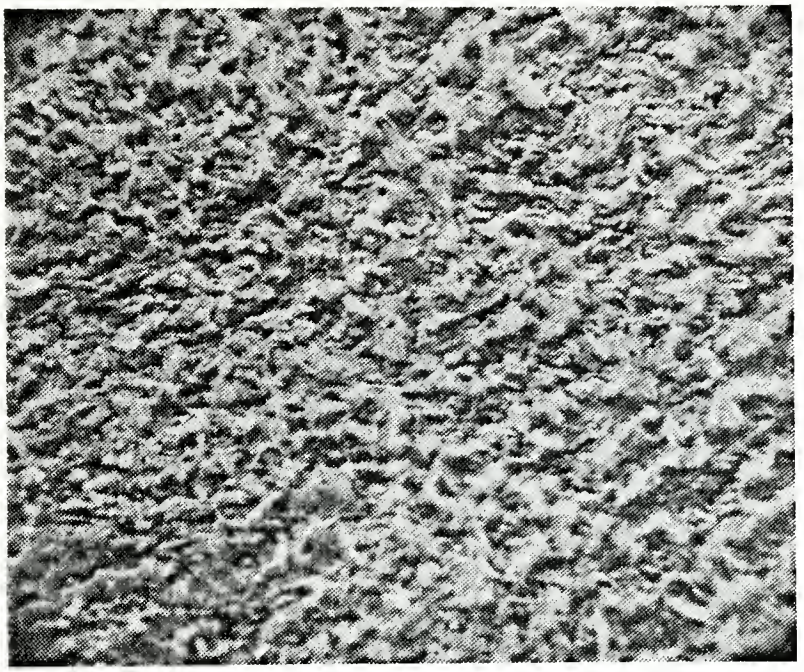

Figure 109. Typical corroded surface of CDA 280 in PSP experiments. (290X).

The surface of a 4 hour PSP specimen was then cleaned chemically. SEM showed a "mud-caked" appearance (figure 110) but still one could see the fissures created in the selective corrosion of the zinc-rich phase (figures 111 and 112). With this material, step-like ridges within the grains were not nearly so common as with the other brass and pure copper specimens. However, a few may be seen in figure 113.

In summary, CDA 280 ("Muntz metal") corrodes by selective attack of the zinc rich beta phase which must therefore be anodic to the alpha material that it surrounds. Hexagonal zinc oxide platelets form next to the corroding beta phase fissures, eventually forming a thick corrosion product over the whole alpha surface. The presence of hypochlorite ion in the aerated synthetic seawater electrolyte

greatly increases the rate and depth of penetration of the beta phase. Comparison macrophotographs of the IML specimens with and without corrosion products attached for the two electrolytes are shown in figures 187 and 193.

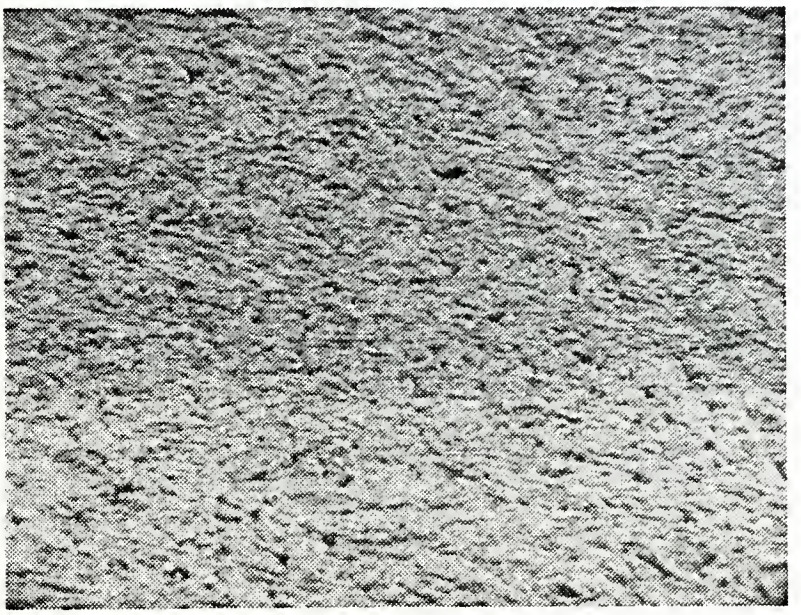

Figure 110. Mud-caked appearance of cleaned CDA 280 PSP coupon, showing the selective corrosion of zinc-rich beta phase material. (140X).

Figure 111. Selective beta phase corrosion about zinc deficient alpha phase material in CDA 280 exposed to hypochlorite ion. (700X).

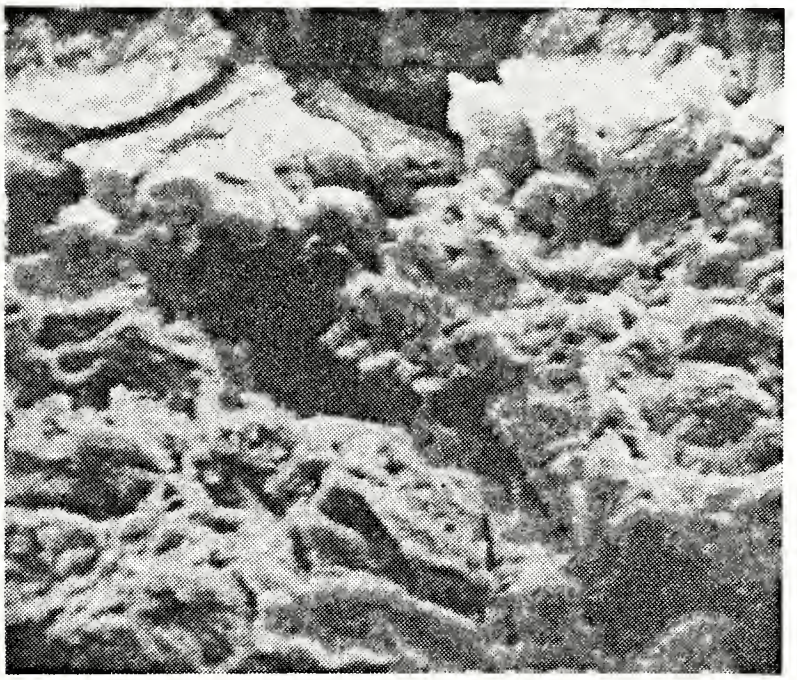

Figure 112. Detail of one typical fissure in zinc-rich phase. (2800X).

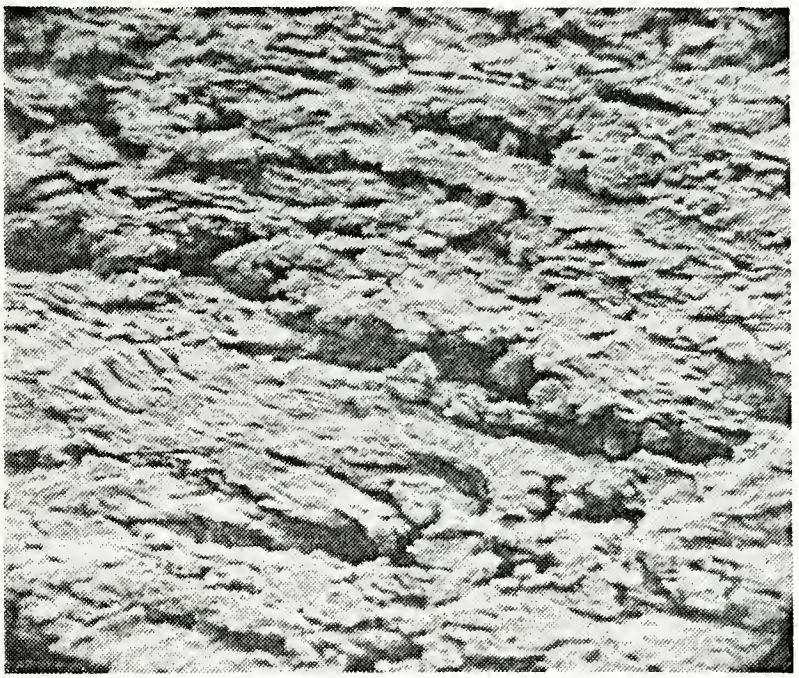

Figure 113. A few crystallographic etched planes may be seen in grain to left of center. CDA 280 exposed in PSP experiments to aerated synthetic seawater containing hypochlorite ion. (700X).

4. The Copper-Nickel Alloys (The Cupronickels)

Copper nickels 90/10 and 70/30 were developed for long duration service in marine environments. They are inherently more inert in seawater than the brasses and are highly resistant to impingement attack in turbulent flowing seawater. The corrosion rates for both alloys are quite sensitive to the amount of sulfide ion present in the electrolyte, however, and care must be taken in stagnant waters due to anaerobic sulfide-producing bacteria which may be present [38]. Due to their resistance to impingement attack, both alloys are used widely throughout the U.S. Navy for shipboard piping.

a. CDA 706 (90/10 copper-nickel) in Synthetic Seawater

(1) Results Without Added Hypochlorite Ion. Visually, this material was unattacked in the aerated synthetic seawater in the IML experiments. For example, see figures 114 and 115. There appeared to be no surface roughening and no color change. This is also demonstrated nicely in the comparative macrophotographs in figures 190 and 196.

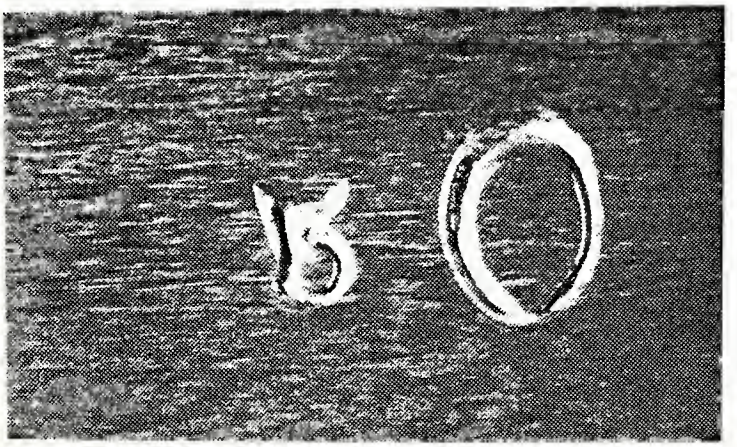

Figure 114. Upper end of CDA 706 IML coupon exposed to aerated synthetic seawater for 34 days. (7.5X).

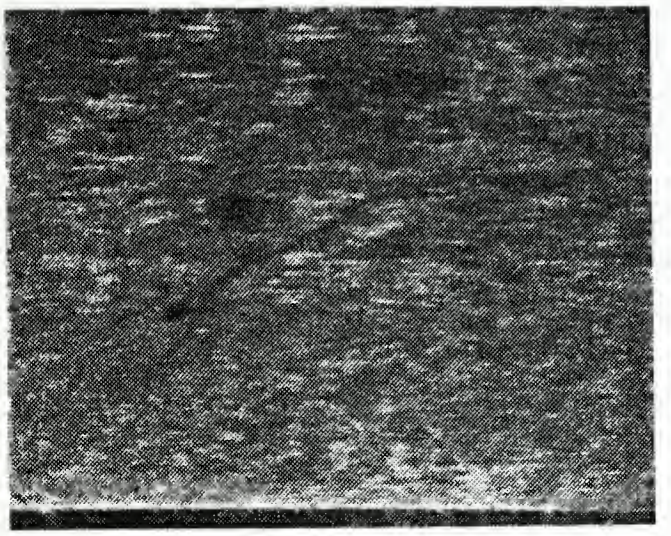

Figure 115. Lower end of CDA 706 IML specimen exposed to aerated synthetic seawater for 34 days. (7.5X).

SEM observations on this material showed areas with thin films on them (figures 116 and 117) but no apparent attack by the electrolyte. The films are probably salt solution stains from the corrodent.

Figure 116. Thin dielectric films formed over parts of the IML specimens after 34 day exposure to aerated synthetic seawater. (20X).

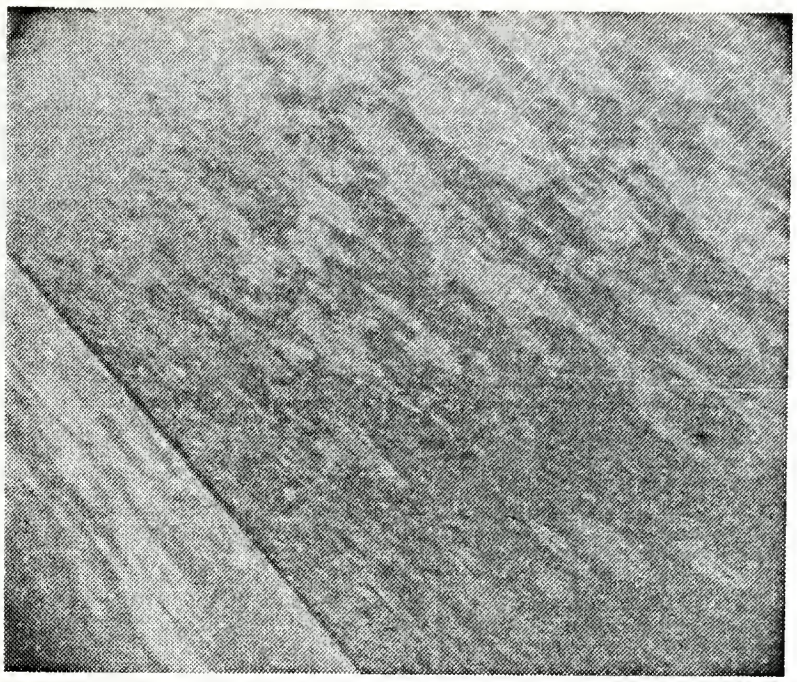

Figure 117. Same specimen as figure 116, but looking at a different face. (22X).

X-ray fluorescence analysis of one of the dielectric areas (figure 118) shows the presence of slight traces of chlorine and bromine. Also to be noted in all X-ray fluorescence spectra of this alloy is the presence of the iron peak. Iron is added to this alloy at about the 1% level to better resist impingement attack [35]. A small amount of white particulate matter collected in the identification mark (figure 119) and it was originally thought that this might be corrosion products. The materials accumulated charge in the electron beam of the SEM making high magnification photos nearly impossible. X-ray fluorescence analysis showed a strong chlorine peak and it is hypothesized that this material is merely residual sodium chloride.

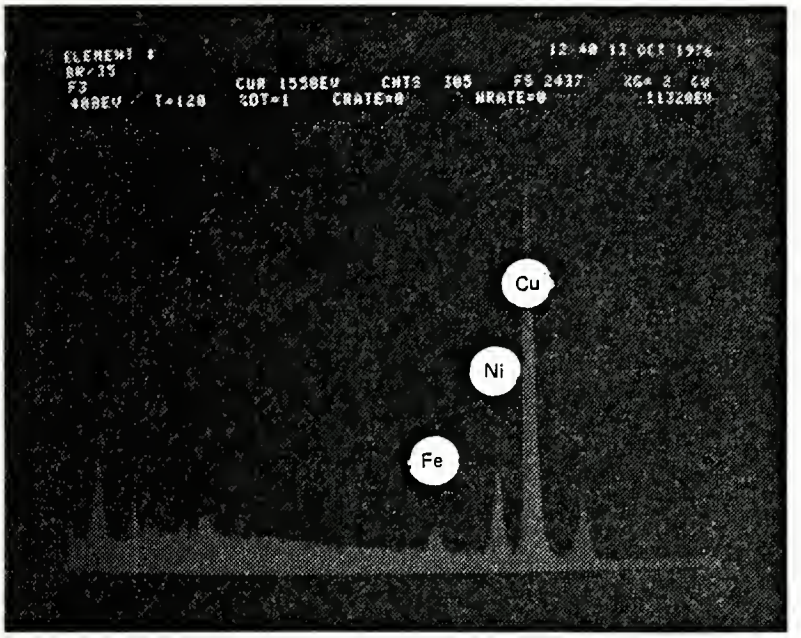

Figure 118. X-ray fluorescence analysis of thin dielectric patches shown in the previous figure.

Figure 119. White crystalline product in the identification mark of CDA 706 IML coupon. (76X).

The chemically cleaned specimen showed the presence of a few shallow pits at high magnification (figure 120).

Figure 120. Shallow pit-like imperfections in the surface of a chemically cleaned CDA 706 IML coupon, previously exposed for 34 days to aerated synthetic seawater. (1300X).

PSP runs seemed to follow a different corrosion product development than the IML tests. The specimens, which were initially a silvery color changed to a dull brass yellow color upon PSP at +100 mV greater than E_{corr}. At shorter exposures, a tight compact film is present (figure 121) which has roughly the same elemental composition as the base metal (figure 122). On longer exposures, the surface color more nearly approaches that of metallic copper, i.e., red. The thin film thickens a bit and cracks when placed in the SEM vacuum system (figures 123 and 124). X-ray fluorescence analysis shows an enrichment in the iron content of the film (figure 125).

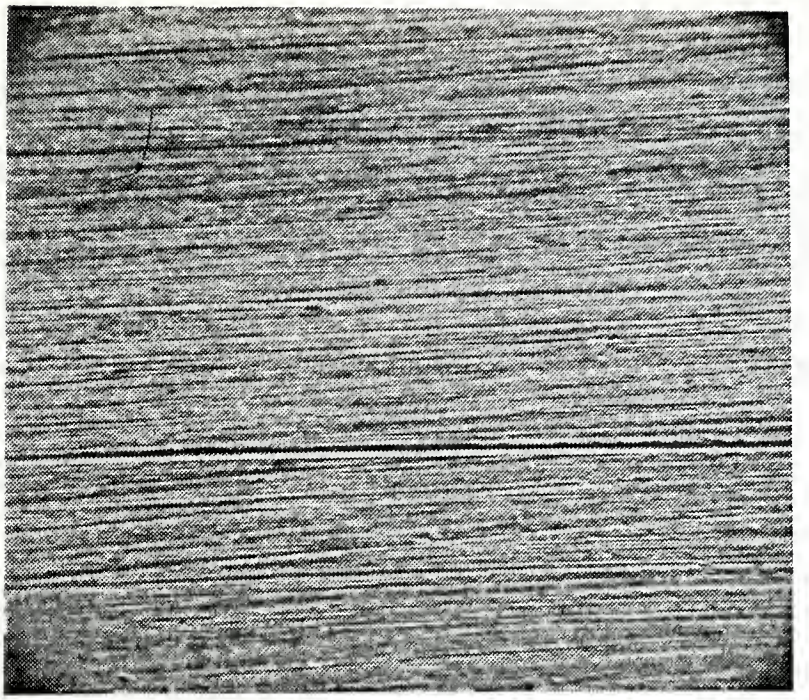

Figure 121. Thin dielectric film formed on short exposures to aerated synthetic seawater. (141X).

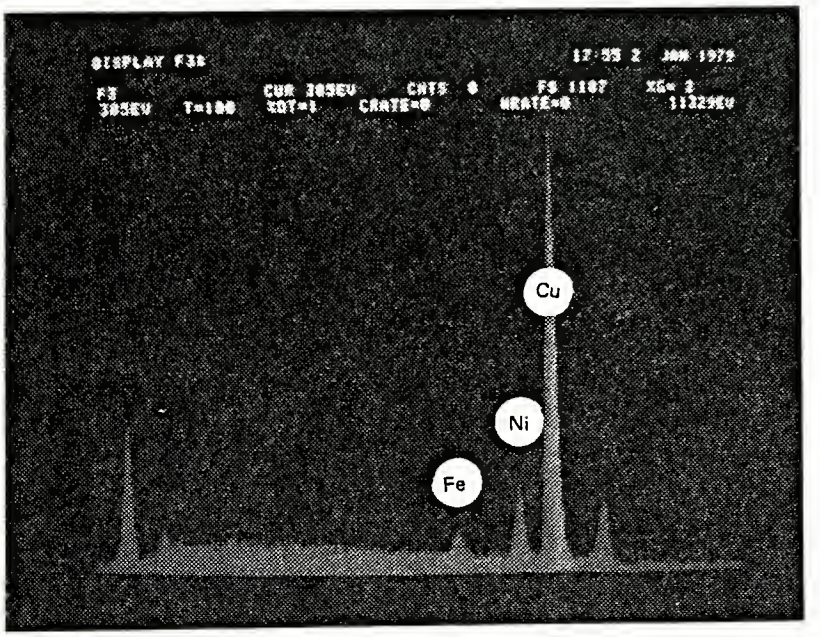

Figure 122. X-ray fluorescence analysis of thin film shows essentially base metal composition. Note 1% iron peak.

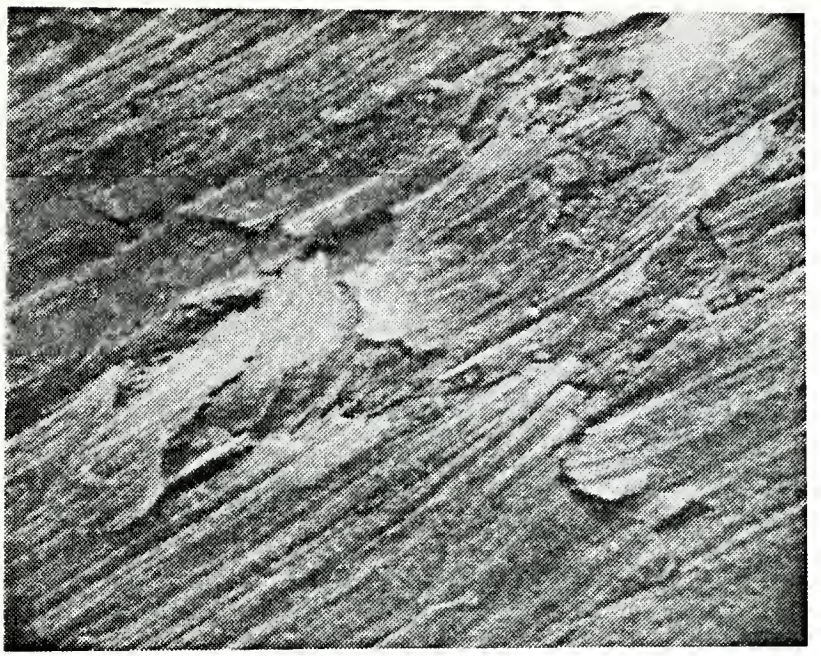

Figure 123. Thicker dielectric film forms as duration of exposure increases. Cracks are due to vacuum in SEM. (700X).

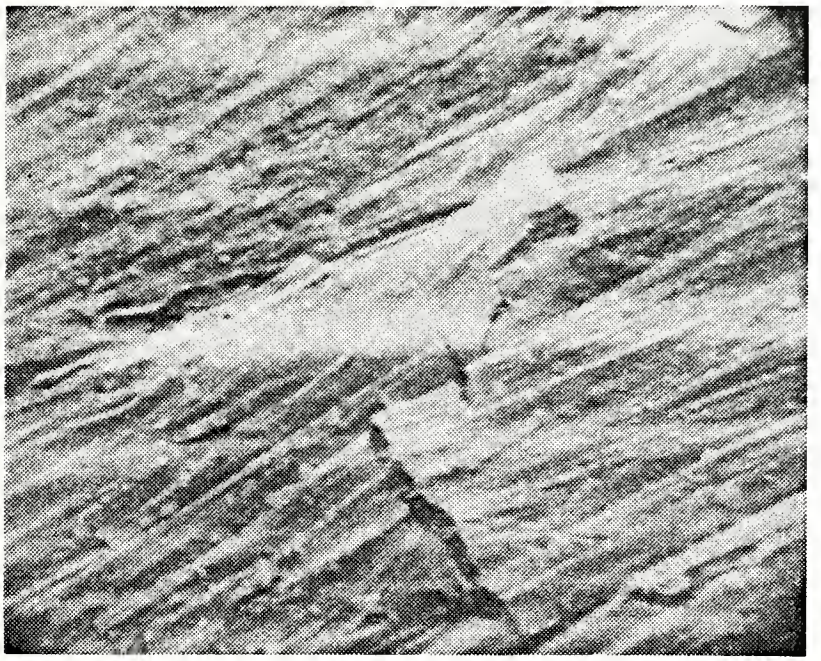

Figure 124. Higher magnification of figure 123. (1420X).

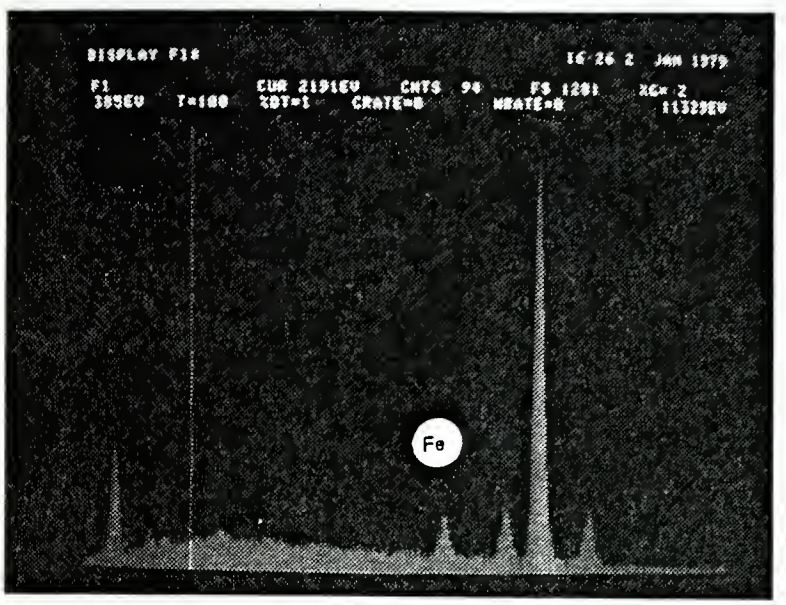

Figure 125. X-ray fluorescence analysis of film of figure 124, showing enrichment of the iron content compared to shorter PSP exposures.

Upon much longer (20 hour) exposures, the film thickens even more (figure 126) and it also shows the presence of very small particles on the surface of the film (figure 127). The dielectric film cracks easily in the SEM vacuum chamber (figure 128). X-ray fluorescence analysis of this film shows yet a greater increase in the iron level (figure 129). Beneath areas where the dielectric film has broken away, some intergranular corrosion is evident (figures 131 and 131).

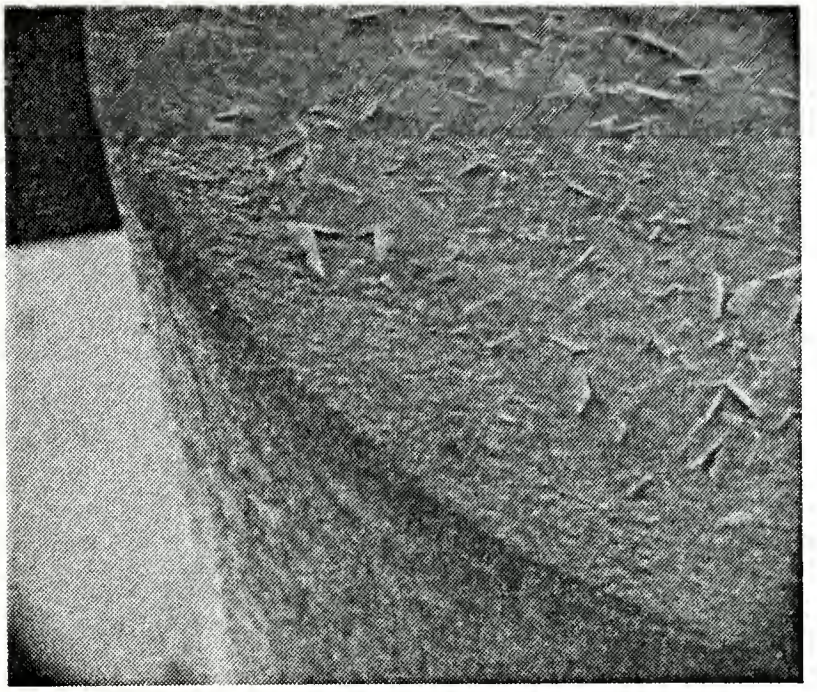

Figure 126. Low magnification SEM micrograph of filmed over CDA 706 PSP specimen exposed to aerated synthetic seawater for 20 hours. (31X).

Figure 127. Cracked dielectric film showing a myriad of small particles on the film. (280X).

Figure 128. Fragile dielectric film on CDA 706 cracks due to vacuum in SEM chamber. (140X).

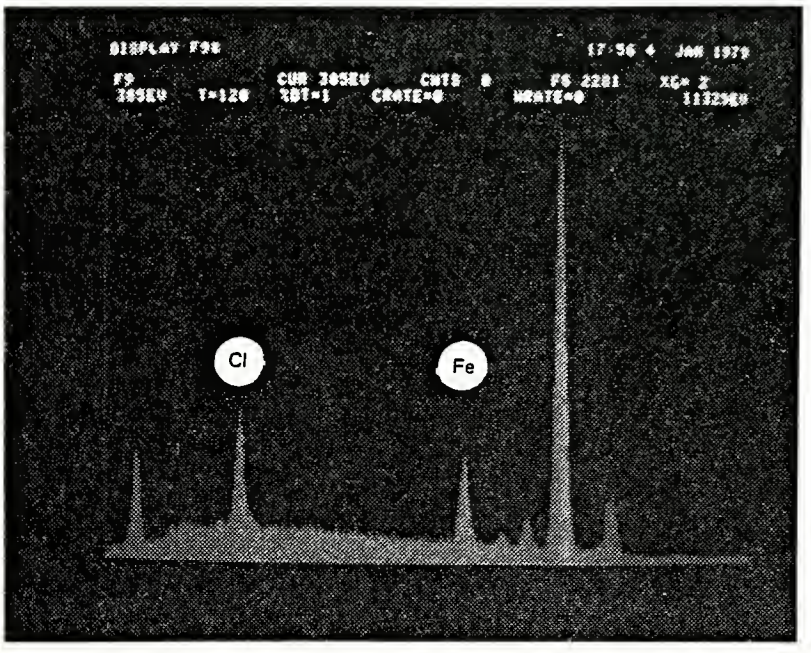

Figure 129. Increasing iron and chlorine levels in corrosion product film of CDA 706 PSP coupon after 20 hour exposure to aerated synthetic seawater.

Figure 130. Evidence of intergranular corrosion occuring beneath film (which has broken away from the specimen). (152X).

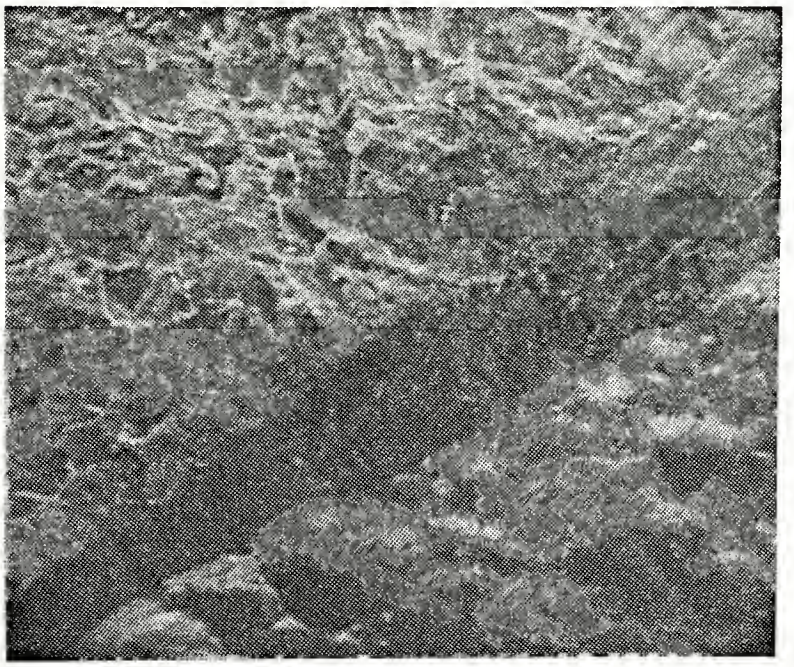

Figure 131. High magnification view of one selectively corroded grain boundary in CDA 706 PSP coupon exposed to aerated synthetic seawater for 20 hours. (790X).

In summary, then, in aerated synthetic seawater, the low uniform corrosion rate of about 1mdd (4.1 μmpy) is born out by surface observations on the IML specimens. Here, a slow, rather uniform corrosion is achieved. In the PSP runs, a different corrosion mechanism may be operative as the film utilizes increasing amounts of iron from within the alloy. There is evidence of intergranular corrosion in the PSP measurements.

(2) Results With 200 ppm Added Sodium Hypochlorite.

Specimens from the IML experiments had virtually every color of the rainbow across them. Predominant were reds, greens and especially black. As in previous hypochlorite runs, it appeared that the corrosion products had somehow formed at the top and then run down the side of the specimens. It is informative to look at the comparative macrophotographs in figures 190 and 196. Here, the corrosion is highly locallized with a few areas almost untouched, but the rest of the surface has distinct patches with various corrosion products attached. See figures 132 through 135.

Figure 132. Multiple patches of corrosion products on CDA 706 exposed to aerated synthetic seawater containing hypochlorite ion. (7.5X).

Figure 133. Another area of specimen shown in figure 132. Light colored area is green. Dark colored areas are velvety black. (7.5X).

Figure 134. Top of IML test coupon on CDA 706. Exposed for 34 days in aerated synthetic seawater containing 200 ppm sodium hypochlorite. (7.5X).

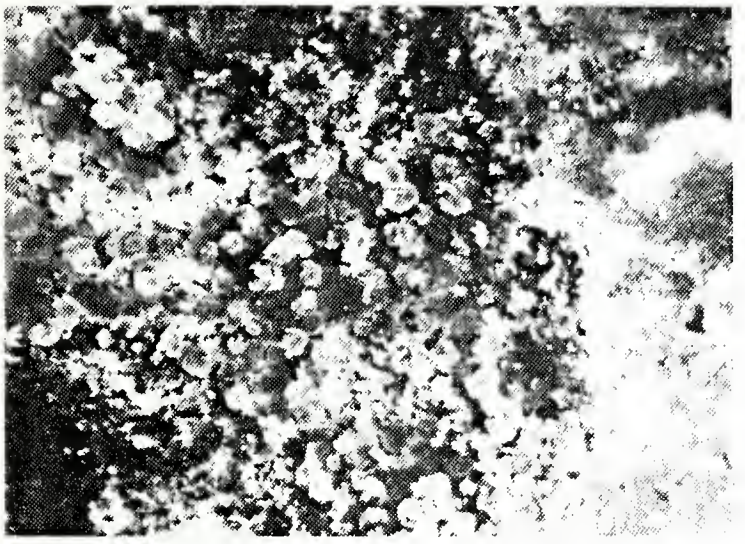

Figure 135. Enlarged view of crystalline patch at right of previous figure. (30X).

The black areas became very loose when they were dried and then observed in the SEM (figure 136). X-ray fluorescence analysis of these scales showed the presence of copper, nickel, iron, and chlorine as well as a trace of calcium. See figure 137. Rather universally distributed rounded particles of small size are shown in figure 138. They appear to be lodged in rows of machine marks. No X-ray fluorescence analysis was performed. The greenish areas became highly charged (figure 139) making high magnification SEM work difficult. These areas appear "mud-like" with cracks in them (figure 140). X-ray fluorescence analysis was not unique, showing the typical copper, nickel, iron and chlorine. When the specimen was chemically cleaned and re-examined by SEM, definite grain boundary attack was noted over most of the surface (figure 141).

The interior of the grains did not show steps from preferrential etching of high energy, non-close-packed planes (figure 142).

Figure 136. Scaly nature of the black dried corrosion products from the IML experiments. (21X).

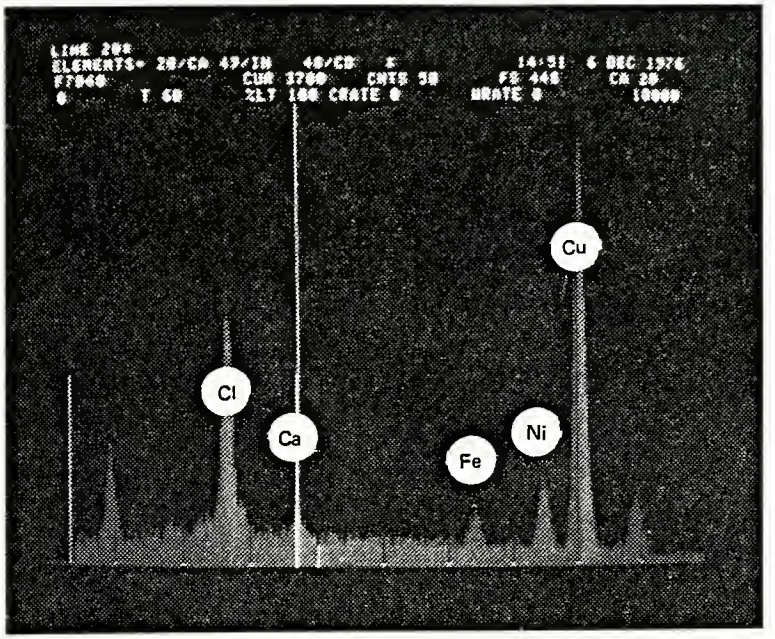

Figure 137. X-ray fluorescence analysis of the black, scaly corrosion products. Large amounts of copper and chlorine are shown, with lesser amounts of nickel, calcium and iron.

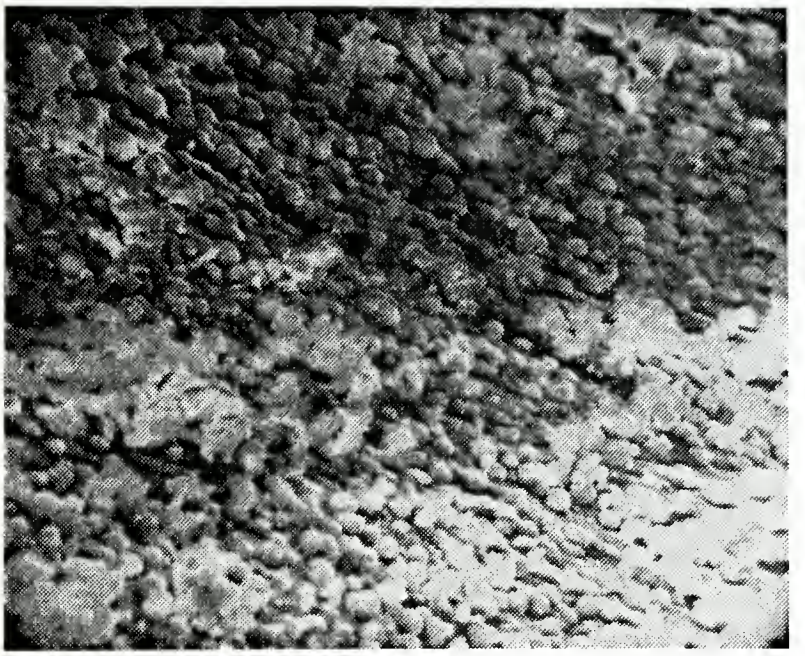

Figure 138. Rounded small particles attached over most of the surface of the IML specimens with hypochlorite ion added to the electrolyte. (1100X).

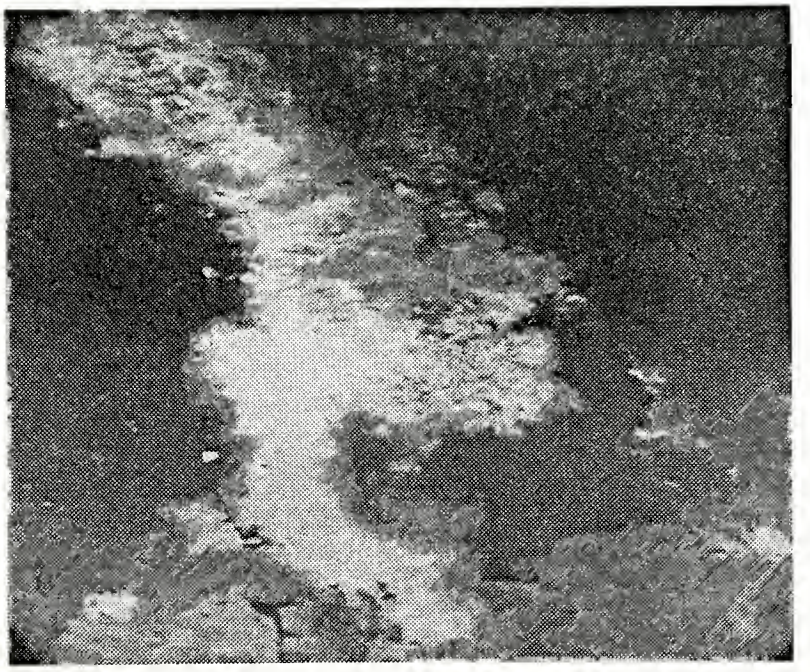

Figure 139. Low magnification SEM micrograph of highly charged green corrosion product attached to CDA 706 IML coupon immersed for 34 days in aerated synthetic seawater containing 200 ppm sodium hypochlorite. (24X).

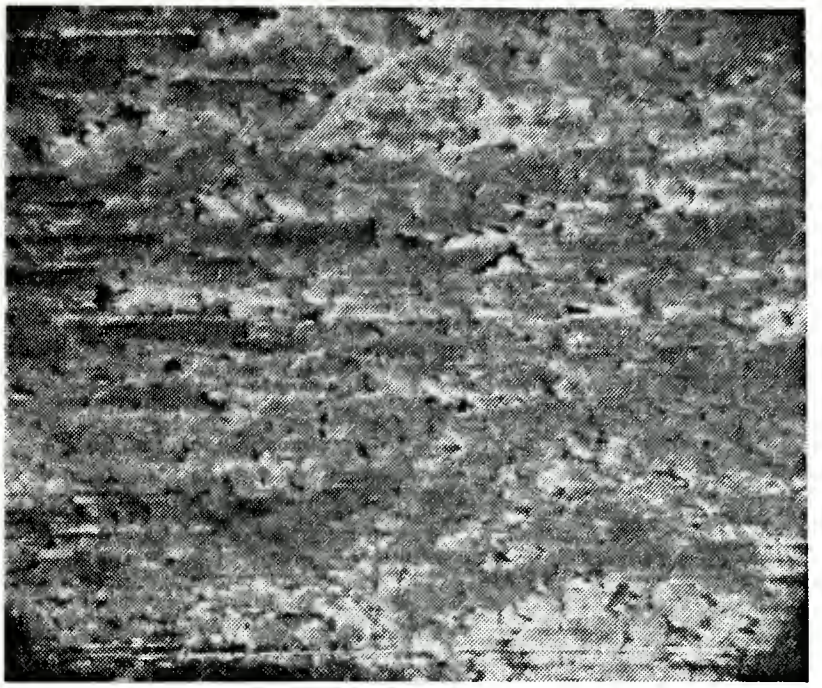

Figure 140. High magnification view of green corrosion product of figure 139. Specimen charging causes erratic photorecord. (1200X).

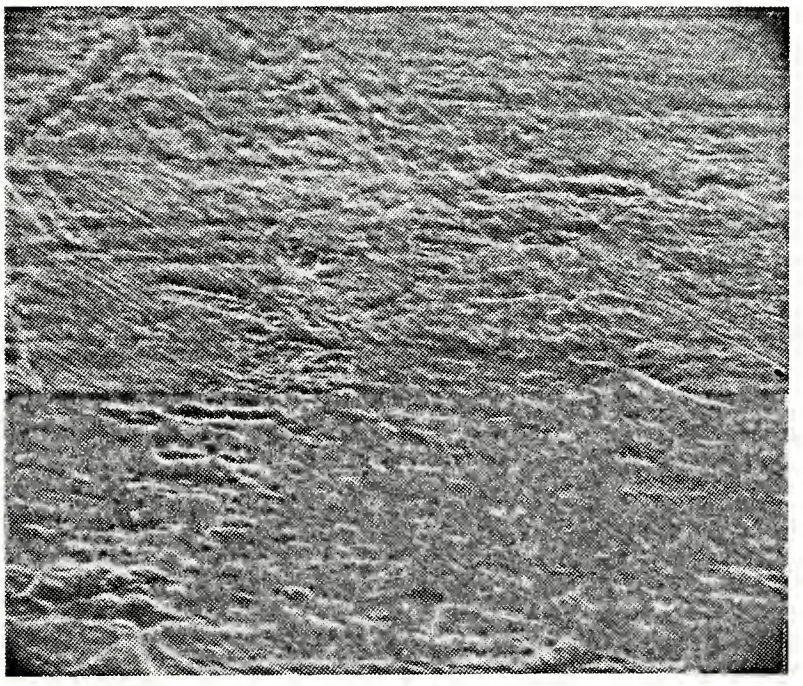

Figure 141. Selective grain boundary attack noted on CDA 706 IML coupon after removal of the corrosion products. (135X).

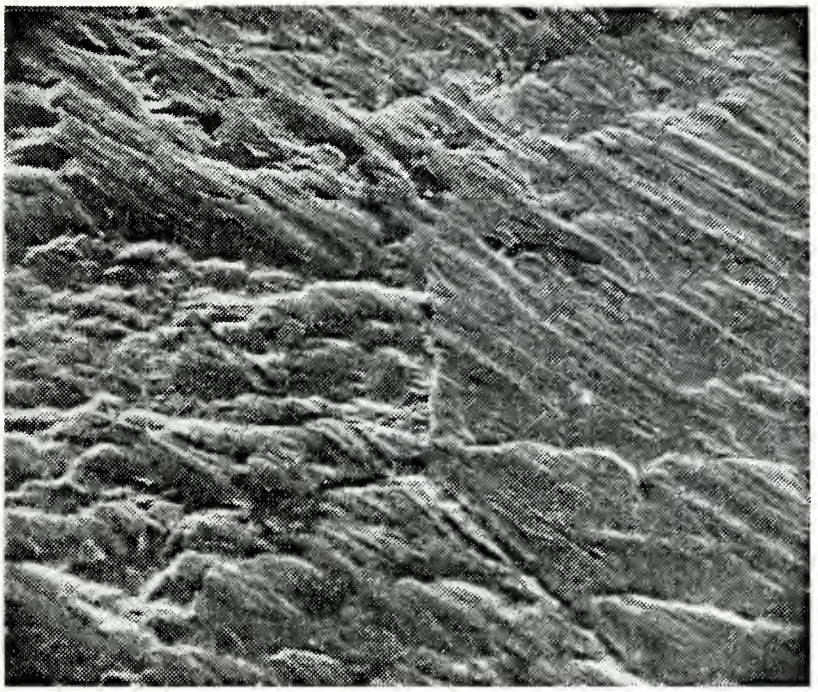

Figure 142. Magnified view of previous figure, to show the lack of parallel stairsteps within the grains. (670X).

For the short-time PSP measurements in hypohalite-containing corrodent, a visible color change occurs from silvery to a bronze color with a very thin white precipitate formed on the surface. This film appears porous on higher magnification (figure 143). On 4 hour PSP exposure, facetting is seen even with the naked eye. The color of the specimen changes to reddish during corrosion. Most of the corrosion products fall off the specimen surface upon merely touching the specimen holder. Observation at various magnifications in the SEM shows very deep intergranular corrosion (figure 144), especially at the juncture of three grains (figure 145). The characteristic stairsteps within the grains are also visible, as shown in figures 146 and 147.

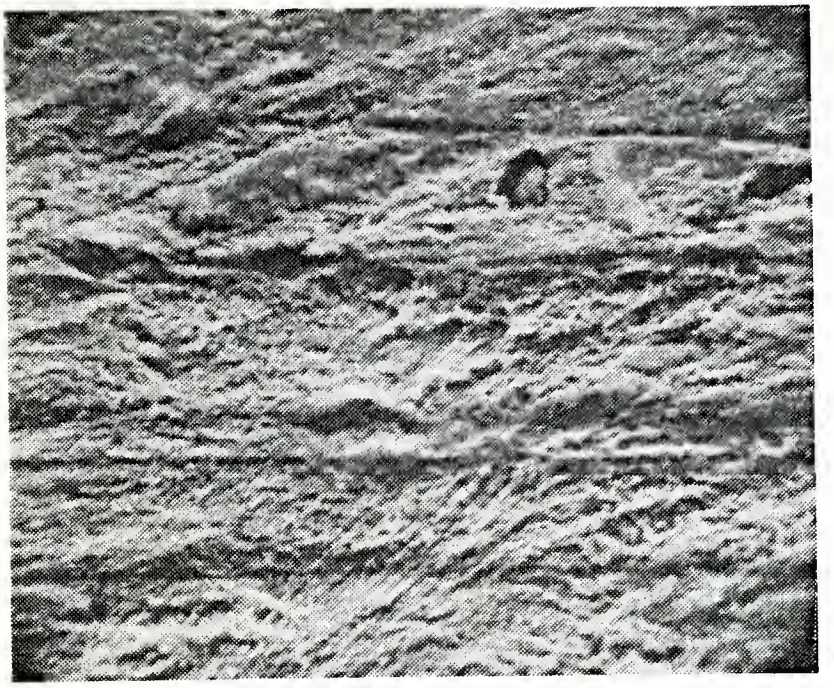

Figure 143. Porous thin film occuring on PSP 1 hour exposure of CDA 706 to hypochlorite-containing corrodent. (1400X).

Figure 144. Deep fissures at grain boundaries of CDA 706 PSP 4 hour run. (242X).

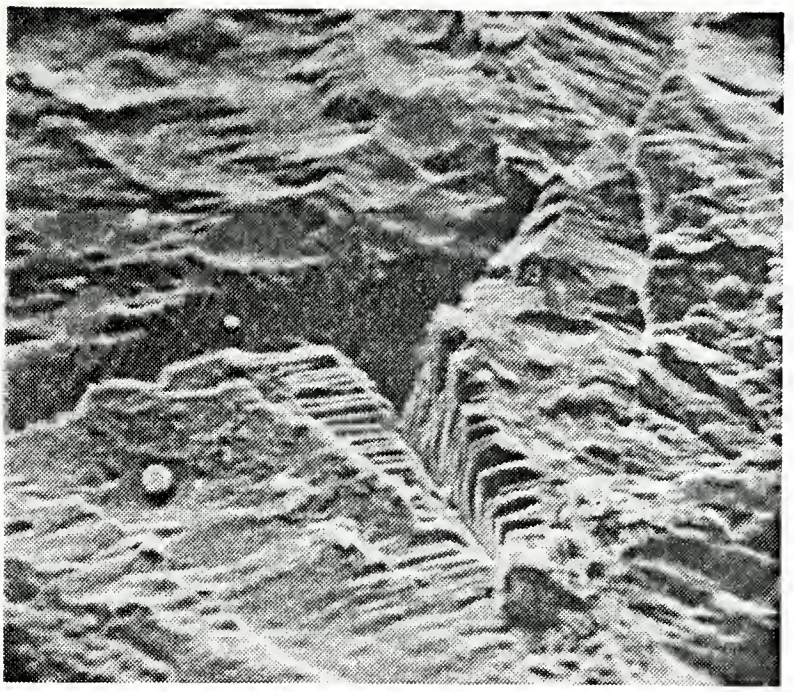

Figure 145. Very sharp, steep intergranular corrosion at the juncture of three grains in CDA 706 exposed to aerated synthetic seawater plus 200 ppm sodium hypochlorite. (1420X).

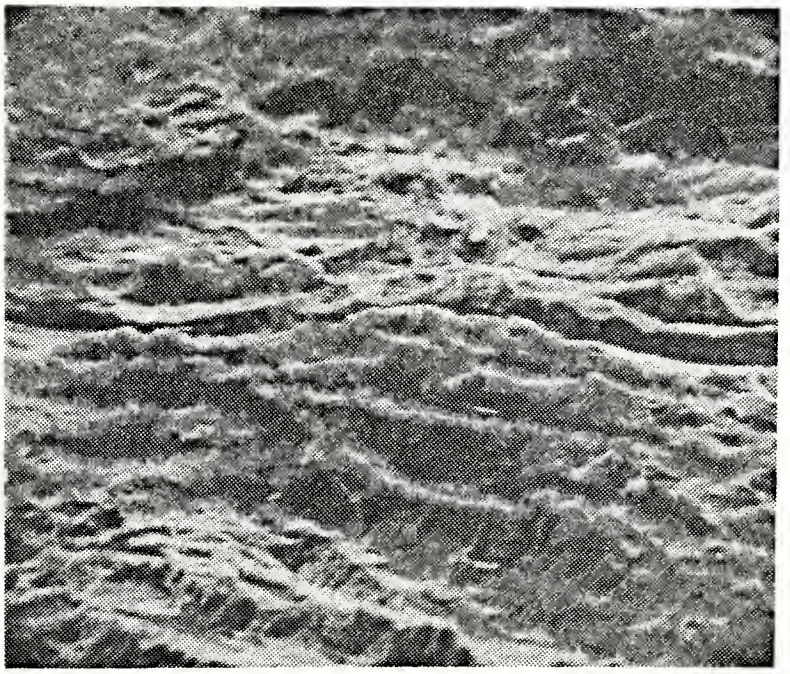

Figure 146. Parallel stairsteps formed within the grains of PSP coupon. (1420X).

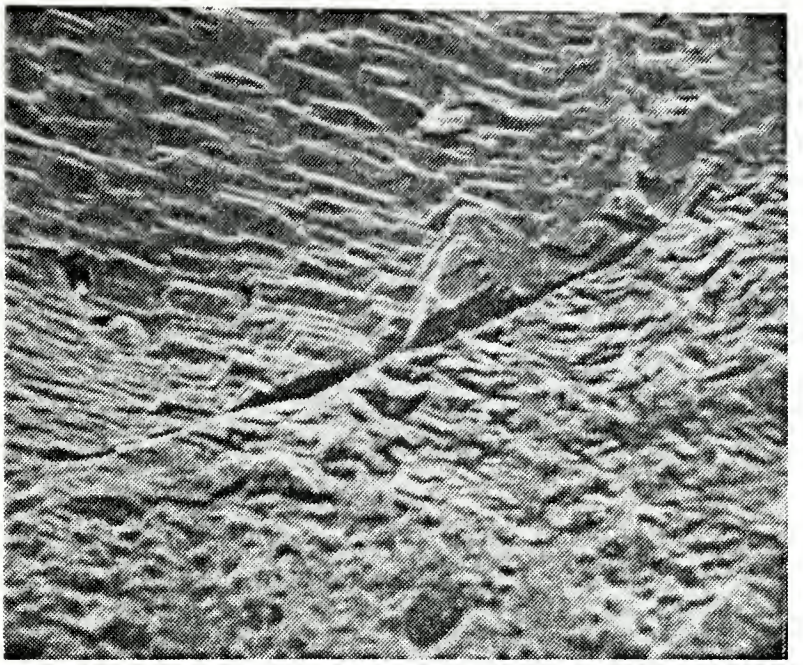

Figure 147. A second view of parallel stairsteps formed within the grains of CDA 706 in the PSP tests. (1400X).

A one-point experiment was performed in which the solution was stirred rapidly while the PSP run was being made. This gave entirely different results from the non-stirred experiments. A green precipitate appeared on some areas of the specimen with a thick, "mud-caked" appearance as shown in figure 148. X-ray fluorescence analysis of this highly charging area showed predominantly copper and chlorine lines. This result is compared to the pure base metal X-ray fluorescence spectrum (dots) in figure 149. The base metal was also corroded preferrentially at the grain boundaries, as shown in figure 150.

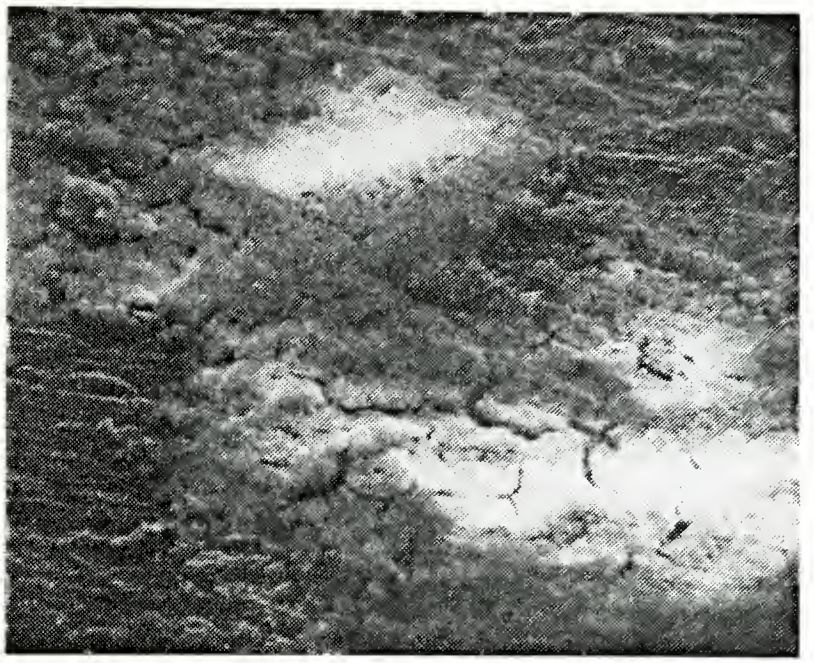

Figure 148. Green thick film formed when electrolyte containing hypochlorite ion was rapidly stirred. (282X).

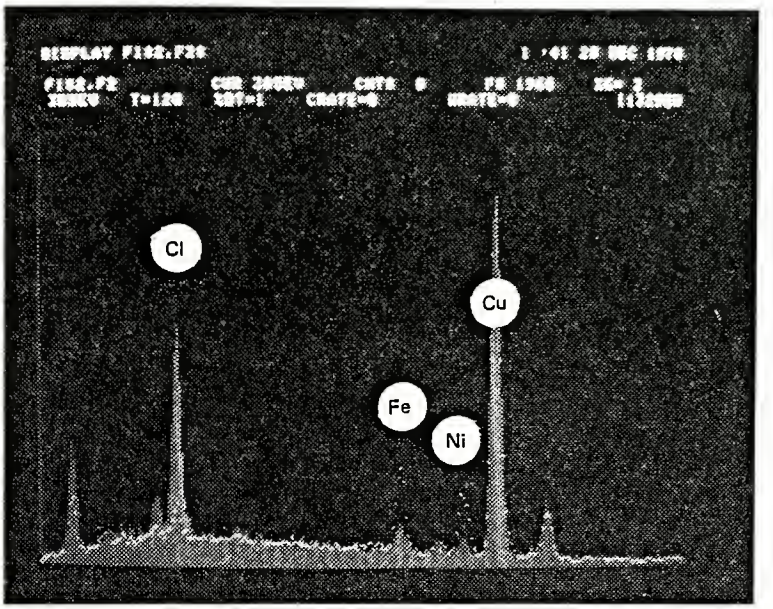

Figure 149. A comparison of the X-ray fluorescence spectra of pure CDA 706 and of the green corrosion product formed when the corrodent was rapidly stirred. The base metal is represented by the dots.

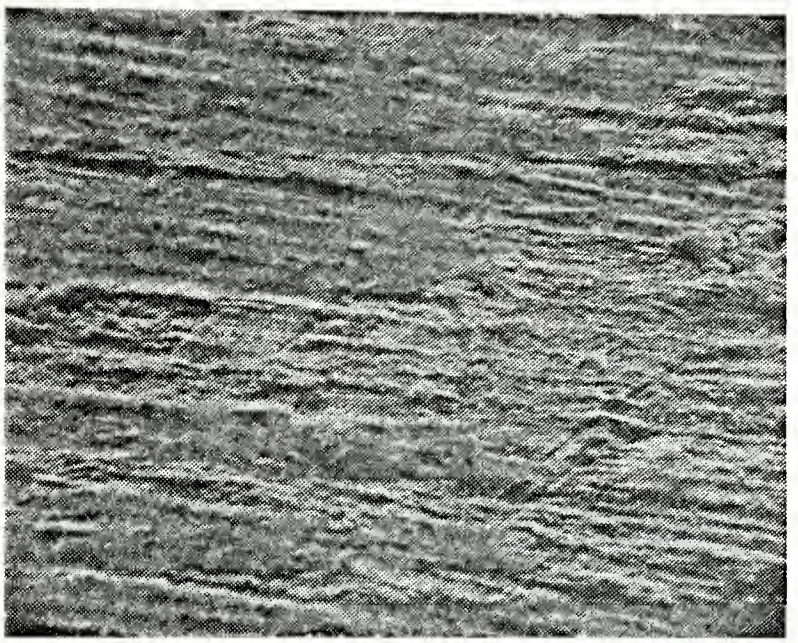

Figure 150. Grain boundary corrosion of CDA 706 in hypochlorite-containing electrolyte which was rapidly stirred during the corrosion process (PSP). (280X).

In summary, copper-nickel 90/10 (CDA 706) is more corrosion resistant than pure copper, but it ultimately suffers from grain boundary attack. It appears that several different corrosion processes occur in the IML experiments, while in the PSP runs, intergranular corrosion predominates, occuring very rapidly. Also, velocity of the electrolyte apparently can have an influence on the composition of the corrosion product as well as its physical structure.

b. CDA 715 (70/30 Copper-Nickel)

(1) Results With No Added Hypochlorite Ion.

CDA 715 is a high-nickel copper alloy and would therefore be expected to show much of the inertness of nickel to salt solutions. In these tests, there was virtually no corrosion observed. A thin green stain proceeded down one face of an IML specimen as shown in figure 151. This was revealed using light microscopy with very low angle illumination.

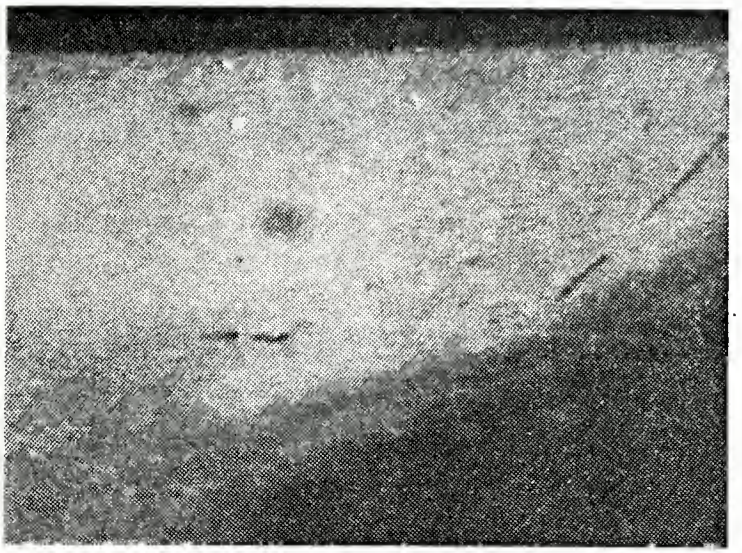

Figure 151. Thin light green stain proceeding down one face of CDA 715 IML test coupon after 34 days exposure to aerated synthetic seawater. (7.5X).

SEM examination in the area of the identification mark showed a collection of white crystals (figures 152 and 153), that X-ray fluorescence analysis indicates to be mostly residual sodium chloride (figure 154). A dielectric layer (light colored in figure 155) tends to show sensitivity to the electron beam (figure 156).

Figure 152. White crystals in identification stamped marking of CDA 715. (32X).

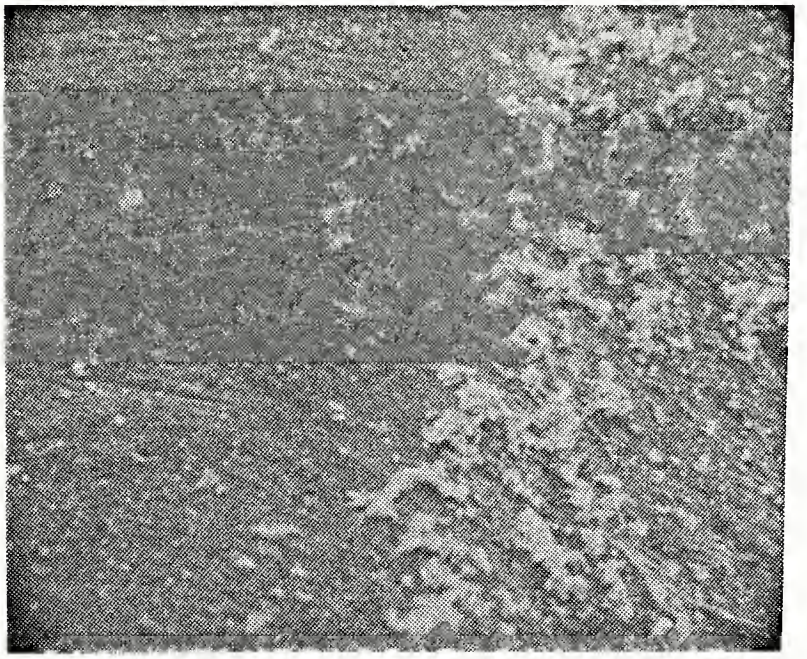

Figure 153. Higher magnification view of white crystals of figure 152. (300X).

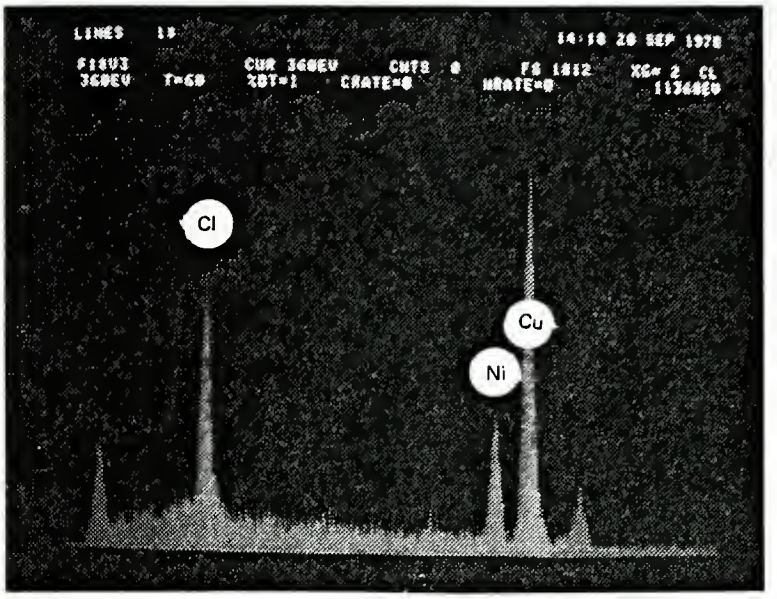

Figure 154. X-ray fluorescence analysis of white crystals of figure 153. Copper, nickel and chlorine are predominant peaks.

Figure 155. Green dielectric stain on surface of CDA 715 IML coupon. (43X).

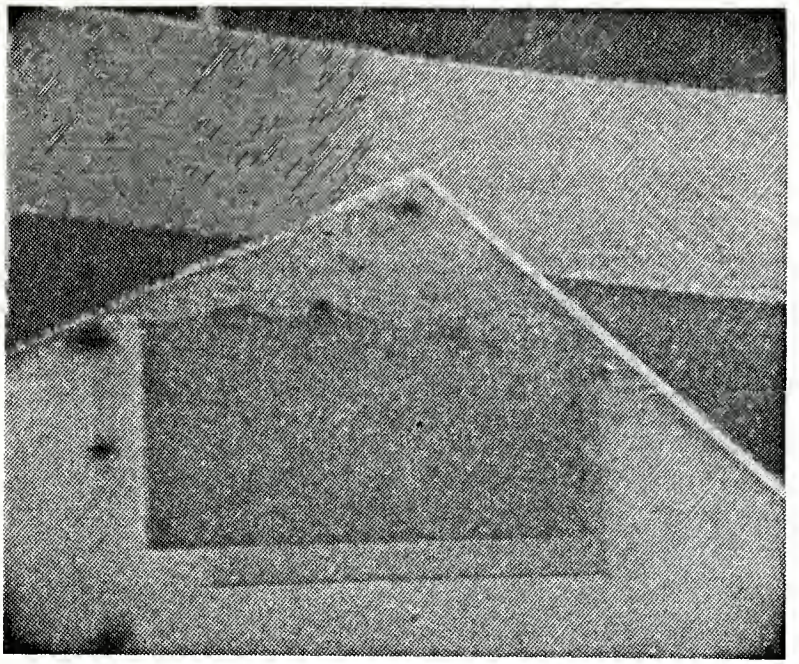

Figure 156. Square areas are those previously examined at higher magnification and which are damaged by the electron beam in the SEM. (17X).

The darker area surrounding the dielectric film is perforated occasionally as if a bubble had sat there for a long period of time (see figure 157).

Figure 157. Perforation in dark film on IML specimen of CDA 715 at very high magnification. (2000X).

The cleaned IML specimens showed almost no corrosion damage (see especially the comparative macrophotographs in figures 189 and 195). At high magnification, a few shallow pits were visible (figure 158).

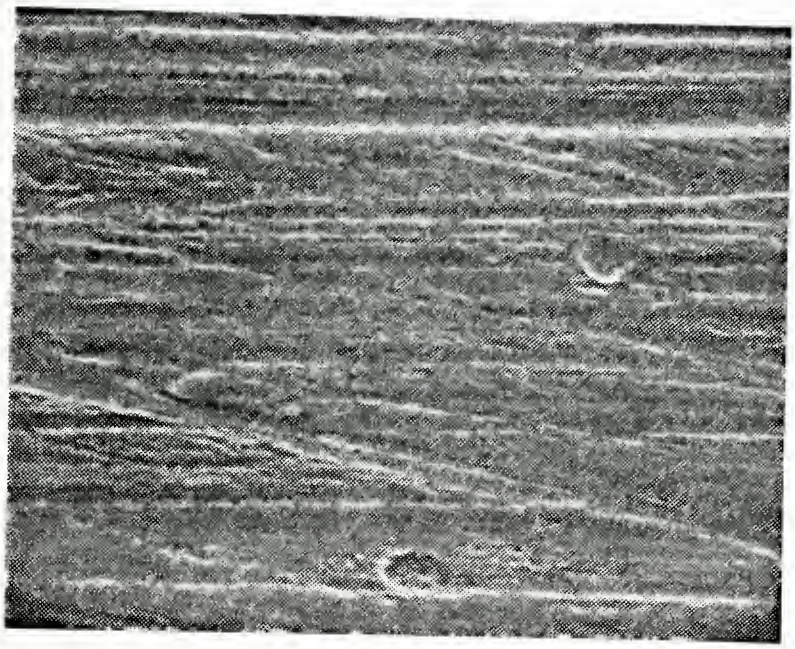

Figure 158. Tiny shallow pits observed at high magnification in CDA 715 IML coupon which had been previously exposed to aerated synthetic seawater for 34 days and then cleaned. (1300X).

PSP runs of increasing duration in the aerated seawater corrodent show only the formation of a very thin brown or black stain (figure 159). At high magnification, the film is porous at short PSP exposures (figure 160), but the pores gradually fill up for longer duration runs (figure 161) and there is some evidence of very minor localllized corrosion at long exposures (figure 162).

In summary, CDA 715 copper-nickel alloy withstands aerated synthetic seawater well, with a low, uniform corrosion rate.

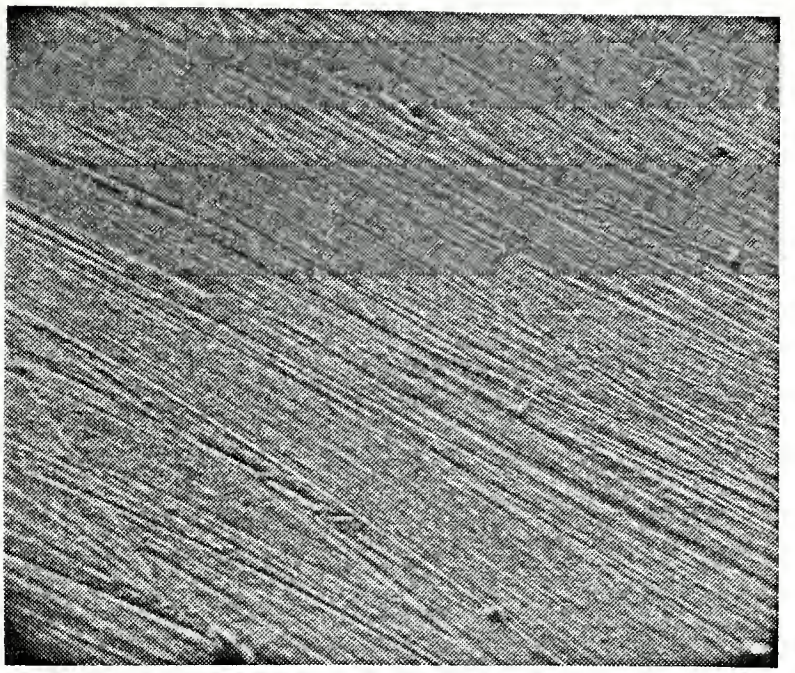

Figure 159. Thin dielectric film covering surface of CDA 715 PSP coupon. (148X).

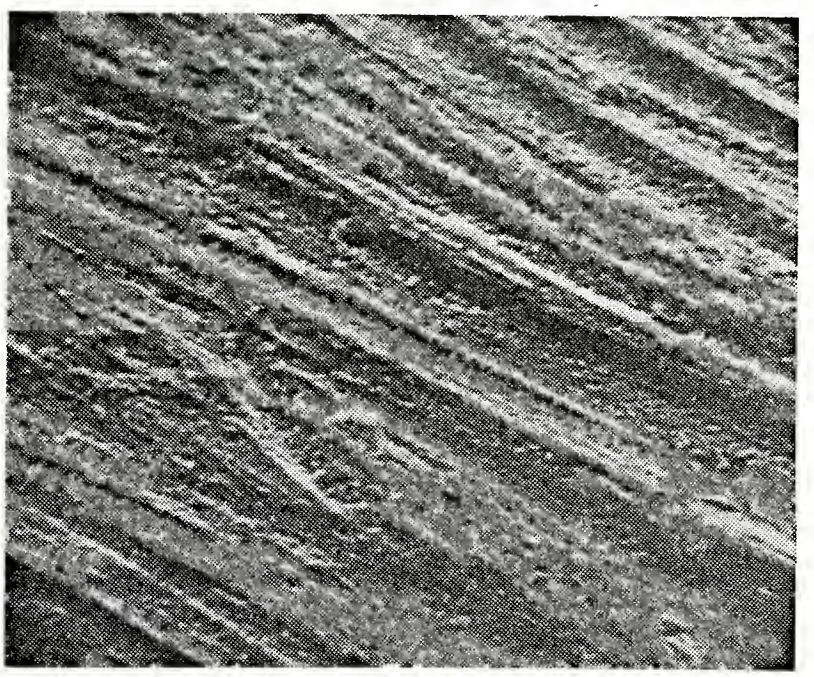

Figure 160. Porous nature of dielectric film formed by short exposures in aerated synthetic seawater. (1470X).

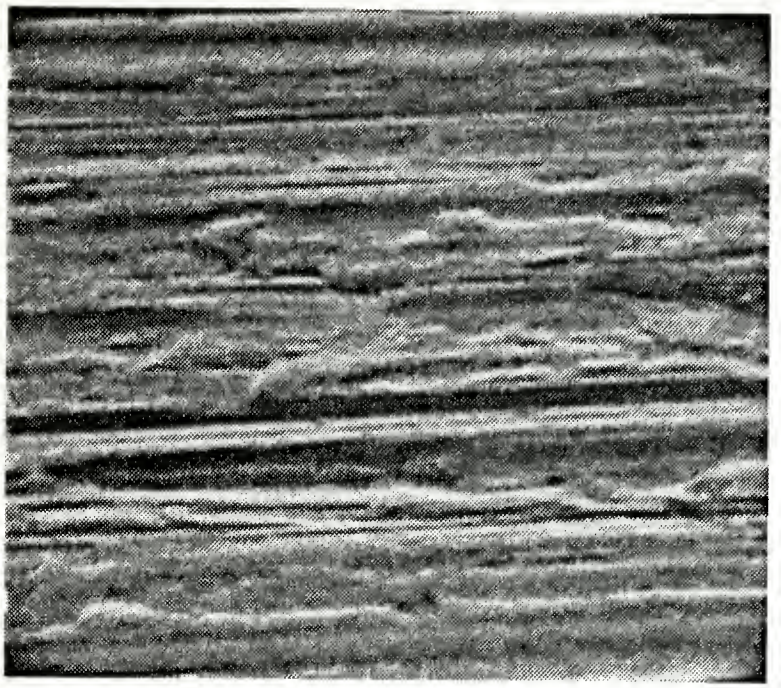

Figure 161. Uniform compact film on four hour PSP coupon of CDA 715. (1490X).

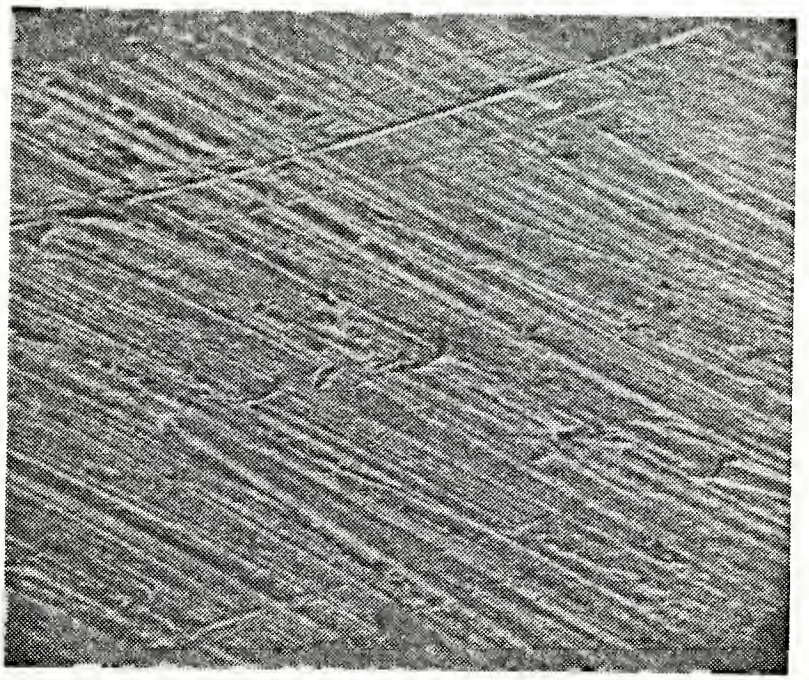

Figure 162. Possible locallized corrosion on CDA 715 specimen exposed to aerated synthetic seawater for 12 hours in the PSP experiments. (320X).

(2) Results With 200 ppm Added Sodium Hypochlorite.

This material-electrolyte combination produced the most startling corrosion product formation of all the IML experiments. The specimen emerged from the corrodent with a thick, powdery coating over virtually all of the specimen surface, although there were a few tiny patches of light green at the top and down one side. The contrast with the CDA 715 IML run without hypochlorite ion is striking. This can best be seen in the comparative macrophotographs in figures 189 and 195. See also figure 163. There were also perfect hemispheres of translucent white spread throughout the black precipitate (figures 164 and 165).

Figure 163. Light green patch at top of IML coupon which is otherwise covered with thick black velvety corrosion products. (7.5X).

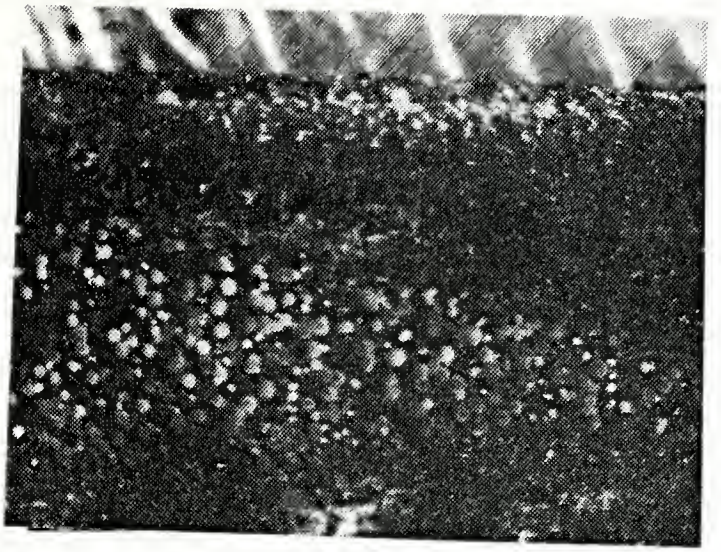

Figure 164. White translucent hemispherical crystals attached to CDA 715 IML specimen exposed previously to hypochlorite-containing corrodent. (7.5X).

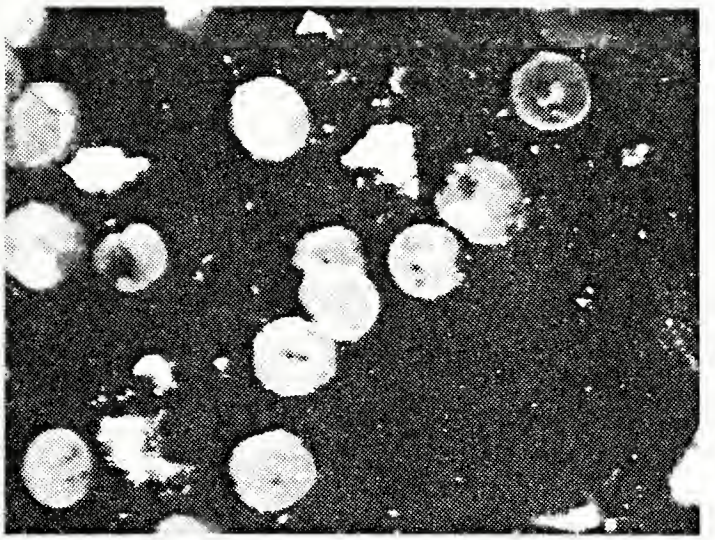

Figure 165. Detail of white hemispheres spread over matte black corrosion products. (30X).

SEM observations were also revealing. Pronounced grain boundary attack in areas not covered by the black velvety corrosion product was immediately evident. See figures 166 and 167.

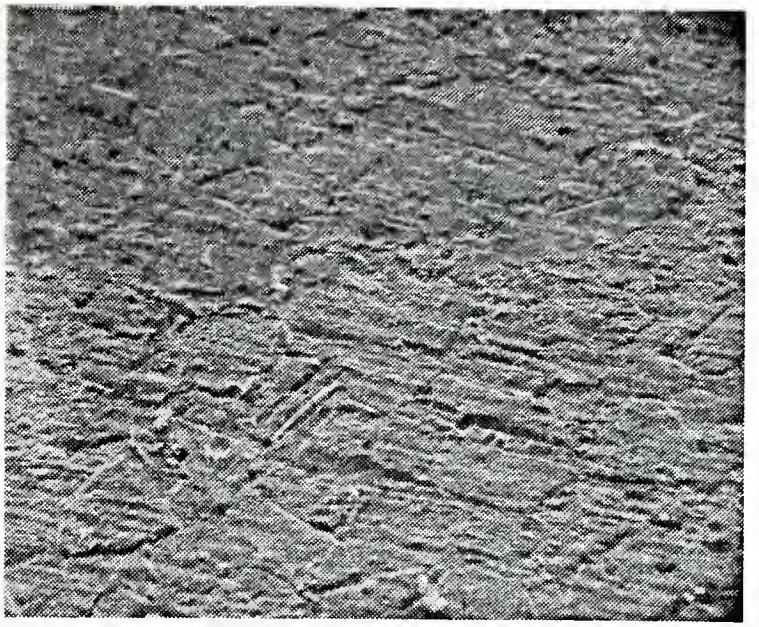

Figure 166. Pronounced grain boundary attack near top of IML test coupon. (152X).

Figure 167. Grain boundary attack on another area of the specimen shown in figure 166. (276X).

In addition, the internal structure of each of the grains was unusual, not so much stair-stepped as in the other materials, but consisting more of geometric arrangements of pointed structures. See figures 168 and 169.

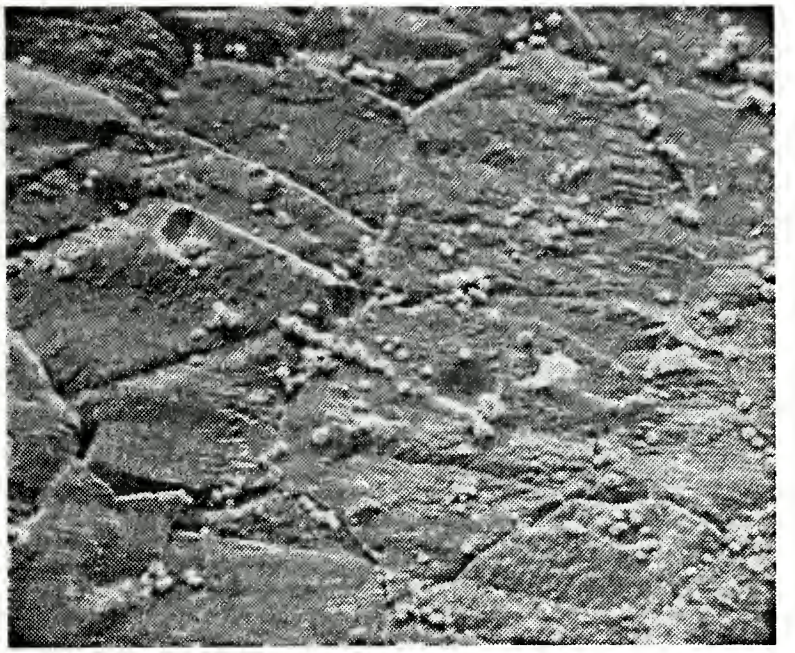

Figure 168. Etched grain boundaries and corroded grain interiors. Pointed structures internal to grain are visible. (750X).

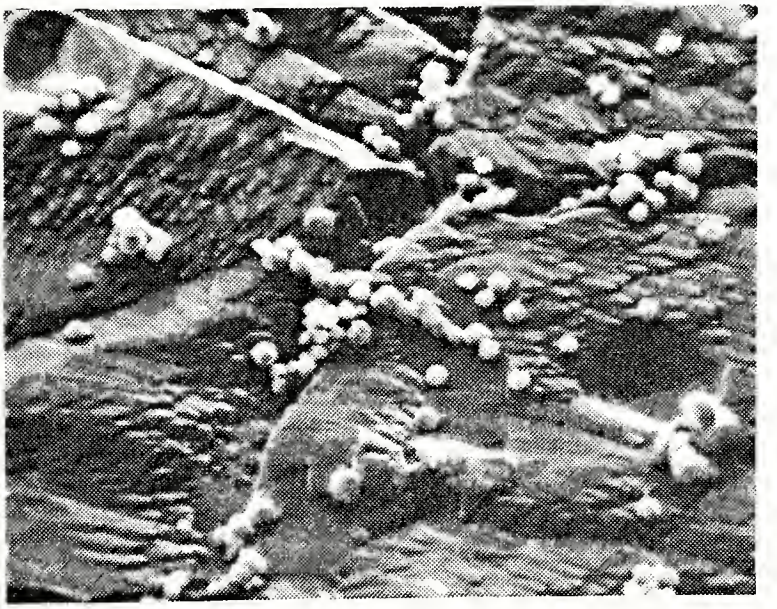

Figure 169. Enlargement of figure 168 showing preferrentially corroded grain boundaries and pointed structures. (1500X).

Also evident are several geometrically shaped holes where crystals apparently have fallen out (figure 170). Note also the small complex cubic/octahedral/dodecahedral crystals spread over the surface in figure 170.

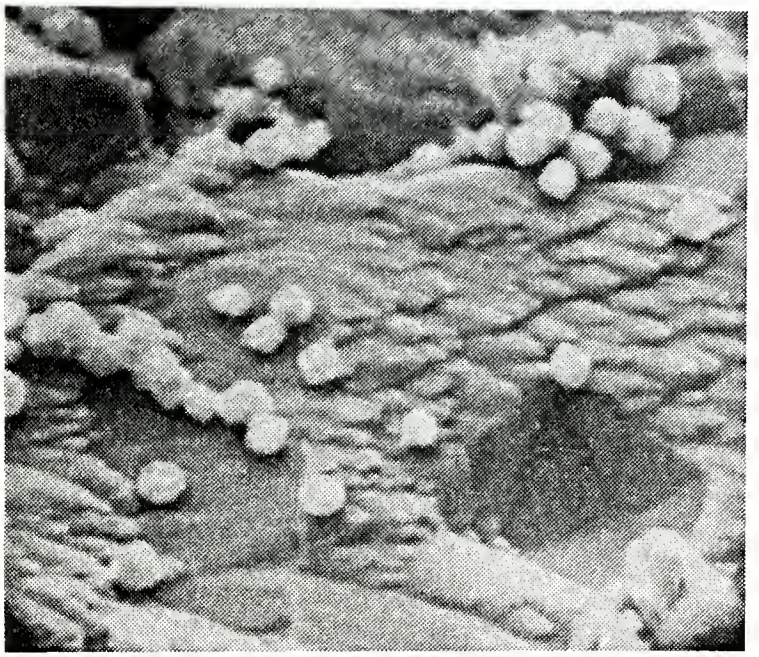

Figure 170. Large geometrically shaped hole within one grain, approximately complementary in shape to the smaller light colered crystals of complex geometry. CDA 715 test coupon. (3000X).

In the velvet black area (figure 171) a high concentration of nickel and calcium exists, with a lesser amount of chlorine present (figure 172). When this area was chemically cleaned to remove the corrosion products, selective grain boundary corrosion was again evident (figure 173), but with the added feature of whole grain removal (figure 174) as well as shallow pit formation (figure 175).

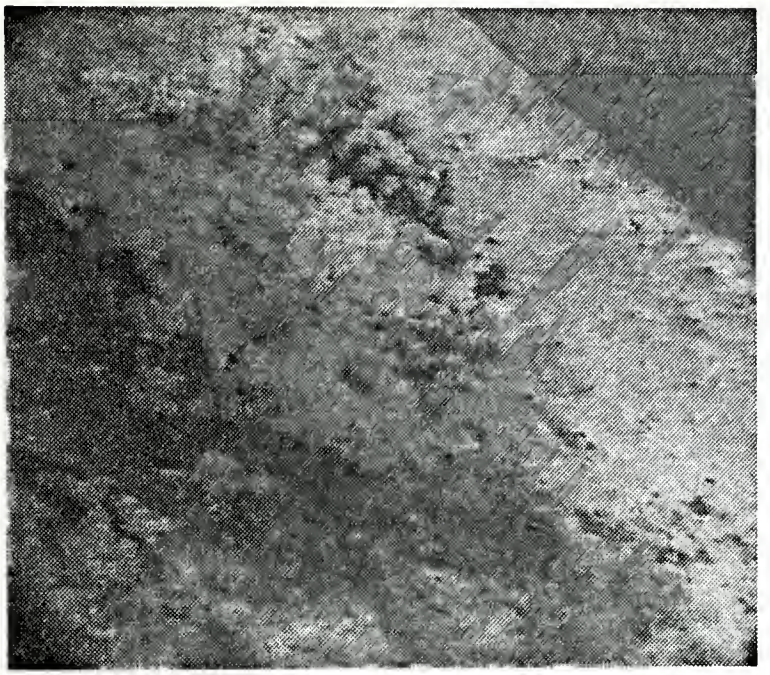

Figure 171. Velvety black area appears whitish in SEM as it charges somewhat. (21X).

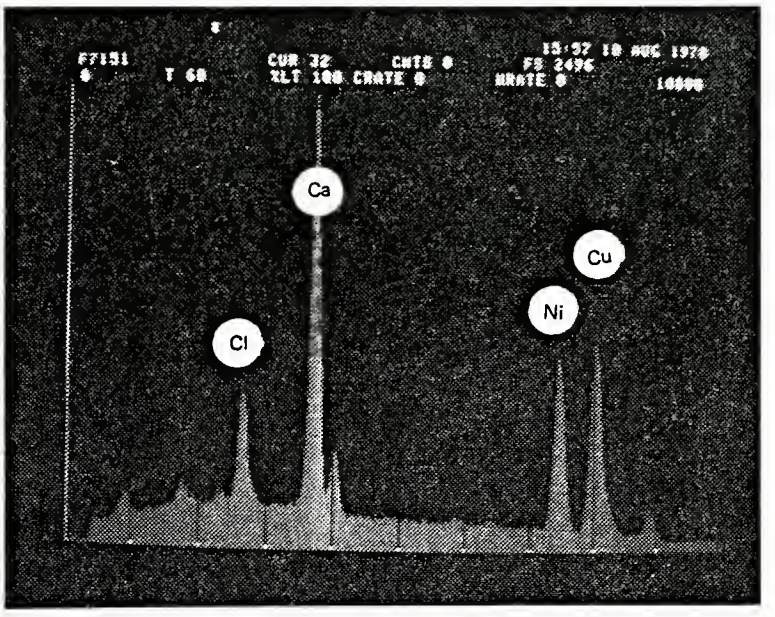

Figure 172. X-ray fluorescence analysis of velvet black area shows the presence of high concentrations of nickel and calcium, with a lesser amount of chlorine.

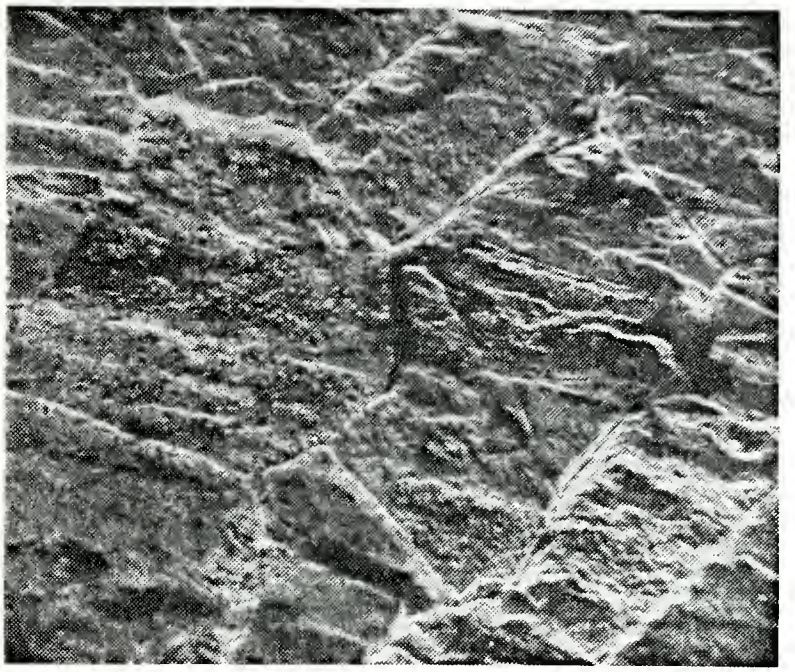

Figure 173. Selective grain boundary corrosion of CDA 715 IML coupon exposed for 34 days to hypochlorite-containing electrolyte and then cleaned. (600X).

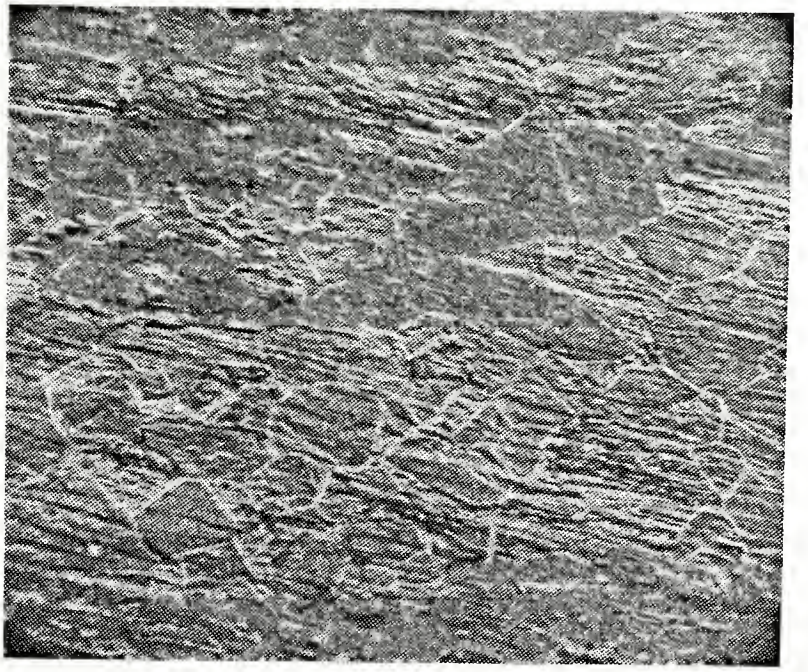

Figure 174. Loss of several whole grains in area underneath the black velvety corrosion product. (120X).

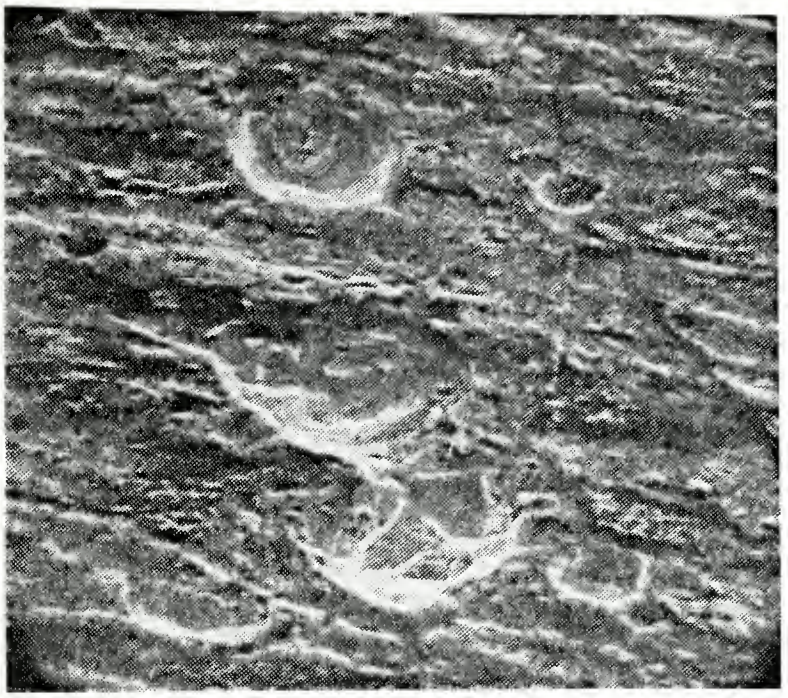

Figure 175. Shallow pits evident at high magnification of CDA 715 IML test coupon. (1220X).

It is felt that a different corrosion mechanism previailed in the PSP tests for this material/electrolyte combination. On short exposures (12 minutes), white filmy precipitates formed on the surface, but immediately fell off on removal of the specimen from the corrosion cell. Upon longer exposures (60 minutes), the specimen again produced the white filmy corrosion product, most of which fell off on removal of the specimen from the flask. The surface shows ridges (figure 176), which on closer inspection are found to be composed of triangular crystallites. See figures 177 and 178. Intergranular attack is already evident but apparently the triangular crystallites are not associated with the grain boundaries. However, these crystallites orient differently within each grain (figure 179). X-ray fluorescence analysis

shows only copper and chlorine compose the crystallites -- no nickel is present (figure 180).

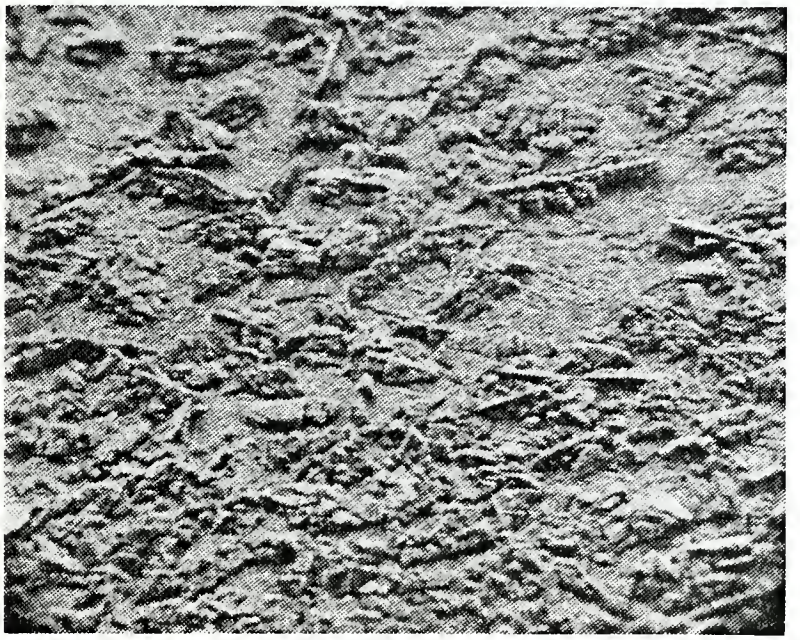

Figure 176. Ridged structures evident in the 60 minute PSP exposure of CDA 715 to electrolyte containing hypochlorite ion. (150X).

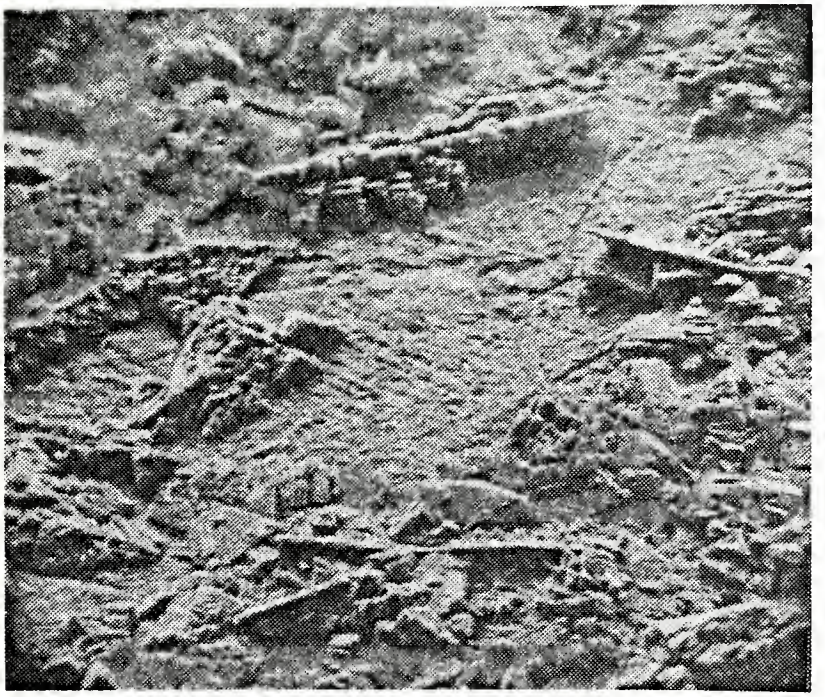

Figure 177. Magnified view of previous photograph, showing the triangular nature of the crystalline products. (300X).

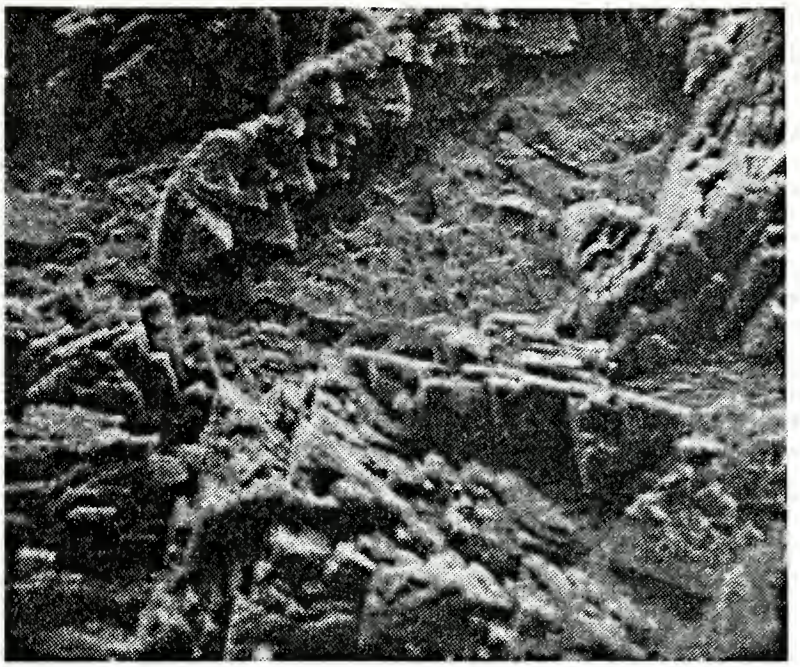

Figure 178. Further magnification of figure 176, showing the triangular crystallites attached to the specimen surface. These crystallites are apparently not associated with the grain boundaries. (750X).

Figure 179. Triangular crystallites oriented at different angles within individual grains. (1500X).

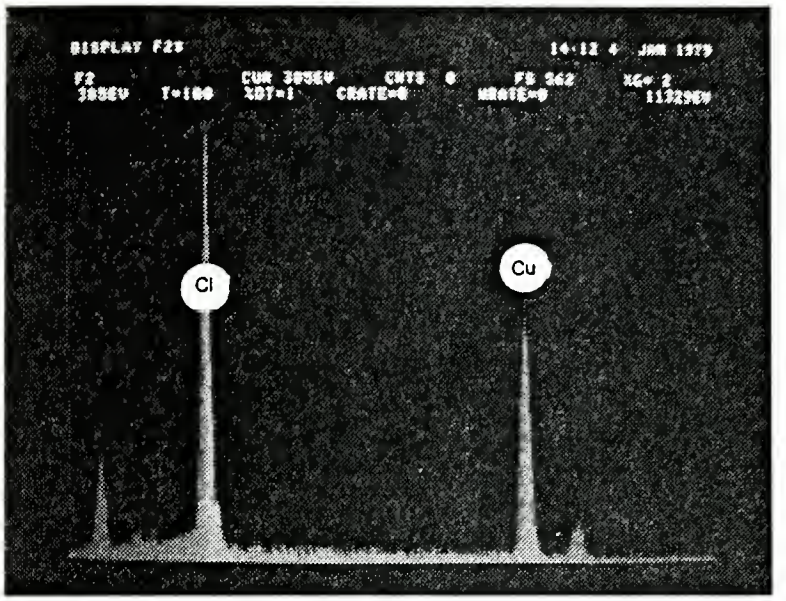

Figure 180. X-ray fluorescence spectrum of triangular crystallites, showing presence of major chlorine and copper lines. No nickel is seen.

This can be seen more easily by comparing the X-ray fluorescence spectra of areas without triangular crystallites (dots) to those with crystallites (lines). See figure 181.

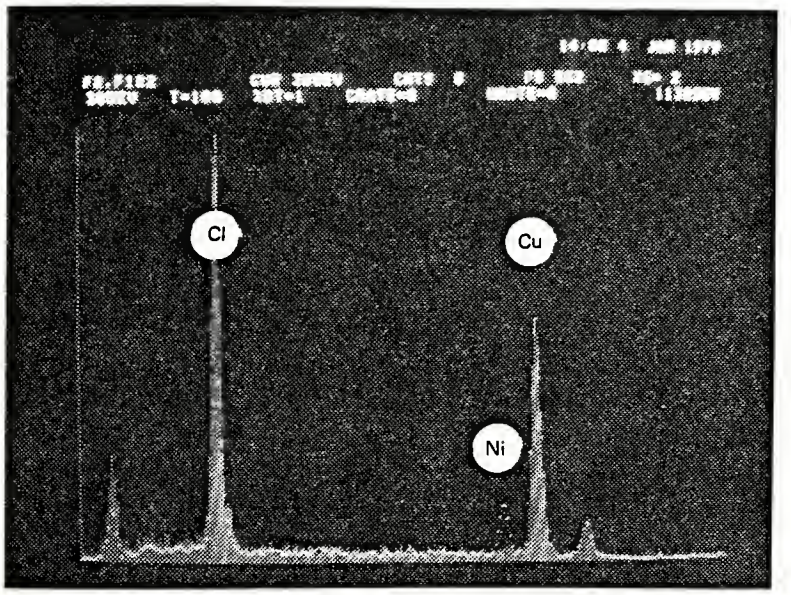

Figure 181. X-ray fluorescence analysis of triangular crystallites (lines) and areas with crystallites attached (dots). Note absence of nickel in the crystallites.

On much longer PSP exposure (8 hours), the triangular crystallite regions grow closer together, as shown in figures 182 and 183.

Figure 182. Compacted, heavy growth of the crystallite corrosion product on long term PSP exposure to aerated synthetic seawater containing hypochlorite ion. (65X).

Figure 183. Magnified view of previous figure, showing compacted triangular crystallite growth. (260X).

X-ray fluorescence analysis remains the same as before -- copper and chlorine only. The crystallite spacing is closer on the longer exposures (figure 184). Also different grains still show different crystallite orientations (figure 185). No black precipitate ever formed in the PSP runs.

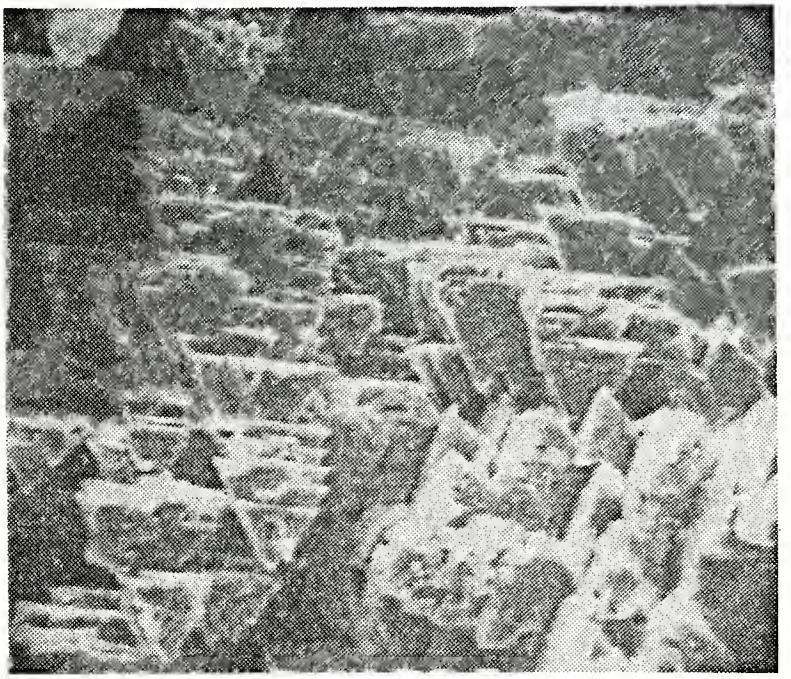

Figure 184. Long term PSP exposure of CDA 715 to hypochlorite-containing media results in closely spaced triangular crystallites. (1150X).

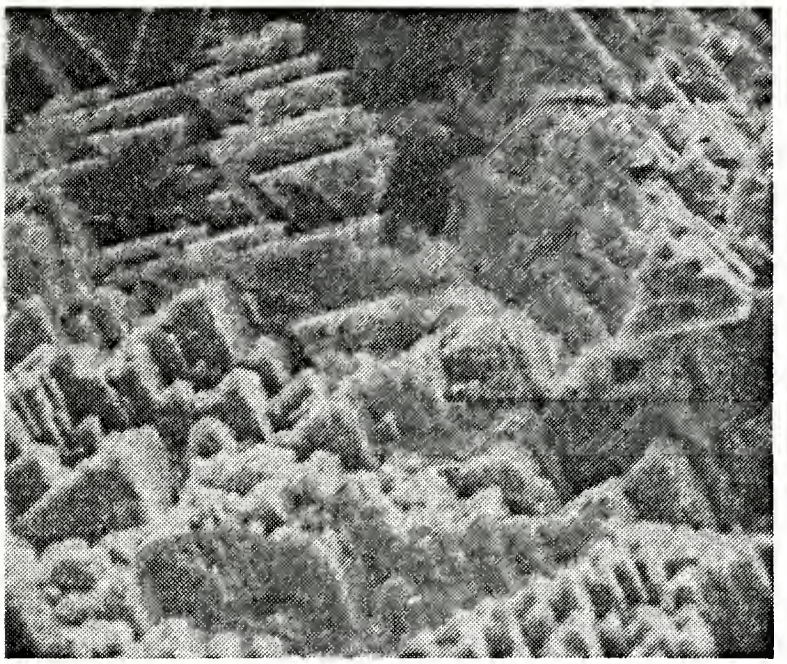

Figure 185. Note various orientations of crystallites in different grains, separated by grain boundaries with essentially no crystallite growth. (1300X).

In summary the two major modes of corrosion testing (IML and PSP) produced different corrosion products on CDA 715. In IML, a predominant corrosion product was nickel related -- probably an oxide of nickel. With the PSP method, X-ray fluorescence analysis suggests a copper related corrosion product containing a large amount of chlorine. However, both methods of testing produced grain boundary attack. The addition of hypochlorite ion rapidly accelerates the grain boundary attack in this material.

5. Summary of Microscopic Examinations

a. CDA 101 (OFHC Copper)

For copper immersed in aerated synthetic seawater, general observations are that the metal initially corrodes by minute pitting and that these pits may later merge to give a more generalized corrosion mode. There is also selective corrosion at deep machine marks.

For copper immersed in hypochlorite-containing aerated synthetic seawater, corrosion rates are markedly increased. This combination of air and electrolyte is very corrosive to copper, with the grain boundaries being preferentially attacked. A complicated dissolution-precipitation process is indicated by the presence of porous pitting over most of the surface and by the complex cubic crystallites of pure copper present. The pitting and dissolution-precipitation appear to be carried out underneath a complicated corrosion product blanket containing copper, chlorine, bromine and no doubt oxygen (as the oxides or hydroxides of copper).

b. CDA 260 (70/30 Copper/Zinc--"Cartridge Brass")

The IML specimens showed a porous corroded surface developed at long exposure times. The PSP experiments showed layers of corrosion products, beneath which was evident classical grain boundary attack. Inside each of the grains were stepped structures, which correspond to the corrosion of non-close-packed planes as described by Vermilea [36].

Those specimens corroded in an electrolyte of aerated synthetic seawater containing added hypochlorite ion

showed predominantly layer type of dezincification, as well as intergranular attack.

c. CDA 280 (60/40 Copper/Zinc -- "Muntz Metal")

In aerated synthetic seawater electrolyte, selective beta phase corrosion was seen, with the formation of zinc oxide hexagonal platelets (similar to that for pur zinc immersed in synthetic seawater [37]. Here a compact film is first formed, and then on these basement layers, an outcropping of small zinc oxide platelets appears, with an increase in the thickness of the compact film as well as the size and number of platelets with increasing exposure time.

In media containing hypochlorite ion, this material corrodes by selective attack of the zinc-rich beta phase which is anodic to the alpha material that surrounds it. Hexagonal zinc oxide platelets form next to the corroding beta phase fissures, eventually forming a thick corrosion product over the whole alpha surface. The presence of hypochlorite ion greatly increases the rate and depth of the penetration of the beta phase.

d. CDA 706 (90/10 Copper/Nickel)

In aerated synthetic seawater alone, the low uniform corrosion rate of about 1 mdd (4.1 μmpy) is born out by surface observations of the IML specimens. Here, a slow, rather uniform corrosion is achieved. In the PSP runs, a different corrosion mechanism may be operative, as the film utilizes increasing amounts of iron from within the alloy. There is also evidence of intergranular corrosion.

In an electrolyte containing hypochlorite ion, CDA 706 is more corrosion resistant than pure copper, but it ultimately suffers from grain boundary attack. It appears that several different corrosion processes were operative in the IML experiments, while in the PSP runs, intergranular corrosion rapidly occured. It is of note that the velocity of the electrolyte can change the composition of the corrosion products as well as their physical structure.

e. CDA 715 (70/30 Copper/Nickel)

This alloy, subjected to aerated synthetic seawater, displays a low, uniform corrosion rate. It withstands this electrolyte well.

In aerated synthetic seawater containing added hypochlorite ion, the two modes of testing produced different corrosion products. In the IML method, a predominant corrosion product was nickel related -- perhaps a nickel oxide such as NiO_2. In the PSP method, x-ray fluorescence analysis suggests a copper-related corrosion product containing large amounts of the element chlorine. However, both methods of testing produced grain boundary attack. The addition of hypochlorite ion to the corrosive medium rapidly accelerats the grain boundary attack of this material.

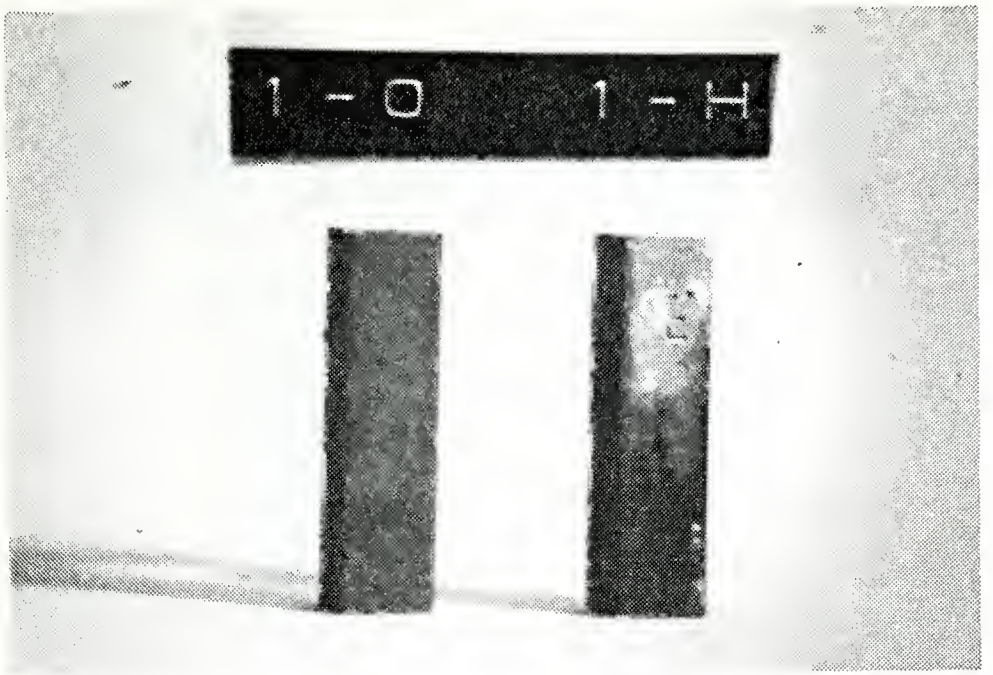

Figure 186. CDA 260 macrophotograph of IML test coupons in aerated synthetic seawater (left) and with added hypochlorite ion (right).

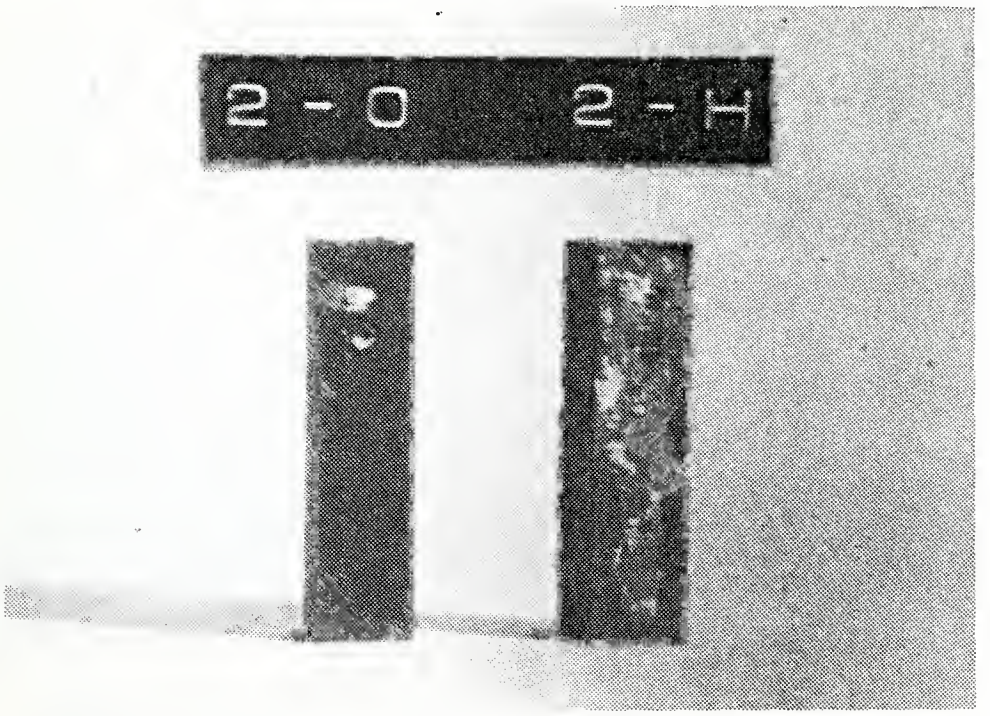

Figure 187. CDA 280 macrophotograph of IML test coupons in aerated synthetic seawater (left) and with added hypochlorite ion (right).

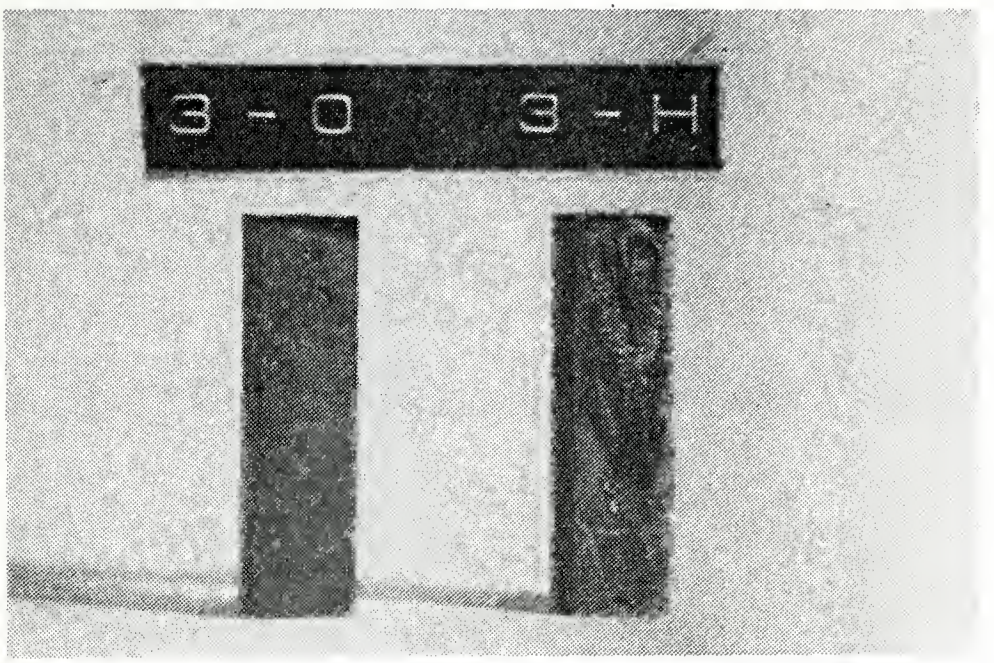

Figure 188. CDA 101 macrophotograph of IML test coupons in aerated synthetic seawater (left) and with added hypochlorite ion (right).

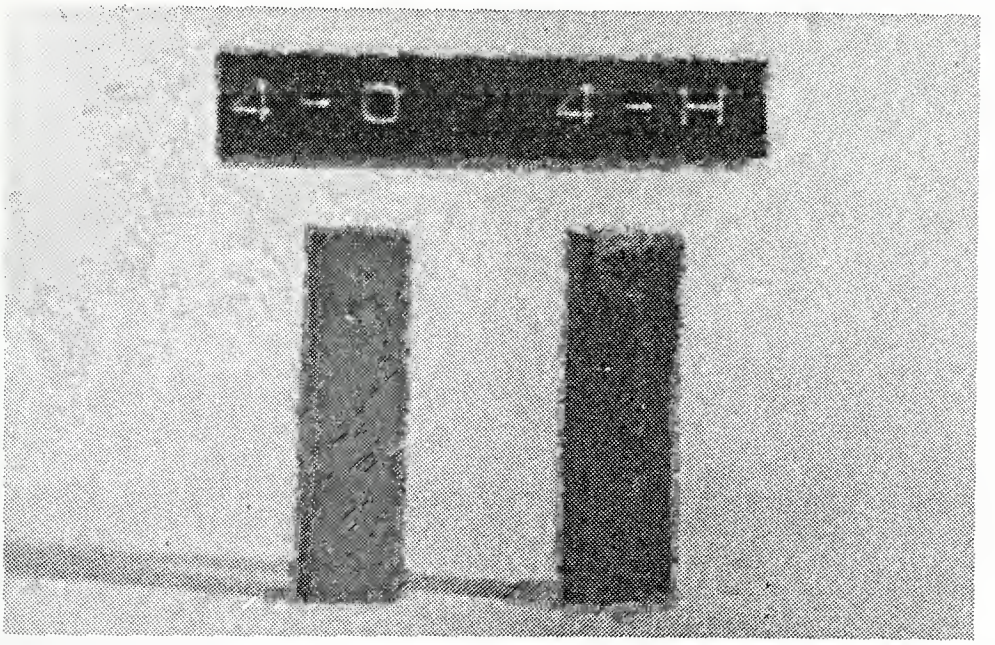

Figure 189. CDA 715 macrophotograph of IML test coupons in aerated synthetic seawater (left) and with added hypochlorite ion (right).

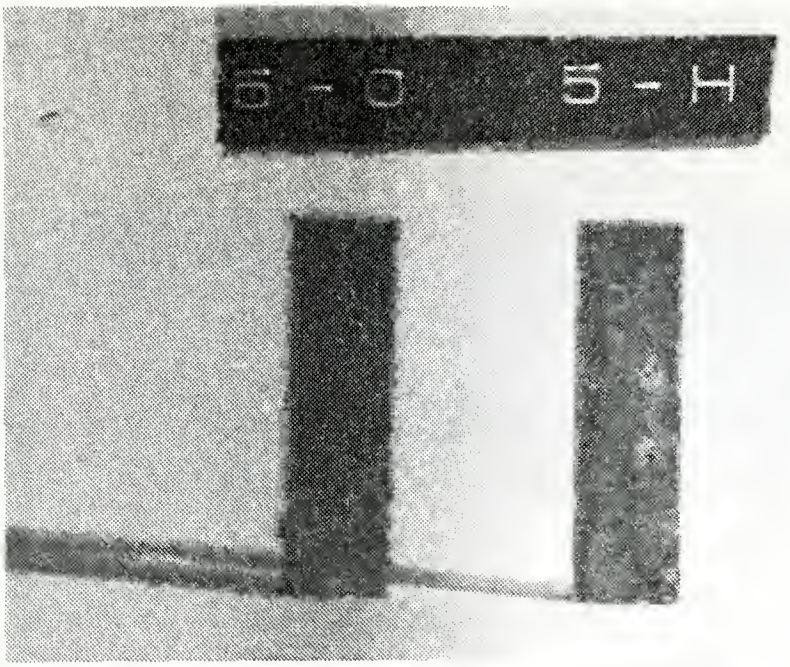

Figure 190. CDA 706 macrophotograph of IML test coupons in aerated synthetic seawater (left) and with added hypochlorite ion (right).

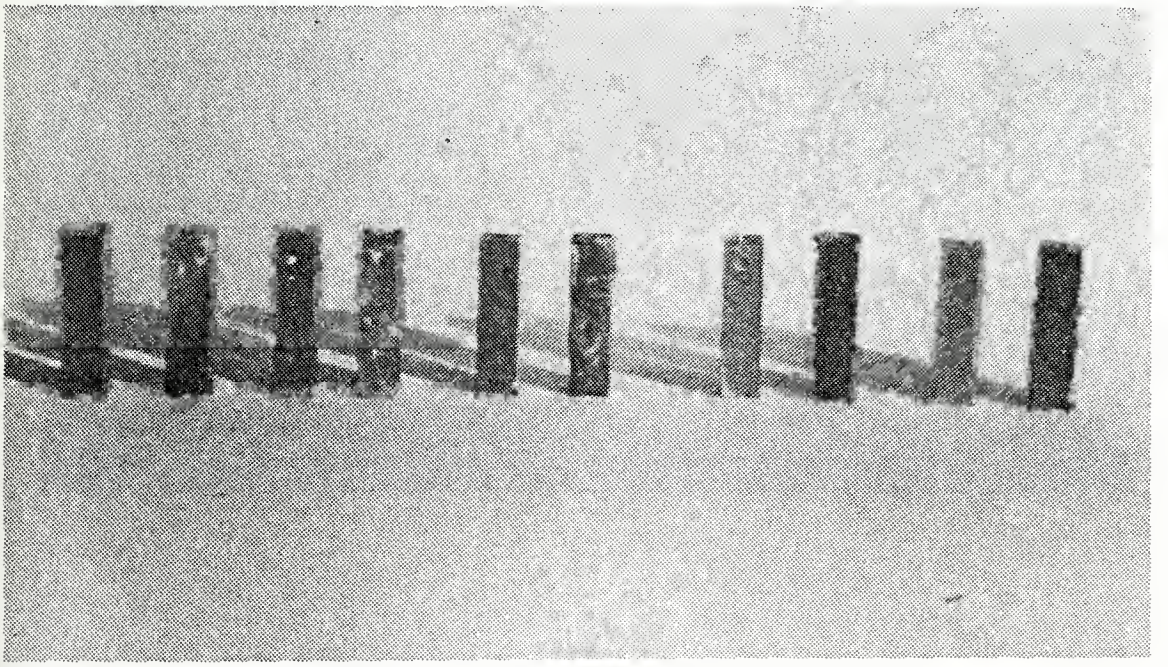

Figure 191. Complete set of IML specimens. From left to right, CDA 260, Cda 280, CDA 101, CDA 706, and CDA 715.

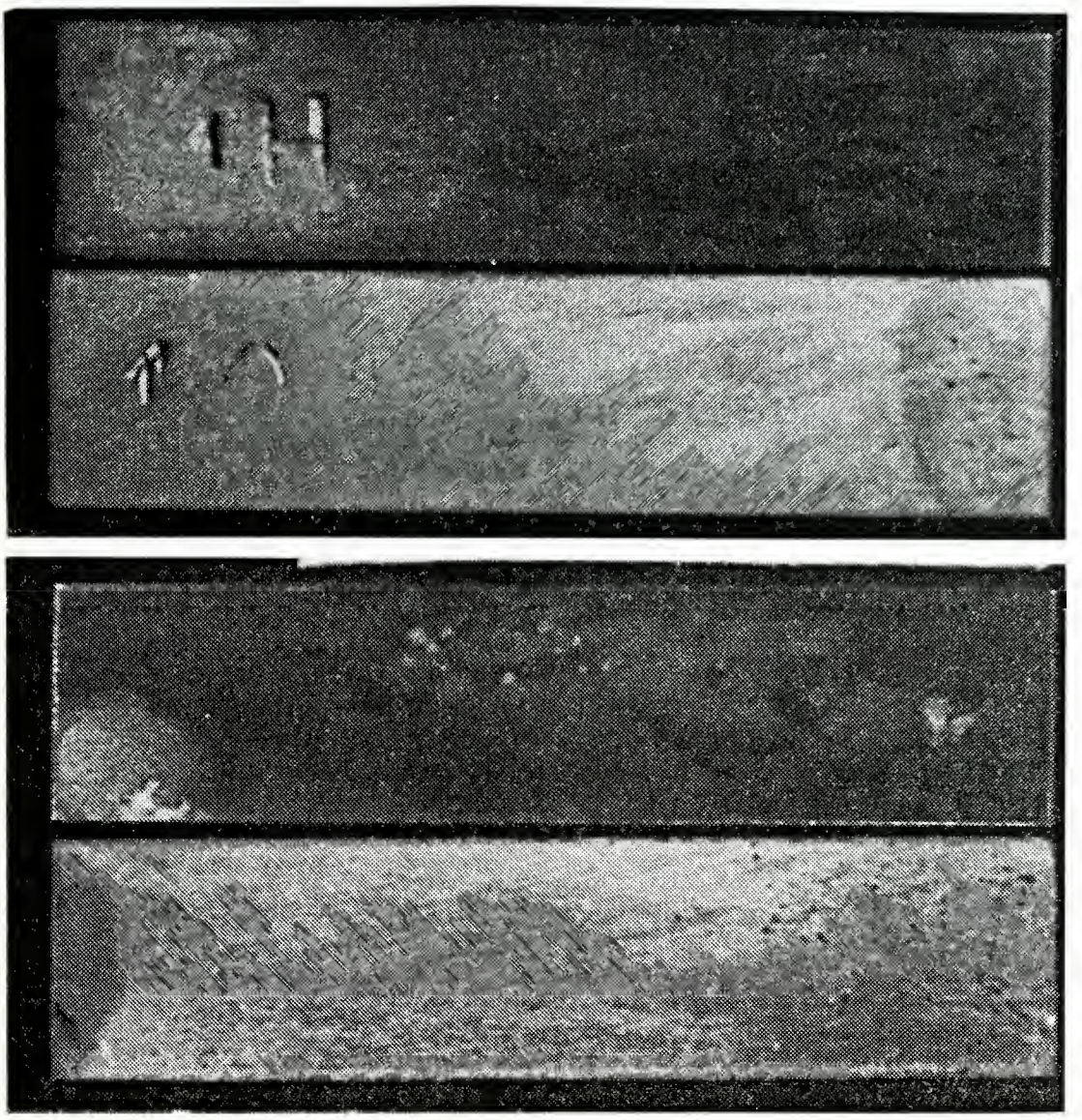

Figure 192. CDA 260 IML specimens. In each photo, the specimen exposed to hypochlorite ion is on the top.

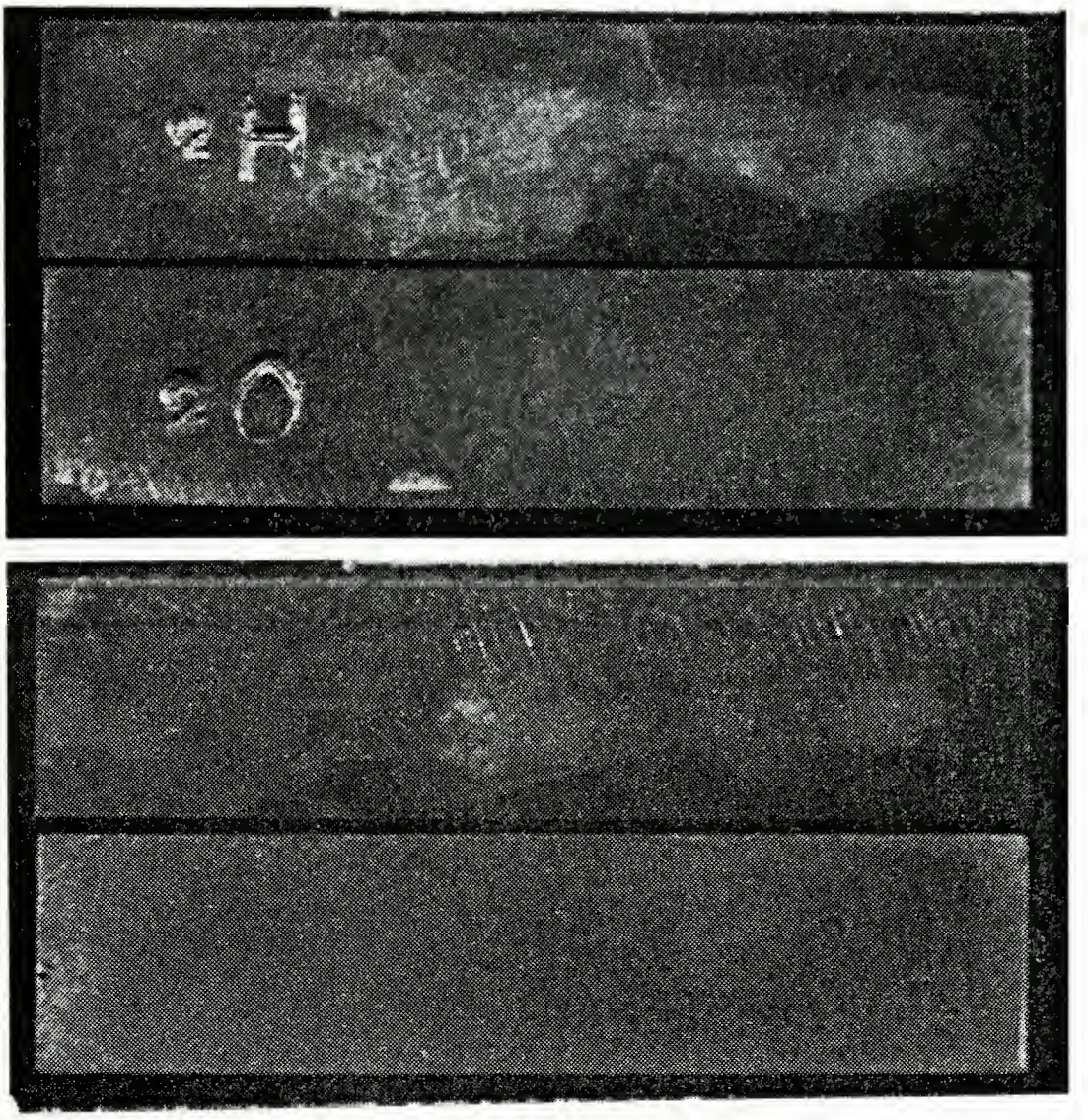

Figure 193. CDA 280 IML specimens. In each photo, the specimen exposed to hypochlorite ion is on the top.

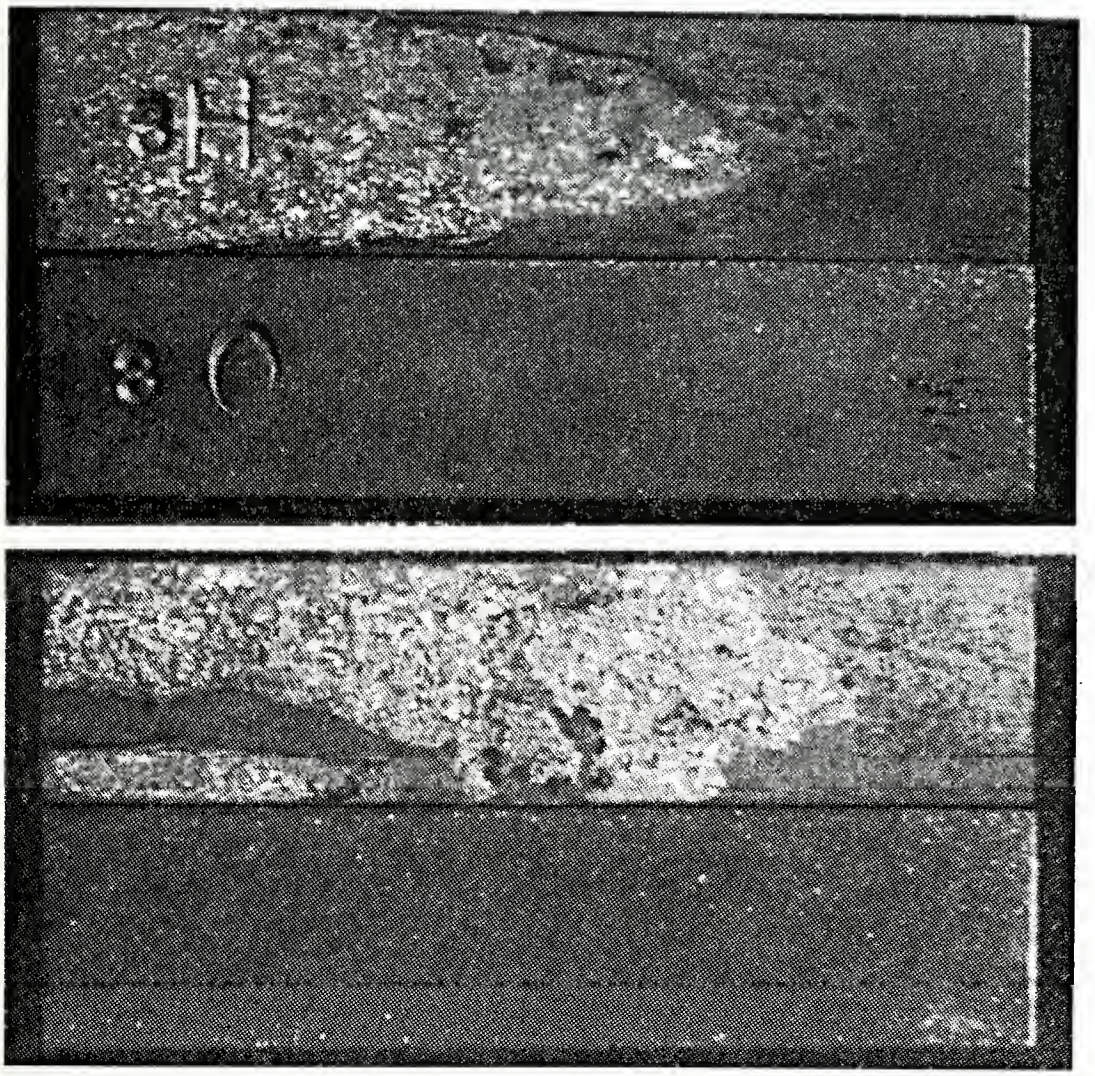

Figure 194. CDA101 IML specimens. In each photo, the specimen exposed to hypochlorite ion is on the top.

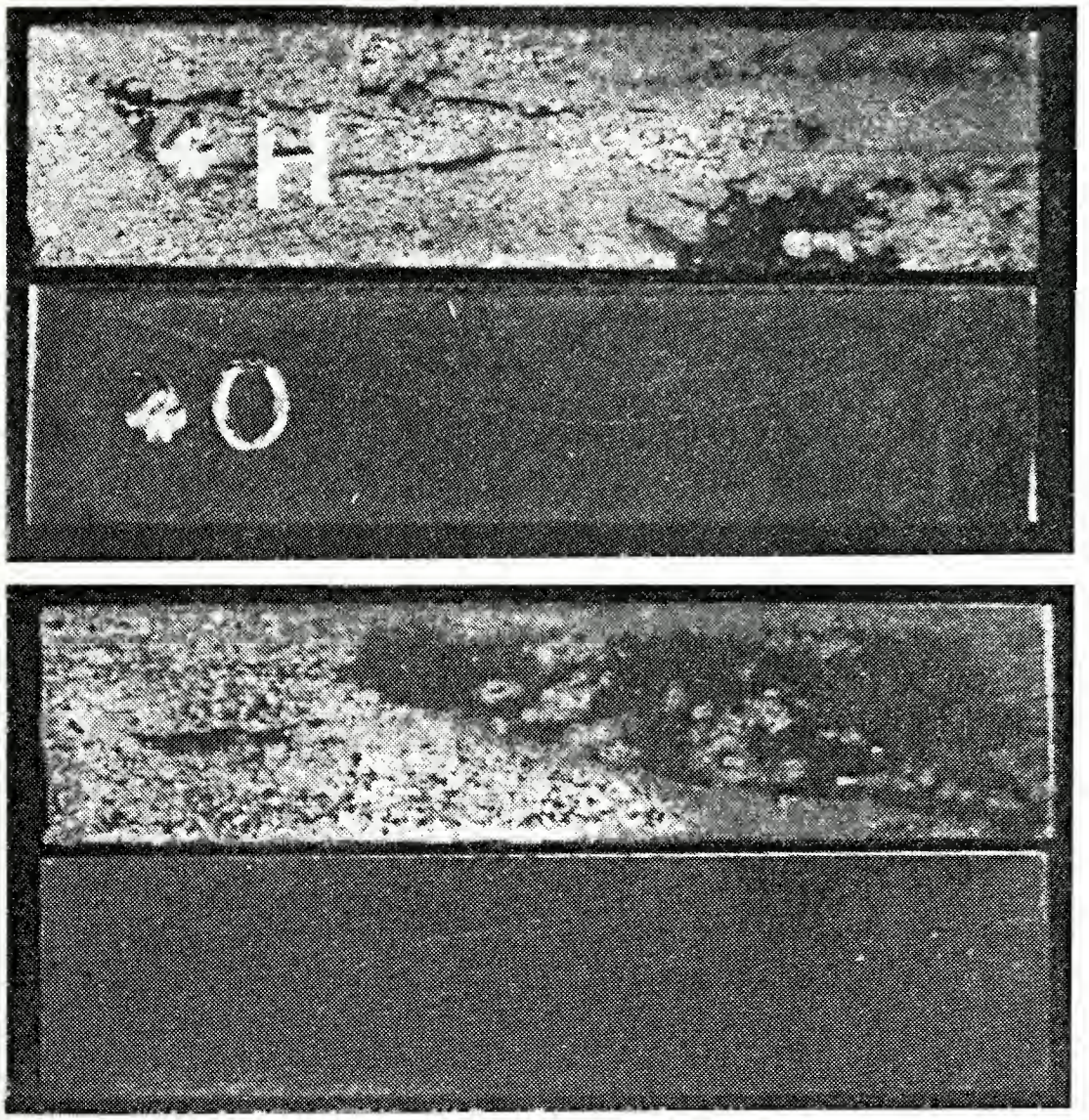

Figure 195. CDA 715 specimens. In each photo, the specimen exposed to hypochlorite ion is on the top.

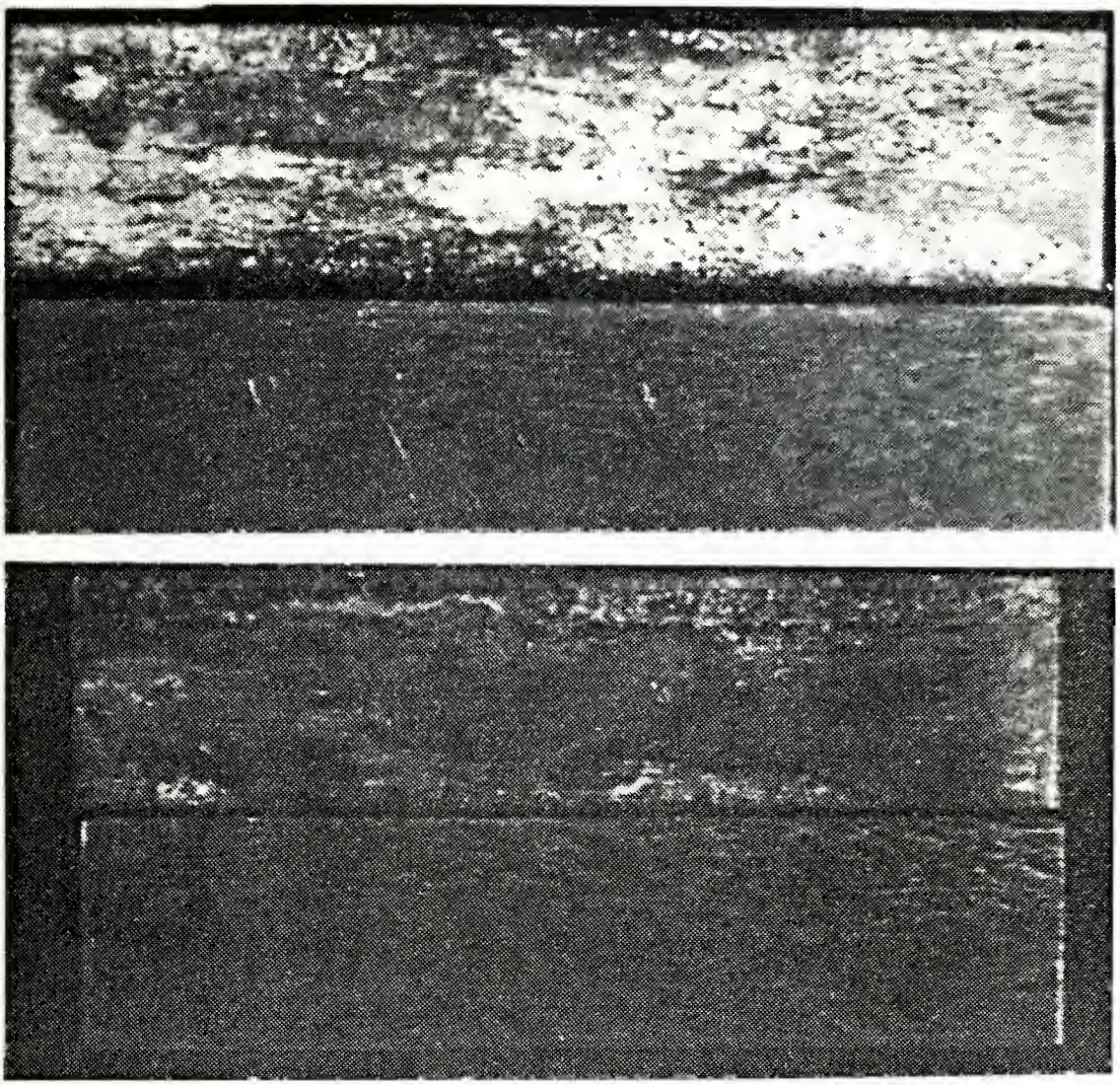

Figure 196. CDA 706 IML specimens. In each photo, the specimen exposed to hypochlorite ion is on the top.

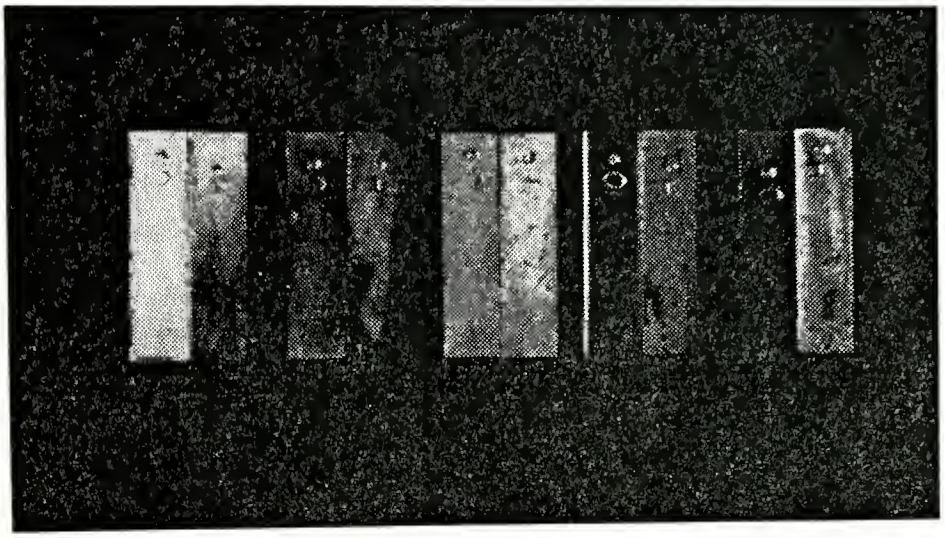

Figure 197. IML specimens after being cleaned. From left to right,CDA 260, CDA 280, CDA 101, CDS 715 and CDA 706. For each pair of specimens, the one to the right was exposed to hypochlorite ion.

C. CORROSION PRODUCT COMPOSITION

While some of the constituents of the several corrosion products could be determined by X-ray fluorescence techniques, it was in general impossible to assign a stoichiometry to them. X-ray fluorescence analysis is theoretically limited to the elements with atomic number greater than 9, hence, leaving out the all-important low atomic number elements such as hydrogen, carbon, nitrogen, and oxygen.

In two cases, however, there was enough corrosion product available for X-ray diffraction spectrometry (XRD) to be performed. For pure copper (CDA 101) immersed in aerated synthetic seawater containing hypochlorite ion, 4 main compounds were found to compose the green corrosion product. In order of decreasing concentration, they were:

$CuCl_2 \cdot 3Cu(OH)_2$

$CuCl_2$

(?)

Cu_2O

The third strongest set of peaks was not identified. Of the remainder, all are green except for Cu_2O, and it might account for the dark line separating the green and white areas on the specimens.

For 70/30 copper/nickel (CDA 715) immersed in aerated hypochlorite solution, the corrosion product was a velvety black. When analyzed by XRD, it, too, showed four major constituents listed below in order of decreasing concentration.

$NaCl$

$CuCl_2 \cdot 3Cu(OH)_2$

$CaCO_3$

NiO

It is hypothesized that the sodium chloride was present simply because it adhered to the black precipitate while in the electrolyte, and that the calcium carbonate was formed by the aeration process on the electrolyte. The presence of $CuCl_2 \cdot 3Cu(OH)_2$ accounts for the greenish corner observed on the IML specimen. Finally, NiO is indeed very black.

D. ELECTROLYTIC MEDIUM EFFECTS

1. Sodium Hypochlorite

The addition of 200 ppm sodium hypochlorite to synthetic seawater had the same effect for all of the materials tested. This effect was to shift the corrosion potentials in the positive direction by 50 to 100 mV (on a reduction potential scale). Price [19] also observed this phenomenon. The positive shift in reduction potential is accompanied by an increase in the observed corrosion rates. See also figure C-1(b).

2. Dissolved oxygen

Replacing the purified compressed air purge of the electrolyte with purified, deoxygenated nitrogen in all cases shifted the corrosion potentials in the negative direction by 50 to 100 mV (on a reduction potential scale). The negative shift in reduction potential is accompanied by a moderate decrease in the corrosion rates.

E. GENERALIZATION OF RESULTS

1. Corrosion Modes

a. In Aerated Synthetic Seawater.

Of the materials tested in this medium, CDA 706 and CDA 715 alloys showed virtually no attack, whereas CDA 101 (pure copper) showed slightly more corrosion. It also eventually protects itself from more rapid corrosion with a passivating film of copper oxide. CDA 260 and CDA 280 (the brasses) both showed dealloying -- the 2 phased Muntz metal at the interface between the alpha and beta phases, and the cartridge brass at the grain boundaries.

b. In Aerated Synthetic Seawater Containing Added Hypochlorite Ion.

In this medium, CDA 715 (70/30 copper/nickel) and CDA 280 ("Muntz Metal") both showed very rapid dealloying. Both became structurally weak and showed signs of deep local pitting. CDA 706 (90/10 copper/nickel) and CDA 260 ("Cartridge Brass") also showed signs of dealloying , but at a lesser rate than CDA 715 and CDA 280. There was both locallized pitting and grain boundary attack with these two alloys. CDA 101 (pure copper) showed the worst example of pitting. It pitted rapidly and deeply over large areas of the specimens.

2. Corrosion Rate Hierarchy

It is dangerous to predict hierarchies (such as those to follow) since they are based strictly on penetration rates. For example, a penetration rate measurement for "cartridge brass" will predict a much longer service life than is actually

attainable, due to the localized nature of the attack by the corrodent (e.g., grain boundaries dissolve rapidly relative to the balance of the grains). CDA 280 ("Muntz Metal") rapidly dezincifies in synthetic seawater alone, and on the addition of hypochlorite ion, dezincification rate greatly increases. Yet, if one believes the penetration rate data exclusively, Muntz metal is the most corrosion resistant material on the list. Yet another disparity is the one based on how one generates the hierarchy list. Using the averages of the penetration rates for each of the three methodologies used, CDA 715 shows up on the middle of the list for synthetic seawater containing dissolved oxygen and hypochlorite ion. However, if one examines figure 18, or Table IV, it can be seen that this material is the most corrosion resistant when its corrosion rate is measured with the PDP method, while it is next to the least resistant when measured by the other two methods.

With these strong cautions, a set of three rate hierarchies are presented for the differing conditions of the tests. For specimens in unstirred synthetic seawater containing about 4 ppm dissolved oxygen:

CDA 715 (70/30 copper nickel)	Most Resistant
CDA 280 ("Muntz metal")	
CDA 706 (90/10 copper nickel)	
CDA 260 ("Cartridge brass")	
CDA 101 (OFHC copper)	Least Resistant

If one replaces the dissolved oxygen with purified nitrogen gas that has been deoxygenated, the corrosion rate hierarchy is:

CDA 280	Most Resistant
CDA 715	
CDA 101	
CDA 260	Least Resistant

Finally, if one adds 4 ppm dissolved oxygen and 200 ppm of sodium hypochlorite to the synthetic seawater, the corrosion rate hierarchy appears to be:

CDA 280	Most Resistant
CDA 260	
CDA 715	
CDA 706	
CDA 101	Least Resistant

Figure 18 and Table IV illustrate these results.

IV. DISCUSSION AND CONCLUSIONS

A. COMPARISON WITH PREVIOUS WORK

Price [19] showed, by potentiokinetic methods, a drastic increase in corrosion rates upon the addition of 100 ppm hypochlorite ion to the electrolyte used. Some of his results are listed in Table I of this thesis.

Absolute measurements of corrosion rates by PDP are sometimes suspiciously high when compared to actual long-term immersions, and therefore should be viewed with caution, due to variations in methodology used. In comparing the present work to that of Price, it is seen that the addition of ca. 100 ppm of hypochlorite ion has the effect of increasing the corrosion rates no more than about ten times over that without added hypochlorite (all methods), whereas Price saw a 30-40 fold increase for copper and copper-nickel and an 8-9 fold increase for brass. Our combined works agree, however, in that for the metals tested, corrosion rates do increase sizeably upon the addition of hypochlorite ion to aerated synthetic seawater -- so much so that none would appear to be suited for long term use near the Chloropac generator.

It will be of interest to see the effects observed in the actual shipboard tests now being conducted at Pearl Harbor Naval Shipyard, using the Chloropac generator, real piping systems with their associated galvanic couples, and real seawater containing organic chemicals not in the synthetic seawater used in these tests.

In an effort to place the work of this thesis in perspective with the work of other researchers, a comparison table is provided (see Table V).

B. THE ROLE OF THE MEDIUM.

1. Hypochlorite Ion

There were three major elements which composed the alloys studied. These were copper, nickel and zinc. The reactions of hypochlorite ion with each of these materials deserves some mention.

a. Reactions of Nickel Ion with Hypochlorite Ion.

The reaction of hypochlorite ion with nickel ion in basic solution is rapid, forming initially nickel dioxide, NiO_2 [44]. This material as well as other hydrated oxides of nickel(II) are the black slimy materials that were observed on both copper-nickels in the IML experiments. NiO_2 is unstable, liberating oxygen on reduction by water, and forming one of the many mixed oxides containing Ni(III) and Ni(IV).

A simple experiment was performed in which nickel (II) chloride solution was treated with a small amount of sodium hypochlorite solution in a beaker. The green salt solution rapidly became dark black, and formed the slimy particles, which visually appeared to be the same as in the IML experiments with CDA 706 and 715. Minutes later, oxygen bubbles appeared throughout the solution, and the black slimy precipitate eventually settled to the bottom of the container.

There is some chemical evidence, then, that in the IML experiments, the cupronickels began to "denickelify",

TABLE V. A COMPARISON OF MEASURED CORROSION RATES IN AERATED ELECTROLYTE.

Alloy* ID No.	R_{mpy}, This Work			R_{mpy}, Other Studies					
	PDP	LPM	IML	PDP [19]	IML[a] [39]	IML[b] [40]	IML[c] [41]	IML[d] [42]	IML[e] [43]
101-0	3.7	2.6	1.5	2.6	5.6	0.8	1.0	0.4-2.8	-
101-H	23	9.8	5.4	110	-	-	-	-	-
260-0	3.8	0.9	0.4	-	5.8	-	2.0	-	-
260-H	9.8	0.9	0.3	-	-	-	-	-	31
280-0	0.7	0.6	0.3	3.9[f]	-	-	3.5	0.6-4.3[f]	-
280-H	8.3	0.8	0.6	33.1[f]	-	-	-	-	-
706-0	3.3	1.1	0.2	-	-	-	1.2	-	-
706-H	15	1.4	1.5	-	-	-	-	-	-
715-0	2.3	0.4	0.2	1.4	-	-	1.2	0.3-1.5	-
715-H	5.7	2.2	3.8	45.4	-	-	-	-	-

NOTES:

a. 3% sodium chloride solution
b. 0.5N sodium chloride solution, 25°C
c. Ocean exposure for ca. one year
d. Various coastal marine sites
e. Solution of sodium hypochlorite containing 9% available chlorine.
f. Data reported are actually for CDA 484 (Naval Brass), which varies slightly from Muntz metal composition. CDA 484: 59.85 copper, 39.2 zinc, 0.75 tin; CDA 280: 60 copper, 40 zinc

* -O means no added hypochlorite ion.
-H means added hypochlorite ion

with the specimens becoming covered with the black nickel dioxide and the surface of the specimen under the black layer becoming copper colored. This would also account for the great chlorine demand of the cupronickels. For further information regarding the nickel dioxide formation, see reference 45.

b. Reactions of Copper Ion with Hypochlorite Ion.

The reaction of hypochlorite ion with copper is less understood. It is known that copper(II) salts may react with hypochlorite ion in strongly alkaline media to form copper(III) complex ions. For example, $Cu(IO_6)_2^{7-}$ is a known copper(III) complex ion. Also, several alkaline earth cuprates are known in the solid state, but these dissolve with decomposition in aqueous alkaline solution. Copper(III) survives no more than a few seconds in solution, no doubt oxidizing the water to oxygen in the process. For further information, the reader is referred to references 46,47, and 48.

It is doubtful whether the solutions used in this research were alkaline enough for the formation of copper(III). Pourbaix [49] has calculated a potential-pH diagram including the compounds copper(III) ion and CuO_2^-. The simple experiment described previously for nickel solutions was repeated for copper(II) ion solution with hypochlorite. In concentrated solutions of both ions, a hydrous gel was formed that was light blue white in color. In dilute solutions, a darker blue-green gel was formed. In both cases,

however, chlorine gas was evolved, possibly indicating at least a transient formation of a higher oxidation state of copper, or a pH shift in the solution due to the copper(II) ion, which is appreciably acidic. Rabald [50] suggests that copper ion "catalyzes" decomposition of hypochlorite to lower oxidation states.

c. Reactions of Zinc Ion with Hypochlorite Ion.

The reaction of zinc ion with hypochlorite solutions in all cases led to the formation of white hydrated precipitates, presumably mixed salts of zinc hydroxide and zinc chloride. A ZnO_2 compound is said to exist, being prepared by the addition of zinc hydroxide in 1M sodium hydroxide to hydrogen peroxide. However, little thermodynamic data exists [51].

It is apparent from the SEM micrographs and the X-ray diffraction data that the ultimate fate of zinc ion in hypochlorite solution is to form crystalline zinc oxide platelets.

2. Dissolved Oxygen

In all cases studied (aerated synthetic seawater alone) replacement of dissolved oxygen in the electrolyte with purified deoxygenated nitrogen gas led to decreased corrosion rates. Reinhart [41] also notes a decrease in corrosion rates of the copper alloys in long term IML tests in real seawater with decreasing dissolved oxygen. For the corrosion of copper to occur in seawater, oxygen must be present and must diffuse through both the incipient oxide

layer and the corrosion products layers to the metal's surface. Therefore, replacement of the dissolved oxygen with purified nitrogen should lower the corrosion rate. In addition, the decrease in corrosion rate was accompanied by an average of 50-100 mV shift to more negative reduction potentials for the samples tested. The exact relationship between the shift in corrosion potential and corrosion rate was not determined in this research.

C. THE ROLE OF THE BASE METAL

1. Multiple Phases

In the brasses of high zinc content (over 30%), dezincification is a predominant failure mode, increasing with increasing zinc content. Dezincification is favored by galvanic contact of the brass with a more noble metal, chloride ion, high temperatures and the presence of residual stresses in the metal [52]. It is especially prevalent in Muntz metal (CDA 280). For example, in one reported test, 28% of a 3 mm thick test specimen was affected in a long-term IML test [41]. Here, it appears that copper and zinc are both initially dissolved, and then the copper is redeposited at the less active alpha phase dissolution sites and the zinc then continues to dissolve from the beta phase in an anodic reaction [53]. In the PSP runs done in this research, one first sees surface roughening followed by the beta phase being attacked and formation of a crystalline corrosion product of hydrated zinc oxide platelets [37]. Dezincification was also seen in CDA

260 (cartridge brass) but not to the extent of that for the Muntz metal. The mechanisms may be different for the two brasses, however, since the two-phase brass appears to dezincify more or less uniformly over large areas of the surface, whereas in the brass with the lower zinc content, highly localized plug type dezincification is the more common mode in seawater [54]. This is born out in part by the observations during the PSP runs in which the Muntz metal produced a whitish corrosion product (basic zinc chloride and zinc oxide) whereas the predominant corrosion product on the cartridge brass was greenish (probably basic copper chloride).

The initial removal of both copper and zinc followed by redeposition of copper and continued removal of zinc is only one proposed mechanism for dezincification. The other hypothesis is that simple dissolution of zinc occurs. It is difficult to see how this process could occur beyond the first few atomic layers, however, since the zinc ions would have to find their way to the electrolyte through very fine pores in the copper. It cannot account for the depth of penetration observed in plug-type dezincification. The dual dissolution of copper and zinc ions followed by redeposition of copper at cathodic areas has been difficult to prove directly, but it certainly could account for the depth of penetration and the layered structure observed by many researchers. For further details, see references 53 and 55.

2. Grain Boundaries

In most of the cases tested, especially when hypochlorite ion was added to the electrolyte, the grain boundaries were preferrentially attacked with respect to the rest of the grain. Grain boundaries are areas of high surface energy, due to the mismatch of atom layers at the edges of the two neighboring grains. Vermilea [36] has written an interesting paper on microscopic corrosion processes at the grain boundaries as well as within the grains. Since the simple crystal faces (such as the cubic) are of lowest energy, atoms arranged in higher order planes (with higher surface energy) that are exposed to an electrolyte will act as anodes and will tend to be preferrentially corroded compared to the simpler, lower order arrangement. The "stair-steps" seen within the grains on many test specimens are hypothesized to be associated with low order, low energy crystal planes.

D. WARNINGS ABOUT CORROSION MEASUREMENTS UTILIZING ELECTROCHEMICAL METHODS.

It is apparent from figure 18, if the IML measurements are taken as the standard (i.e., they most closely approximate real service conditions),

(1) that LPM measurements closely approximate the mass loss rates, and

(2) that potentiodynamic measurements can be considerably in error in predicting corrosion rates.

These ideas are well documented within this paper and in the

open literature as well [56]. It is felt that PDP measurements of corrosion rates should be used only for comparative studies and not for absolute measurements. This is because the specimen surface may be changed drastically during an anodic polarization run. Also, the concentration gradient from the metal surface to the electrolyte is a strong function of the solution velocity and therefore stirring the solution at different rates will give different corrosion current densities. (It is hypothesized that this stirring factor is the major cause of discrepancy between the results of this research and that done by Price). In addition, it is often difficult to find a Tafel slope on the E vs. log I plot. LPM methodology is inherently less disturbing to the sample and its environment, since the potential change is of the order of ±20 mV about the corrosion potential of the freely corroding material.

E. WHICH MATERIAL TO USE?

For areas around the Chloropac generator, where high concentrations of hypohalite ions may exist, it appears that none of the materials tested would be adequate for long term use. The cupronickels tend to form fairly shallow pits and their overall corrosion rates are moderate. However, if the black nickel precipitate were continuously removed in the rapidly flowing seawater required for Chloropac operation, it is anticipated that corrosion rates could be much higher.

The brasses actually showed the most resistance to hypochlorite in terms of simple penetration rates, but they

suffer from locallized dealloying and grain boundary attack, leading to structural instability.

Copper is known to be sensitive to flow effects [39], and to deteriorate rapidly by pitting above 4 feet per second [52]. With the added influence of hypochlorite ion contributing to pitting, it is clear that it should not be used.

F. RECOMMENDATIONS FOR FURTHER STUDY

Several tasks need to be accomplished. They include:

(1) testing of other material of Navy interest, such as the Monels, bronzes, and steels. Such test could be accomplished largely in the laboratory, as were the tests reported here.

(2) testing of materials of interest in flowing seawater containing the hypochlorite foulinf inhibitor. The flow should be well characterized, as for example, in a hydrodynamically characterized flow channel.

(3) an amplification of the tests reported here to include several modern corrosion inhibitors plus the added hypochlorite ion. (Note: the Sherwin-Williams Company has recently reported the use of several corrosion inhibitors in conjunction with the hypochlorite treatment of water [66] . Inhibitors used were of the tolyltriazole and benzotriazole types.)

(4) test data should be gathered from the Naval Research Laboratory's antifouling test programs in use for about 1 year at Pearl Harbor Naval Shipyard, using actual shipboard piping. The test data should be correlated with the laboratory experiments reported here.

At the more fundamental level, there need to be:

(1) accurate chemical characterization of the products of reaction of copper, zinc, and nickel in chloride solutions containing added hypochlorite ion.

(2) a determination of the kinetics of the reactions of copper, nickel and zinc with solutions of hypochlorite ion in strong chloride solutions.

(3) development of expertise in, and the acquisition and employment of other surface beam analytical techniques, such as Auger Electron Spectroscopy, which will allow determination of composition vs. depth for the multilayer corrosion products noted in this research.

APPENDIX A: BASIC CORROSION TERMINOLOGY AND REPRESENTATIVE CALCULATIONS

A. ELECTROCHEMICAL NOMENCLATURE

Anodic Current- The rate of charge flow in a direction which results in oxidation of an electrode material or solution component.

Auxilliary Electrode- (not "counter electrode") - The electrode in a three electrode experiment which provides a current path in series with the solution and the working electrode. The potential of the auxilliary electrode is not controlled with respect to the reference electrode.

Cathodic Current- The rate of charge flow in a direction which results in reduction of an electrode material or solution component.

Negative Potentials-(not "cathodic potentials")- Potentials negative with respect to a specified reference electrode or redox couple.

Positive Potentials-(not "anodic potentials")- Potentials positive with respect to a specified reference electrode or redox couple.

Voltammetry- Finite current methods in which a current response is measured as a function of a potential waveform increasing in amplitude in a positive or negative direction. The waveform may be a ramp, a pulse train, a sine wave, or various combinations thereof.

Working Electrode- (not "indicator" or "test" electrode)- The electrode at which the reaction of interest takes place.

B. CALCULATIONS USED IN DETERMINING CORROSION RATES FROM LINEAR POLARIZATION MEASUREMENTS.

Calculations of corrosion current from LPM measurements are based on the standard Stearn-Geary expression [57].

$$R_p = \frac{\Delta E}{\Delta I} = \frac{(\beta_a)\cdot(\beta_c)}{2.3\ I_{corr}\ (\beta_a + \beta_c)}$$

where: R_p is the polarization resistance, ohms

ΔE is the change in applied potential, volts

ΔI is the change in current, amperes

β_a is the anodic Tafel slope

and β_c is the cathodic Tafel slope.

Rearranging this equation,

$$I_{corr} = \frac{(\beta_a)\cdot(\beta_c)}{2.3\ (\beta_a + \beta_c)} \cdot \frac{\Delta I}{\Delta E} = \frac{k}{R_p}$$

where k is a constant.

Stearn and Geary determined the value for the constant, k, by assuming a theoretical value of 0.12 volts for the two Tafel slopes. Pye [58] calculated k for many materials and came to the same result, i.e., k = 0.026 volts.

Corrosion calculations utilize the corrosion current density, i.e., $i_{corr} = I_{corr}$/ surface area. Therefore, the form of the equation for determining the corrosion current density utilizing linear polarization measurements is

where: C is the weight % of the metal in the alloy,

and n is the total number of constituents in the alloy.

For these calculations, the following tables were developed to use in the calculation of i_{corr}.

TABLE A-1

METAL	ATOMIC WEIGHT (A)	ELECTRONS LOST, (Z)	TYPICAL REACTION PRODUCTS
copper	63.54	1	Cu_2O;CuCl
zinc	65.37	2	$ZnCl_2$;$Zn(OH)_2$
nickel	58.71	2	$Ni(OH)_2$;NiO;$NiCl_2$

TABLE A-2

METAL/ ALLOY	NOMINAL COMPOSITION	EQUIVALENT WEIGHT,(e)	DENSITY (ρ)	(0.13e/ρ)
CDA 101	100% copper	63.54	8.94	0.924
CDA 260	70/30 copper/zinc	49.52	8.53	0.755
CDA 280	60/40 copper/zinc	46.12	8.39	0.715
CDA 706	90/10 copper/nickel	56.91	8.94	0.828
CDA 715	70/30 copper/nickel	47.09	8.94	0.685
nickel	100% nickel	29.36	8.94	0.427
zinc	100% zinc	32.69	7.57	0.561

Note that the penetration rate is simply the corrosion current density, i_{corr}, in microamperes per square centimeter, times the factor in the last column of Table A-2; this gives the

$$i_{corr} = \frac{k}{R_p(A)}$$

Calculations for penetration rates were computed from i_{corr} using the following standard engineering equation.

$$R_{mpy} = 0.13\ i_{corr}(e)/(\rho)$$

where i_{corr} must be in microamperes/square centimeter, the density, ρ, of the alloy is in grams/cubic centimeter and the equivalent weight, e, is given in grams. Here the units of the corrosion rate are in mils per year.

The effective equivalent weight (A/Z) of the alloy in question was calculated using the mole fractions of each of the constituents, and an assumption for each of the constituent metals as to the probable number of electrons lost, based on predictions by Pourbaix [49] as to the thermodynamically stable species at the pH in question. Thus,

$$\overline{A} = A_1X_1 + A_2X_2 + \ldots A_iX_i$$

where: X_i is the mole fraction of the ith species,

and $\overline{A}$ is the average atomic weight.

Similarly,

$$\overline{Z} = Z_1X_1 + Z_2X_2 + \ldots Z_iX_i$$

where: Z_i is the electron change for the ith species,

and $\overline{Z}$ is the average electronic change.

The mole fraction for the ith species is defined as

$$X_i = (C_i/A_i)/\sum_{j=1}^{n} (C_j/A_j)$$

penetration rate in mils per year, which can be readily converted to other units, either for penetration rate or mass-loss rate, as shown below.

Penetration rates:	Units
$R_{mpy} = 0.13\ ie/\rho$	mils per year
$R_{mmpy} = 2.54 \times 10^{-2}(R_{mpy})$	millimeters per year
Mass-Loss rate:	
$R_{mdd} = 0.696\rho\ (R_{mpy})$	milligrams per square decimeter per day

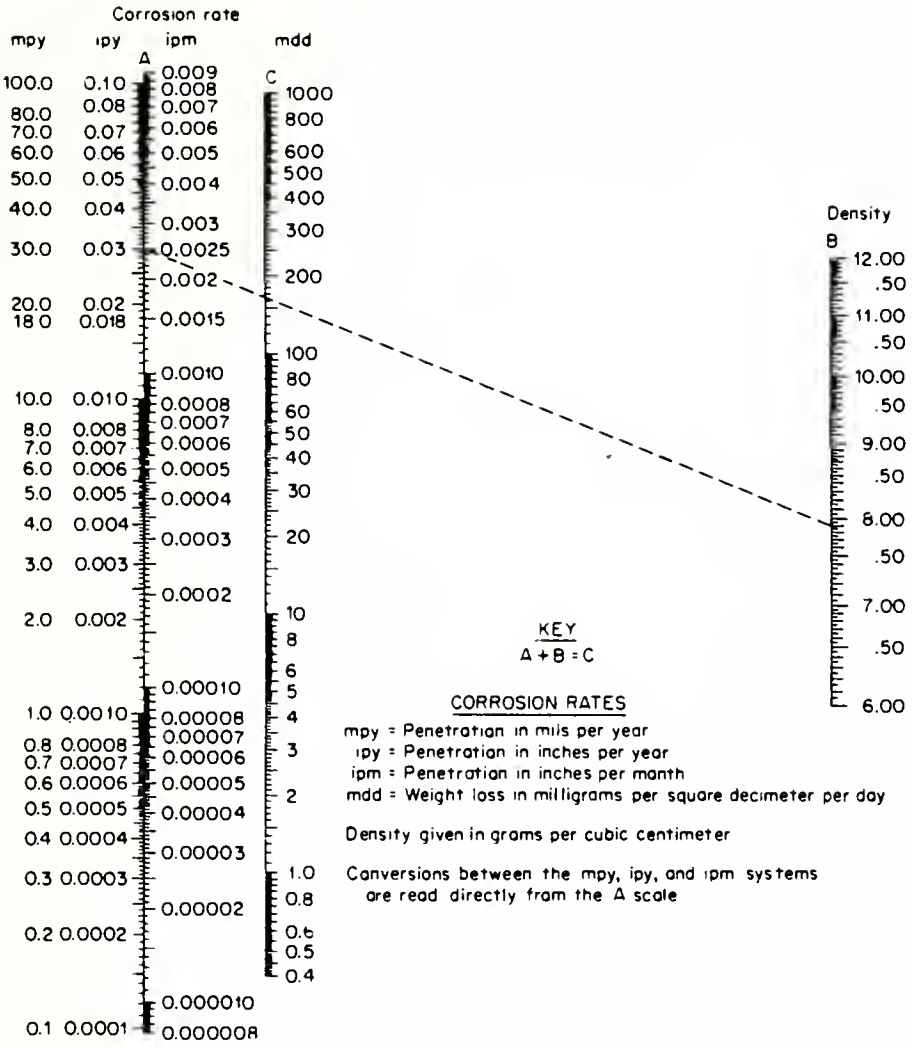

Figure A-1. Corrosion rate nomograph used to interchange between the various units used in corrosion science [60].

APPENDIX B: IMMERSION MASS-LOSS (IML) AND LINEAR POLARIZATION (LPM) TEST DATA.

This appendix contains IML corrosion data as measured by the mass loss technique and the LPM technique. It also contains graphic records of measured variables for the 34 day immersion tests.

TABLE B-I. IMMERSION TEST SPECIMEN DATA

Specimen Number	CDA No.	Dimensions (l x w x h) (cm)	Surface Area (dm^2)	Initial Mass (g)	Final Mass (g)	Mass Loss (mg)	Mass Loss Rate (mdd)
1-0	CDA 260	.877x.892x.658	0.143_{65}	24.0990	24.0887	10.3	2.11
1-H	CDA 260	.891x.891x.632	0.143_{35}	24.1191	24.1092	9.9	2.03
2-0	CDA 280	.891x.893x.632	0.143_{38}	23.7756	23.7679	7.7	1.58
2-H	CDA 280	.894x.894x.645	0.144_{36}	23.9749	23.9579	17.0	3.46
3-0	CDA 101	.899x.890x.612	0.142_{19}	24.9328	24.8884	44.4	9.18
3-H	CDA 101	.899x.885x.604	0.141_{88}	24.7665	24.6039	162.6	33.7
4-0	CDA 715	.892x.887x.625	0.143_{17}	25.1420	25.1371	4.9	1.01
4-H	CDA 715	.885x.891x.630	0.142_{31}	25.0203	24.9064	113.9	23.5
5-0	CDA 706	.871x.896x.627	0.139_{94}	24.7502	24.7433	6.9	1.45
5-H	CDA 706	.896x.880x.632	0.143_{85}	24.9130	24.8681	44.9	9.18

TABLE B-II

INSTANTANEOUS CORROSION RATES FOR THE IML SPECIMENS AS MEASURED BY LINEAR POLARIZATION.

Sample	Elapsed time (hours)	E_{corr} (V_{SCE})	$\Delta I/\Delta E$ ($\mu A/V$)	i_{corr} ($\mu A/cm^2$)	R mpy	R mmpy
1-O	2	-.254	5882	10.64	8.0	.204
2-O	2	-.266	4587	8.31	5.9	.150
3-O	2	-.244	7092	12.96	11.9	.304
4-O	2	-.195	3651	6.63	4.5	.115
5-O	2	-.210	9091	16.89	13.9	.355
1-H	3	-.250	8000	14.86	11.2	.284
2-H	3	-.251	5714	10.29	7.3	.186
3-H	3	-.205	4975	9.11	8.4	.213
4-H	3	-.070	8130	14.85	10.1	.258
5-H	3	-.125	1543	2.78	2.3	.058
1-O	73	-.255	1698	3.07	2.3	.058
2-O	73	-.285	346	.62	.4	.011
3-O	73	-.258	2828	5.17	4.7	.121
4-O	73	-.086	29	.05	.0	.000
5-O	73	-.170	469	.87	.7	.018
1-H	73	-.233	295	.54	.4	.010
2-H	74	-.296	475	.85	.6	.015
3-H	74	-.208	4457	8.16	7.5	.191
4-H	74	-.063	17400	31.78	21.7	.552
5-H	74	-.118	596	1.07	.8	.022
1-O	219	-.244	133	.24	.1	.004
2-O	219	-.310	259	.46	.3	.008
3-O	219	-.254	1837	3.35	3.1	.078
4-O	219	-.140	14	.02	.0	.000
5-O	219	-.238	102	.18	.1	.003
1-H	219	-.176	281	.52	.3	.010
2-H	219	-.306	310	.55	.3	.010
3-H	219	-.133	7619	13.96	12.9	.327
4-H	220	-.201	1657	3.02	2.0	.052
5-H	220	-.105	348	.62	.5	.013
1-O	460	-.244	61	.11	.0	.002
2-O	460	-.346	179	.32	.2	.005
3-O	461	-.249	606	1.10	1.0	.026
4-O	461	-.099	59	.10	.0	.001
5-O	461	-.247	120	.22	.1	.004
1-H	461	-.253	147	.27	.2	.005
2-H	461	-.316	271	.48	.3	.008
3-H	461	-.193	3488	6.39	5.9	.150
4-H	461	-.202	852	1.55	1.0	.027
5-H	461	-.108	1563	2.82	2.3	.059
1-O	819	-.251	138	.24	.1	.004
2-O	819	-.381	123	.22	.1	.004
3-O	819	-.244	655	1.19	1.1	.028
4-O	820	-.200	80	.14	.0	.002
5-O	820	-.150	963	1.78	1.4	.037
1-H	820	-.240	302	.56	.4	.010
2-H	820	-.300	392	.70	.5	.012
3-H	821	-.148	7091	12.99	12.0	.304
4-H	821	-.202	507	.92	.6	.016
5-H	820	-.108	588	1.06	.8	.022

TABLE B-III. COMPARATIVE RESULTS OF THE LONG-TERM IMMERSION TESTS

Specimen Number	CDA Number	IML TESTS		LPM TESTS*	
		R_{mdd}	$R_{\mu mpy}$	R_{mdd}	$R_{\mu mpy}$
1-0	CDA 260	2.11	9.1	5.27	23
1-H	CDA 260	2.03	8.6	5.33	23
2-0	CDA 280	1.58	6.9	3.32	15
2-H	CDA 280	3.46	15	4.54	20
3-0	CDA 101	9.18	38	16.1	67
3-H	CDA 101	33.7	138	60.8	249
4-0	CDA 715	1.01	4.1	2.24	9.1
4-H	CDA 715	23.5	96	13.8	56
5-0	CDA 706	1.45	5.8	6.83	28
5-H	CDA 706	9.18	38	8.69	36

*The LPM numbers shown in this table are calculated from the area under the instantaneous corrosion rate vs. time curve, and reflect the average measured corrosion rate.

Figure B-1 (a-e)

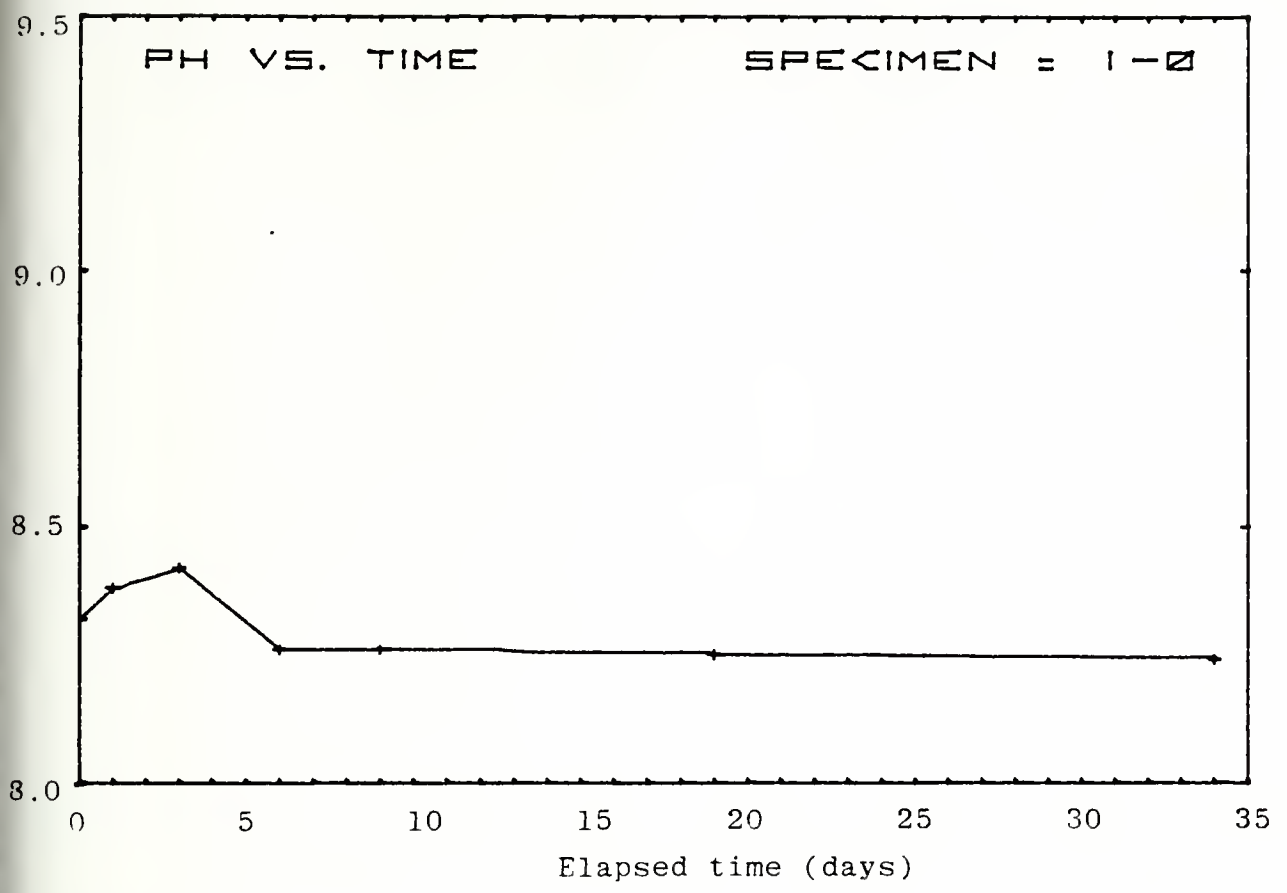
PH VS. TIME
SPECIMEN = 1-Ø
9.5
9.0
8.5
8.0
0
5
10
15
20
25
30
35
Elapsed time (days)

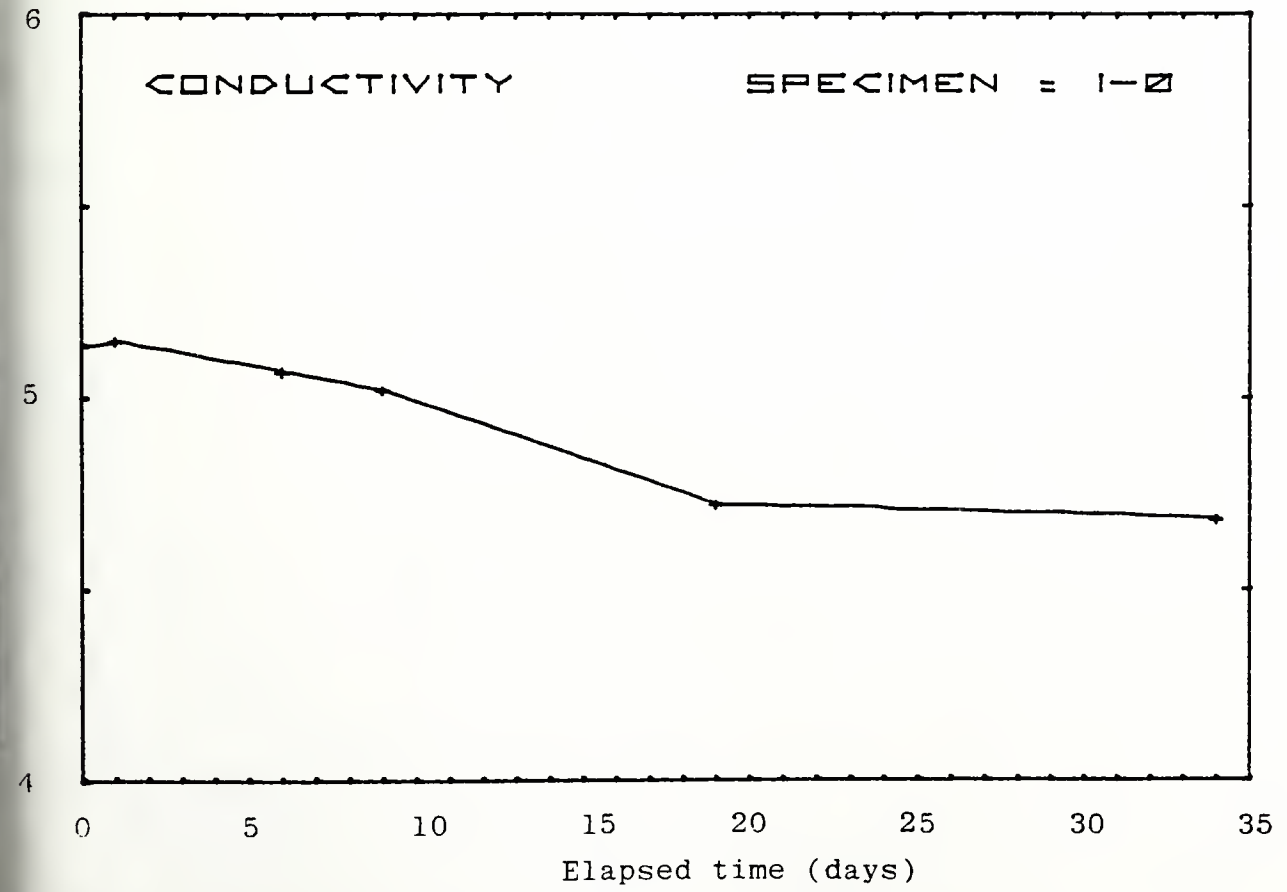
CONDUCTIVITY
SPECIMEN = 1-Ø
6
5
4
0
5
10
15
20
25
30
35
Elapsed time (days)

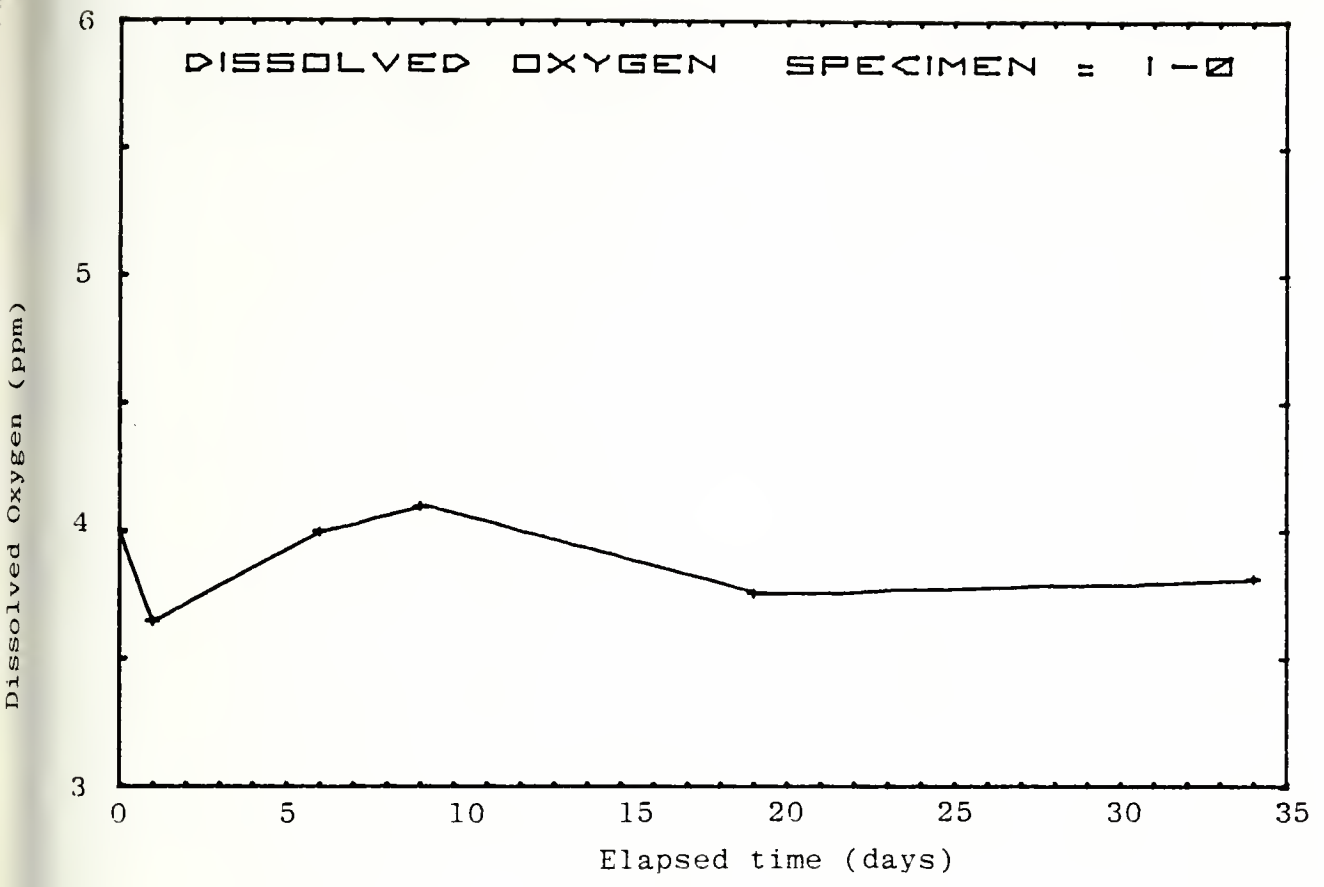
DISSOLVED OXYGEN SPECIMEN = 1-Ø
Dissolved Oxygen (ppm)
6
5
4
3
0
5
10
15
20
25
30
35
Elapsed time (days)

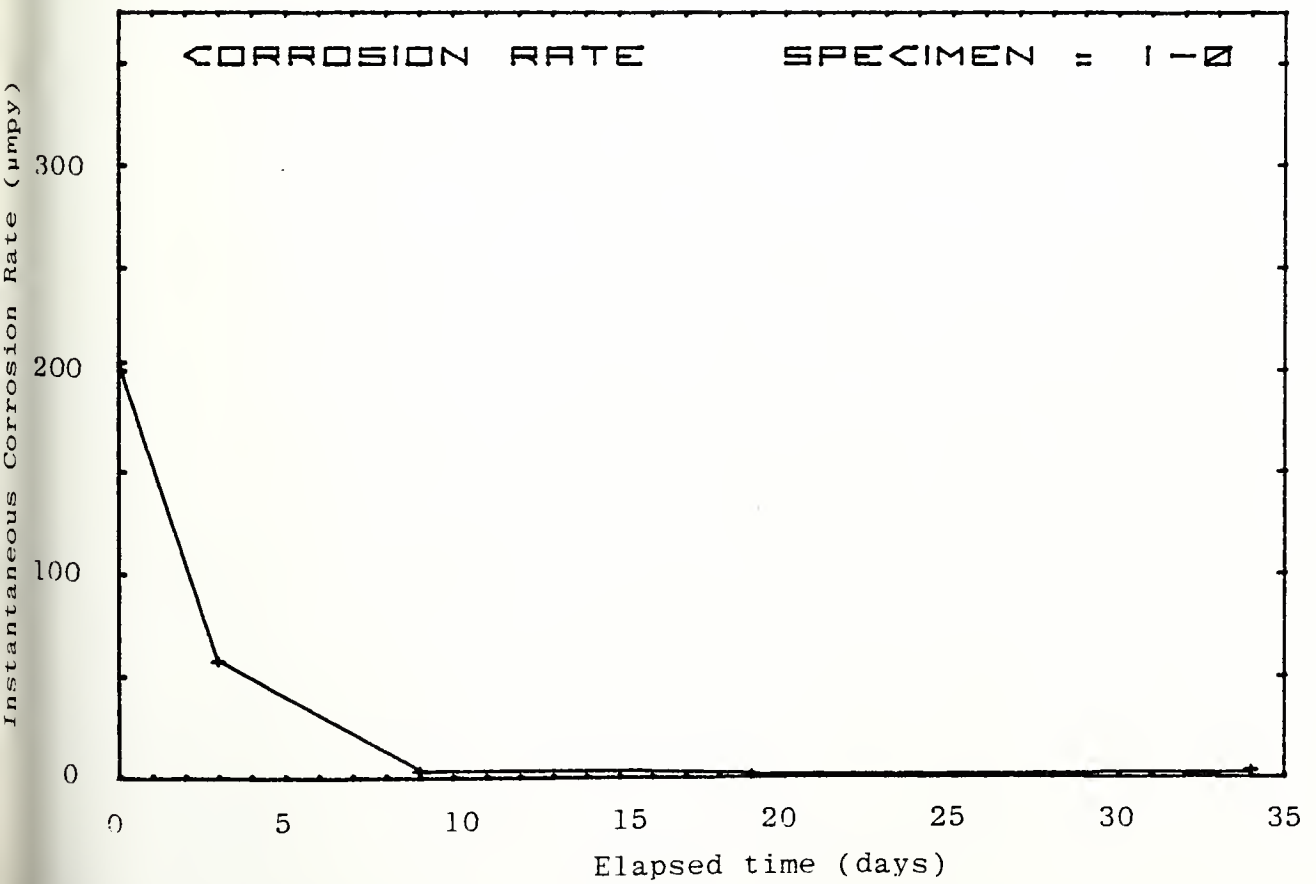
CORROSION RATE SPECIMEN = 1-Ø
Instantaneous Corrosion Rate (µmpy)
300
200
100
0
0
5
10
15
20
25
30
35
Elapsed time (days)

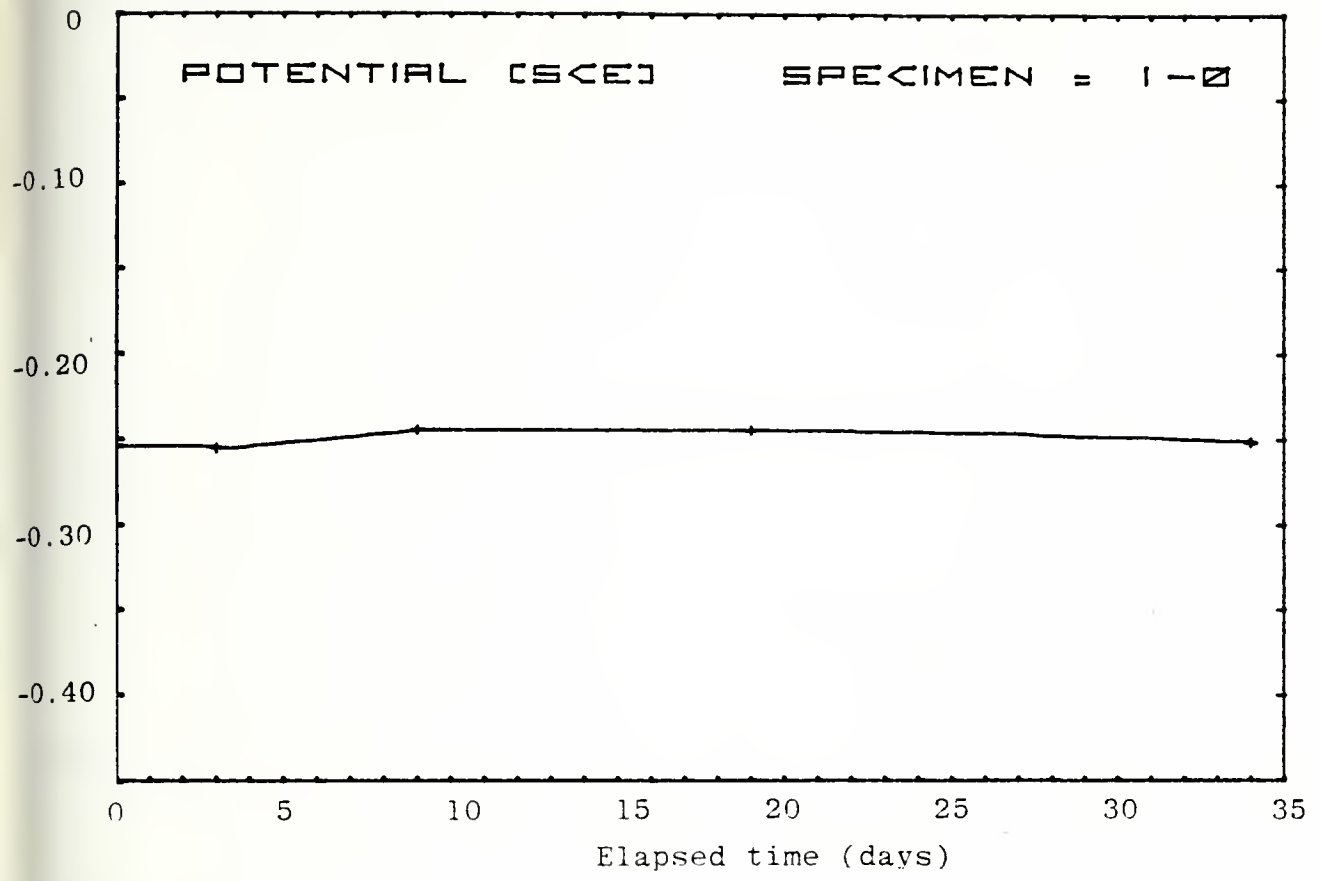
POTENTIAL [SCE]
SPECIMEN = 1-0
0
-0.10
-0.20
-0.30
-0.40
0
5
10
15
20
25
30
35
Elapsed time (days)

Figure B-2 (a-e)

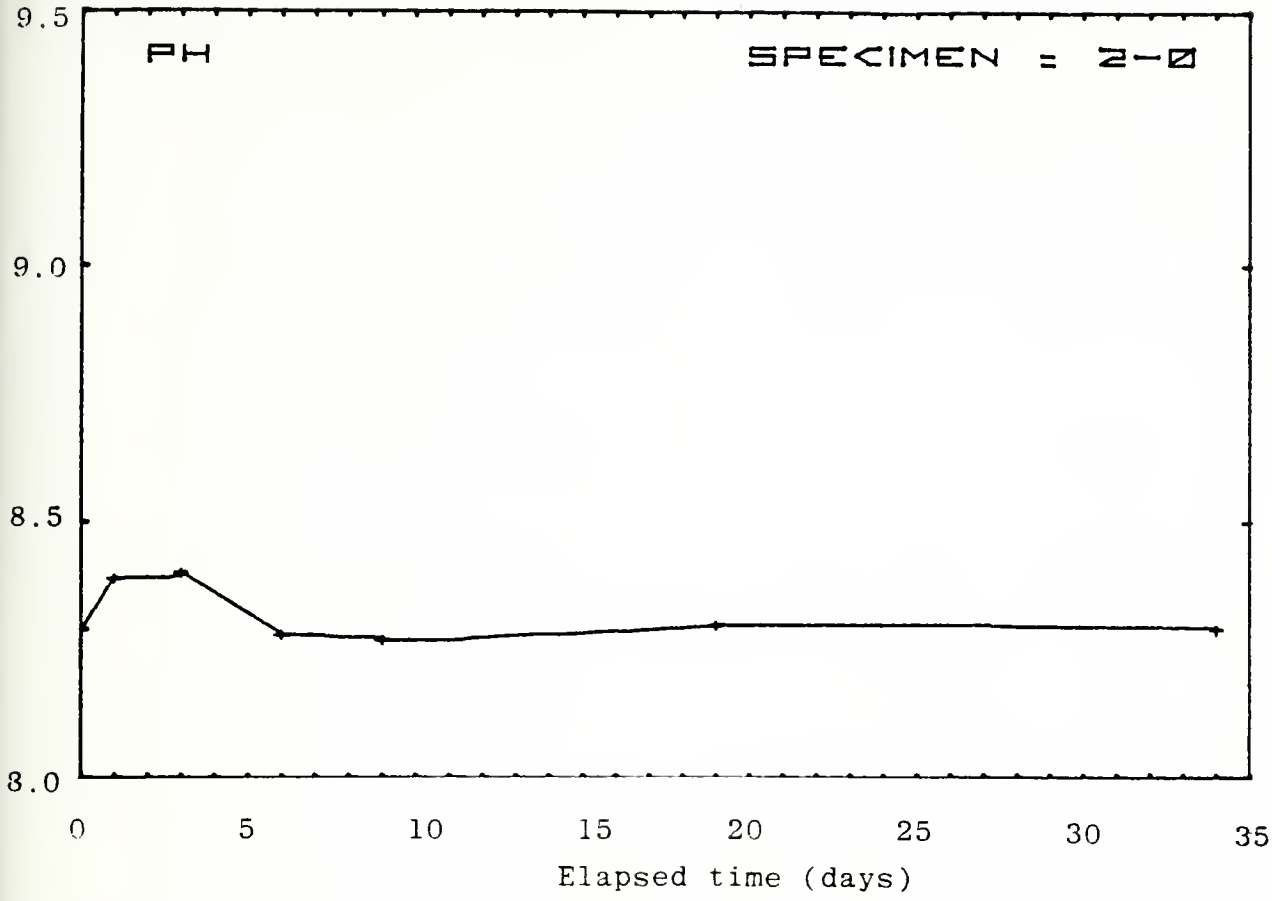
PH
SPECIMEN = 2-0
9.5
9.0
8.5
8.0
pH
0
5
10
15
20
25
30
35
Elapsed time (days)

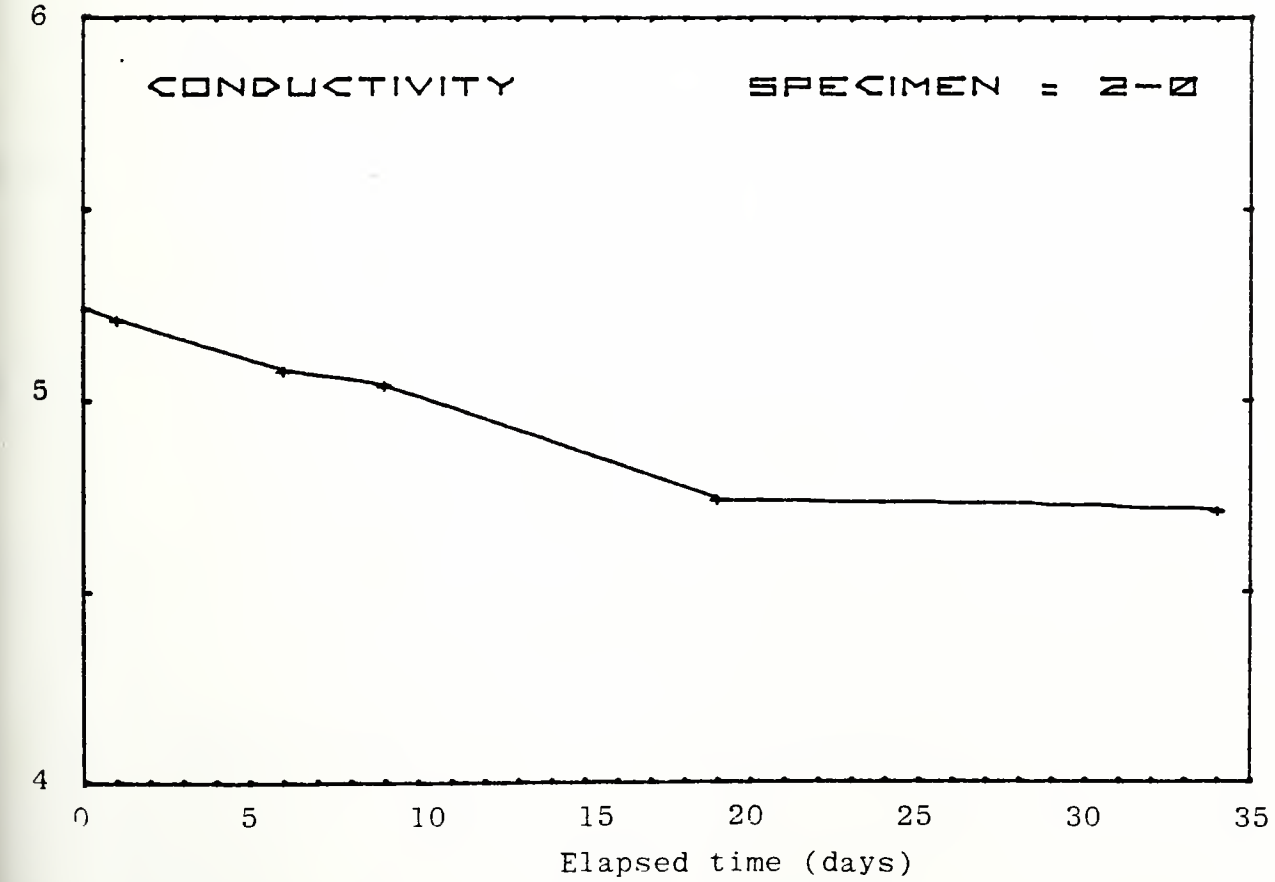
CONDUCTIVITY
SPECIMEN = 2-0
6
5
4
Conductivity ($\Omega^{-1}cm^{-1}$)
0
5
10
15
20
25
30
35
Elapsed time (days)

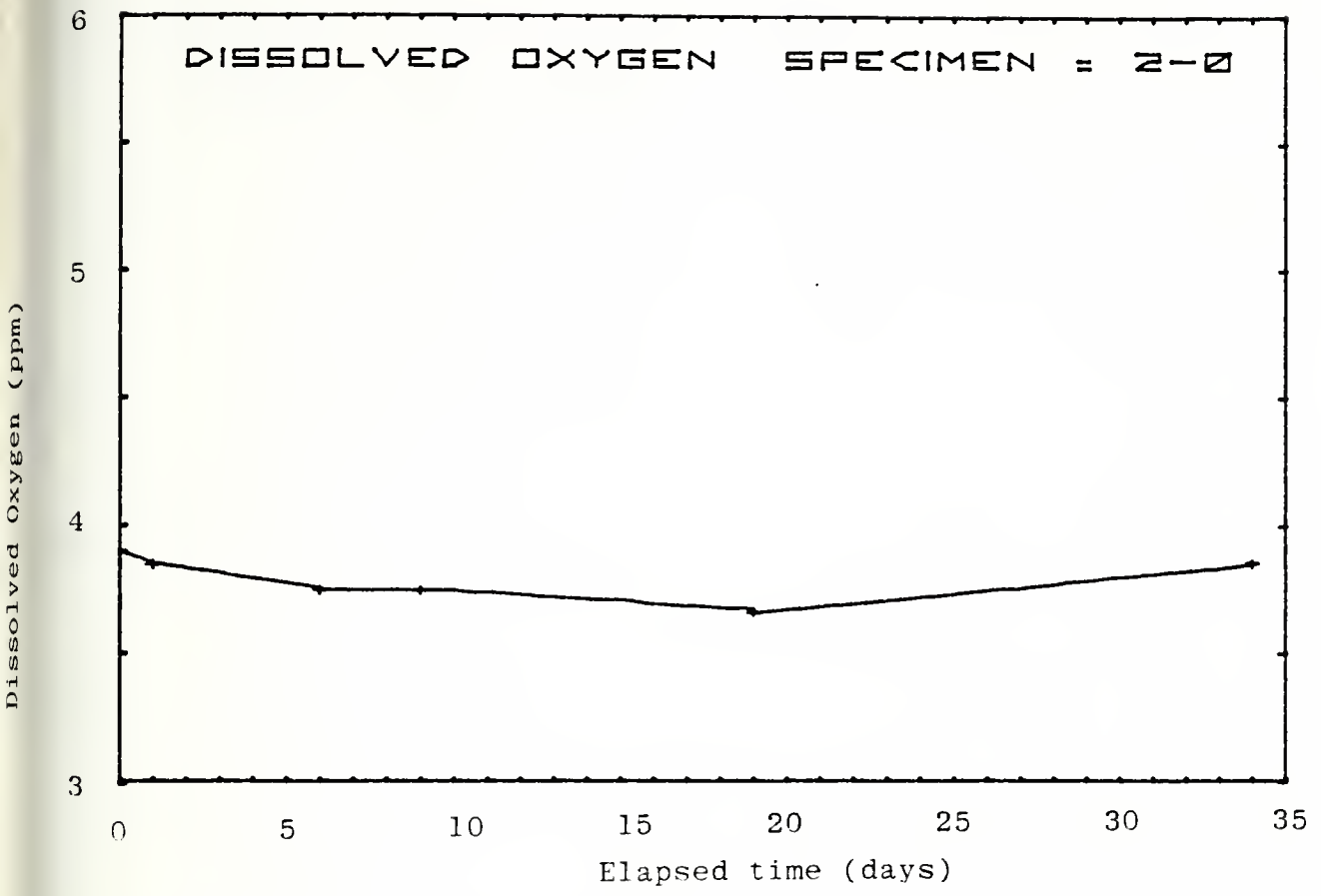
DISSOLVED OXYGEN SPECIMEN = 2-0
Dissolved Oxygen (ppm)
6
5
4
3
0
5
10
15
20
25
30
35
Elapsed time (days)

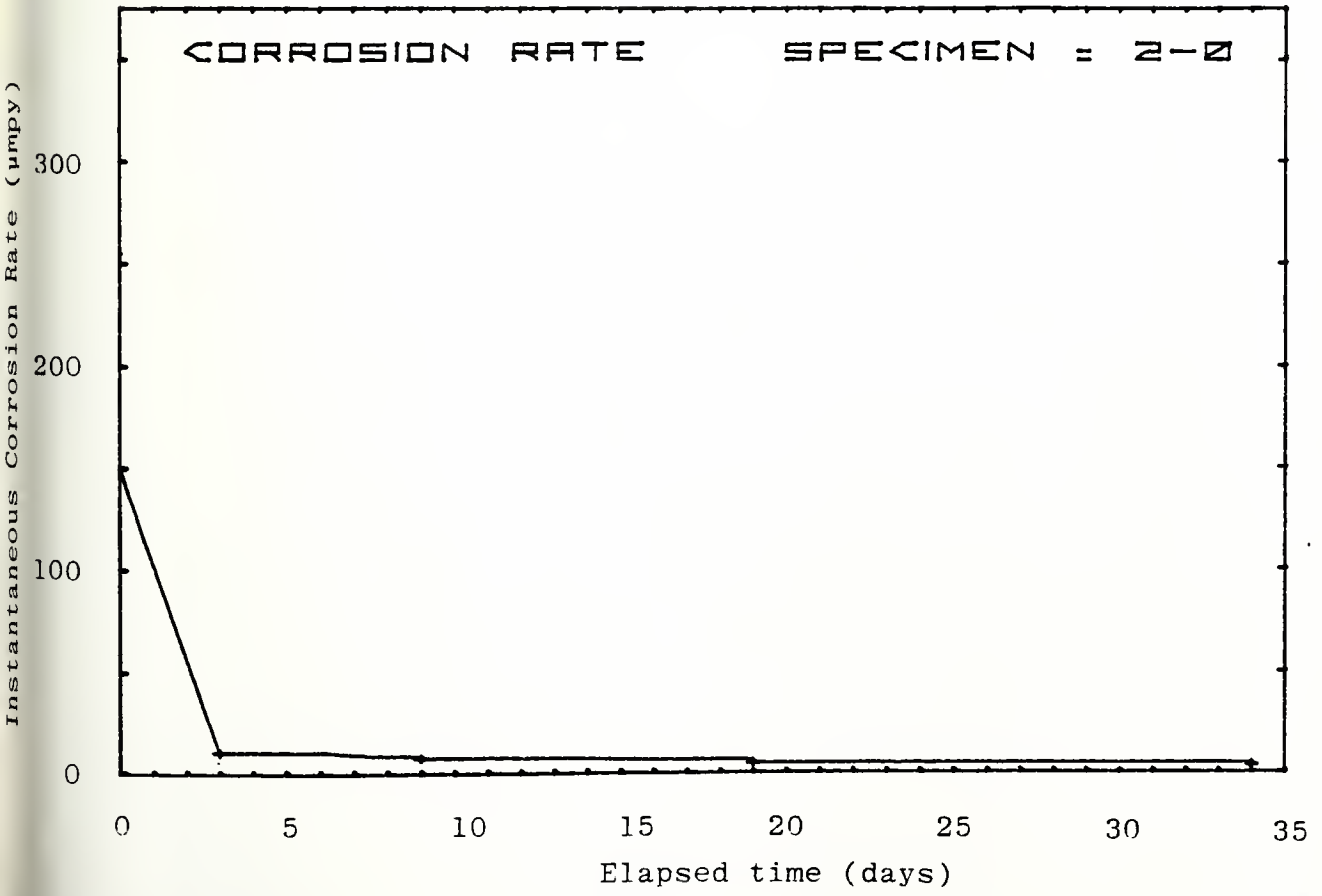
CORROSION RATE SPECIMEN = 2-0
Instantaneous Corrosion Rate (umpy)
300
200
100
0
0
5
10
15
20
25
30
35
Elapsed time (days)

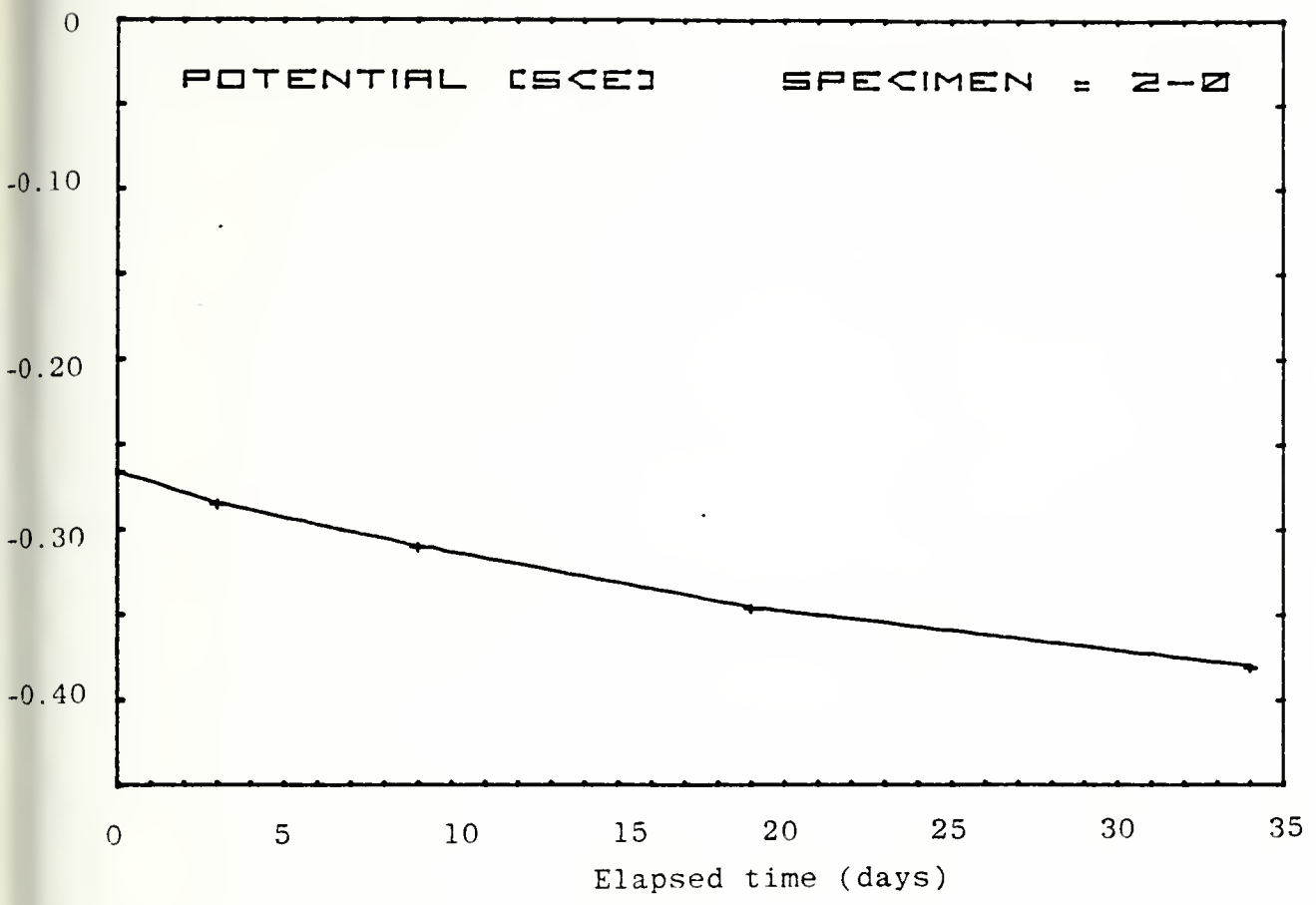
POTENTIAL (SCE)
SPECIMEN = 2-0
0
-0.10
-0.20
-0.30
-0.40
0
5
10
15
20
25
30
35
Elapsed time (days)

Figure B-3 (a-e)

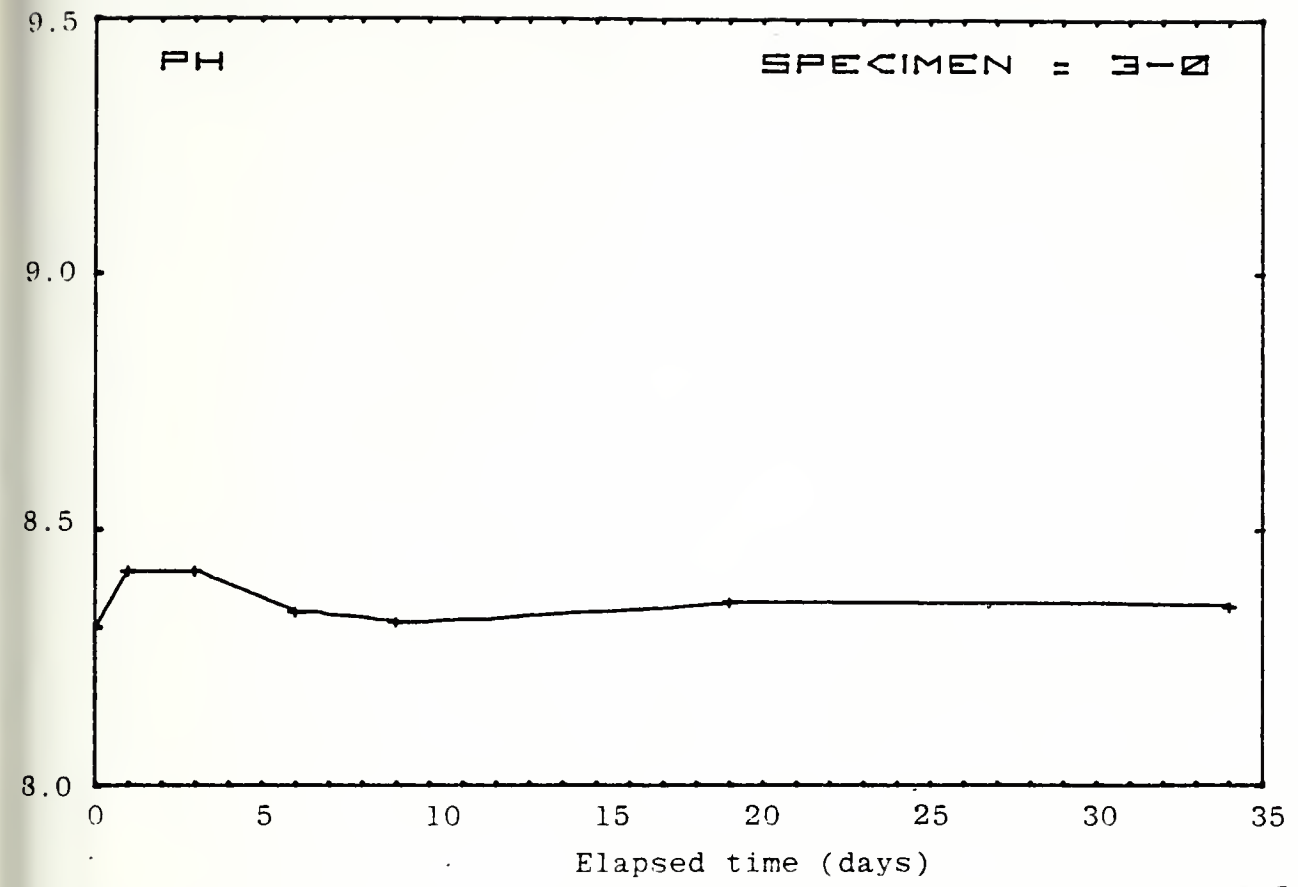
PH
SPECIMEN = 3-0
9.5
9.0
8.5
8.0
0
5
10
15
20
25
30
35
Elapsed time (days)

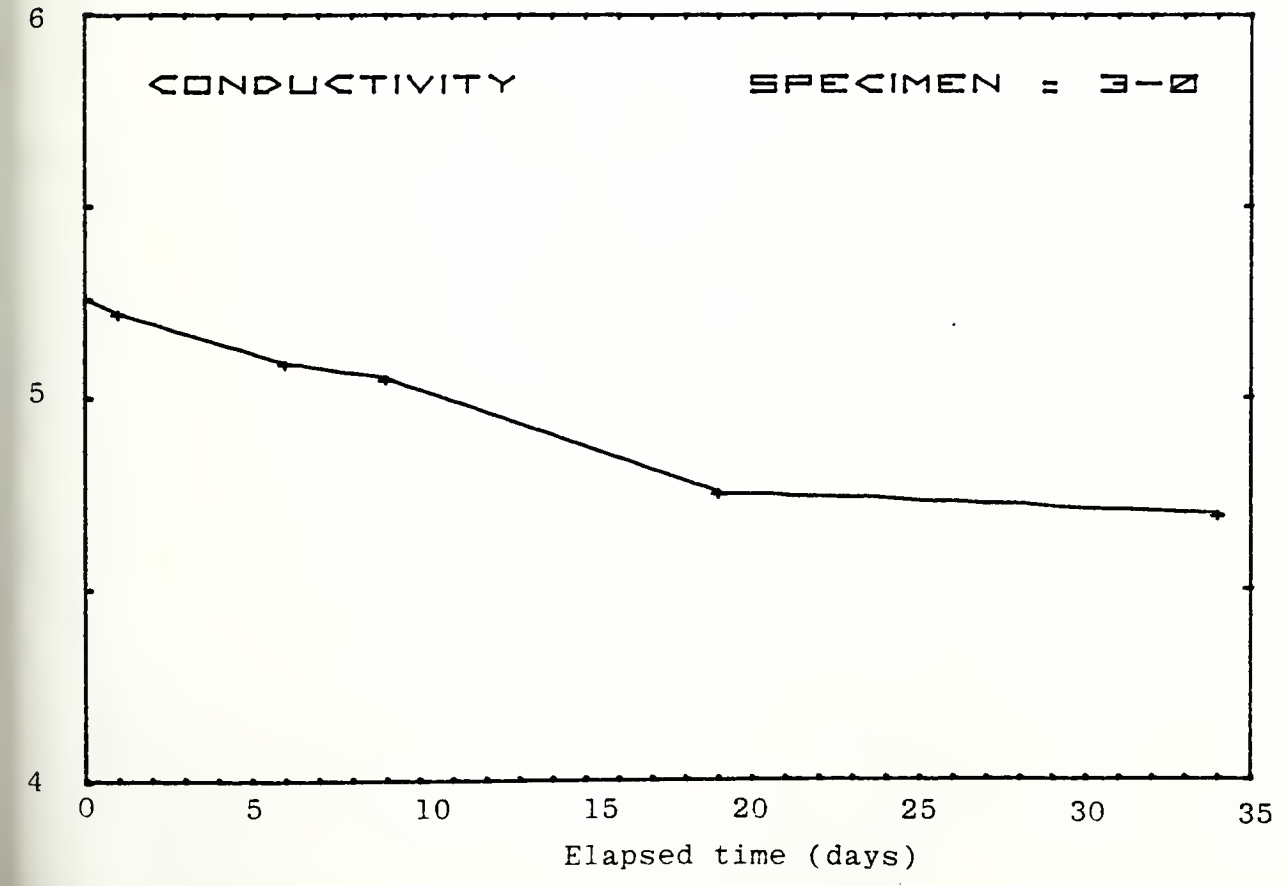
CONDUCTIVITY
SPECIMEN = 3-0
6
5
4
0
5
10
15
20
25
30
35
Elapsed time (days)

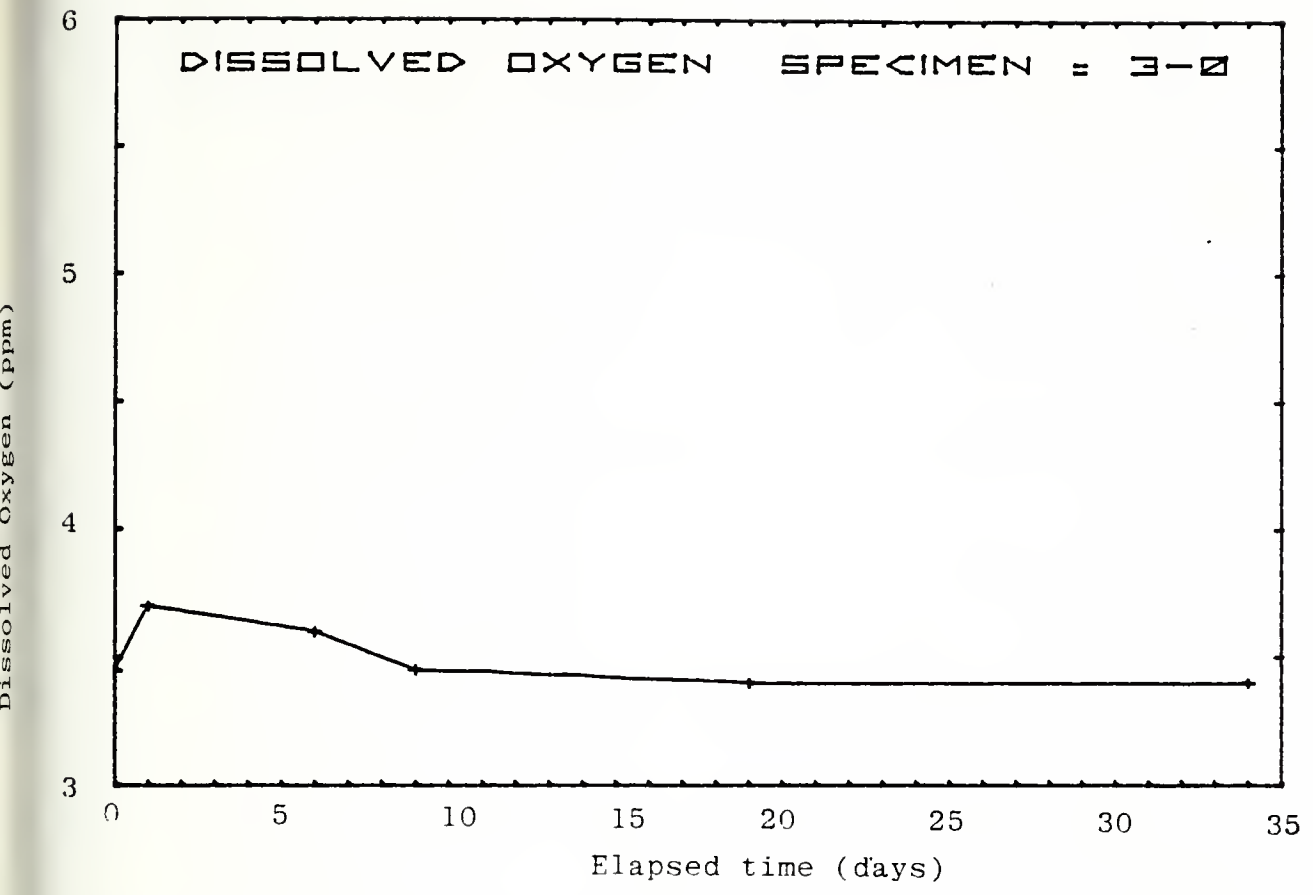
DISSOLVED OXYGEN SPECIMEN = 3-Ø
Dissolved Oxygen (ppm)
6
5
4
3
0
5
10
15
20
25
30
35
Elapsed time (days)

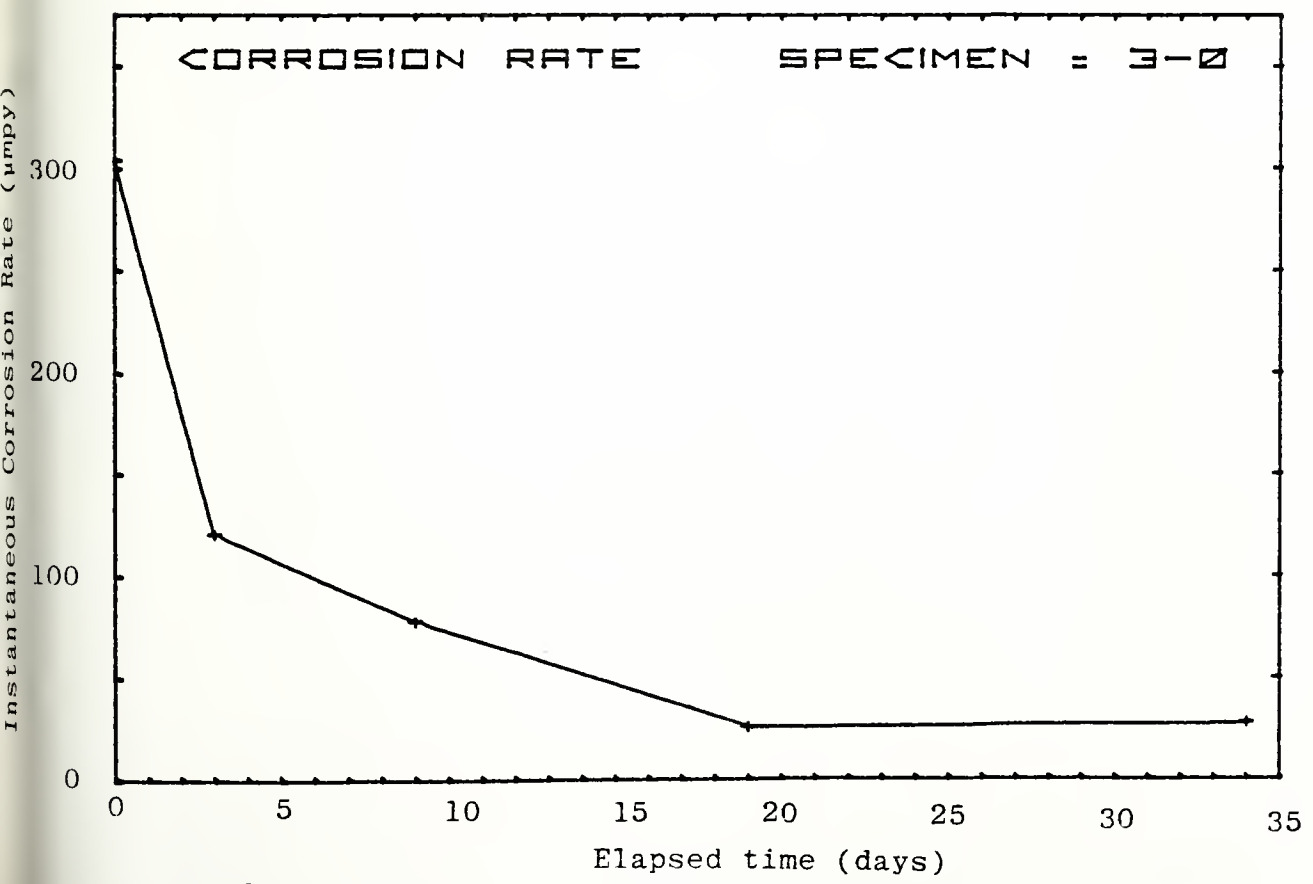
CORROSION RATE SPECIMEN = 3-Ø
Instantaneous Corrosion Rate (µmpy)
300
200
100
0
0
5
10
15
20
25
30
35
Elapsed time (days)

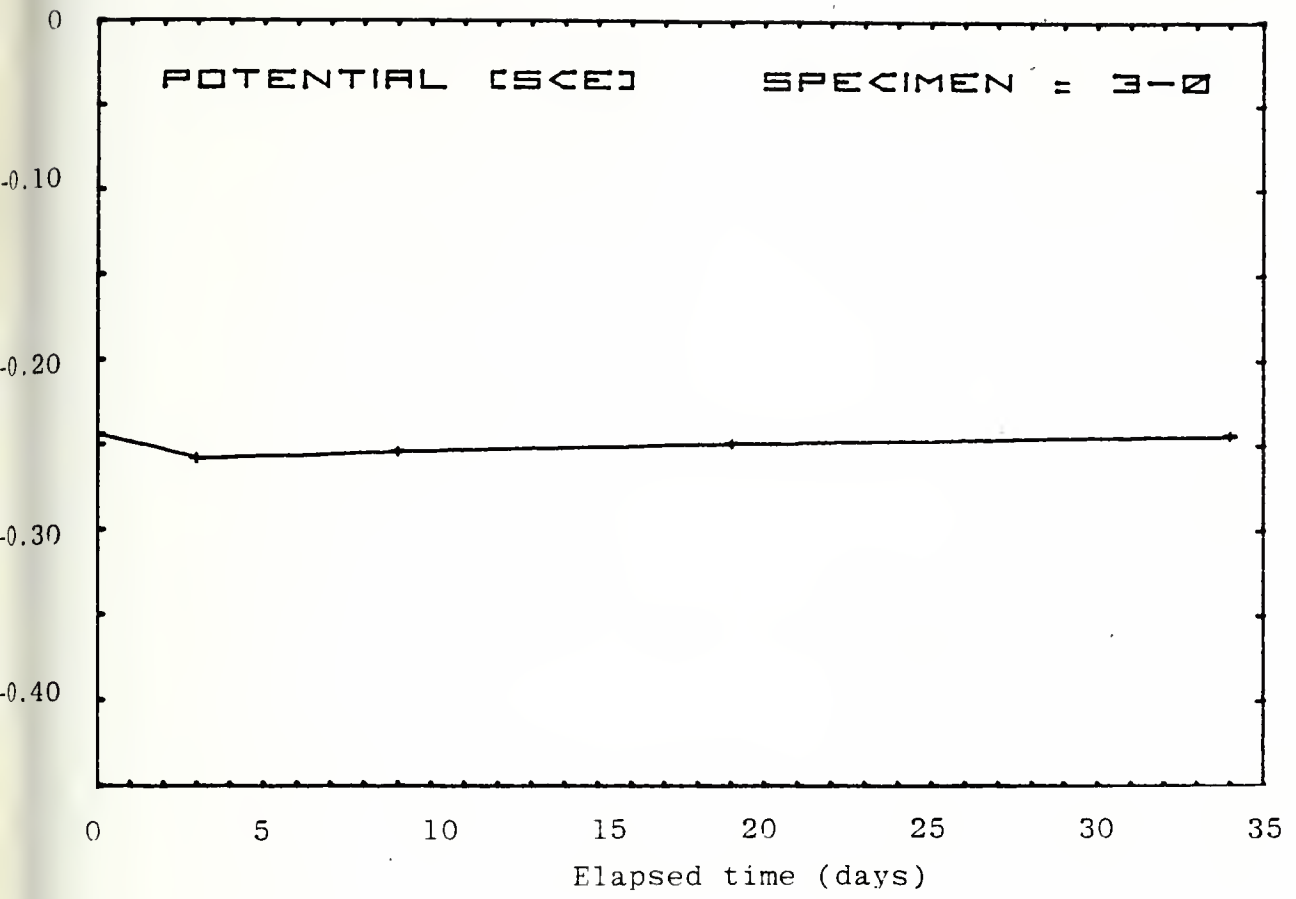
POTENTIAL (SCE)
SPECIMEN = 3-0
0
-0.10
-0.20
-0.30
-0.40
0
5
10
15
20
25
30
35
Elapsed time (days)

Figure B-4 (a-e)

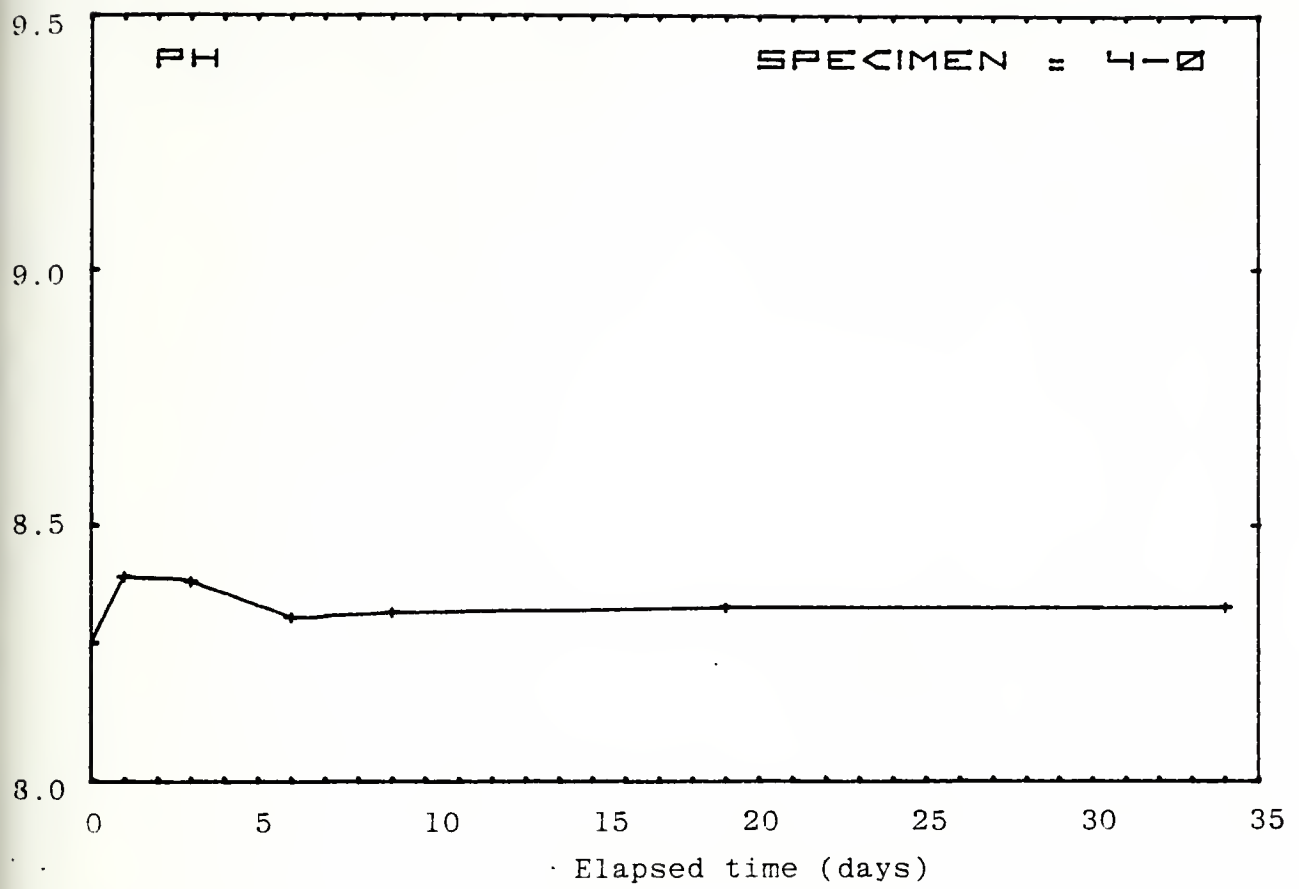
PH
SPECIMEN = 4-0
9.5
9.0
8.5
8.0
pH
0
5
10
15
20
25
30
35
Elapsed time (days)

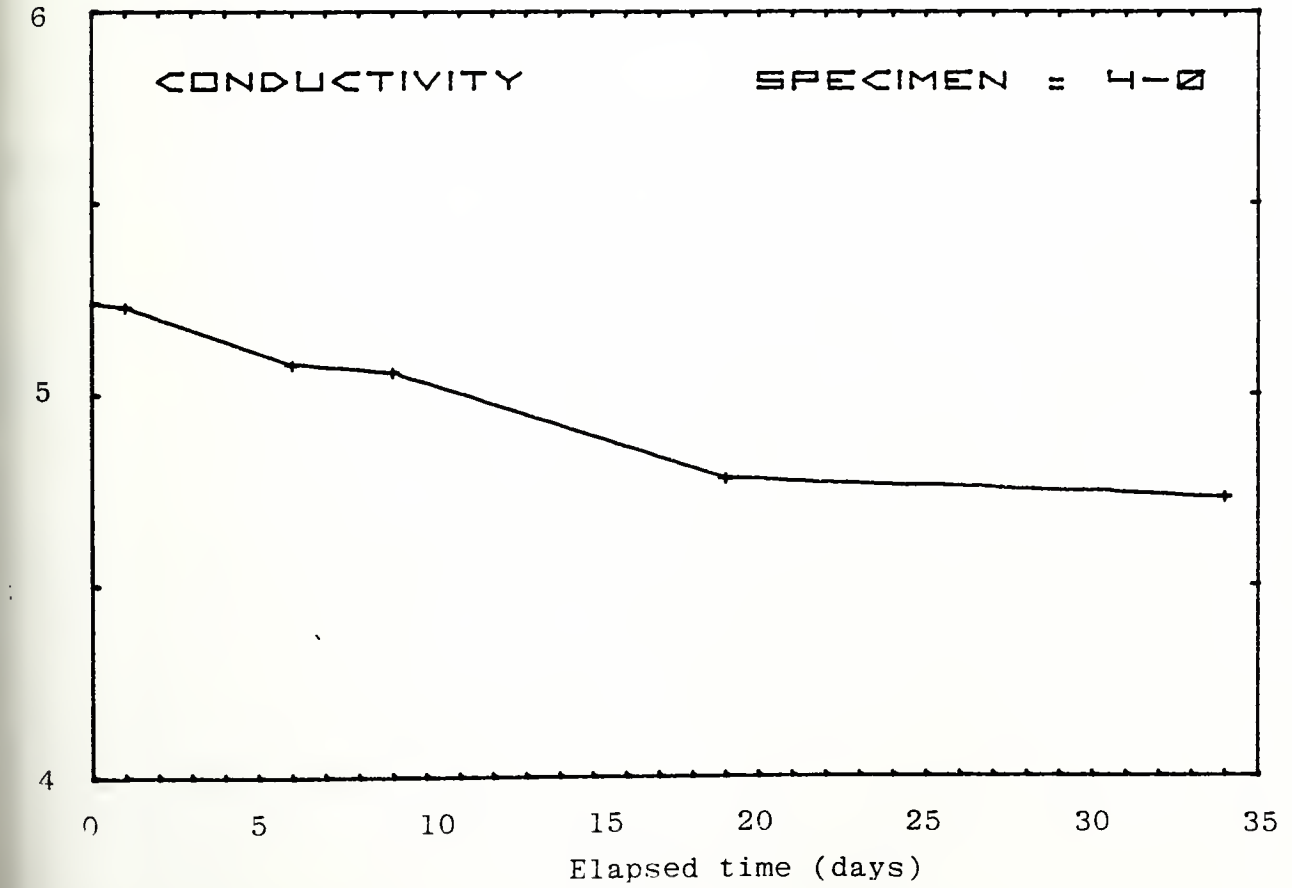
CONDUCTIVITY
SPECIMEN = 4-0
6
5
4
Conductivity (Ω⁻¹cm⁻¹)
0
5
10
15
20
25
30
35
Elapsed time (days)

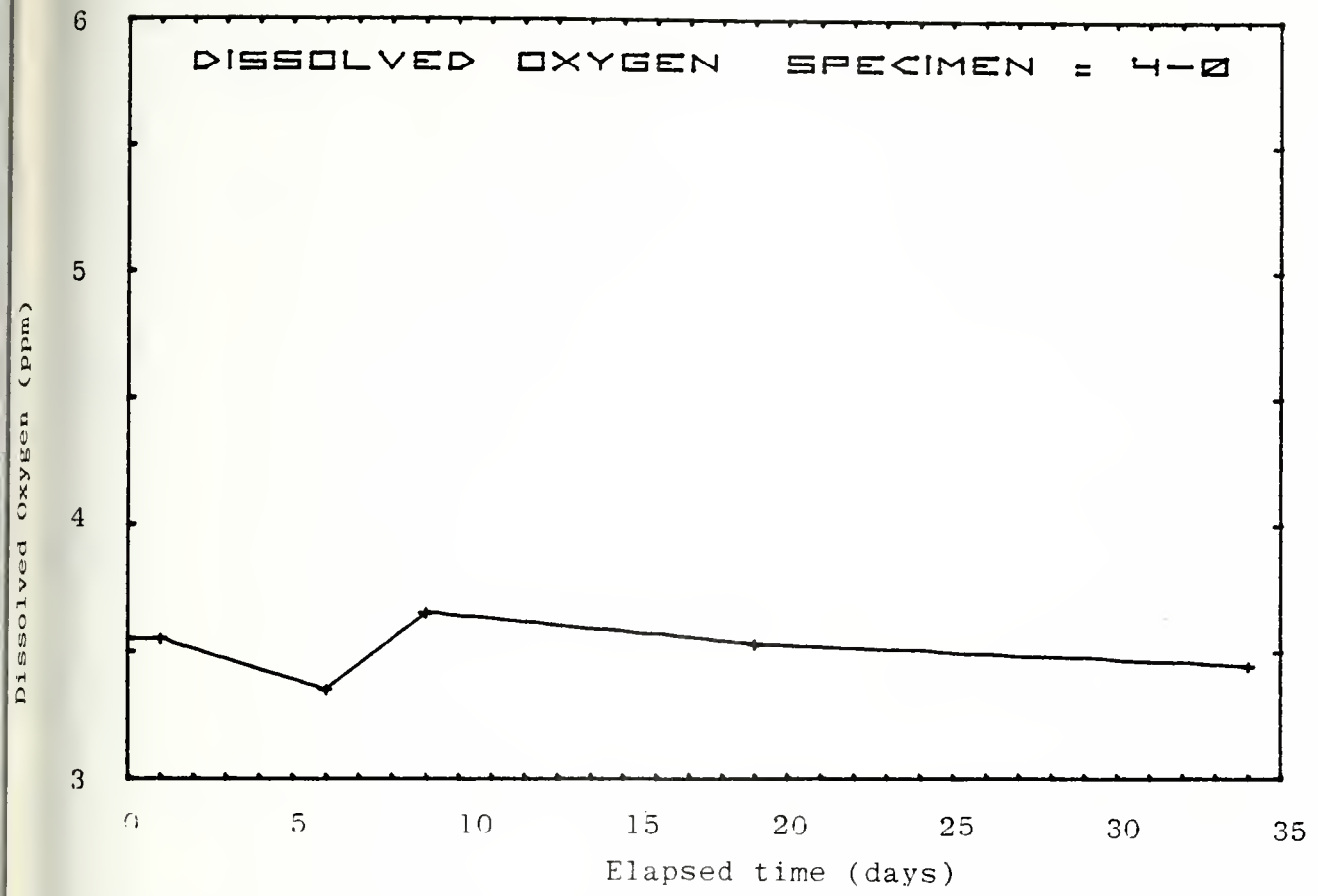
DISSOLVED OXYGEN SPECIMEN = 4-Ø
Dissolved Oxygen (ppm)
6
5
4
3
0
5
10
15
20
25
30
35
Elapsed time (days)

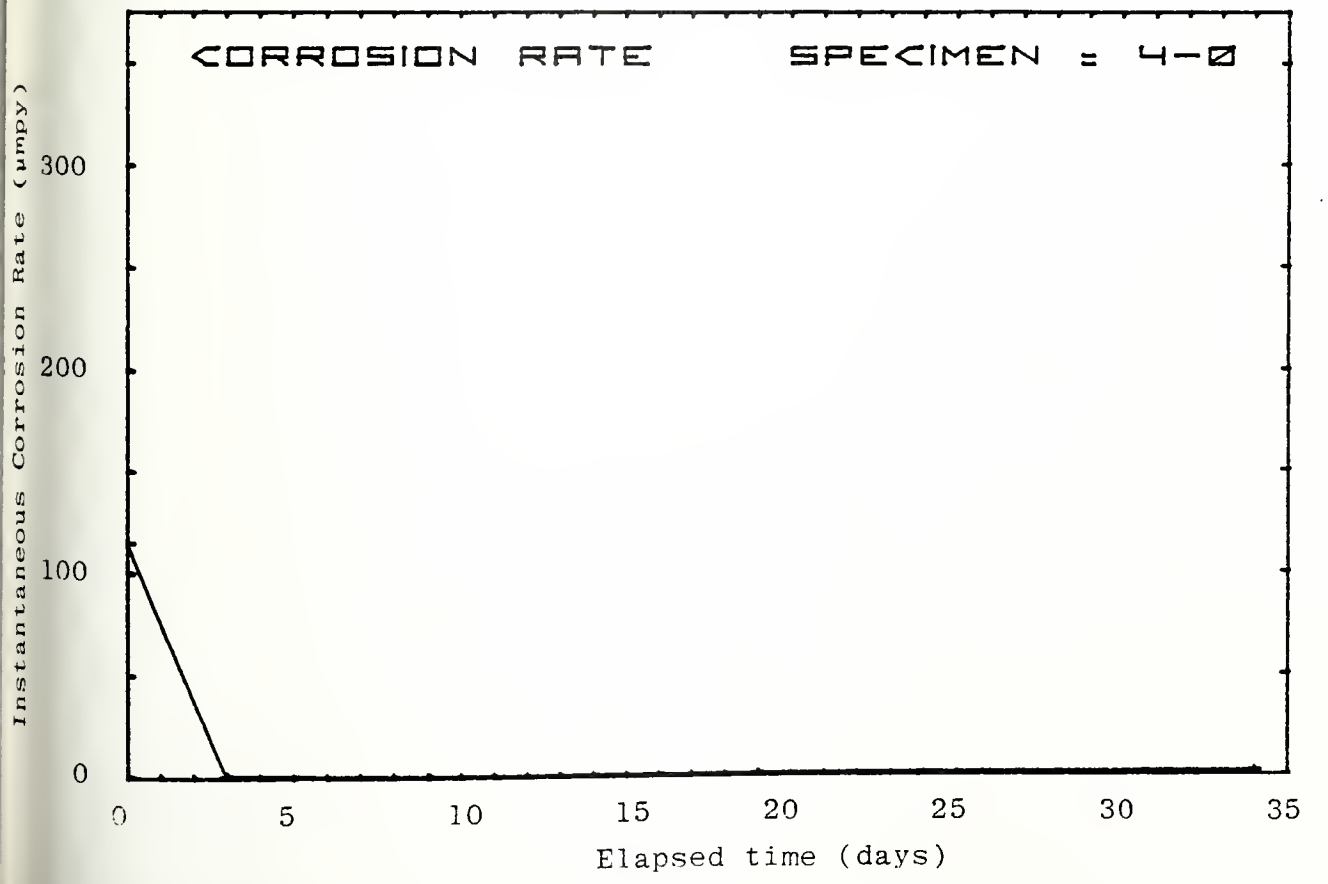
CORROSION RATE SPECIMEN = 4-Ø
Instantaneous Corrosion Rate (umpy)
300
200
100
0
0
5
10
15
20
25
30
35
Elapsed time (days)

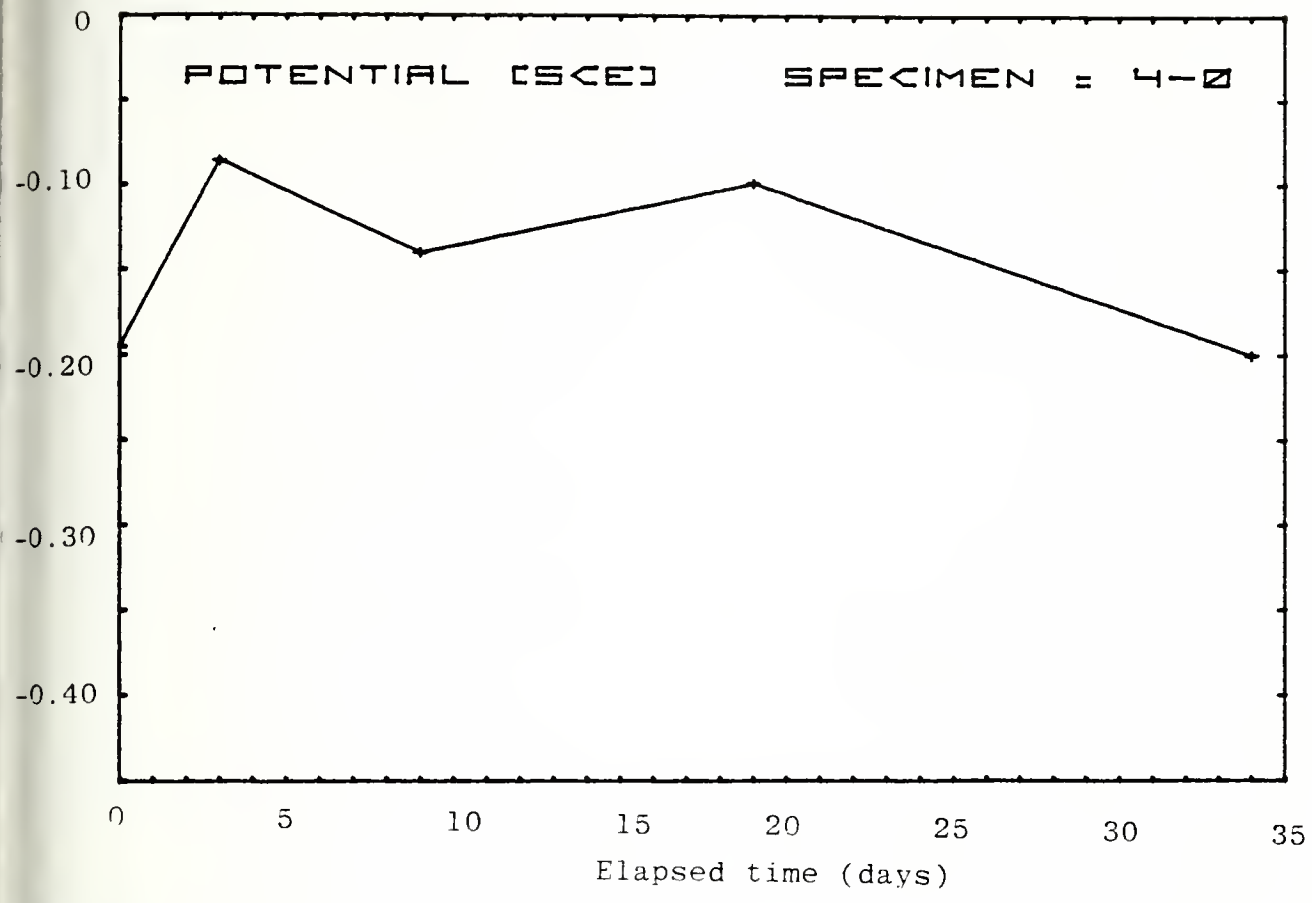
POTENTIAL (SCE)
SPECIMEN = 4-0
0
-0.10
-0.20
-0.30
-0.40
0
5
10
15
20
25
30
35
Elapsed time (days)

Figure B-5 (a-e)

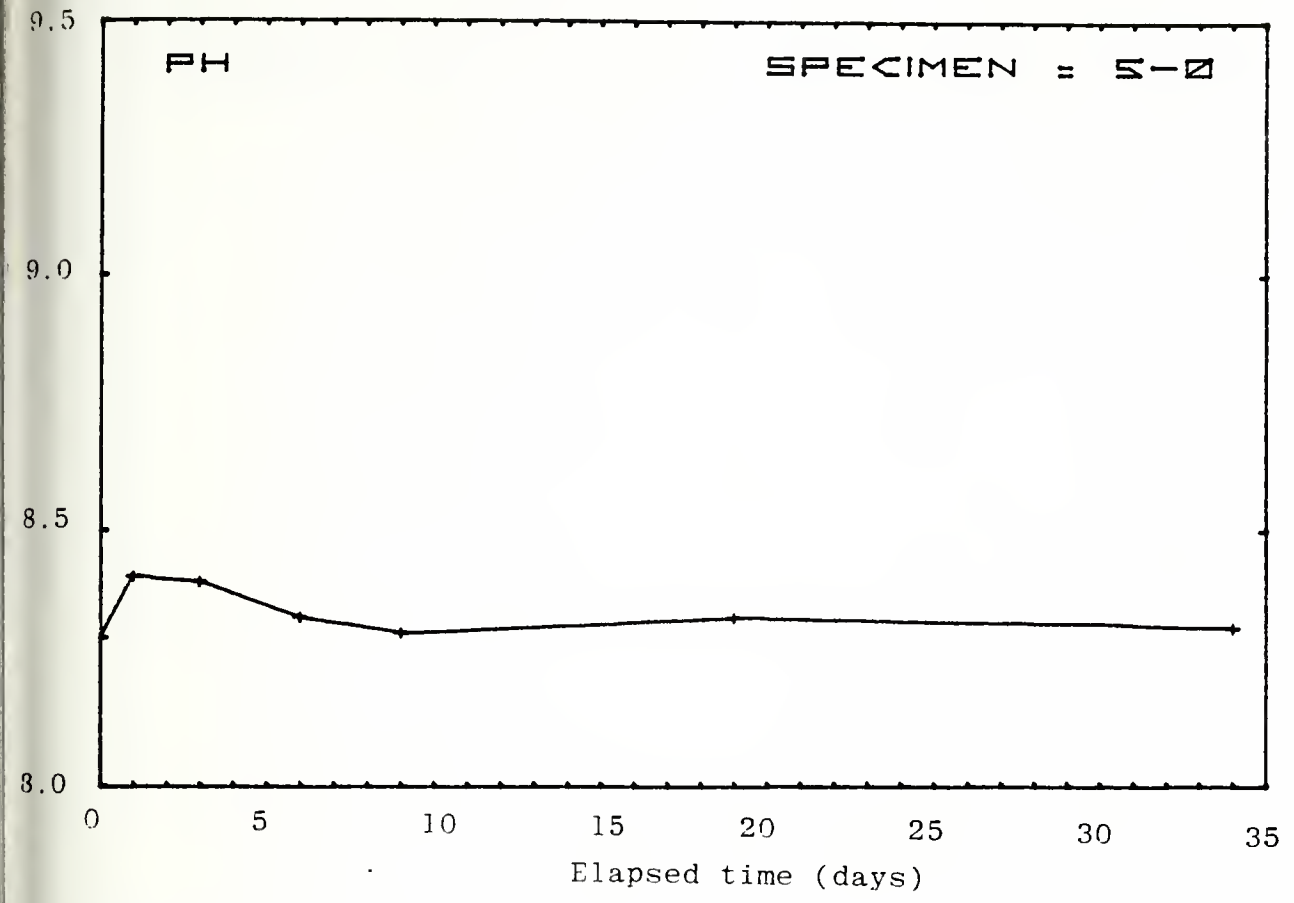
PH
SPECIMEN = 5-Ø
9.5
9.0
8.5
8.0
0
5
10
15
20
25
30
35
Elapsed time (days)

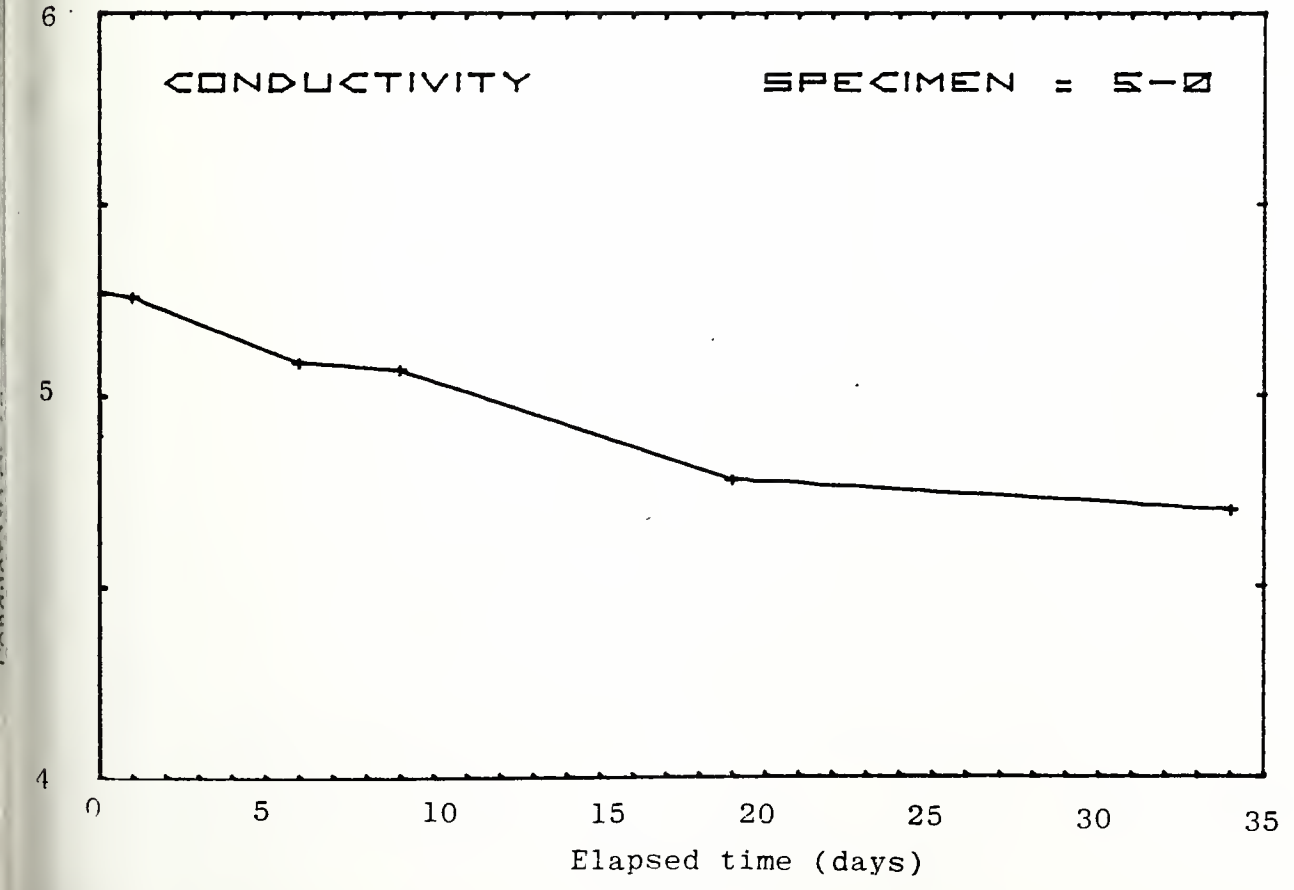
CONDUCTIVITY
SPECIMEN = 5-Ø
6
5
4
0
5
10
15
20
25
30
35
Elapsed time (days)

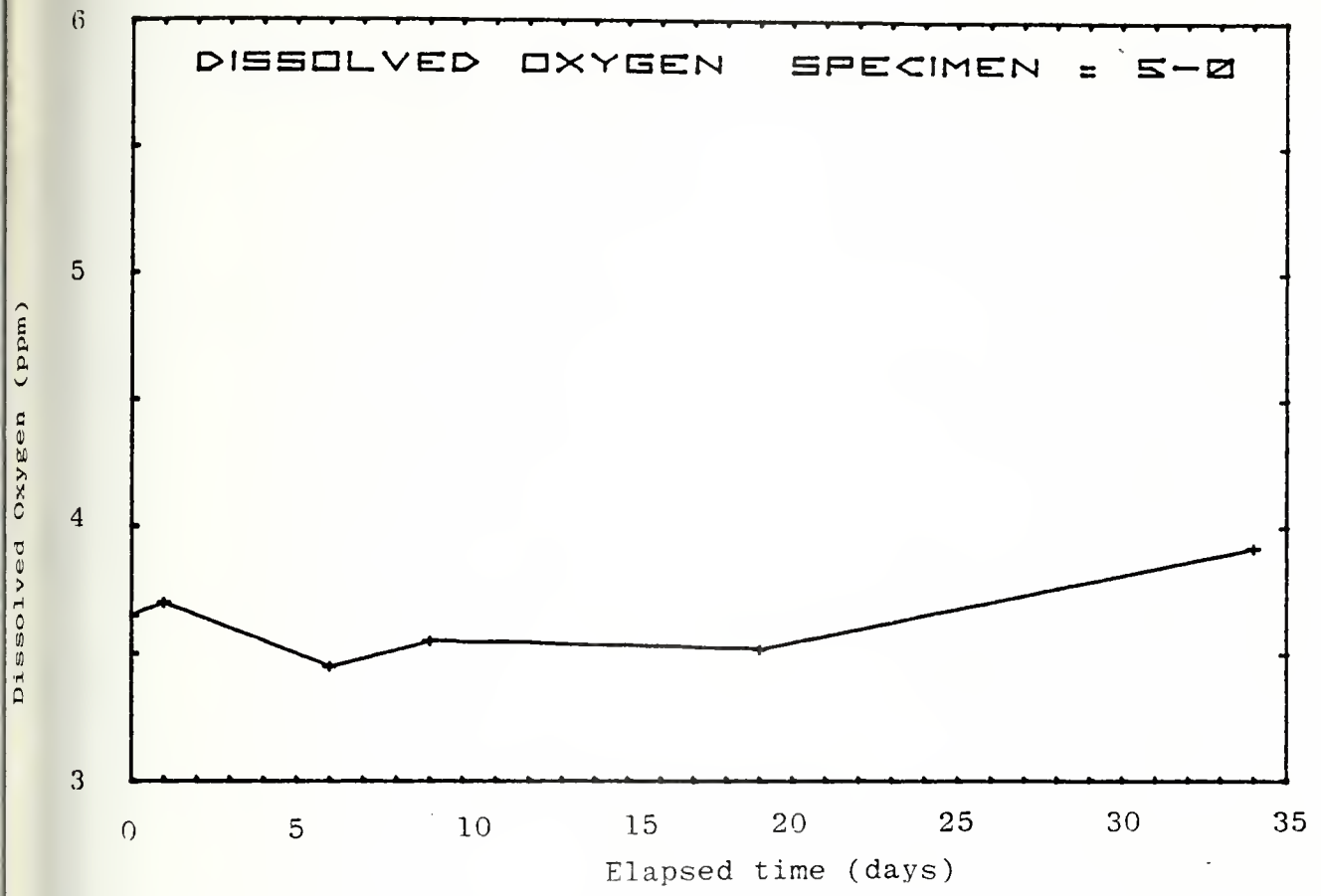
DISSOLVED OXYGEN SPECIMEN = 5-0
Dissolved Oxygen (ppm)
6
5
4
3
0
5
10
15
20
25
30
35
Elapsed time (days)

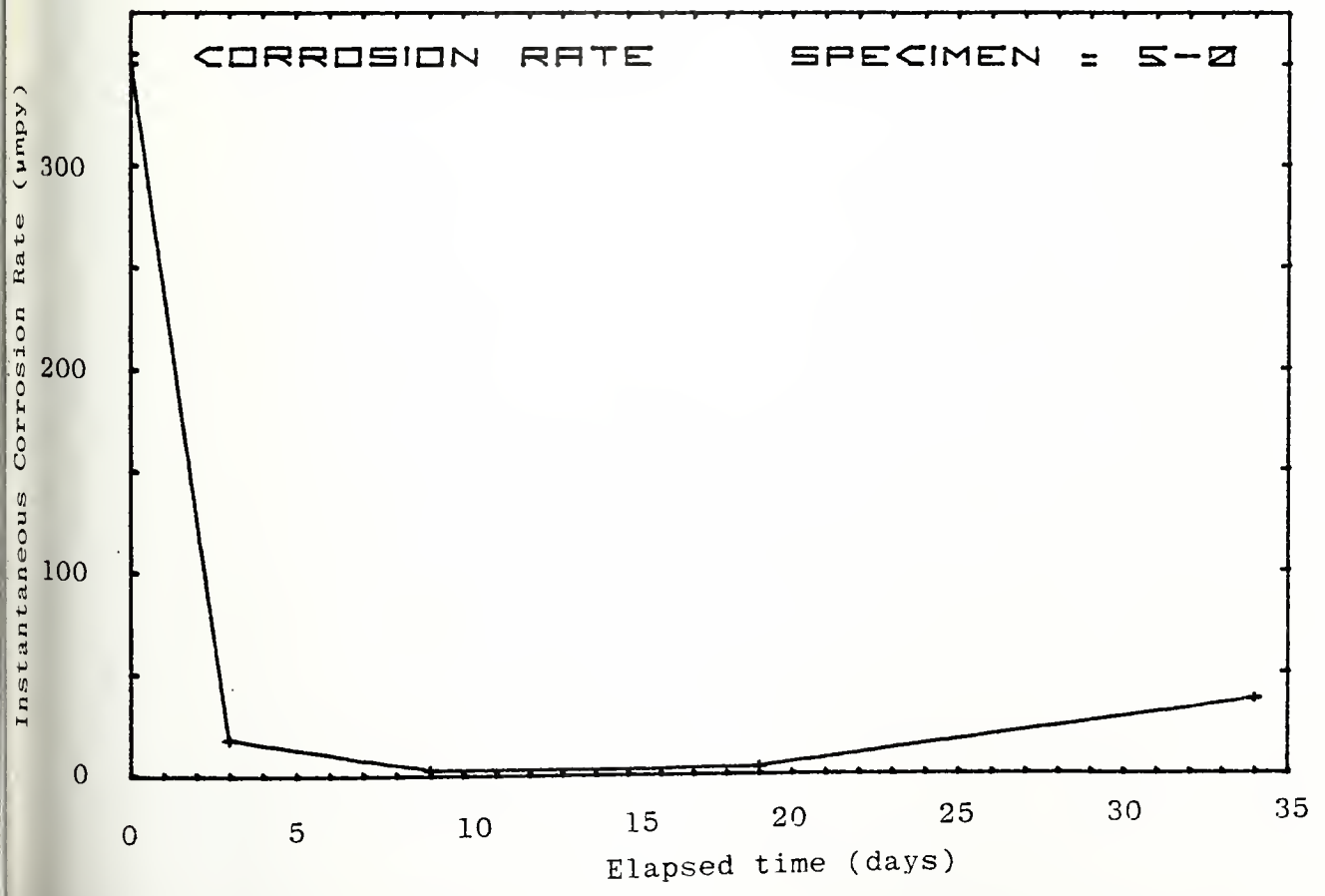
CORROSION RATE SPECIMEN = 5-0
Instantaneous Corrosion Rate (umpy)
300
200
100
0
0
5
10
15
20
25
30
35
Elapsed time (days)

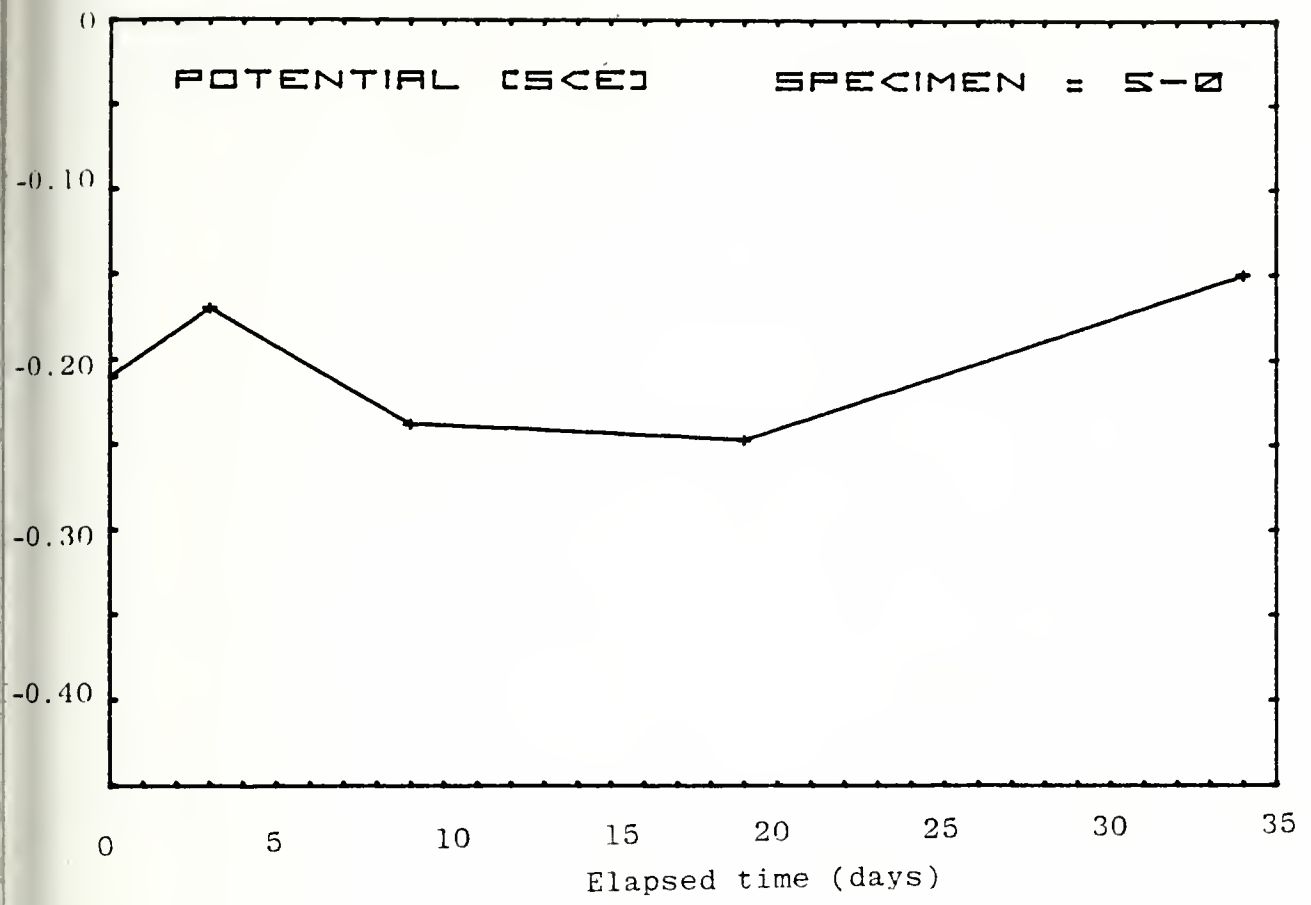
POTENTIAL (SCE)
SPECIMEN = S-0
0
-0.10
-0.20
-0.30
-0.40
0
5
10
15
20
25
30
35
Elapsed time (days)

Figure B-6 (a-e)

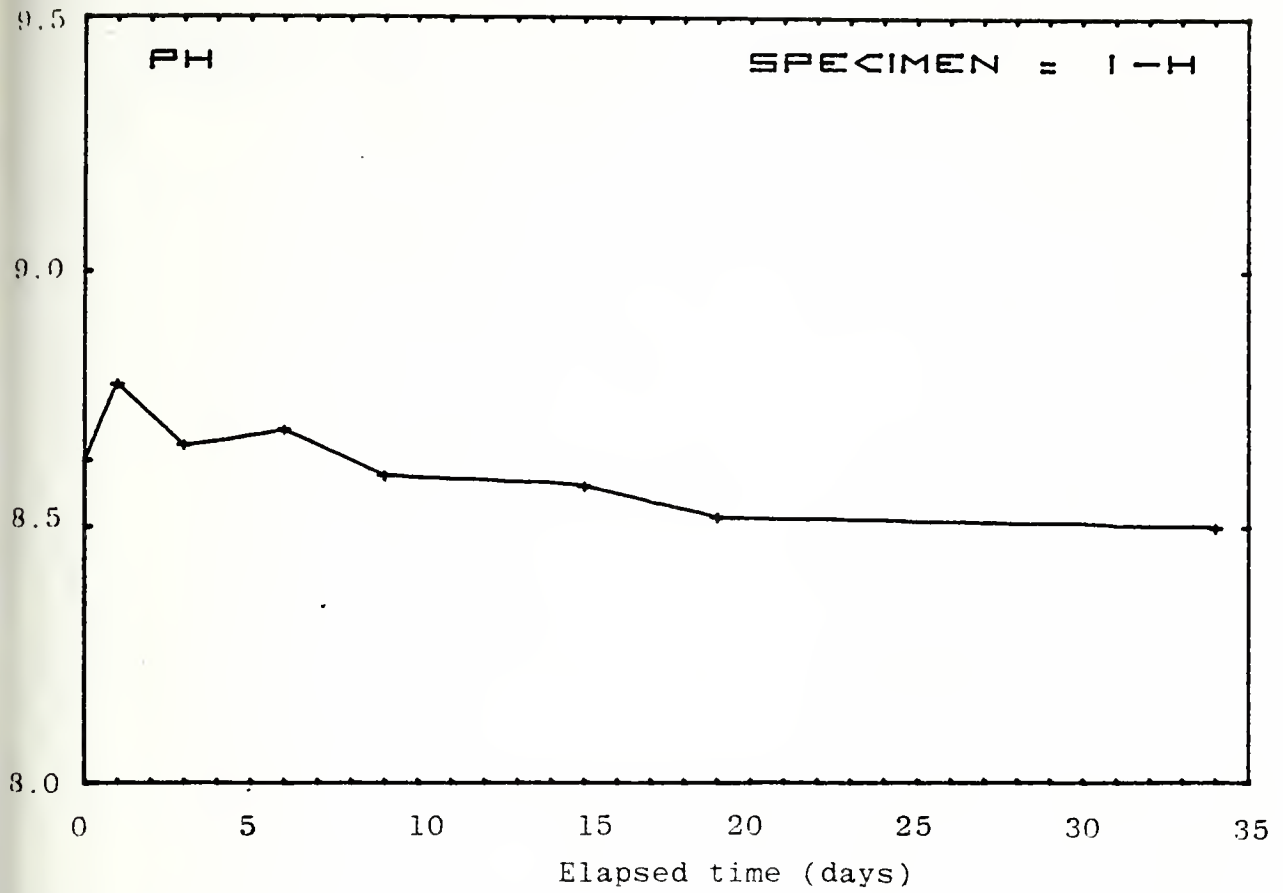
PH
SPECIMEN = 1-H
9.5
9.0
8.5
8.0
0
5
10
15
20
25
30
35
Elapsed time (days)

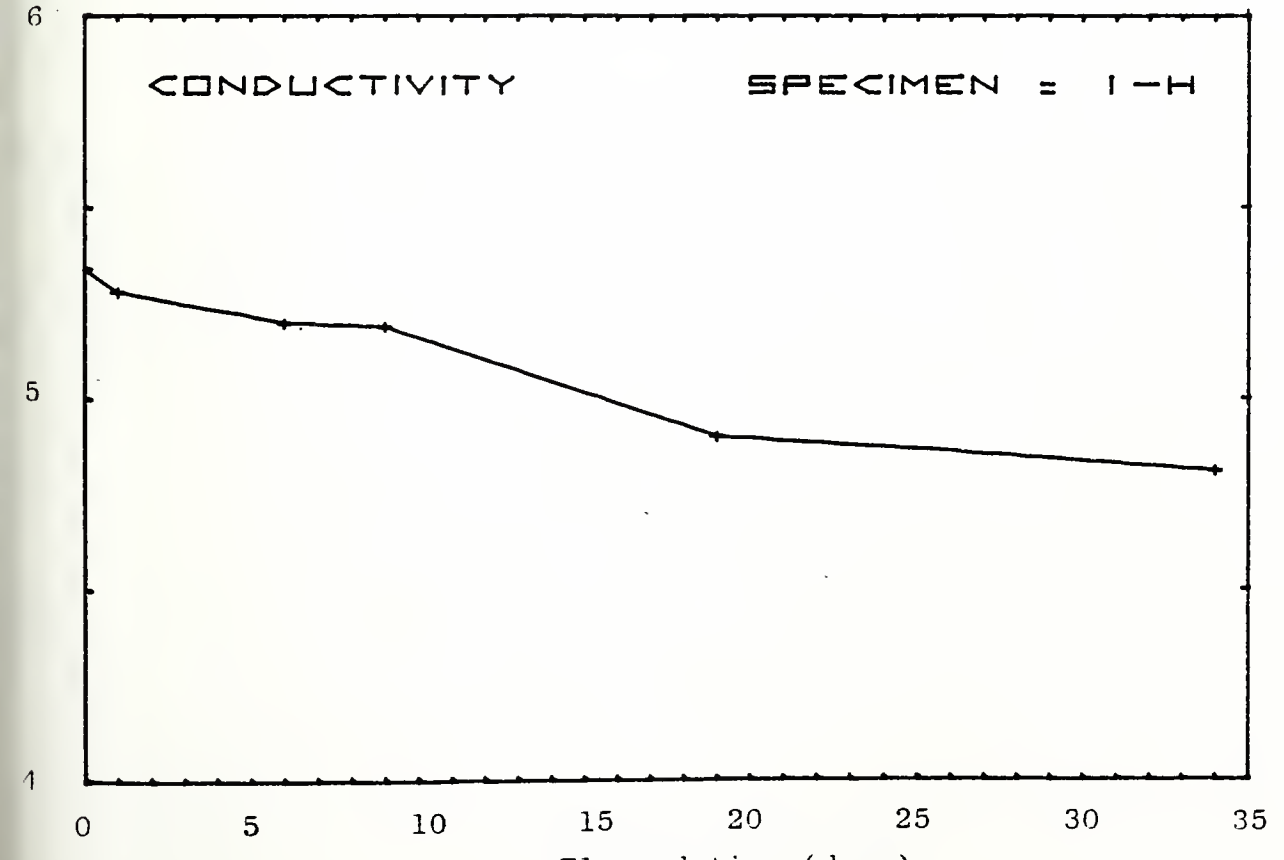
CONDUCTIVITY
SPECIMEN = 1-H
6
5
1
0
5
10
15
20
25
30
35
Elapsed time (days)

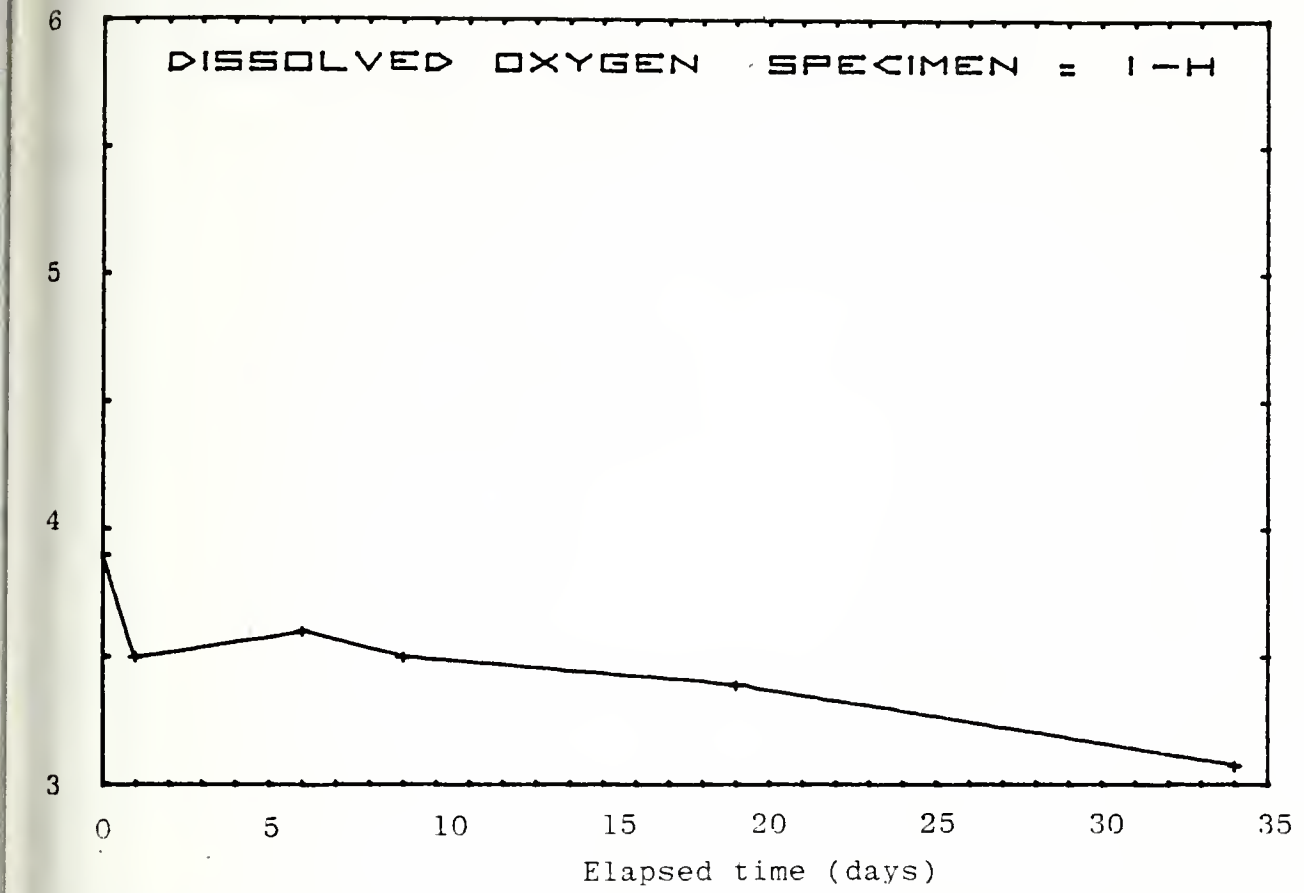
DISSOLVED OXYGEN SPECIMEN = 1-H
6
5
4
3
0
5
10
15
20
25
30
35
Elapsed time (days)

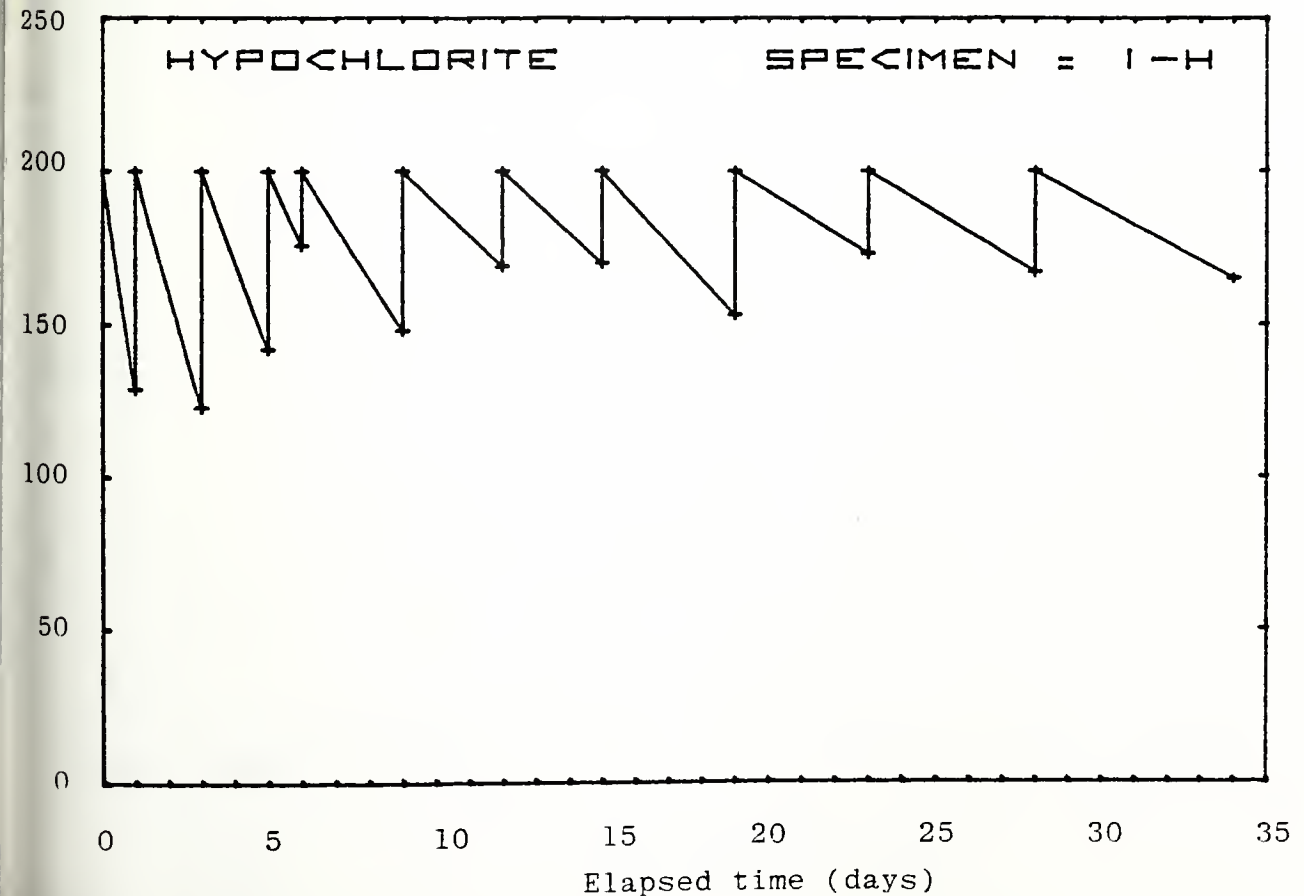
HYPOCHLORITE SPECIMEN = 1-H
250
200
150
100
50
0
0
5
10
15
20
25
30
35
Elapsed time (days)

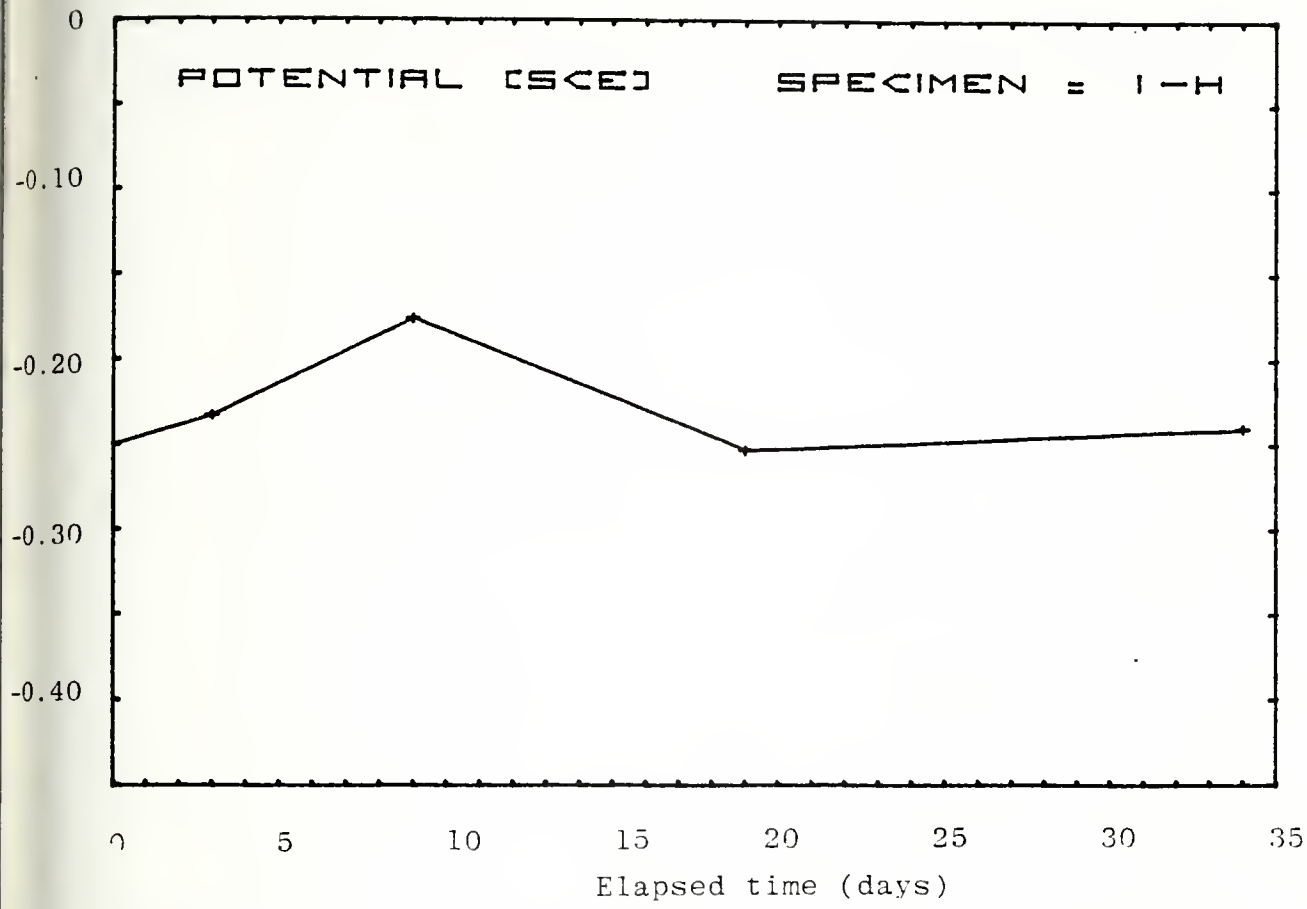
POTENTIAL (SCE)
SPECIMEN = 1-H
0
-0.10
-0.20
-0.30
-0.40
0
5
10
15
20
25
30
35
Elapsed time (days)

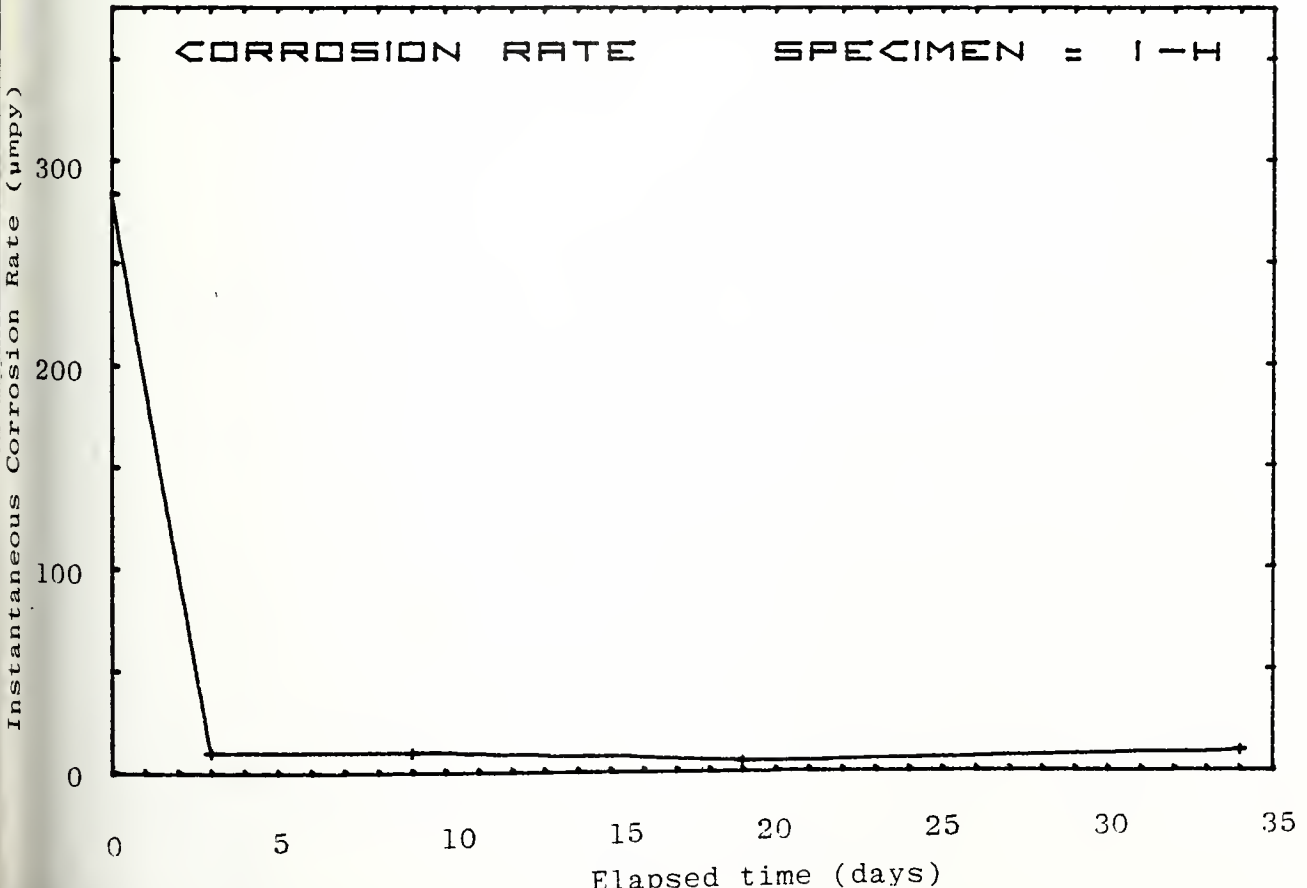
CORROSION RATE
SPECIMEN = 1-H
Instantaneous Corrosion Rate (μmpy)
300
200
100
0
0
5
10
15
20
25
30
35
Elapsed time (days)

Figure B-7 (a-e)

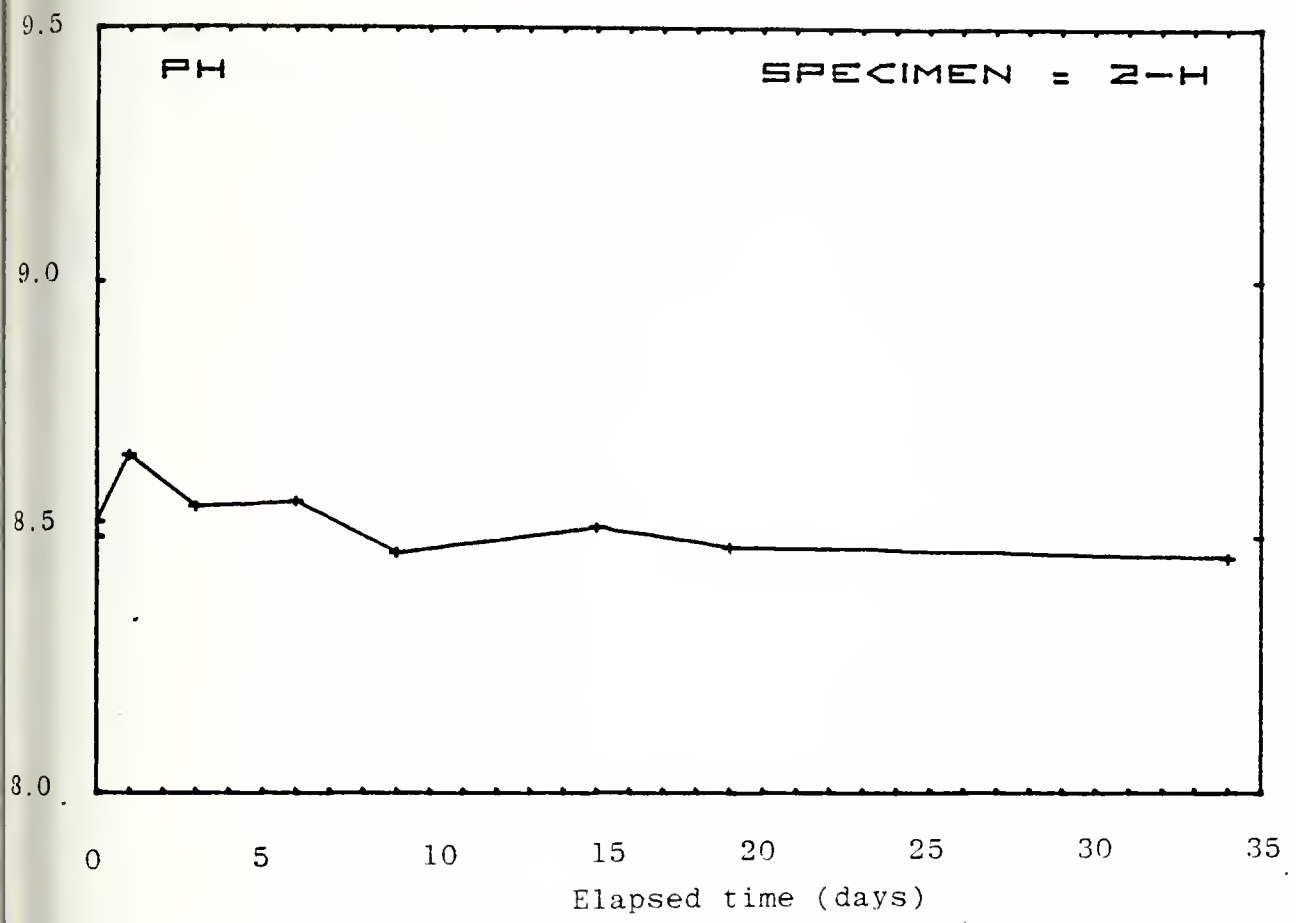
PH
SPECIMEN = 2-H
9.5
9.0
8.5
8.0
0
5
10
15
20
25
30
35
Elapsed time (days)

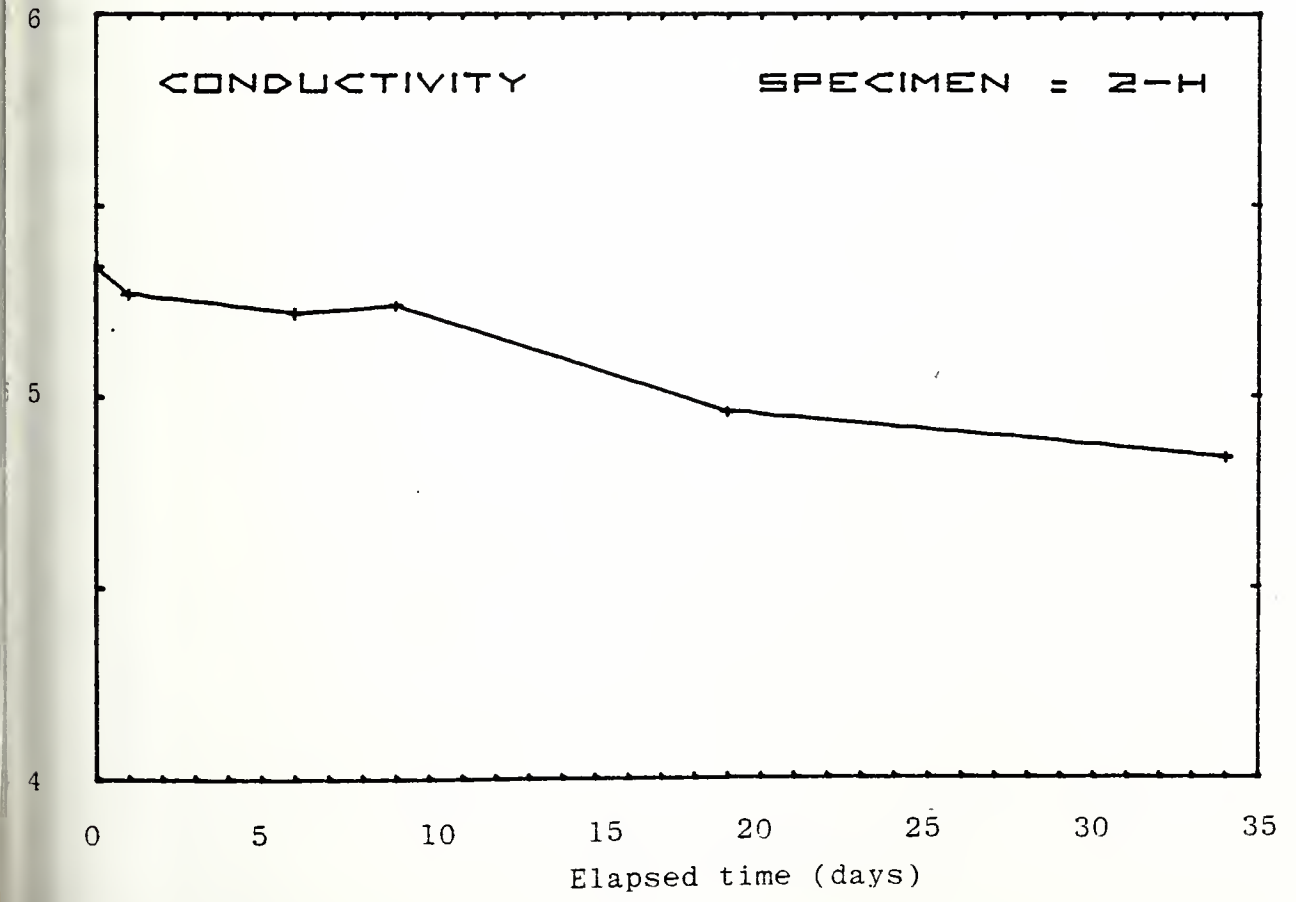
CONDUCTIVITY
SPECIMEN = 2-H
6
5
4
0
5
10
15
20
25
30
35
Elapsed time (days)

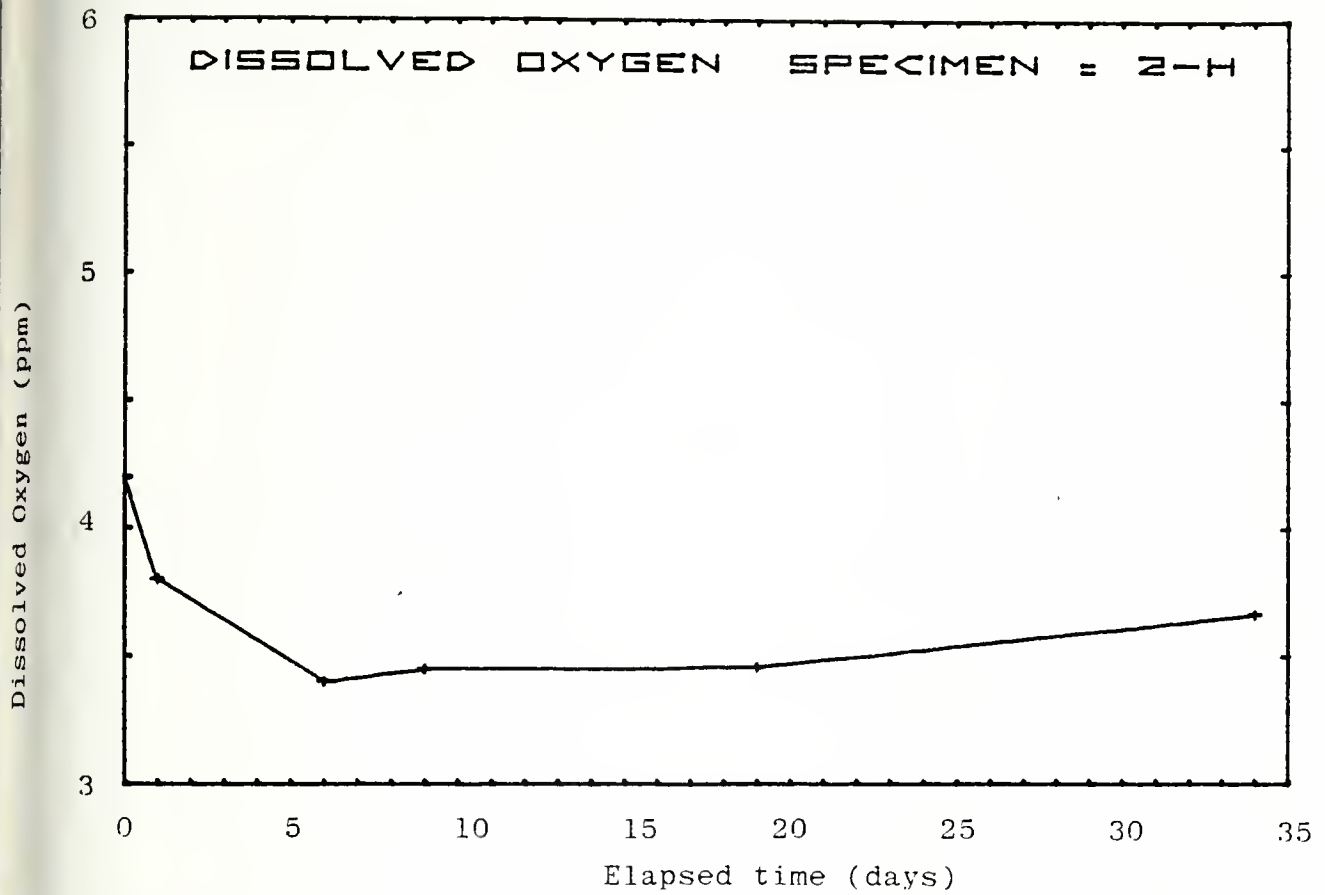
DISSOLVED OXYGEN SPECIMEN = 2-H
Dissolved Oxygen (ppm)
6
5
4
3
0
5
10
15
20
25
30
35
Elapsed time (days)

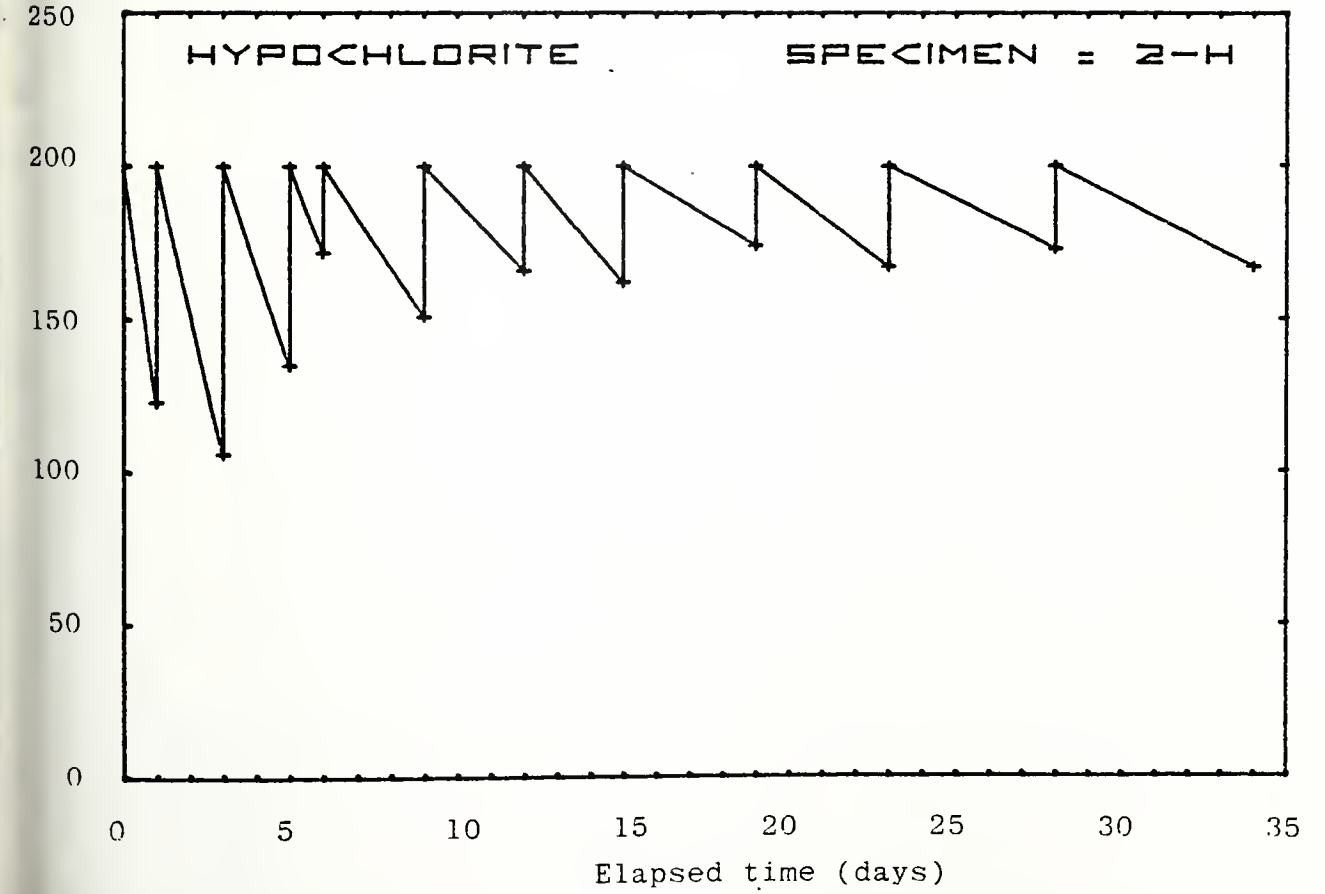
HYPOCHLORITE SPECIMEN = 2-H
250
200
150
100
50
0
0
5
10
15
20
25
30
35
Elapsed time (days)

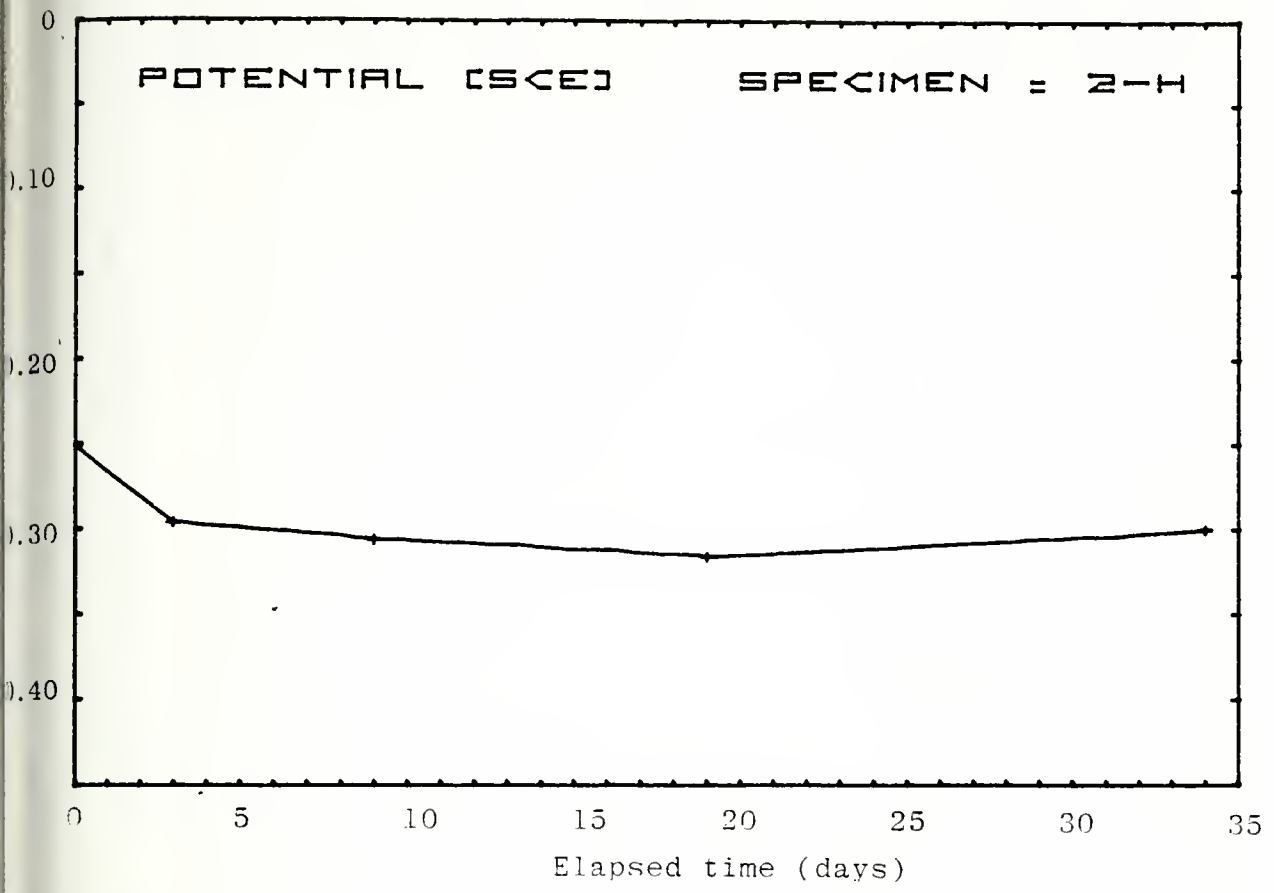
POTENTIAL (SCE) SPECIMEN = 2-H
0
.10
.20
.30
.40
0
5
10
15
20
25
30
35
Elapsed time (days)

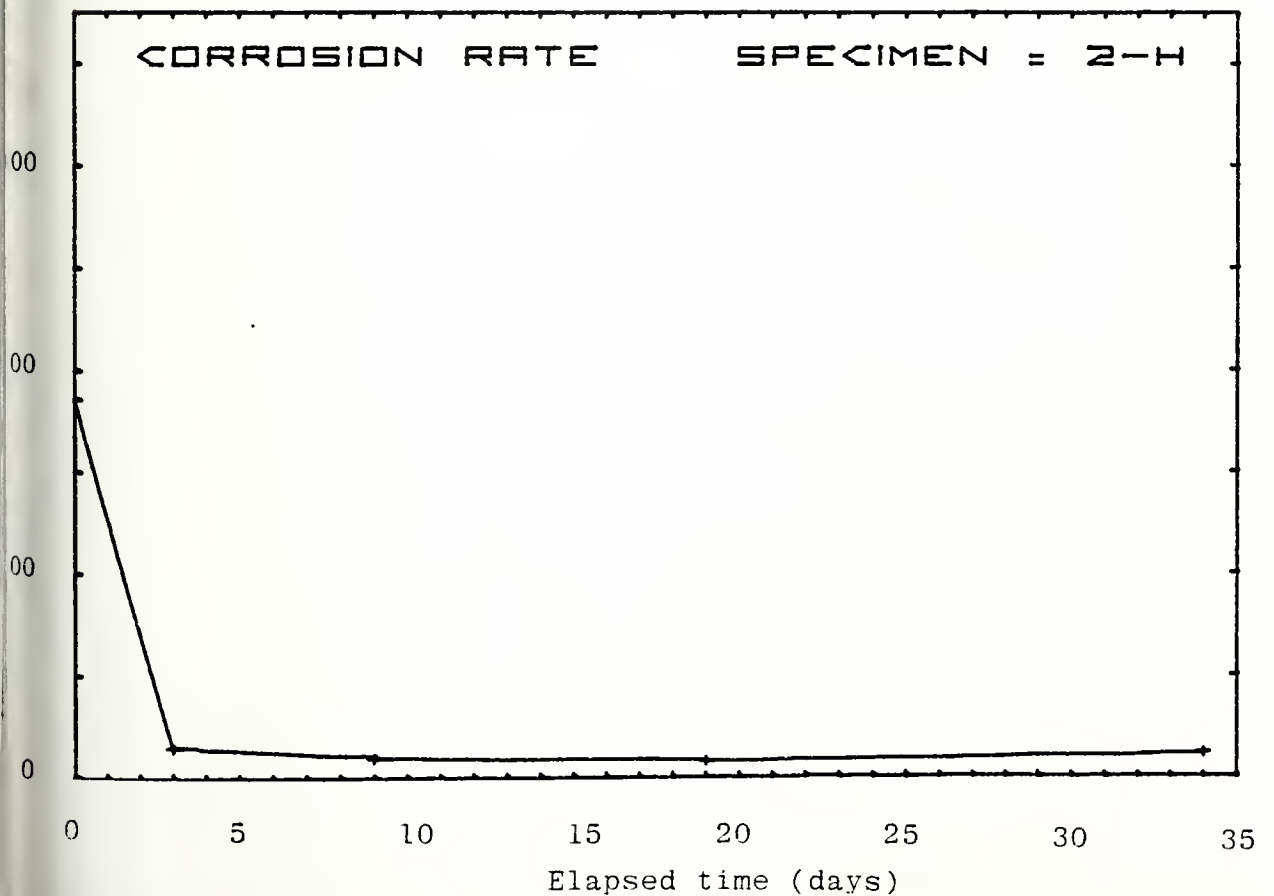
CORROSION RATE SPECIMEN = 2-H
00
00
00
0
0
5
10
15
20
25
30
35
Elapsed time (days)

Figure B-8 (a-e)

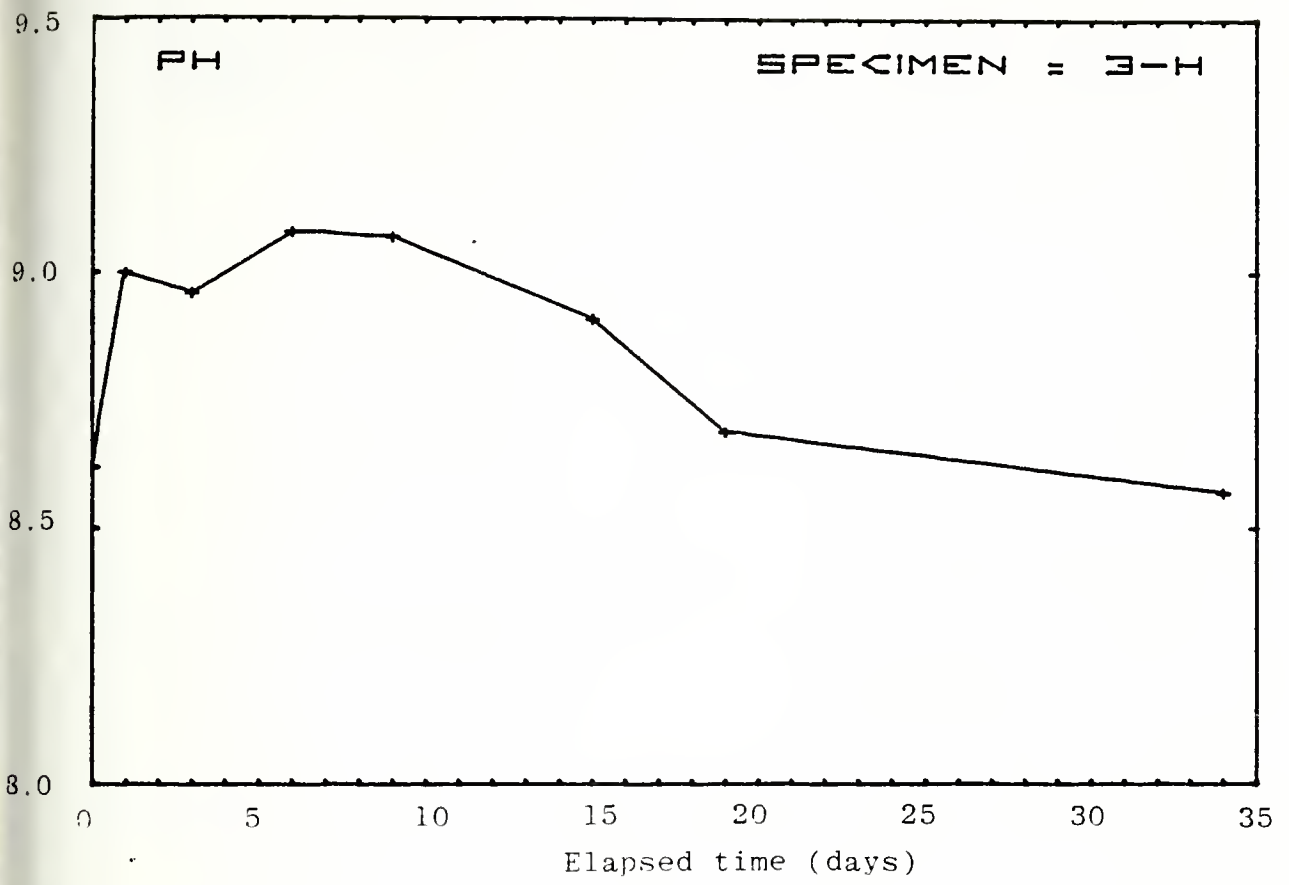
PH
SPECIMEN = 3-H
9.5
9.0
8.5
8.0
0
5
10
15
20
25
30
35
Elapsed time (days)

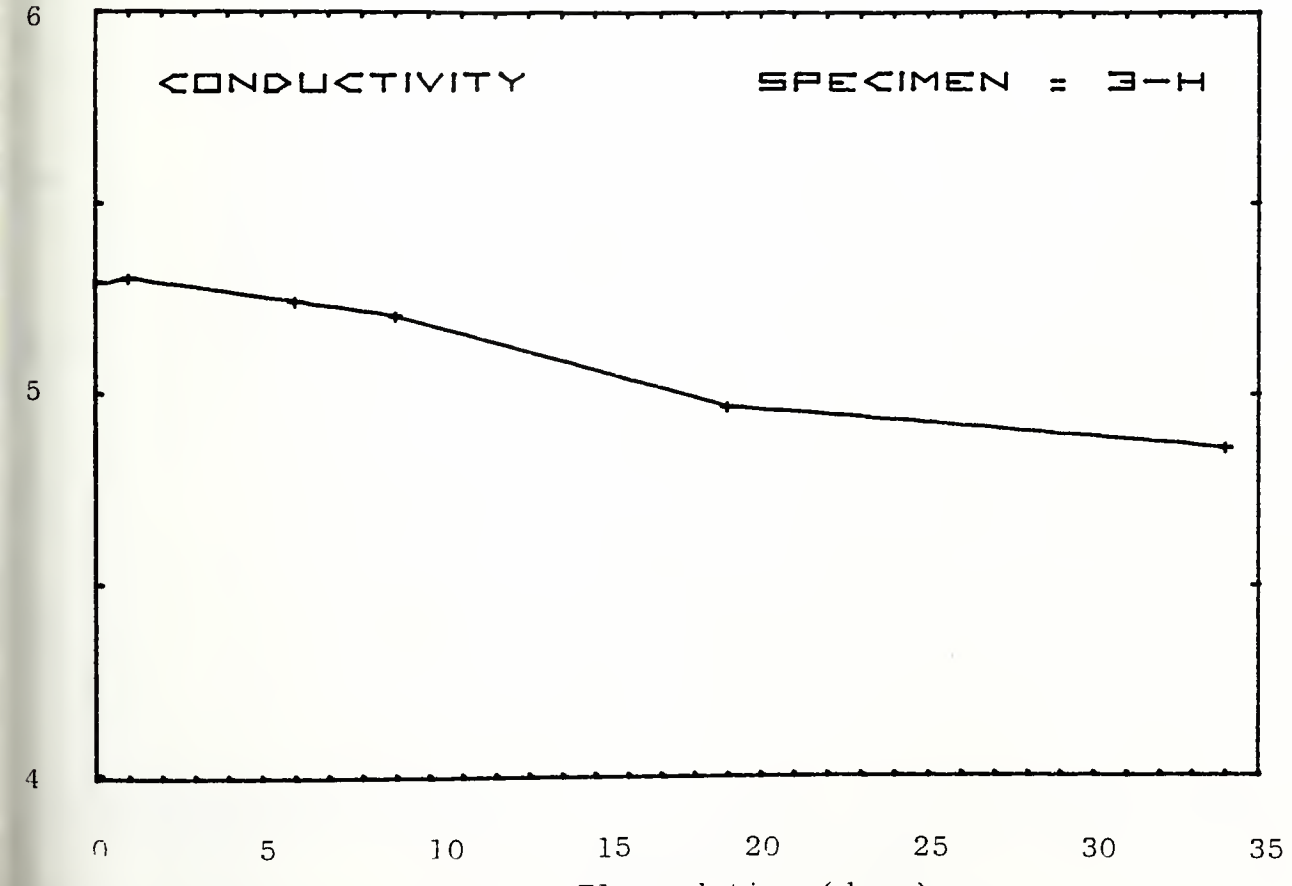
CONDUCTIVITY
SPECIMEN = 3-H
6
5
4
0
5
10
15
20
25
30
35
Elapsed time (days)

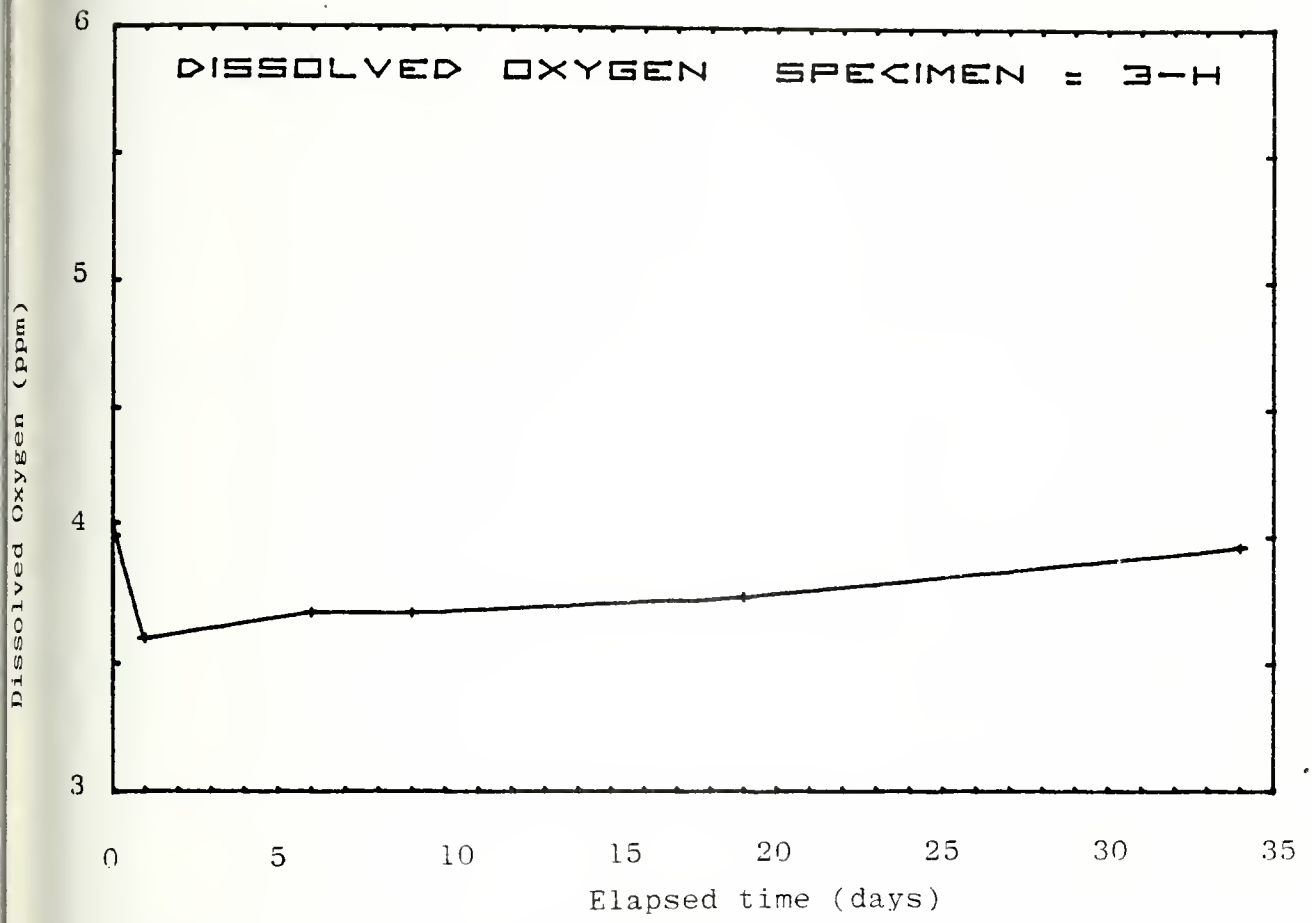
DISSOLVED OXYGEN SPECIMEN = 3-H
Dissolved Oxygen (ppm)
6
5
4
3
0
5
10
15
20
25
30
35
Elapsed time (days)

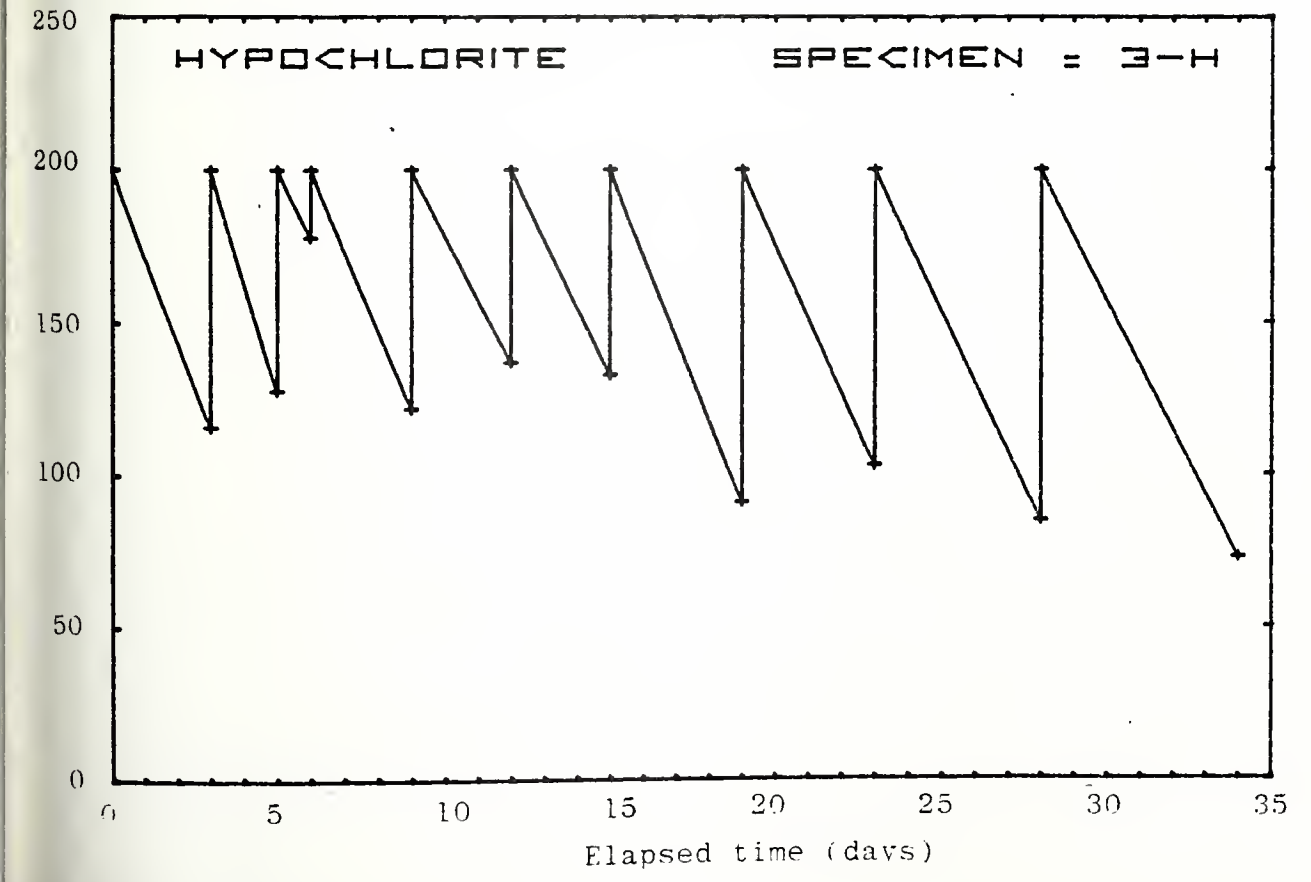
HYPOCHLORITE SPECIMEN = 3-H
250
200
150
100
50
0
0
5
10
15
20
25
30
35
Elapsed time (days)

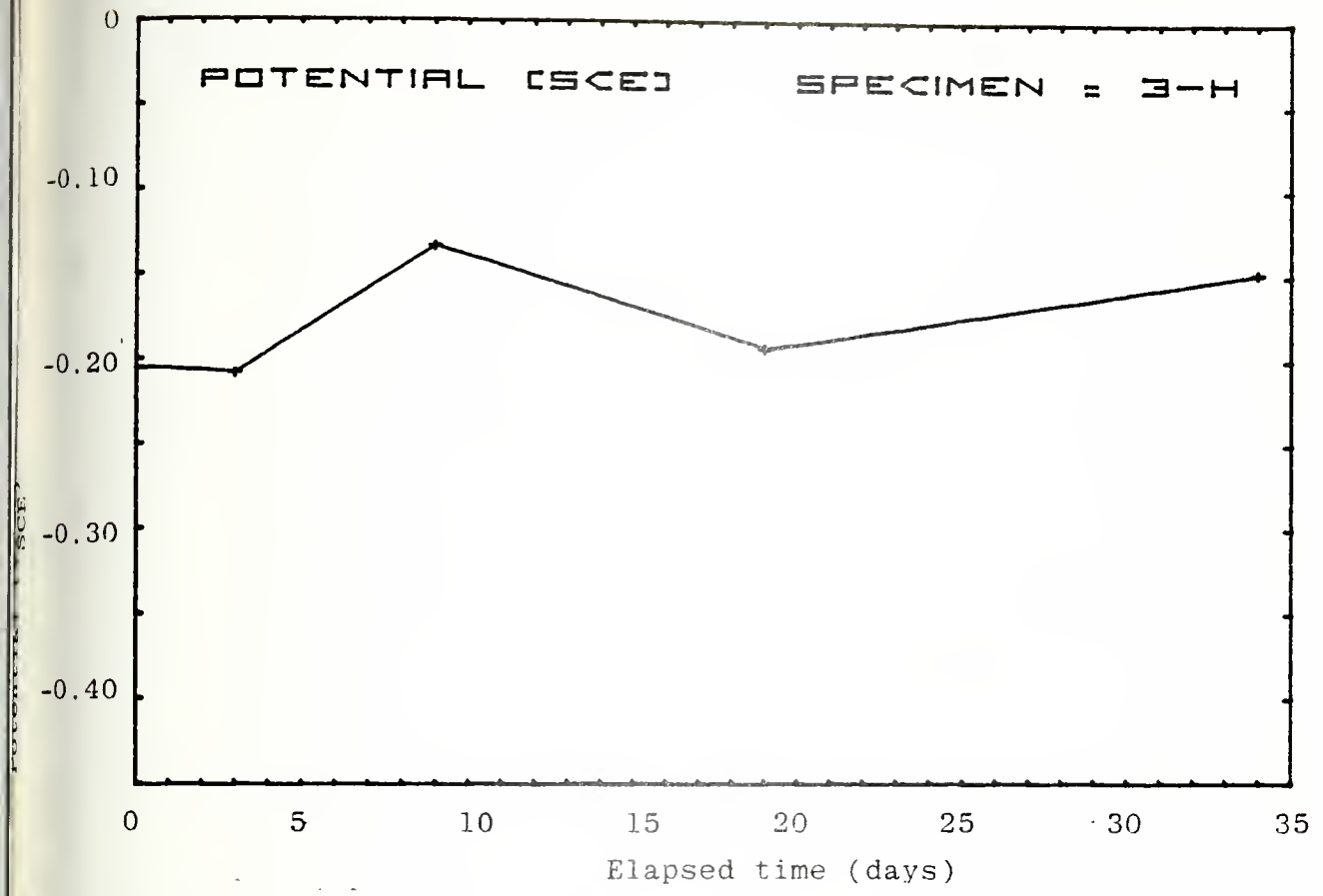
POTENTIAL (SCE)
SPECIMEN = 3-H
0
-0.10
-0.20
-0.30
-0.40
0
5
10
15
20
25
30
35
Elapsed time (days)

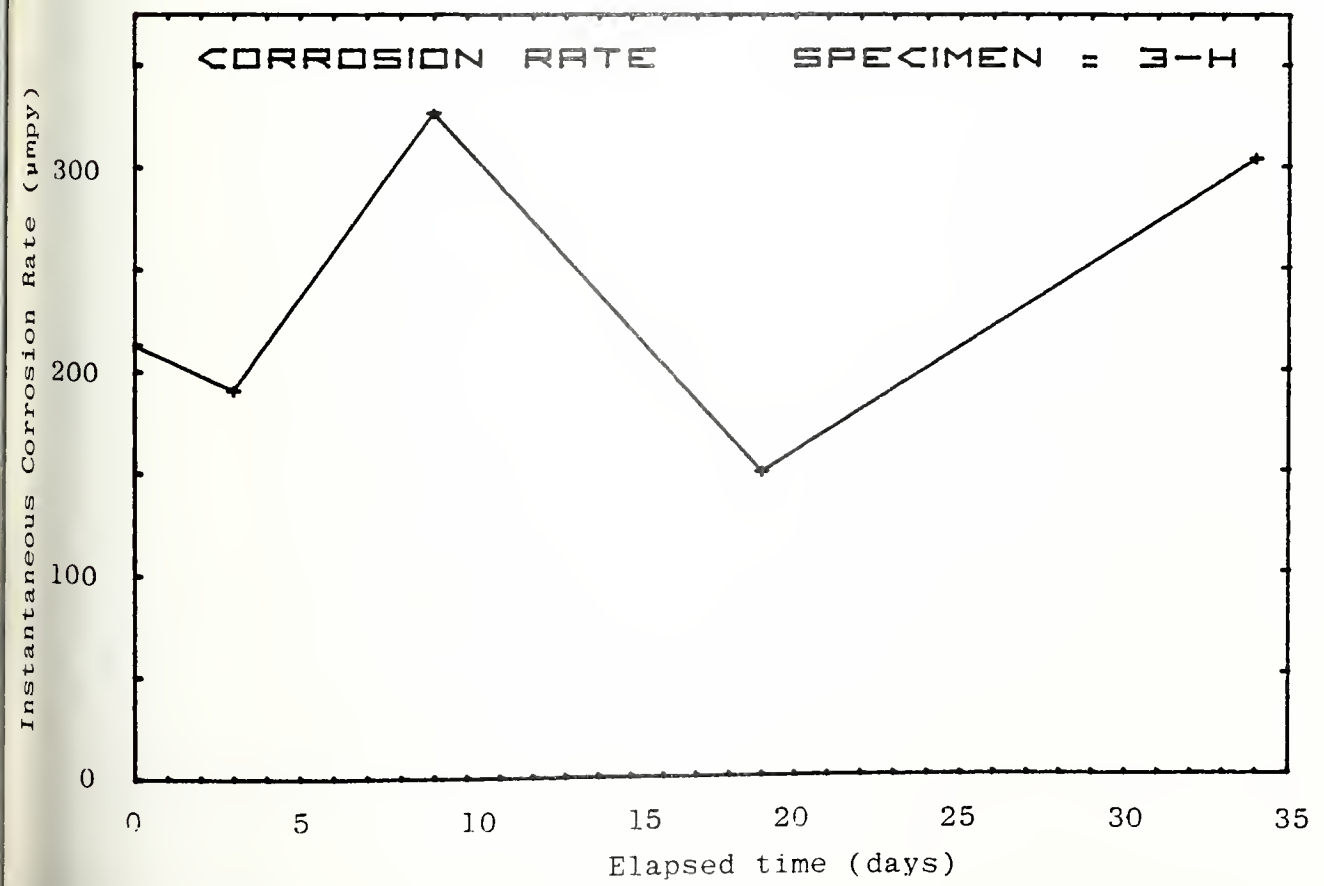
CORROSION RATE
SPECIMEN = 3-H
Instantaneous Corrosion Rate (µmpy)
300
200
100
0
0
5
10
15
20
25
30
35
Elapsed time (days)

Figure B-9 (a-e)

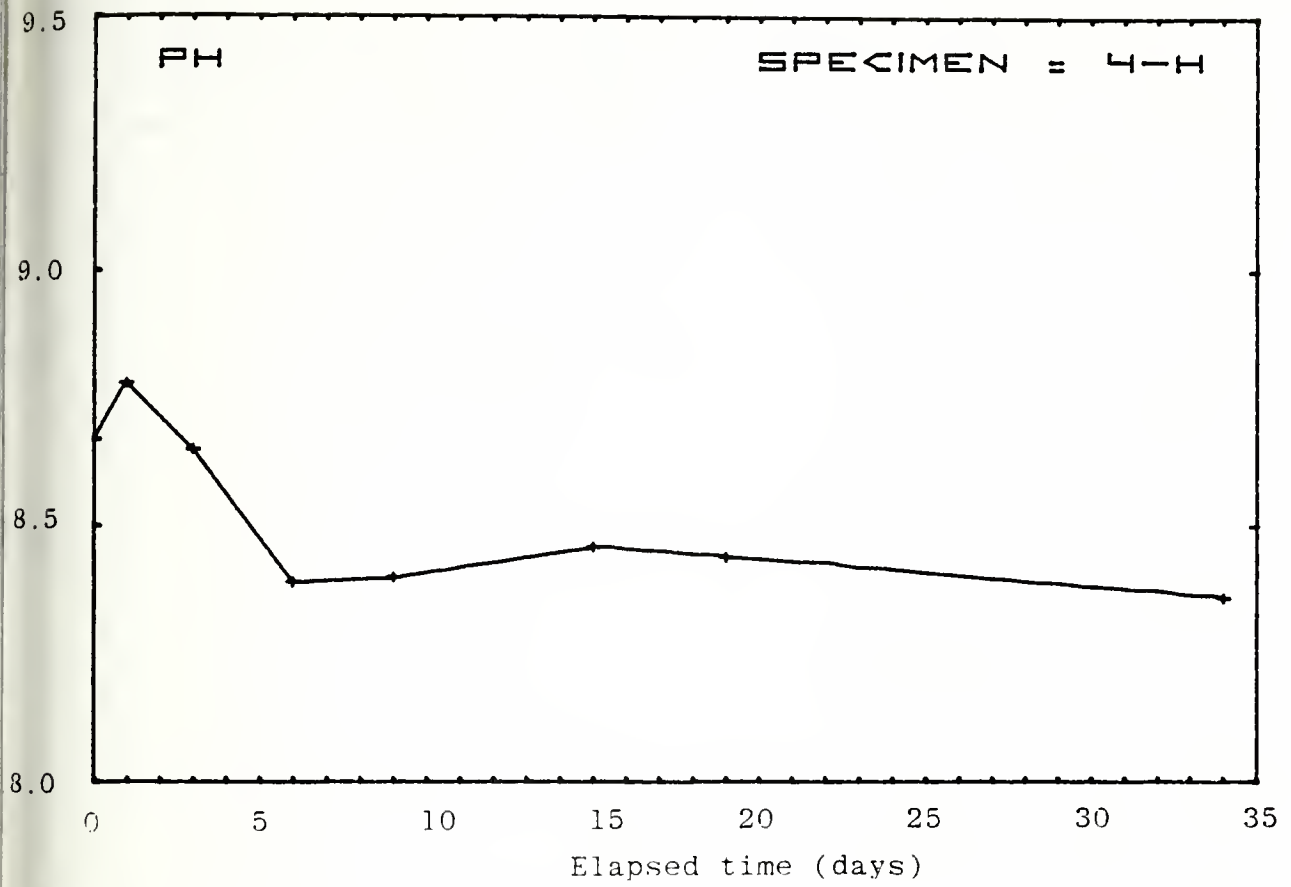
PH
SPECIMEN = 4-H
9.5
9.0
8.5
8.0
0
5
10
15
20
25
30
35
Elapsed time (days)

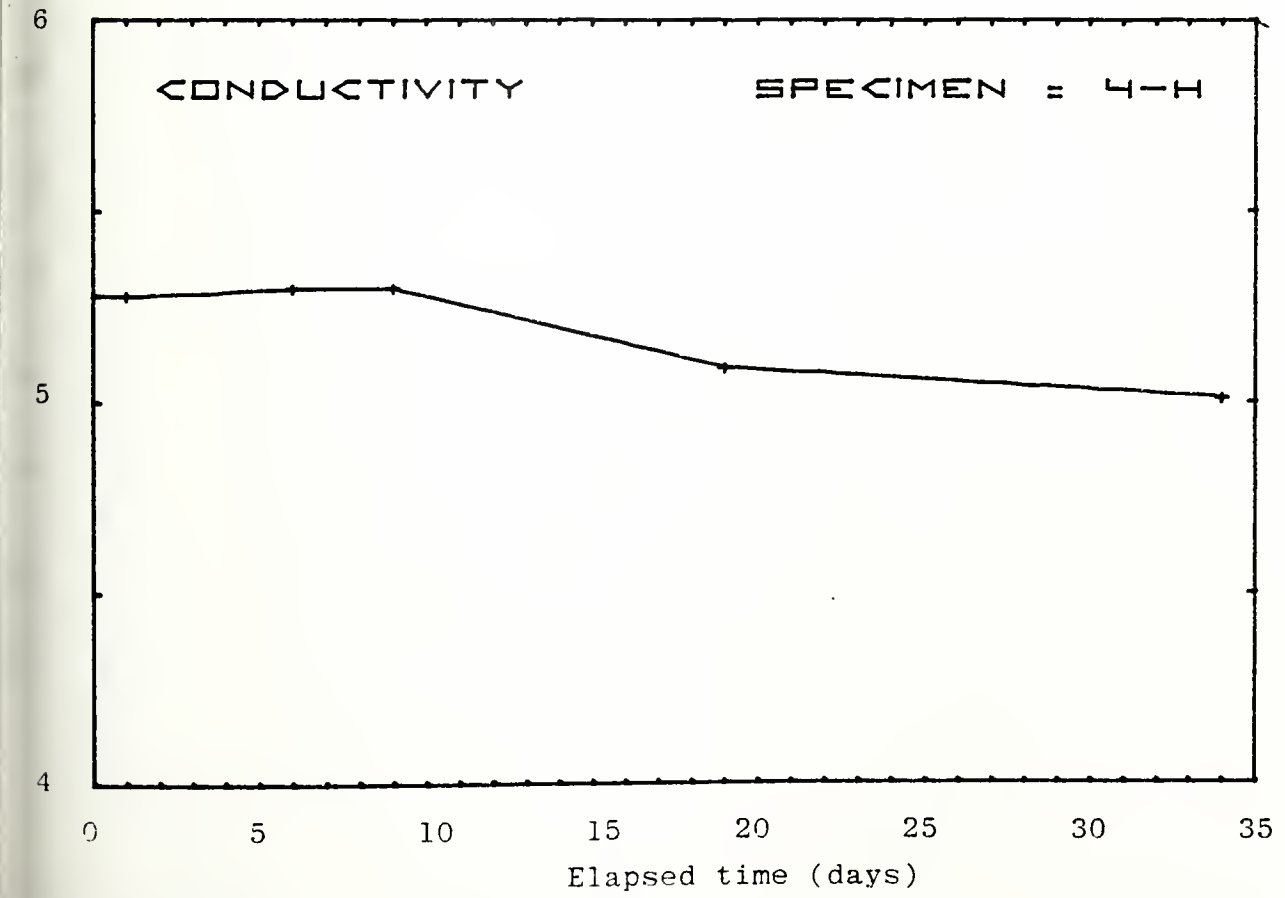
CONDUCTIVITY
SPECIMEN = 4-H
6
5
4
0
5
10
15
20
25
30
35
Elapsed time (days)

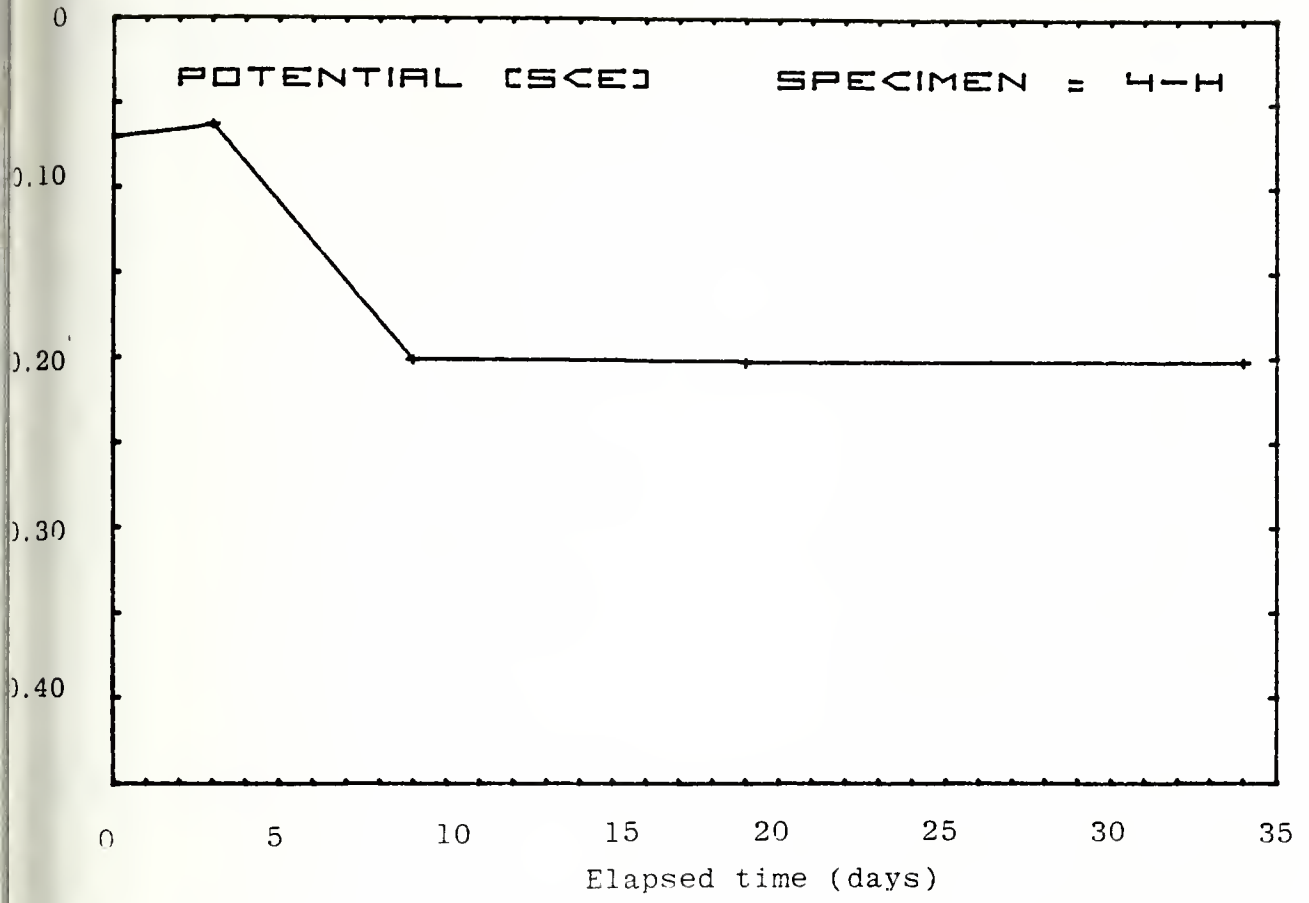
POTENTIAL [SCE] SPECIMEN = 4-H
0
0.10
0.20
0.30
0.40
0
5
10
15
20
25
30
35
Elapsed time (days)

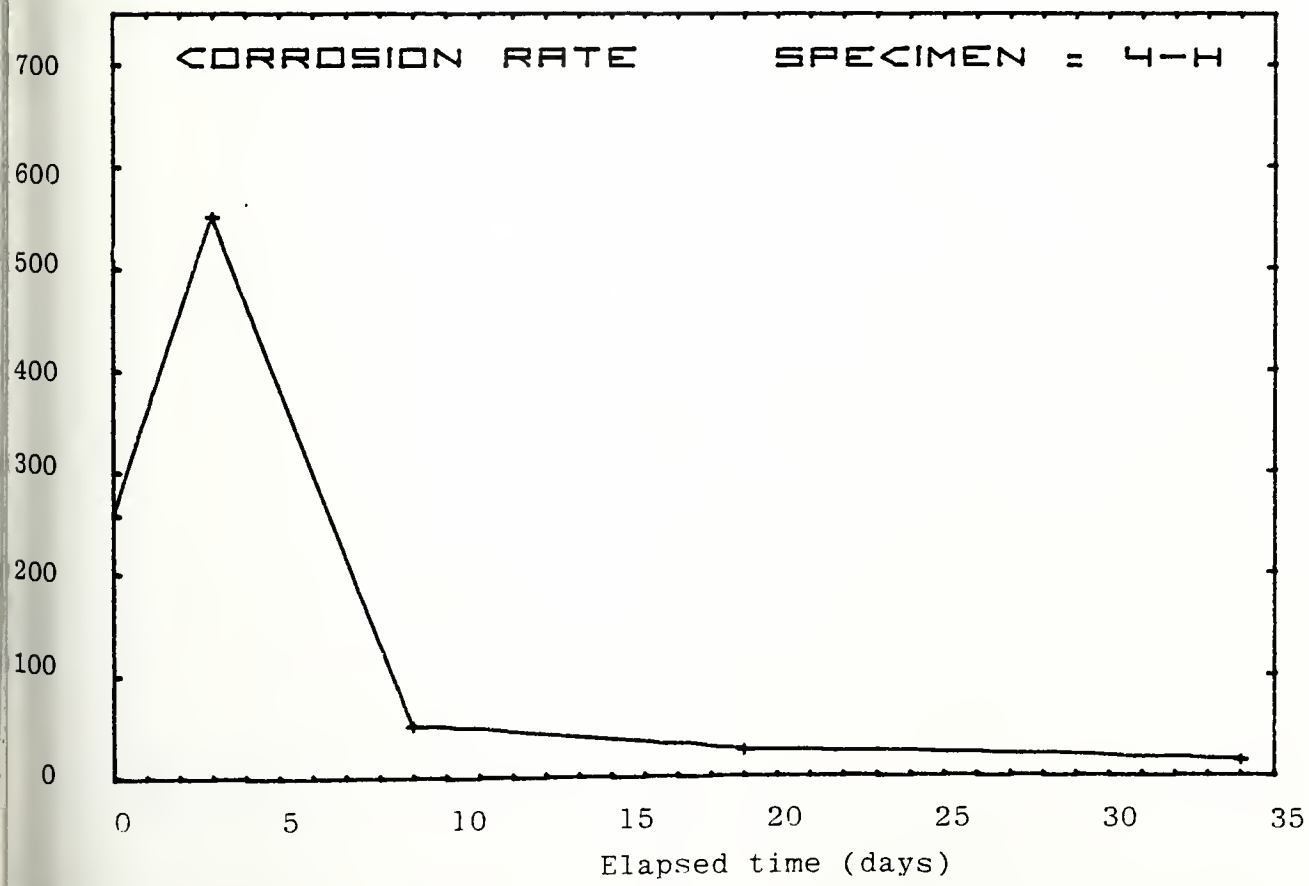
CORROSION RATE SPECIMEN = 4-H
700
600
500
400
300
200
100
0
0
5
10
15
20
25
30
35
Elapsed time (days)

Figure B-10 (a-e)

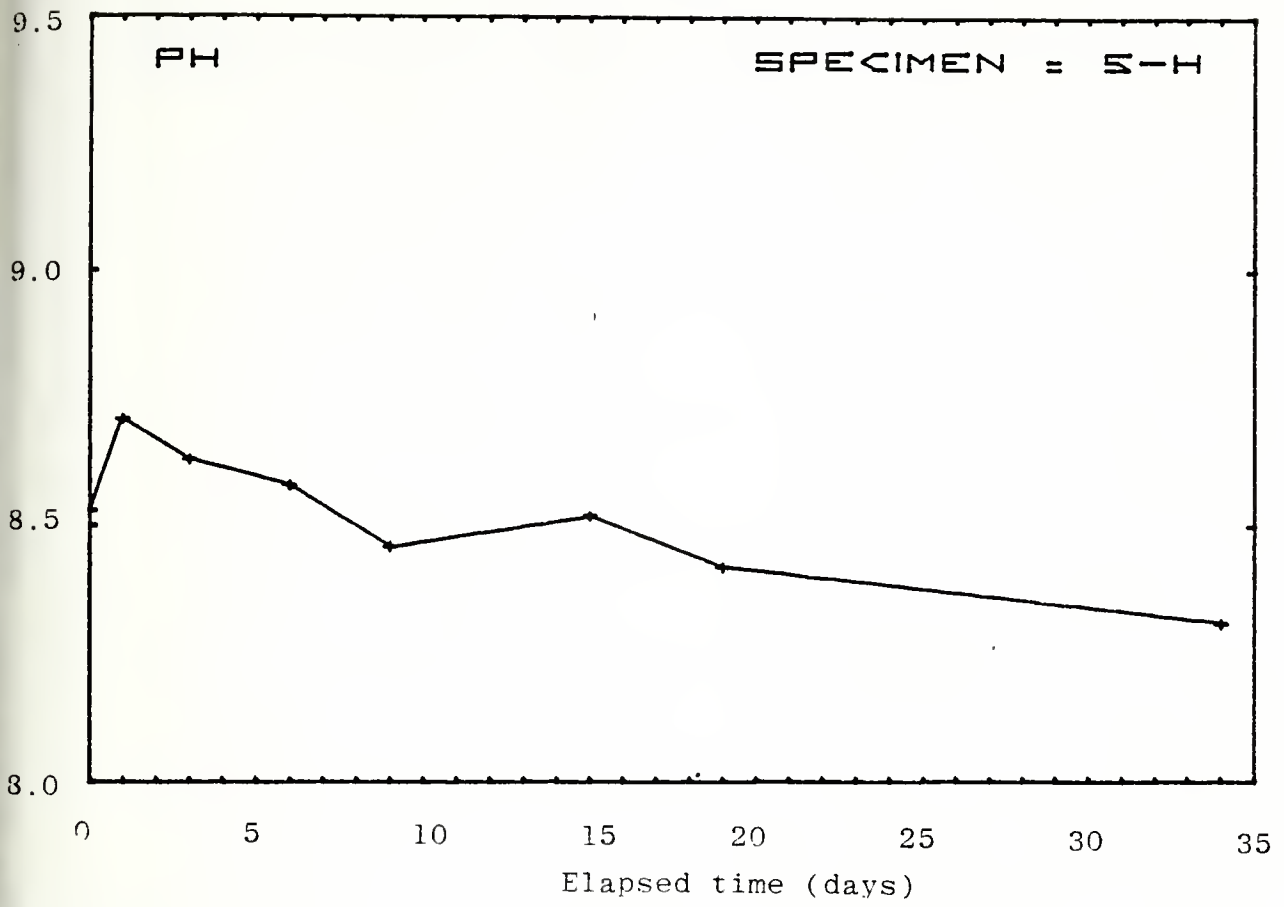

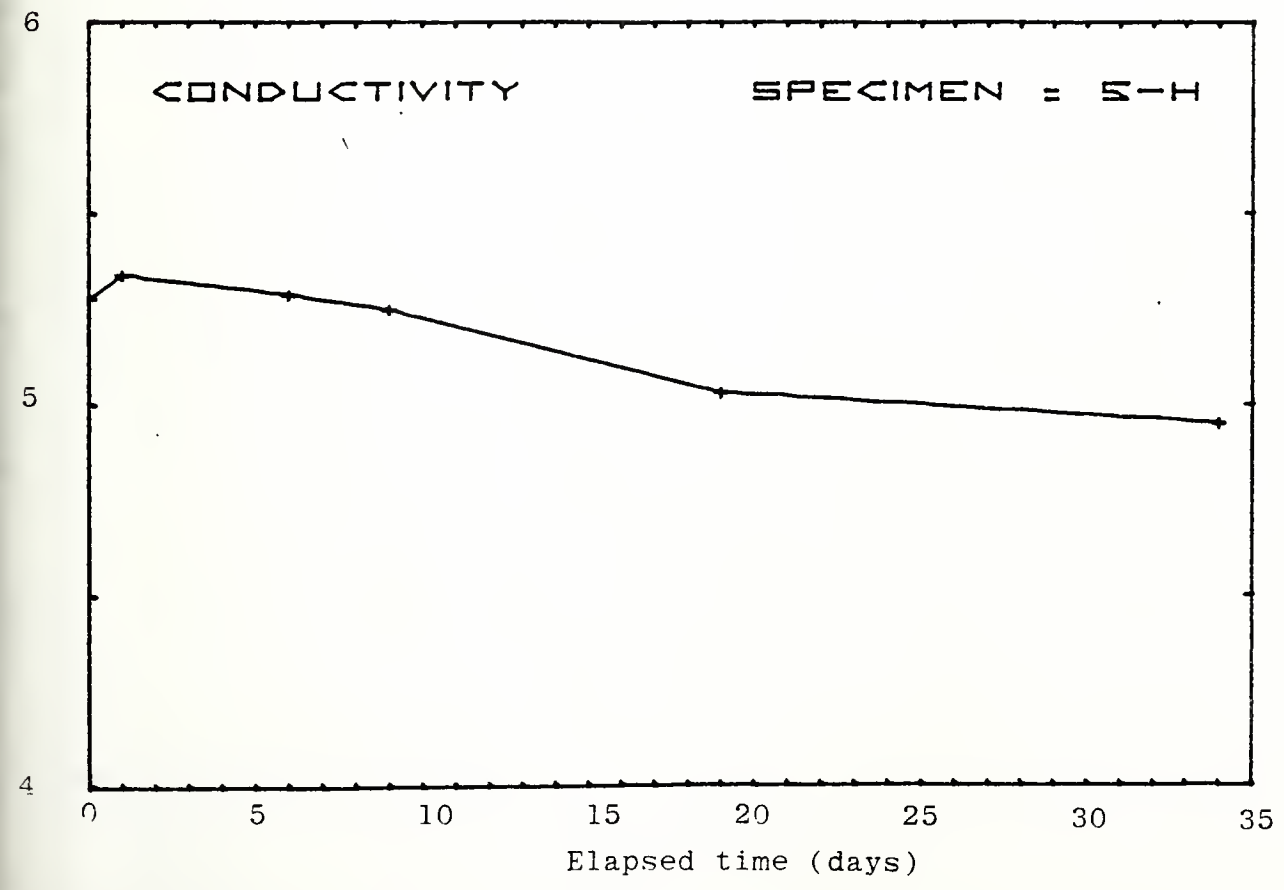

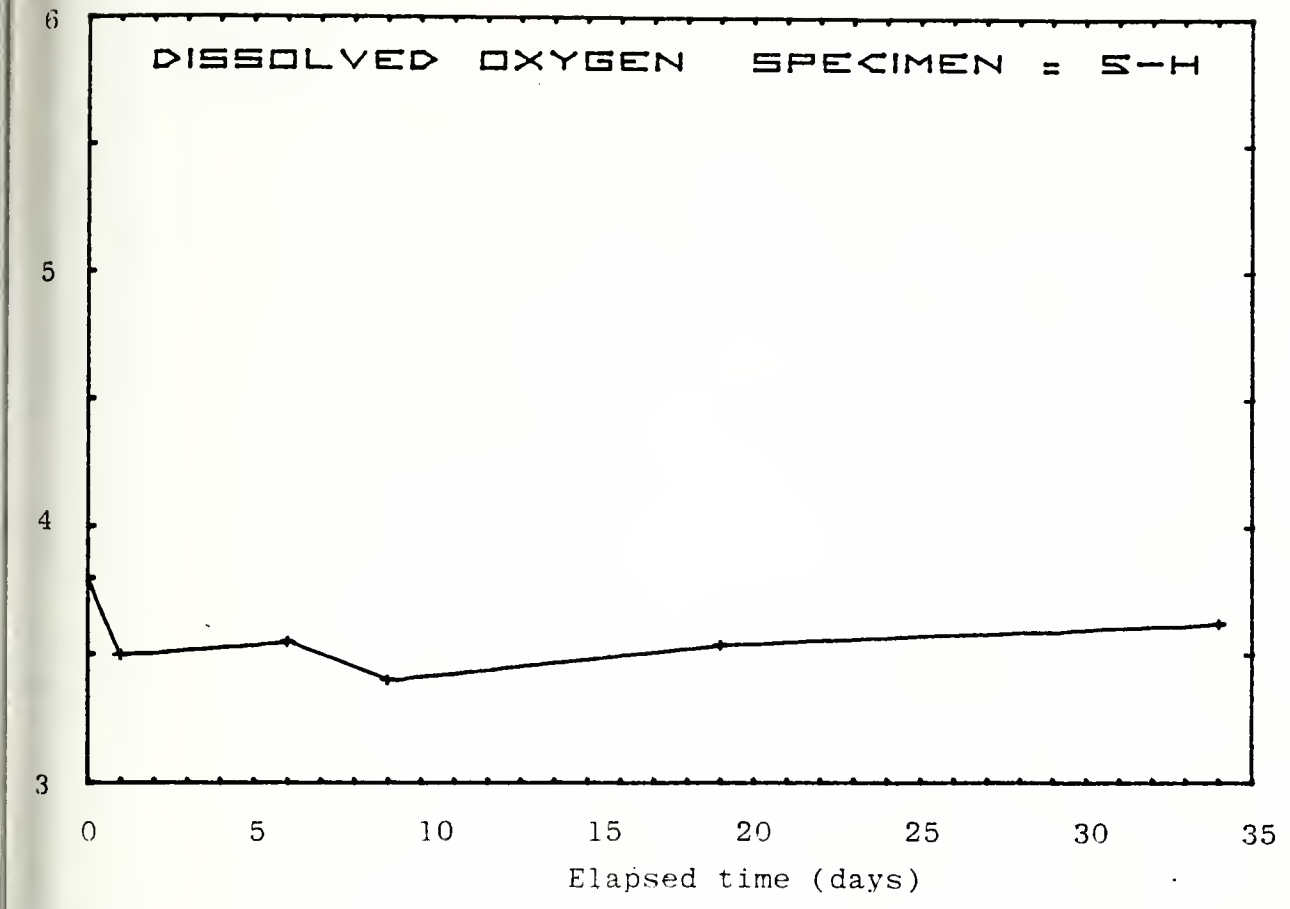
DISSOLVED OXYGEN SPECIMEN = S-H
6
5
4
3
0
5
10
15
20
25
30
35
Elapsed time (days)

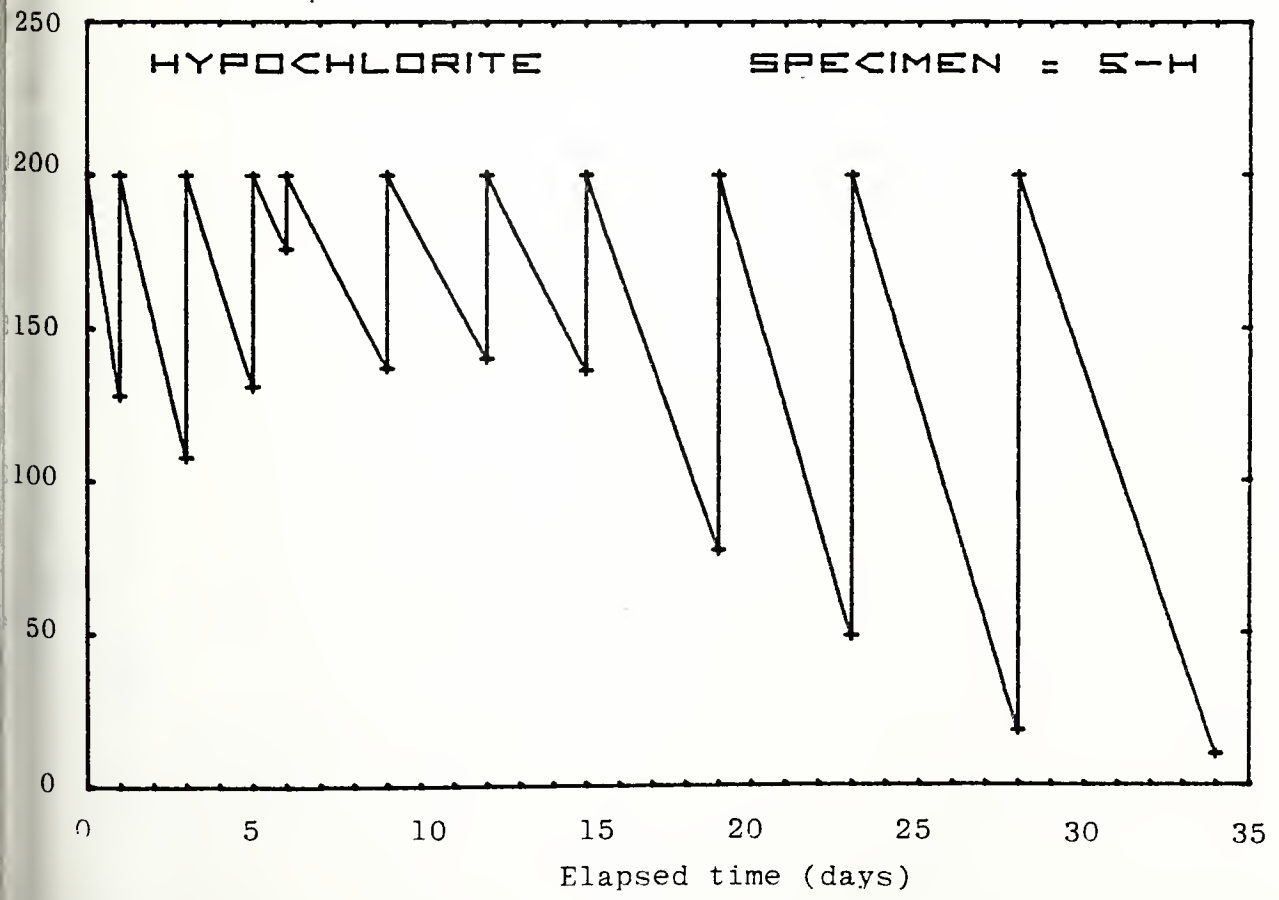
HYPOCHLORITE SPECIMEN = S-H
250
200
150
100
50
0
0
5
10
15
20
25
30
35
Elapsed time (days)

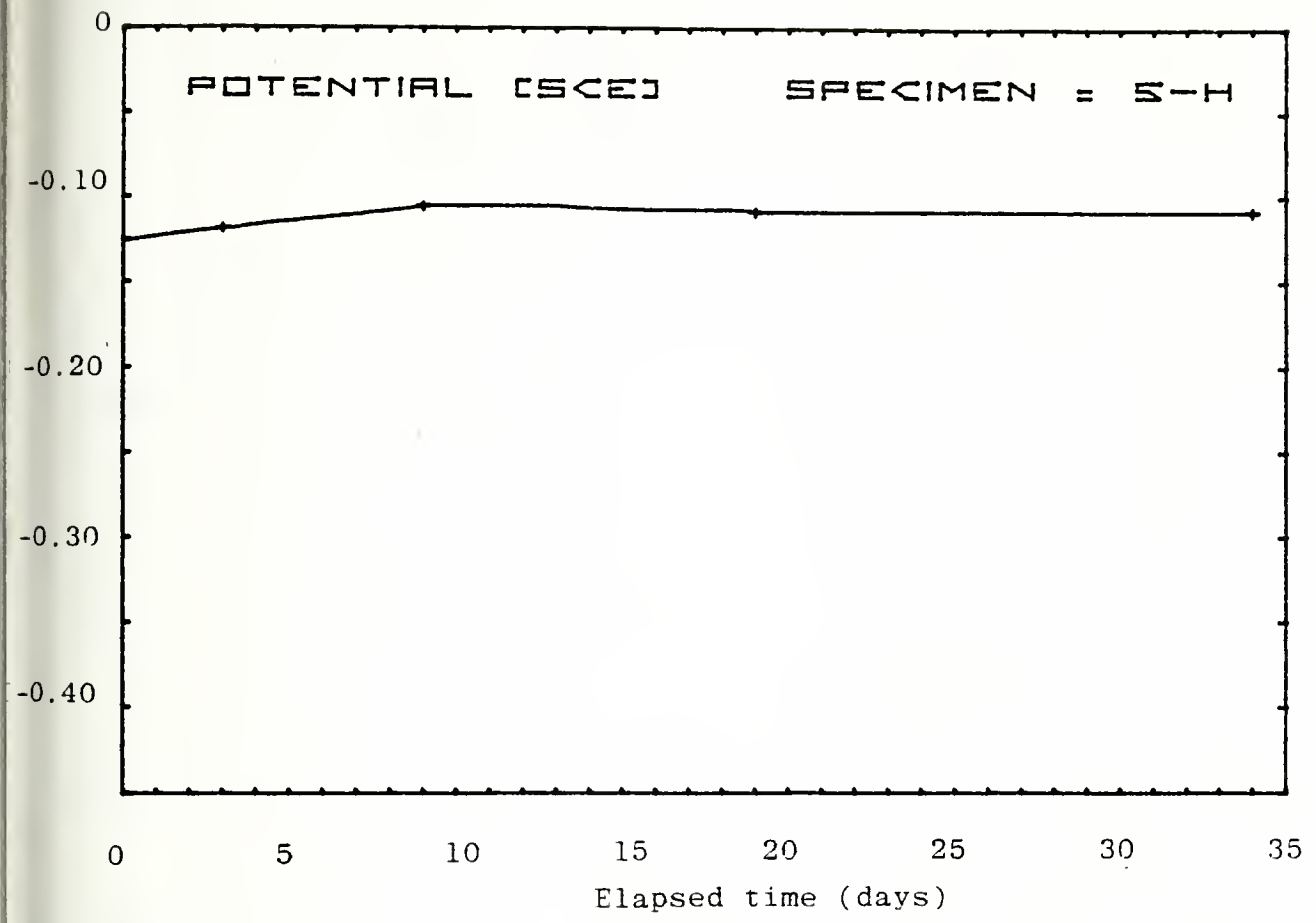
POTENTIAL (SCE)
SPECIMEN = S-H
0
-0.10
-0.20
-0.30
-0.40
0
5
10
15
20
25
30
35
Elapsed time (days)

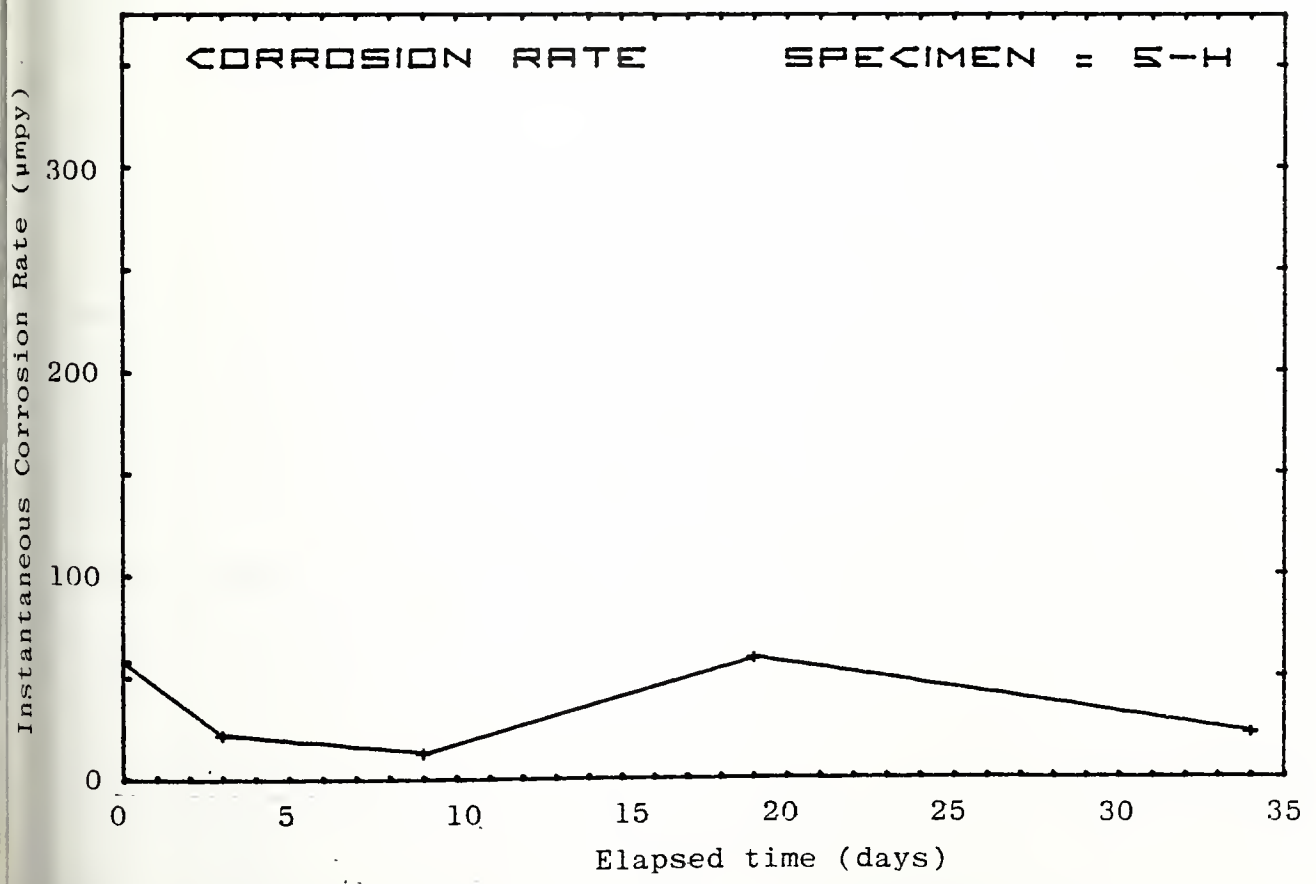
CORROSION RATE
SPECIMEN = S-H
Instantaneous Corrosion Rate (µmpy)
300
200
100
0
0
5
10
15
20
25
30
35
Elapsed time (days)

APPENDIX C

ELECTROCHEMICAL POLARIZATION: METHODOLOGIES AND DATA

I. INTRODUCTION

Electrochemical techniques of corrosion measurement are currently being used extensively by corrosion scientists, primarily due to the rapidity with which these measurements can be made. Long-term corrosion studies, such as mass-loss determinations, may take days or weeks to complete, while an electrochemical experiment will generally take only a few hours. The rapidity of electrochemical measurements is especially useful for those metals or alloys which are highly corrosion resistant.

There are several methodologies employing electrochemical techniques that are used to evaluate and compare metal-electrolyte combinations. For qualitative comparisons of the corrosion process, the technique employed is potentiodynamic polarization. For the interaction of two or more metals in electrical contact, there are galvanic corrosion measurements. To determine the absolute corrosion rate of a metal in a corrosive environment, the corrosion current is needed. This can be determined either from Tafel plot slopes or from linear polarization measurements made near the corrosion potential. Each of these techniques will be discussed briefly in terms of theory and practice.

II. POTENTIODYNAMIC POLARIZATION MEASUREMENTS (PDP)

When a metal is placed in an electrolyte, both oxidation and reduction reactions occur at its surface. After a sufficient period of time, the metal and the electrolyte come to equilibrium with each other and there is no net current flow, i.e., the rate of oxidation equals the rate of reduction. When this equilibrium is obtained, the specimen assumes a potential relative to some arbitrary reference electrode, called the corrosion potential, E_{corr}. Therefore, at the corrosion potential, two types of reactions are porceeding:

1. Metal $\longrightarrow$ (Metal ion)$^{n+}$ + n electrons

   (called oxidation, or "corrosion")

2. (Electron acceptor) + n electrons $\longrightarrow$
   (oxidized form)

   (Electron acceptor $\cdot$ n electrons)
   (reduced form)

   (called reduction or "plating")

Reactions 1 are termed "oxidation reactions" and occur on anodes. These are the corrosion reactions. Reactions 2 are termed "reduction reactions" and usually involve the reduction of the solvent, such as the liberation of hydrogen from an acidic solution or reduction of oxygen to hydroxide ion in aerated basic solutions; they occur at cathodes.

If a voltage is imposed to force the metallic specimen away from the corrosion potential, the specimen is said to

be polarized. For example, if a voltage is applied so that the specimen reduction potential becomes more positive than the corrosion potential, the coupon is no longer at equilibrium (with the anodic and cathodic reactions occuring at equal rates) but now current flows and the anodic reaction predominates over the cathodic reaction. The specimen is anodically polarized and corrosion of the metal is accelerated.

A potentiodynamic polarization study is the characterization of a metal specimen in an electrolyte by its potential-current relationship. The method involves scanning the specimen potential (with respect to a reference electrode) and measuring the current passed in the system. If scanned in the anodic direction, the specimen is forced by the imposed potential to be an anode, and so oxidation (corrosion) reactions will prevail. The specimen will corrode and may react with the solvent in subsequent reaction to become passivated with a non-conducting film of reaction products (such as oxide). A complete current-potential plot can be obtained in a short time, i.e., hours, whereas a coupon immersed in an electrolyte may take many days or weeks to show its corrosion behavior. An idealized current-potential diagram for a material which shows passivity is shown in figure C-1a. Shown are points denoted by numbers which correspond to certain phenomena taking place.

With knowledge of the corrosion characteristics of metals in a given environment, the metals studied can be compared rationally, using this information to put the specimens in

relative priority as to corrosion resistance and selecting the best for further long-term studies. Note that this method is an artificial method of corroding a specimen in a given environment. Its utility lies in the rapidity of the method, but it must not replace or be used solely to predict how a specimen will corrode in the long term, since other mechanisms may prevail.

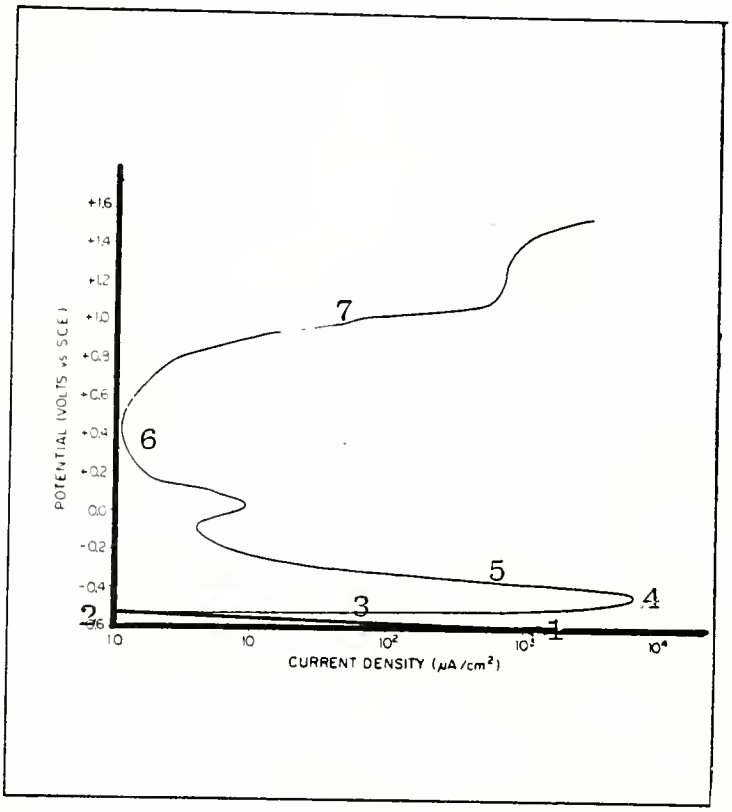

Figure C-1a. Idealized current potential diagram for a material showing passivity. Reference numbers are defined as follows:

1. the cathodic current predominates
2. the system is at E_{corr} - no net current flow.
3. the anodic current predominates
4. critical current density - primary passive potential
5. passivation begins
6. film formation complete - passive region
7. film ruptures - transpassive region

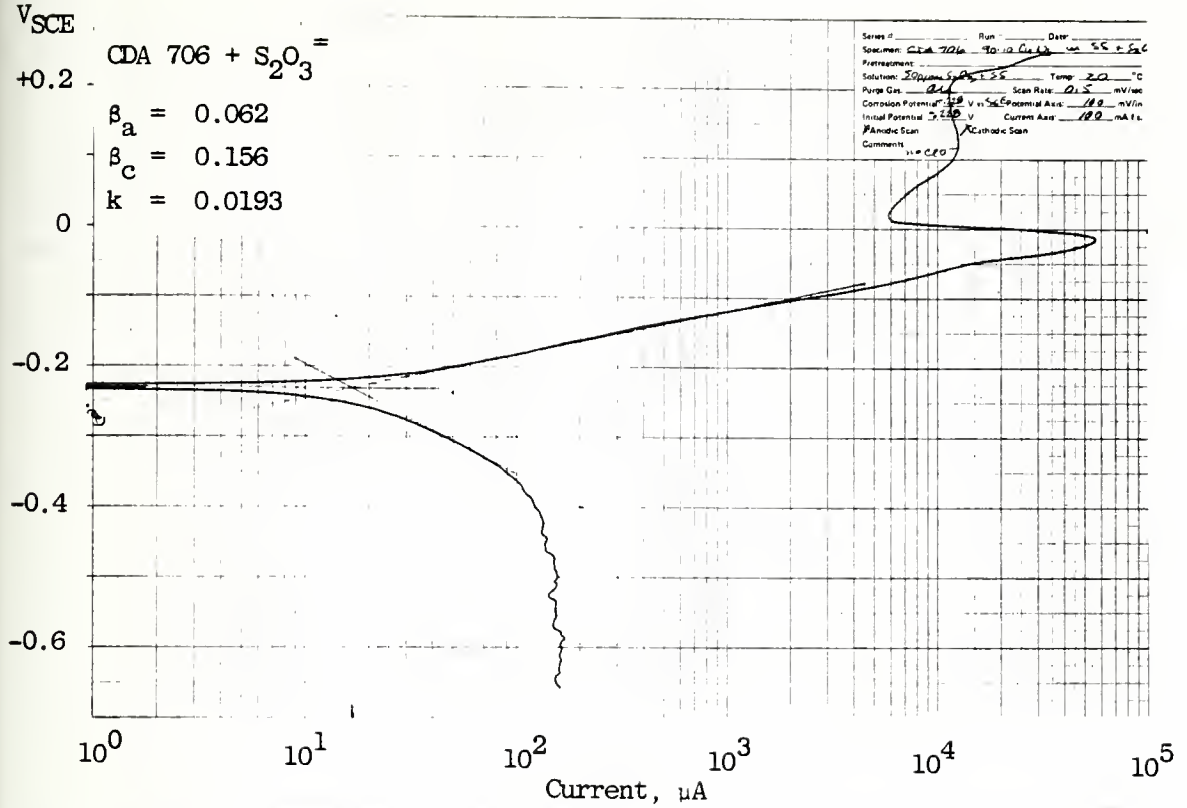

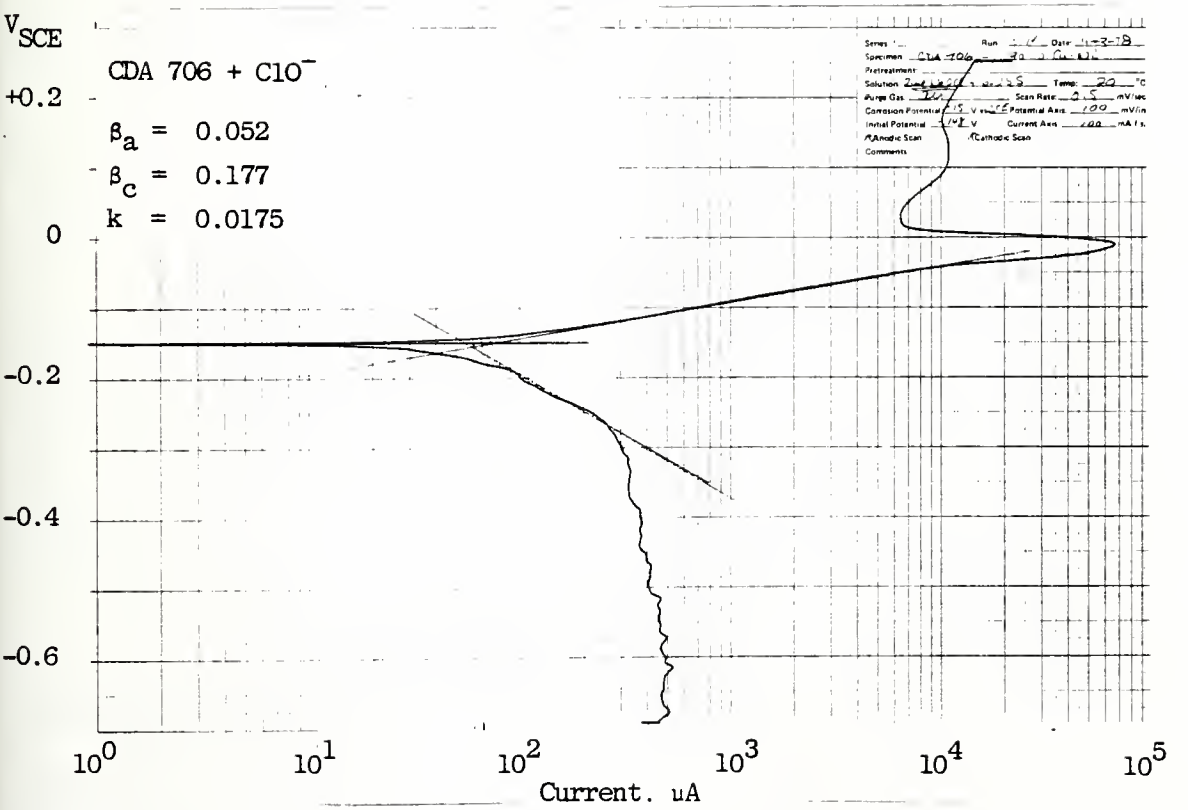

Figure C-1b. Typical potentiodynamic polarization plots of potential vs. current. The top figure is CDA 706 (90-10 copper-nickel) run in synthetic seawater + 50 ppm sodium thiosulfate. The lower figure is the same material run in synthetic seawater + 200 ppm sodium hypochlorite.

III. GALVANIC CORROSION MEASUREMENTS

In a real-life situation, such as a ship in an electrolyte (the ocean), galvanic processes tend to occur. This requires the presence of two or more dissimilar metals (or even two specimens of the same metal in different states, e.g., the active and passive states of stainless steels) connected in an electrolyte. The metal with the more negative reduction potential becomes the anode and corrodes. The other becomes the cathode and is protected from corroding by the "sacrificial" corrosion of the more active anode. This is the principle behind using active metal (zinc, aluminum, magnesium) anodes to protect ship hulls. For recent information on sacrificial anodes, see reference 61.

As in the potentiodynamic polarization measurements, the galvanic coupling of metals may be simulated using electrochemical techniques. Typically, only one metal is immersed in the electrolyte. An inert auxilliary electrode is also inserted and a constant current source (galvanostat) is attached. Since the current flow is constant, the mass-loss for the specimen can readily be calculated from Faraday's Law if the total current-flow time.

$$\text{Mass-loss} = e\ I\ t/F \qquad \text{(C-1)}$$

where e is the equivalent weight of the metal; I is the current in Amperes; t is the time of current flow in seconds; and F is the Faraday constant, 96,484 coulombs/equivalent.

Observations may also be made as to the mode of corrosion by corroding the galvanic specimens for varying lengths of time at constant current, then examining the specimen by microscopic means.

Again, the disadvantage of this electrochemical method is that it does not necessarily represent the real world. It is a more rapid method than IML but it is doubtful that there is ever achieved a truly constant current in galvanic couples. In fact, it is probably more accurate to suggest that after some long period of time, a constant potential difference between the cell members is achieved. Note that this situation can also be modelled electrochemically using a potentiostat to maintain a constant potential between the specimen and some reference electrode. This is the basis for the PSP runs in this research.

IV. TAFEL PLOTS [57]

In order that Tafel plots be discussed, it is necessary first to consider the concepts of activation and concentration polarization. A brief discussion of each of these topics appears below.

A. ACTIVATION POLARIZATION

If the potential of an electrode is displaced from its reversible potential, the velocity of the rate-controlling process in the transformation of reactants to products is changed. This change in rate of reaction is equivalent to a reduction in the activation energy for the process and is

therefore called "activation polarization". An example of this kinetic effect is the reduction of H^+ ion to H_2 gas at a metal surface in acidic media. If a piece of platinum is immersed in strong acid, there is developed a potential relative to some arbitrary reference electrode. No current flows, hence the rate of oxidation is identical to the rate of reduction. This exchange reaction rate may also be expressed in terms of current density, as

$$R_{red} = R_{oxid} = i_o/nF \qquad (C-2)$$

where R is the rate of the reaction and i_o is the "exchange current density". It varies with the metal used and must be determined experimentally.

If a potential is applied to the platinum from an external voltage source, such that the reduction of H^+ ions occurs, and also that the chemical reaction rate is controlled by a slow step requiring an activation energy, then the current flowing obeys the general relationships (at constant temperature),

$$i_{oxid} = i_o e^{\gamma/\beta oxid}$$

$$i_{red} = i_o e^{-\gamma/\beta red}$$

where γ is the magnitude of the polarization[1] and β_{oxid} and β_{red} are constants.

---

[1]Polarization is the displacement of the electrode potential away from its reversible value resulting from passage of a net current. $\gamma = (E_{applied} - E^o)$.

Rearranging and taking logarithms we have

$$\gamma = \beta_a \log_{10}(i_{oxid}/i_o), \text{ and } \beta_a = 2.3\,\beta_{oxid} \quad \text{(C-4a)}$$

$$\gamma = -\beta_c \log_{10}(i_{red}/i_o), \text{ and } \beta_c = 2.3\,\beta_{red} \quad \text{(C-4b)}$$

where β_a and β_c are called "Tafel constants". It is to be noted that the equation of (C-4a) and (C-4b) are equivalent to

$$\gamma = \beta_a(\log i_{oxid} - \log i_o) \quad \text{(C-5a)}$$

$$\gamma = -\beta_c(\log i_{red} - \log i_o) \quad \text{(C-5b)}$$

so that if γ vs. log i is plotted, the slope of the line obtained is β. This is shown schematically in figure C-2 for the hydrogen half cell.

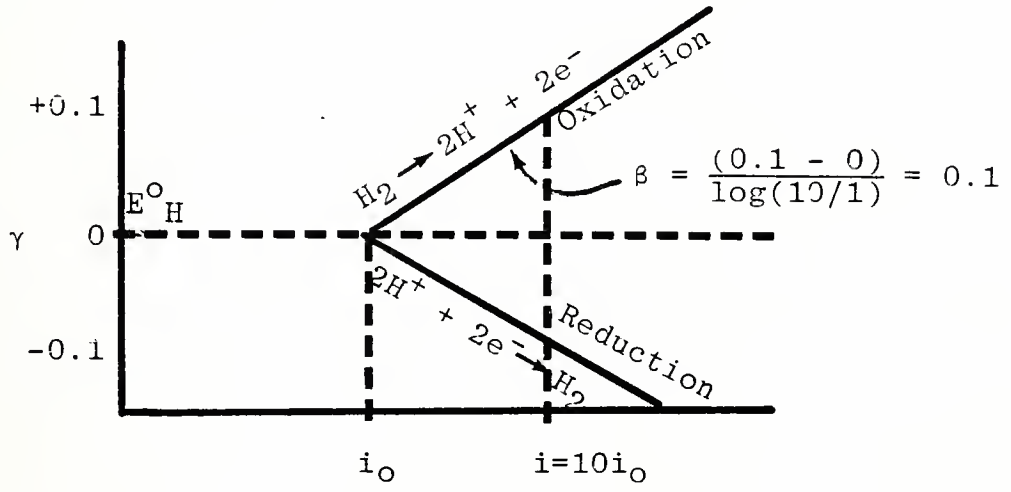

Figure C-2. Graphical determination of Tafel constants, β_a and β_c, from a plot of polarization vs. current density.

When the external potential is applied, the equilibrium is disturbed and the reaction rates R_{oxid} and R_{red} are no longer equal. Experimentally, however, one can measure only the net current flowing, which is the difference between R_{oxid} and R_{red}. In terms of current densities, this is

expressed as

$$i_{net} = i_{oxid} - i_{red} \qquad (C\text{-}6)$$

As the polarization becomes large, i.e., in the negative direction, it is apparent that i_{net} approaches i_{red}. Near the equilibrium potential, i_{oxid} is comparable to i_{red}, and deviation from the linear Tafel relationship occurs due to the considerable contribution to the net current density by the other electrode process. Therefore, Tafel slopes must be measured well away from the equilibrium potential.

B. CONCENTRATION POLARIZATION

At high reduction rates, the electrolyte becomes depleted of reducible ions. Species are generated which cannot be removed from the electrode surface at a sufficiently rapid rate. At this limit, diffusion through the electrolyte controls the reaction rate. The current density representing this limiting rate is i_L and corresponds to the maximum rate of reduction possible for a given system. Mathematically,

$$i_L = (D\ nF\ C_B)/X \qquad (C\text{-}7)$$

where D is the diffusion coefficient, C_B is the concentration of ions in the bulk solution, n is the number of electrons transferred in the redox reaction, F is the Faraday constant, and X is the thickness of the diffusion layer [62]. For a system with no activation polarization,

$$\eta_c = (2.3RT/nF)\log_{10}(1 - (i/i_L)) \qquad (C\text{-}8)$$

A schematic plot of polarization vs. current density for a system exhibiting concentration polarization is shown in figure C-3.

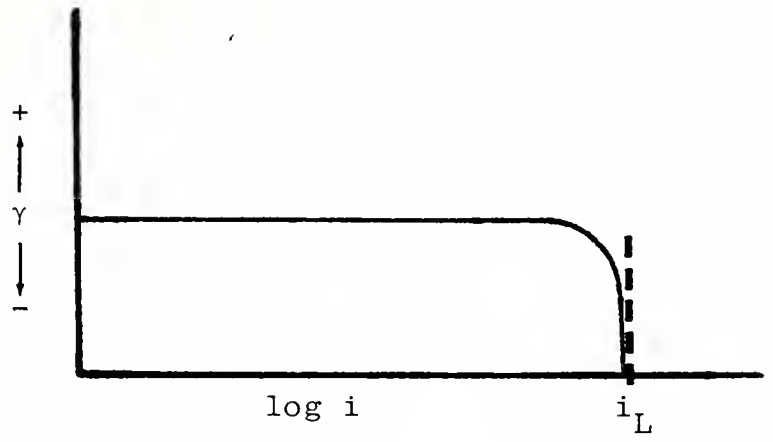

Figure C-3. Polarization vs. current density for a system exhibiting concentration polarization.

C. COMBINED POLARIZATION

When an external voltage source is applied to a metal coupon immersed in an electrolyte, both activation polarization and concentration occur. Activation polarization predominates at low reaction rates (low current densities) and concentration polarization predominates at high reaction rates (high current densities). The total polarization, γ_T, is the sum of γ_{act} and γ_{conc}.

For anodic dissolution (oxidation) of the metal coupon, concentration polarization is not a major concern since there is essentially an infinite supply of metal to be converted to ions. Therefore,

$$\gamma_{oxid} = \beta_a \log(i/i_o). \qquad \text{(C-9)}$$

For the cathodic reduction process, concentration polarization becomes important at high current densities, and hence,

$$\gamma_{red} = -\beta_c \log(i/i_o) + (2.3RT/nF)\log(1 - (i/i_L)) \quad (C-10)$$

This is shown schmatically in figure C-4.

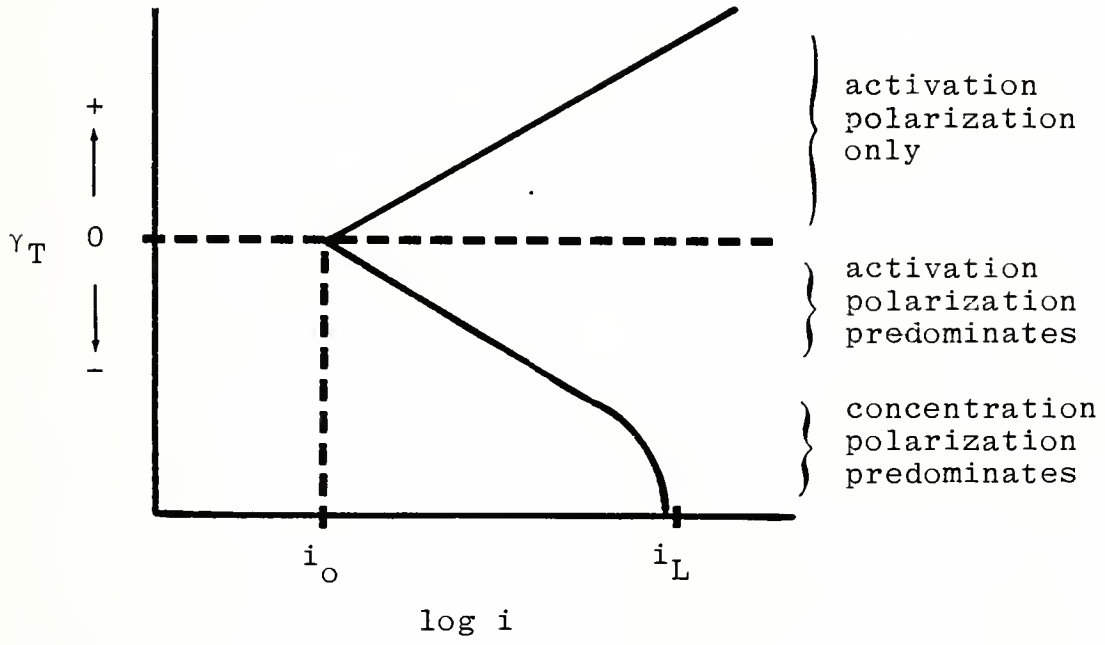

Figure C-4. Diagram of the effects of combined polarization.

D. MIXED ELECTRODES AND CORROSION

The same types of equations described above apply to a metal corroding in an electrolyte. Each component, i.e., the metal and the ions in the electrolyte has its own equilibrium potential, its own i_o, and Tafel slope. At the steady state

corrosion potential, E_{corr}, the rate for the sum of the reduction processes equals the rate for the sum of the oxidation processes, or

$$i_{sum\ red} = i_{sum\ oxid} \qquad \text{(C-11)}$$

This is analogous to the point E^{o} for the half-cell reactions where $i_{red} = i_{oxid}$. For the mixed system, Tafel slopes may be determined as before and their intersection gives i_{corr}. the corrosion current density. Recall that there will be a deviation at low current densities from the true Tafel slope since only the net current density, $(i_{oxid} - i_{red})$ can be measured. Also, if concentration polarization occurs, the cathodic Tafel slope will be minimal in length. Concentration polarization may be reduced by stirring the solution, but this adds a velocity variable to the measured corrosion rate, which may be neither desireable nor reproducible in corrosion studies. In this research, the corrosion current density was determined by the intersection of the anodic Tafel slope and the corrosion potential in cases where concentration polarization was noted. A schematic corrosion polarization curve is shown in figure C-5. This "Tafel plot" is basically an expanded PDP plot and can be obtained in the same manner. Once the corrosion current density, i_{corr}, is known, the corrosion rate of the metal may be calculated from Faraday's law, as in equation (C-1).

The disadvantages associated with the use of Tafel plots to determine corrosion rates are numerous. Primarily, there is the difficulty that, since the surface of the

specimen is changed by the measurement process, two identical specimens and two identical electrolytes are required -- one for the anodic run and one for the cathodic. A complete, two-specimen run takes a minimum of two hours. Concentration polarization may make the cathodic Tafel slope impossible to find. Also, the anodic Tafel slope may not be completely described by the simple equations above (e.g., equation C-9) since the surface of the specimen changes as it is oxidized. The advantages to this method are that it is relatively rapid compared to an IML experiment (which takes weeks or months) and that the Tafel slopes obtained can be used with linear polarization measurements to calculate corrosion rates.

V. LINEAR POLARIZATION MEASUREMENTS

The linear polarization method is a rapid, simple procedure for calculating corrosion current, I_{corr}, and from this, the corrosion current density, i_{corr}, and ultimately the corrosion rate. The measurement is made by scanning through a potential range of $E_{corr} \pm 20$ mV, and recording the resulting current as a linear plot of E vs. I. The slope of the plot, $\Delta E/\Delta I$ is related to the corrosion current, I_{corr}, and the Tafel slope constants, β_a and β_c, by the equation

$$\Delta E/\Delta I = \frac{\beta_a \beta_c}{2.3(\beta_a + \beta_c)\, I_{corr}} \qquad \text{(C-12)}$$

where the two Tafel slope constants must be determined from a Tafel plot [57].

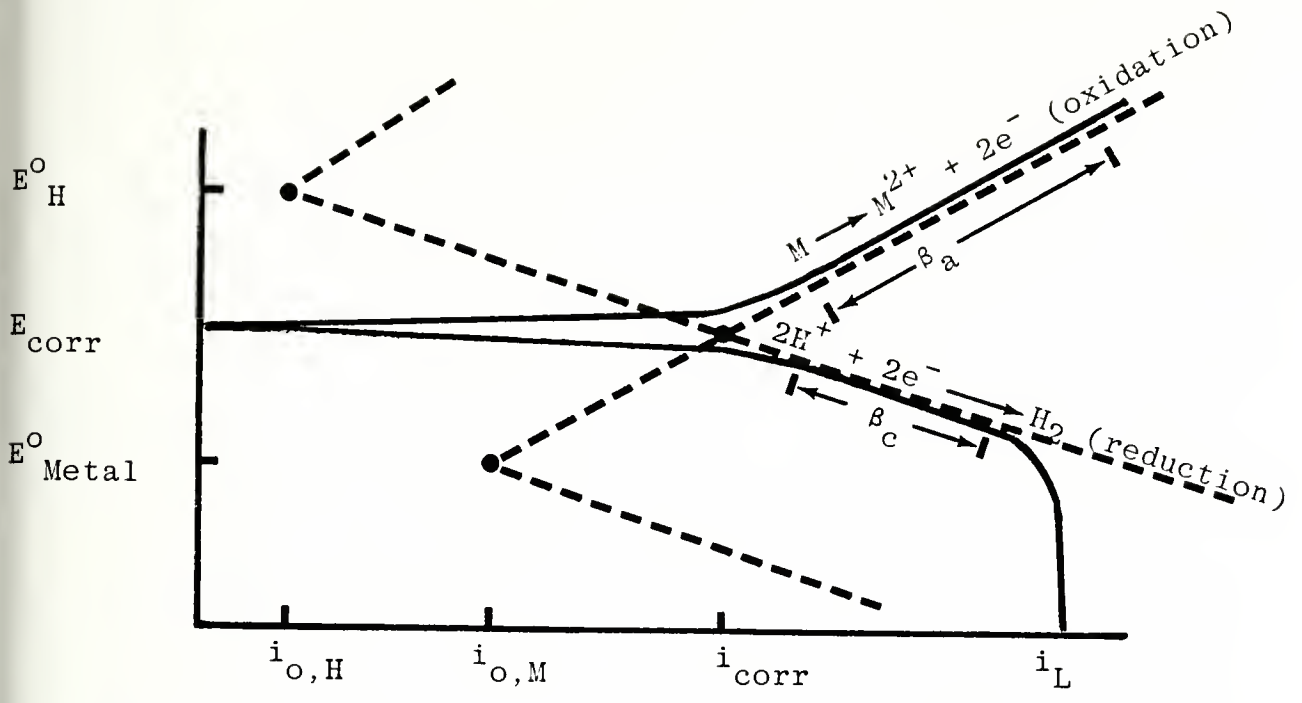

Figure C-5. Potential-current density plot. The solid line is the observed curve.

Rearrangement of equation (C-12) gives,

$$I_{corr} = \frac{\beta_a \beta_c}{2.3(\beta_a + \beta_c)} \frac{\Delta I}{\Delta E} = k \left(\frac{\Delta I}{\Delta E}\right). \qquad \text{(C-13)}$$

This equation is valid only if the ratio γ/β is small, since in the original derivation of equation (C-12), $10^{\gamma/\beta}$ was approximated by a power series, and all higher terms were neglected. Since a typical value of β is on the order of 0.1V, the applied polarization should be less than 20% of this value. Hence, the limited potential excursions about E_{corr} in this method. Figure C-6 shows a schematic linear polarization plot. The corrosion rate is calculated from the corrosion current density, i_{corr}, (where $i_{corr} = I_{corr}$/ specimen surface area) by the relationships given in Appendix A.

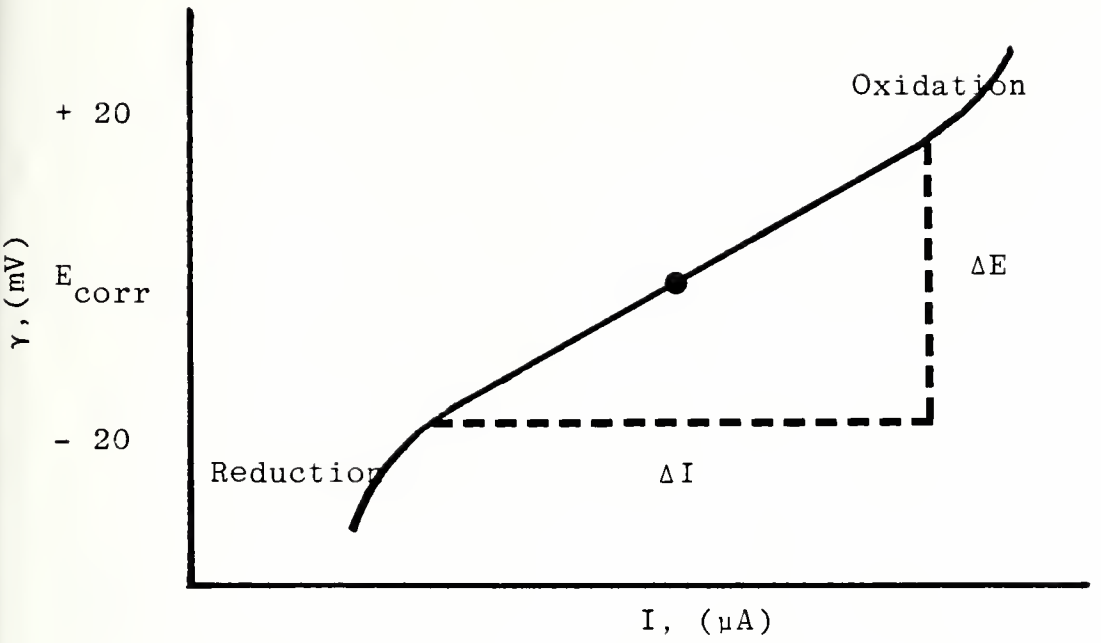

Figure C-6. Schematic of linear polarization plot.

VI. RESULTS OF THE PDP TESTS

Experimental results for the PDP tests run in this research as given in the following tables. For aerated synthetic seawater, the reader is referred to Table C-I. For the results with deaerated synthetic seawater, see Table C-II.

TABLE C-I.

RESULTS OF THE PDP TESTS

ID No.*	I_{corr} (μA)	E_{corr}(SCE) (mV)	β_a (V/decade)	β_c (V/decade)	k	i_{corr} (μA/cm^2)	$R_{\mu mpy}$
101-0	17±5	-252±2	0.070	0.148	0.021	4	94
101-H	105±2	-160±2	0.054	0.187	0.018	25	584
260-0	21±1	-253±1	0.072	0.149	0.021	5	97
260-H	54±1	-226±2	0.053	0.067	0.013	13	249
280-0	4	-287	0.051	---	---	1	18
280-H	70	-210	0.047	---	---	17	310
280-H	29±3	-185±3	0.042	0.167	0.015	7	124
280-H	45±5	-236±2	0.054	0.139	0.017	11	201
706-0	17±2	-230±2	0.062	0.156	0.019	4	84
706-H	66±6	-148±1	0.052	0.177	0.018	16	335
706-H	85	-249	0.064	---	---	20	422
715-0	14±2	-252±4	0.081	0.214	0.026	3	58
715-H	35±2	-120±1	0.046	0.181	0.016	8	145

* -H means added hypochlorite ion

-0 means no added hypochlorite ion

NOTE: All tests reported in this table were for aerated synthetic seawater.

TABLE C-II.

RESULTS OF THE PDP TESTS

ID No.*	I_{corr} (μA)	E_{corr}(SCE) (mV)	β_a (V/decade)	β_c (V/decade)	k	i_{corr} (μA/cm^2)	$R_{\mu mpy}$
101-0	9	-310	0.095	0.160	0.016	2.1	48
101-0	6	-380	0.145	---	---	1.4	33
101-0	6	-325	0.095	0.135	0.024	1.4	33
260-0	12±1	-312±4	0.100	0.191	0.029	3.0	58
280-0	3±1	-355±2	0.090	0.140	0.023	0.74	13
715-0	8±2	-306±5	0.091	0.226	0.028	1.9	33
715-0	5±0.1	-269±10	0.090	0.195	0.027	1.1	19

* -0 means no added hypochlorite ion

NOTE: All the tests reported in this table were for deaerated synthetic seawater.

APPENDIX D. X-RAY DIFFRACTION DATA

All runs were accomplished using copper K_α radiation, wavelength = 1.5418 Å.

Data for Specimen 4-H
CDA 715. Black Powder

2θ	Intensity	d-Spacing
16.3	17.7	5.44
26.3	15.0	3.39
27.3	11.4	3.27
31.8	19.1	2.81
32.5	14.1	2.75
33.2	10.4	2.70
36.1	10.0	2.49
37.3	8.8	2.41
37.9	9.5	2.37
38.5	11.7	2.34
39.8	12.6	2.26
42.9	9.0	2.11
45.5	10.6	1.99
45.8	14.0	1.98
48.4	10.6	1.88
50.2	9.0	1.82

Data for Specimen 3-H
CDA 101. Green Powder

2θ	Intensity	d-Spacing
15.4	11.0	5.75
16.1	29.7	5.50
17.5	6.6	5.07
18.8	3.0	4.72
26.0	2.9	3.43
30.8	7.1	2.90
31.5	10.2	2.84
32.3	26.6	2.77
34.7	3.1	2.59
36.4	6.0	2.47
37.2	2.1	2.42
38.5	3.6	2.34
39.7	22.6	2.27
42.3	4.4	2.14
50.0	8.5	1.87
53.5	8.2	1.71

APPENDIX E. PHYSICO-CHEMICAL REFERENCE DATA

This appendix lists necessary physical and chemical reference data and calculation procedures for use in corrosion computations. It also depicts graphically, the experimentally measured corrosion potentials for the materials studied, both for aerated and deaerated synthetic seawater, and for aerated synthetic seawater containing hypochlorite ion.

TABLE E-I. EMF SERIES [63]

REDUCTION HALF REACTION	STANDARD REDUCTION POTENTIAL (volts)
$ClO^- + H_2O + 2e^- = Cl^- + 2OH^-$	+0.890
$CuO_2^- + H_2) + e^- = Cu(OH)_2$	> +0.8
$Hg^{++}(aq) + 2e^- = 2Hg(l)$	+0.788
$BrO^- + H_2O + 2e^- = Br^- + 2OH^-$	+0.760
$I_2 + 2e^- = 2I^-$	+0.535
$NiO_2 + 2H_2O + 2e^- = Ni(OH)_2 + 2OH^-$	+0.49
$O_2 + 2H_2O + 4e^- = 4OH^-$	+0.401
$Cu^{++}(aq) + 2e^- = Cu(s)$	+0.337
$2H^+(aq) + 2e^- = H_2(g)$	0.000
$HAsO_4^{2-} + 4H^+ + 2e^- = H_3AsO_3 + H_2O$	-0.18 (at pH 8)
$Ni^{++}(aq) + 2e^- = Ni(s)$	-0.250
$Fe^{++}(aq) + 2e^- = Fe(s)$	-0.440
$Ni(OH)_2 + 2e^- = Ni(s) + 2OH^-$	-0.72
$Zn^{++}(aq) + 2e^- = Zn(s)$	-0.763
$2H_2O + 2e^- = H_2(g) + 2OH^-$	-0.828

TABLE E-II

COMPARISON OF THE COMPOSITION OF NATURAL AND ARTIFICIAL SEAWATERS

Ion	Natural seawater (g/kg)	Artificial seawater (g/kg)	Difference %
Cl^-	19.353	19.353	0.0
Na^+	10.760	10.765	0.046
SO_4^{--}	2.712	2.711	0.037
Mg^{++}	1.294	1.295	0.077
Ca^{++}	0.413	0.414	0.24
K^+	0.387	0.387	0.0
HCO_3^-	0.142	0.142	0.0
Br^-	0.067	0.066	1.5
Sr^{++}	0.008	0.008	0.0
H_3BO_3	0.026	0.026	0.0
F^-	0.001	0.001	0.0

For further information, see reference 64.

TABLE E-III. COMPOSITION OF PURGE AIR USED FOR ALL EXPERIMENTS

The purge air used in all experiments in which the electrolyte was aerated was analyzed by gas chromatographic methods. The results are listed below.

Species	Volume % of Mixture
O_2	20.19
CO_2	0.02
Inert gases (N_2, Ar, H_2O)	79.79

TABLE E-IV. HARDNESS DATA FOR CORROSION SPECIMENS

Material Used	Rockwell Hardness Value
CDA 101	F-63
CDA 260	B-30
CDA 280	B-31
CDA 706	F-58
CDA 715	F-60

TABLE E-V. [65]
ALLOY PROPERTIES

WROUGHT ALLOYS

COPPERS

COPPER NO.	DESIGNATION	TYPE	COMPOSITION, PER CENT MAXIMUM (UNLESS OTHERWISE INDICATED) Cu (incl. Ag) (% Min.)	Ag [a] (% Min.)	As	Sb	P	Te	OTHER NAMED ELEMENTS
101 [b]	OFE	Oxygen Free Electronic.....	99.99 [c]		[d]	[d]	.0003	.0010	[d, e]

COPPER-ZINC ALLOYS (BRASSES)

COPPER ALLOY NO.	PREVIOUS TRADE NAME	COMPOSITION, PER CENT MAXIMUM (UNLESS SHOWN AS A RANGE OR MINIMUM.) Cu	Pb	Fe	Zn	P	OTHER NAMED ELEMENTS	TOTAL OTHER ELEMENTS [f]
260	Cartridge Brass, 70%.....	68.5-71.5	.07	.05	Rem.			.15
280	Muntz Metal, 60%	59.0-63.0	.30	.07	Rem.			.20

COPPER-NICKEL ALLOYS

COPPER ALLOY NO.	PREVIOUS TRADE NAME	COMPOSITION, PER CENT MAXIMUM (UNLESS SHOWN AS A RANGE OR MINIMUM) Cu + ELEMENTS WITH SPEC. LIMITS (% Min.) [g]	Pb	Fe	Zn	Ni	Mn	OTHER NAMED ELEMENTS
706	Copper Nickel, 10%.....	99.5	.05	1.0-1.8	1.0	9.0-11.0	1.0	-
715	Copper Nickel, 30%.....	99.5	.05	.40-.7	1.0	29.0-33.0	1.0	

NOTES

a Figures in parentheses are troy ounces per avoirdupois ton.

b These are high conductivity coppers which have in the annealed condition a minimum conductivity of 100% IACS.

c The 99.99 value for Cu is exclusive of Ag.

d The total of the seven following elements, Se, Te, Bi, As, Sb, Sn and Mn not to exceed 40 ppm (.0040%).

e Hg, max., 1 ppm (.0001%); Zn, max., 1 ppm (.0001%); Cd, max., 1 ppm (.0001%); S, max., 18 ppm (.0018%); Pb, max., 10 ppm (.0010%); Se, max., 10 ppm (.0010%); Bi, max., 10 ppm (.0010%); Oxygen, max., 10 ppm (.0010%).

f Analysis is regularly made for the elements for which specific limits are listed except Zn. If, however, the presence of other elements is suspected or indicated in the course of routine analysis, further analysis shall be made to determine that the total of these "other" elements is not in excess of the limits specified.

g Specific limits are defined as any numerical values, whether maximum only, minimum only, or ranges

COPPER No. 101 *(OXYGEN FREE ELECTRONIC)*

Composition – percent

	Nominal	Minimum	Maximum
Copper	....	99.99	....
Residual Deoxidants	....	None	
Phosphorus	....	....	.0003
Tellurium	....	....	.0010
Other Named Elements**	....	....	....

* Hg, max., 1 ppm, (.0001%); Zn, max., 1 ppm, (.0001%); Cd, max., 1 ppm, (.0001%); S, max., 18 ppm, (.0018%); Pb, max., 10 ppm, (.0010%); Se, max., 10 ppm (.0010%); Bi, max., 10 ppm (.0010%); Oxygen max., 10 ppm, (.0010%).

** The total of the seven following elements, Se, Te, Bi, As, Sb, Sn and Mn not to exceed 40 ppm, (.0040%).

Nearest Applicable A S T M Specifications

Flat Products	B48, B133, B152, B187 B272, B432, F68
Pipe	B42, B188, F68
Rod	B12, B49, B133 B187, F68
Shapes	B133, B187, F68
Tube	B68, B75, B188, B280 B372, F68
Wire	B1, B2, B3, F68

Physical Properties

	English Units	C. G. S. Units
Melting Point (Liquidus)	1981 F	1083 C
Melting Point (Solidus)	1981 F	1083 C
Density	.323 lb /cu in @ 68 F	8.94 gm /cu cm @ 20 C.
Specific Gravity	8.94	8.94
Coefficient of Thermal Expansion	.0000094 per °F from 68 F to 212 F	.0000170 per °C from 20 C to 100 C
Coefficient of Thermal Expansion	.0000096 per °F from 68 F to 392 F	.0000173 per °C from 20 C to 200 C
Coefficient of Thermal Expansion	.0000098 per °F from 68 F to 572 F	.0000177 per °C from 20 C to 300 C
Thermal Conductivity	226 Btu /sq ft /ft /hr /°F @ 68 F	.934 cal /sq cm /cm /sec /° C @ 20 C
Electrical Resistivity (Annealed)	10.3 Ohms (circ mil /ft) @ 68 F	1.71 Microhm-cm @ 20 C
Electrical Conductivity* (Annealed)	101 % IACS @ 68 F	.586 Megmho-cm @ 20 C
Thermal Capacity (Specific Heat)	.092 Btu /lb °F @ 68 F	.092 cal /gm /° C @ 20 C
Modulus of Elasticity (Tension)	17,000,000 psi	12,000 Kg /sq mm
Modulus of Rigidity	6,400,000 psi	4,500 Kg /sq mm

*Volume and weight basis, minimum value

Typical Uses

ELECTRICAL AND ELECTRONIC: bus bars, bus conductors and other conductors, wave guides, hollow conductors, lead-in wires and anodes for vacuum tubes, vacuum seals, transistor components, glass to metal seals, coaxial cables and coaxial tubes, klystrons, micro-wave tubes, automotive rectifiers

Common Fabrication Processes

Blanking, coining, coppersmithing, drawing, etching, forming and bending, heading and upsetting, hot forging and pressing, piercing and punching, roll threading and knurling, shearing, spinning, squeezing and swaging, stamping

Fabrication Properties

Capacity for Being Cold Worked ..... Excellent
Capacity for Being Hot Formed ..... Excellent
Hot Forgeability Rating (Forging Brass = 100) 65
Hot Working Temperature ..... 1400-1600 F or 750-875 C
Annealing Temperature ..... 700-1200 F or 375-650 C
Machinability Rating (Free Cutting Brass = 100) 20

Suitability for being joined by:
Soldering ..... Excellent
Brazing ..... Excellent
Oxyacetylene Welding ..... Fair
Gas Shielded Arc Welding ..... Good
Coated Metal Arc Welding ..... Not Recommended
Resistance Welding: Spot ..... Not Recommended; Seam ..... Not Recommended; Butt ..... Good

The values listed above represent reasonable approximations suitable for general engineering use. Due to commercial variations in composition and to manufacturing limitations, they should not be used for specification purposes. See applicable A S T M specification references.

COPPER No. 101 *(Continued)*

Forms and Tempers Most Commonly Used

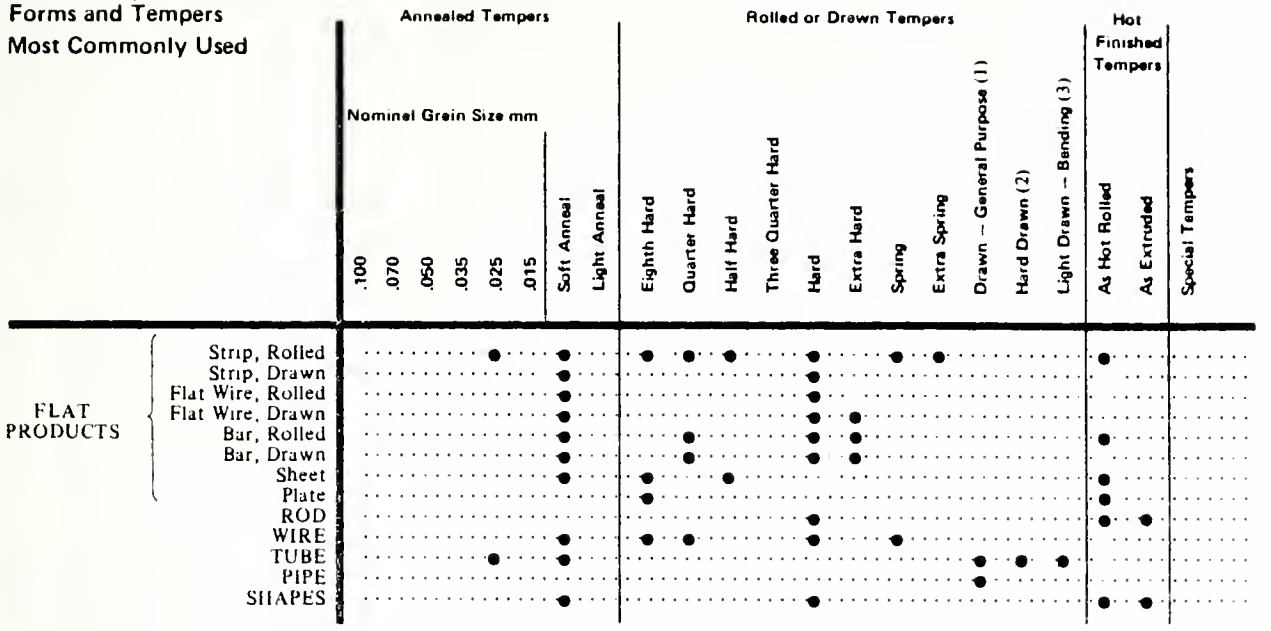

1. DRAWN – GENERAL PURPOSE temper is used for general purpose tube only, usually where there is no real requirement for high strength or hardness on the one hand or for bending qualities on the other.

2. HARD DRAWN temper is used only where there is need for a tube as hard or as strong as is commercially feasible for the size in question.

3. LIGHT DRAWN – BENDING temper is used only where a tube of some stiffness, but yet capable of readily being bent (or otherwise moderately cold worked) is needed.

Mechanical Properties

Form	Size Section in.	Temper	Tensile Strength ksi	Yield Strength (.5% Ext. under Load) ksi	Yield Strength (.2% Offset) ksi	Elongation in 2 in. %	Rockwell Hardness F	Rockwell Hardness B	Rockwell Hardness 30T	Shear Strength ksi	Fatigue Strength ksi	Fatigue Strength Million Cycles
FLAT PRODUCTS	.040 in.	.050 mm	32.0	10.0	....	45	40	–	–	22.0	....	....
		.025 mm	34.0	11.0	....	45	45	–	–	23.0	11.0	100
		Eighth Hard	36.0	28.0	....	30	60	10	25	25.0	....	....
		Quarter Hard	38.0	30.0	....	25	70	25	36	25.0	....	....
		Half Hard	42.0	36.0	....	14	84	40	50	26.0	13.0	100
		Hard	50.0	45.0	....	6	90	50	57	28.0	13.0	100
		Spring	55.0	50.0	....	4	94	60	63	29.0	14.0	100
		Extra Spring	57.0	53.0	....	4	95	62	64	29.0	....	....
		As Hot Rolled	34.0	10.0	....	45	45	–	–	23.0	....	....
	.250 in.	.050 mm	32.0	10.0	....	50	40	–	–	22.0	....	....
		Eighth Hard	36.0	28.0	....	40	60	10	–	25.0	....	....
		Quarter Hard	38.0	30.0	....	35	70	25	–	25.0	....	....
		Hard	50.0	45.0	....	12	90	50	–	28.0	....	....
		As Hot Rolled	32.0	10.0	....	50	40	–	–	22.0	....	....
	1.0 in.	Hard	45.0	40.0	....	20	85	45	–	26.0	....	....
ROD	1.0 in.	.050 mm	32.0	10.0	....	55	40	–	–	22.0	....	....
	.250 in.	Hard (40%)	55.0	50.0	....	10	94	60	–	29.0	....	....
	1.0 in.	Hard (35%)	48.0	44.0	....	16	87	47	–	27.0	17.0	100
	2.0 in.	Hard (16%)	45.0	40.0	....	20	85	45	–	26.0	....	....
	1.0 in.	As Hot Rolled	32.0	10.0	....	55	40	–	–	22.0	....	....
WIRE	.080 in.	.050 mm	35.0	....	....	35*	–	–	–	24.0	....	....
		Hard	55.0	....	....	1.5**	–	–	–	29.0	....	....
		Spring	66.0	....	....	1.5**	–	–	–	33.0	....	....
TUBE	1.0 in. OD X .065 in.	.050 mm	32.0	10.0	....	45	40	–	–	22.0	....	....
		.025 mm	34.0	11.0	....	45	45	–	–	23.0	....	....
		Light Drawn (15%)	40.0	32.0	....	25	77	35	45	26.0	....	....
		Hard Drawn (40%)	55.0	50.0	....	8	95	60	63	29.0	....	....
SHAPES	.500 in.	.050 mm	32.0	10.0	....	50	40	–	–	22.0	....	....
		Hard (15%)	40.0	32.0	....	30	–	35	–	26.0	....	....
		As Hot Rolled	32.0	10.0	....	50	40	–	–	22.0	....	....
		As Extruded	32.0	10.0	....	50	40	–	–	22.0	....	....

* Elongation in 10 inches. ** Elongation in 60 inches.

The values listed above represent reasonable approximations suitable for general engineering use. Due to commercial variations in composition and to manufacturing limitations, they should not be used for specification purposes. See applicable A.S.T.M. specification references.

COPPER ALLOY No. 260 *(CARTRIDGE BRASS, 70%)*

Composition – percent

	Nominal	Minimum	Maximum
Copper	70	68.5	71.5
Lead	....	....	.07
Iron	....	....	.05
Zinc	30	Remainder	
Total Other Elements	....	....	.15

Nearest Applicable A S T M Specifications

Flat Products	B19, B36, B134
Pipe	
Rod	
Shapes	B129
Tube	B135
Wire	B134

Physical Properties

	English Units	C. G. S. Units
Melting Point (Liquidus)	1750 F	955 C
Melting Point (Solidus)	1680 F	915 C
Density	.308 lb /cu in @ 68 F	8.53 gm /cu cm @ 20 C
Specific Gravity	8.53	8.53
Coefficient of Thermal Expansion	per °F from 68 F to 212 F	per °C from 20 C to 100 C
Coefficient of Thermal Expansion	per °F from 68 F to 392 F	per °C from 20 C to 200 C
Coefficient of Thermal Expansion	.0000111 per °F from 68 F to 572 F	.0000199 per °C from 20 C to 300 C
Thermal Conductivity	70 Btu /sq ft /ft /hr /°F @ 68 F	.29 cal /sq cm /cm /sec /° C @ 20 C
Electrical Resistivity (Annealed)	37.0 Ohms (circ mil /ft) @ 68 F	6.16 Microhm-cm @ 20 C
Electrical Conductivity* (Annealed)	28 % IACS @ 68 F	.162 Megmho-cm @ 20 C
Thermal Capacity (Specific Heat)	.09 Btu /lb °F @ 68 F	09 cal /gm /° C @ 20 C
Modulus of Elasticity (Tension)	16,000,000 psi	11,200 Kg /sq mm
Modulus of Rigidity	6,000,000 psi	4,200 Kg /sq mm

* Volume Basis

Typical Uses

ARCHITECTURAL: grillwork
AUTOMOTIVE: radiator cores and tanks
ELECTRICAL: flashlight shells, lamp fixtures, reflectors, screw shells, socket shells
HARDWARE: bead chain, chain, eyelets, fasteners, grommets, finish hardware articles (hinges, kick plates, locks, push plates, etc.), stencils
INDUSTRIAL: pump and power cylinders and liners
MUNITIONS: ammunition components
PLUMBING: plumbing accessories, plumbing brass goods
WIRE: pins, rivets, screws, springs

Common Fabrication Processes

Blanking, drawing, etching, forming and bending, heading and upsetting, piercing and punching, shearing, spinning, squeezing and swaging, stamping

Fabrication Properties

Capacity for Being Cold Worked ..... Excellent
Capacity for Being Hot Formed ..... Fair
Hot Forgeability Rating (Forging Brass = 100) .....
Hot Working Temperature ..... 1350-1550 F or 725-850 C
Annealing Temperature ..... 800-1400 F or 425-750 C
Machinability Rating (Free Cutting Brass = 100) 30

Suitability for being joined by:
Soldering ..... Excellent
Brazing ..... Excellent
Oxyacetylene Welding ..... Good
Gas Shielded Arc Welding ..... Fair
Coated Metal Arc Welding ..... Not Recommended
Resistance Welding: Spot ..... Good; Seam ..... Not Recommended; Butt ..... Good

The values listed above represent reasonable approximations suitable for general engineering use. Due to commercial variations in composition and to manufacturing limitations, they should not be used for specification purposes. See applicable A S T M specification references.

COPPER ALLOY No. 260 *(Continued)*

Forms and Tempers Most Commonly Used

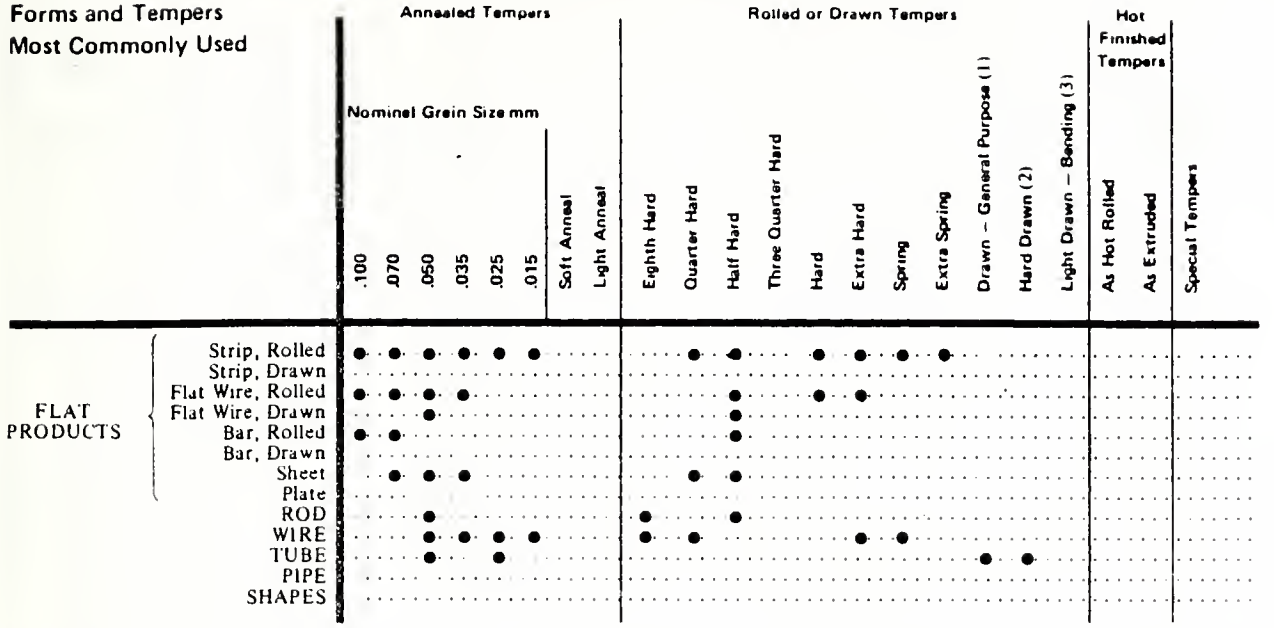

1. DRAWN – GENERAL PURPOSE temper is used for general purpose tube only, usually where there is no real requirement for high strength or hardness on the one hand or for bending qualities on the other.

2. HARD DRAWN temper is used only where there is need for a tube as hard or as strong as is commercially feasible for the size in question.

3. LIGHT DRAWN – BENDING temper is used only where a tube of some stiffness, but yet capable of readily being bent (or otherwise moderately cold worked) is needed.

Mechanical Properties

Form	Size Section in.	Temper	Tensile Strength ksi	Yield Strength (.5% Ext. under Load) ksi	Yield Strength (.2% Offset) ksi	Elongation in 2 in. %	Rockwell Hardness F	Rockwell Hardness B	Rockwell Hardness 30T	Shear Strength ksi	Fatigue Strength ksi	Fatigue Strength Million Cycles
FLAT PRODUCTS	.040 in.	.100 mm	44.0	11.0	....	66	54	–	11	....	13.0	100
		.070 mm	46.0	14.0	....	65	58	–	15	32.0	13.0	100
		.050 mm	47.0	15.0	....	62	64	–	26	....	....	....
		.035 mm	49.0	17.0	....	57	68	–	31	34.0	14.0	100
		.025 mm	51.0	19.0	....	55	72	–	36	....	....	....
		.015 mm	53.0	22.0	....	54	78	–	43	35.0	14.0	100
		Quarter Hard	54.0	40.0	....	43	–	55	54	36.0	....	....
		Half Hard	62.0	52.0	....	25	–	70	65	40.0	18.0	100
		Hard	76.0	63.0	....	8	–	82	73	44.0	21.0	100
		Extra Hard	86.0	65.0	....	5	–	88	76	46.0	....	....
		Spring	94.0	65.0	....	3	–	91	77	48.0	23.0	100
		Extra Spring	99.0	65.0	....	3	–	93	78	....	....	....
WIRE	.080 in.	.050 mm	48.0	....	....	64	–	–	–	....	....	....
		.035 mm	50.0	....	....	60	–	–	–	34.0	....	....
		.025 mm	52.0	....	....	58	–	–	–	....	....	....
		.015 mm	54.0	....	....	56	–	–	–	....	....	....
		Eighth Hard	58.0	....	....	35	–	–	–	38.0	....	....
		Quarter Hard	70.0	....	....	20	–	–	–	....	....	....
		Extra Hard	124.0	....	....	4	–	–	–	....	....	....
		Spring	130.0	....	....	3	–	–	–	60.0	22.0	100
TUBE	1.0 in. OD X .065 in.	.050 mm	47.0	15.0	....	65	64	–	26	....	....	....
		.025 mm	52.0	20.0	....	55	75	–	40	....	....	....
		Hard Drawn (35%)	78.0	64.0	....	8	–	82	73	....	....	....
ROD	1.0 in.	.050 mm	48.0	16.0	....	65	65	–	–	34.0	....	....
		Eighth Hard (6%)	55.0	40.0	....	48	–	60	–	36.0	....	....
		Half Hard (20%)	70.0	52.0	....	30	–	80	–	42.0	22.0	50

The values listed above represent reasonable approximations suitable for general engineering use. Due to commercial variations in composition and to manufacturing limitations, they should not be used for specification purposes. See applicable A.S.T.M. specification references.

COPPER ALLOY No. 280 *(MUNTZ METAL, 60%)*

Composition – percent

	Nominal	Minimum	Maximum
Copper	60	59.0	63.0
Lead	....	....	.30
Iron	....	....	.07
Zinc	40	Remainder	
Total Other Elements	....	....	.20

Nearest Applicable A S T M Specifications

Flat Products	
Pipe	
Rod	
Shapes	
Tube	B111, B135, B395
Wire	

Physical Properties

	English Units	C. G. S. Units
Melting Point (Liquidus)	1660 F	905 C
Melting Point (Solidus)	1650 F	900 C
Density	.303 lb /cu in @ 68 F	8.39 gm /cu cm @ 20 C.
Specific Gravity	8.39	8.39
Coefficient of Thermal Expansion	per °F from 68 F to 212 F	per °C from 20 C to 100 C
Coefficient of Thermal Expansion	per °F from 68 F to 392 F	per °C from 20 C to 200 C
Coefficient of Thermal Expansion	.0000116 per °F from 68 F to 572 F	.0000208 per °C from 20 C to 300 C
Thermal Conductivity	71 Btu /sq ft /ft /hr /°F @ 68 F	.29 cal /sq cm /cm /sec /° C @ 20 C
Electrical Resistivity (Annealed)	37.0 Ohms (circ mil /ft) @ 68 F	6.16 Microhm-cm @ 20 C
Electrical Conductivity* (Annealed)	28 % IACS @ 68 F	.162 Megmho-cm @ 20 C
Thermal Capacity (Specific Heat)	.09 Btu /lb °F @ 68 F	.09 cal /gm /° C @ 20 C
Modulus of Elasticity (Tension)	15,000,000 psi	10,500 Kg /sq mm
Modulus of Rigidity	5,600,000 psi	3,900 Kg /sq mm

* Volume Basis

Typical Uses

ARCHITECTURAL: panels and large sheets, trim
HARDWARE: large nuts and bolts
INDUSTRIAL: brazing rod, condenser plates; condenser, evaporator and heat exchanger tubes; hot forgings

Common Fabrication Processes

Blanking, forming and bending, hot forging and pressing, hot heading and upsetting, shearing

Fabrication Properties

Capacity for Being Cold Worked ..... Fair
Capacity for Being Hot Formed ..... Excellent
Hot Forgeability Rating (Forging Brass = 100) 90
Hot Working Temperature ..... 1150-1450 F or 625-800 C
Annealing Temperature ..... 800-1100 F or 425-600 C
Machinability Rating (Free Cutting Brass = 100) 40

Suitability for being joined by:
Soldering ..... Excellent
Brazing ..... Excellent
Oxyacetylene Welding ..... Good
Gas Shielded Arc Welding ..... Fair
Coated Metal Arc Welding ..... Not Recommended
Resistance Welding: Spot ..... Good; Seam ..... Not Recommended; Butt ..... Good

The values listed above represent reasonable approximations suitable for general engineering use. Due to commercial variations in composition and to manufacturing limitations, they should not be used for specification purposes. See applicable A S T M specification references.

COPPER ALLOY No. 280 *(Continued)*

Forms and Tempers Most Commonly Used

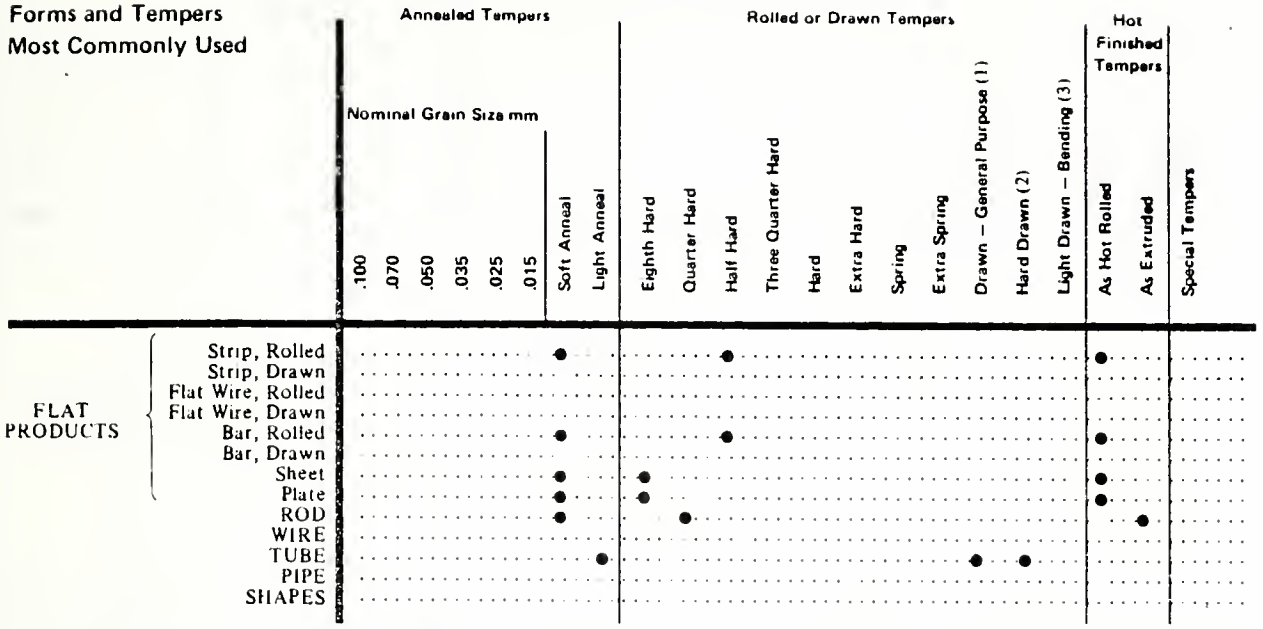

1. DRAWN – GENERAL PURPOSE temper is used for general purpose tube only, usually where there is no real requirement for high strength or hardness on the one hand or for bending qualities on the other.

2. HARD DRAWN temper is used only where there is need for a tube as hard or as strong as is commercially feasible for the size in question.

3. LIGHT DRAWN – BENDING temper is used only where a tube of some stiffness, but yet capable of readily being bent (or otherwise moderately cold worked) is needed.

Mechanical Properties

Form	Size Section in.	Temper	Tensile Strength ksi	Yield Strength (.5% Ext. under Load) ksi	Yield Strength (.2% Offset) ksi	Elongation in 2 in. %	Rockwell Hardness F	Rockwell Hardness B	Rockwell Hardness 30T	Shear Strength ksi	Fatigue Strength ksi	Fatigue Strength Million Cycles
FLAT PRODUCTS	.040 in.	Soft Anneal	54.0	21.0	....	45	80	--	46	40.0	...	...
		As Hot Rolled	54.0	21.0	....	45	85	--	49	40.0	....	....
		Eighth Hard	60.0	35.0	....	30	--	55	54	42.0	....	....
		Half Hard	70.0	50.0	....	10	--	75	67	44.0	....	....
ROD	1.0 in.	Soft Anneal	54.0	21.0	....	50	80	--	--	40.0	....	....
		Quarter Hard	72.0	50.0	....	25	--	78	--	45.0	....	....
		As Extruded	52.0	20.0	....	52	78	--	--	39.0	....	....
TUBE	1.0 in. OD X .065 in.	Light Anneal	56.0	23.0	....	50	82	--	47	....	....	....
		Hard Drawn (30%)	74.0	55.0	....	10	--	80	--	....	....	....

The values listed above represent reasonable approximations suitable for general engineering use. Due to commercial variations in composition and to manufacturing limitations, they should not be used for specification purposes. See applicable A.S.T.M. specification references.

COPPER ALLOY No. 706 *(COPPER NICKEL, 10%)*

Composition – percent

	Nominal	Minimum	Maximum
Copper	88.6	....	....
Lead	....	....	.05
Iron	1.4	1.0	1.8
Zinc	....	....	1.0
Nickel	10	9.0	11.0
Manganese	....	....	1.0
Copper + Elements with Specific Limits	....	99.5	....

Nearest Applicable A S T M Specifications

Flat Products	B122, B151, B171, B402, B432
Pipe	B466, B467
Rod	B151
Shapes	
Tube	B111, B359, B395, B466, B467, B543, B552
Wire	

Physical Properties

	English Units	C. G. S. Units
Melting Point (Liquidus)	2100 F	1150 C
Melting Point (Solidus)	2010 F	1100 C
Density	.323 lb /cu in @ 68 F	8.94 gm /cu cm @ 20 C.
Specific Gravity	8.94	8.94
Coefficient of Thermal Expansion	per °F from 68 F to 212 F	per °C from 20 C to 100 C
Coefficient of Thermal Expansion	per °F from 68 F to 392 F	per °C from 20 C to 200 C
Coefficient of Thermal Expansion	.0000095 per °F from 68 F to 572 F	.0000171 per °C from 20 C to 300 C
Thermal Conductivity	26 Btu /sq ft /ft /hr /°F @ 68 F	.11 cal /sq cm /cm /sec /°C @ 20 C
Electrical Resistivity (Annealed)	115 Ohms (circ mil /ft) @ 68 F	19.1 Microhm-cm @ 20 C
Electrical Conductivity* (Annealed)	9.0 % IACS @ 68 F	.0522 Megmho-cm @ 20 C
Thermal Capacity (Specific Heat)	.09 Btu /lb °F @ 68 F	.09 cal /gm /°C @ 20 C
Modulus of Elasticity (Tension)	18,000,000 psi	12,700 Kg /sq mm
Modulus of Rigidity	6,800,000 psi	4,800 Kg /sq mm

* Volume Basis

Typical Uses

INDUSTRIAL: condensers, condenser plates, distiller tubes, evaporator and heat exchanger tubes, ferrules, salt water piping

Common Fabrication Processes

Forming and bending, welding

Fabrication Properties

Capacity for Being Cold Worked ..... Good
Capacity for Being Hot Formed ..... Good
Hot Forgeability Rating (Forging Brass = 100) .....
Hot Working Temperature ..... 1550-1750 F or 850-950 C
Annealing Temperature ..... 1100-1500 F or 600-825 C
Machinability Rating (Free Cutting Brass = 100) 20

Suitability for being joined by:
Soldering ..... Excellent
Brazing ..... Excellent
Oxyacetylene Welding ..... Fair
Gas Shielded Arc Welding ..... Excellent
Coated Metal Arc Welding ..... Good
Resistance Welding: Spot ..... Good; Seam ..... Good; Butt ..... Excellent

The values listed above represent reasonable approximations suitable for general engineering use. Due to commercial variations in composition and to manufacturing limitations, they should not be used for specification purposes. See applicable A.S.T.M. specification references.

COPPER ALLOY No. 706 *(Continued)*

Forms and Tempers Most Commonly Used

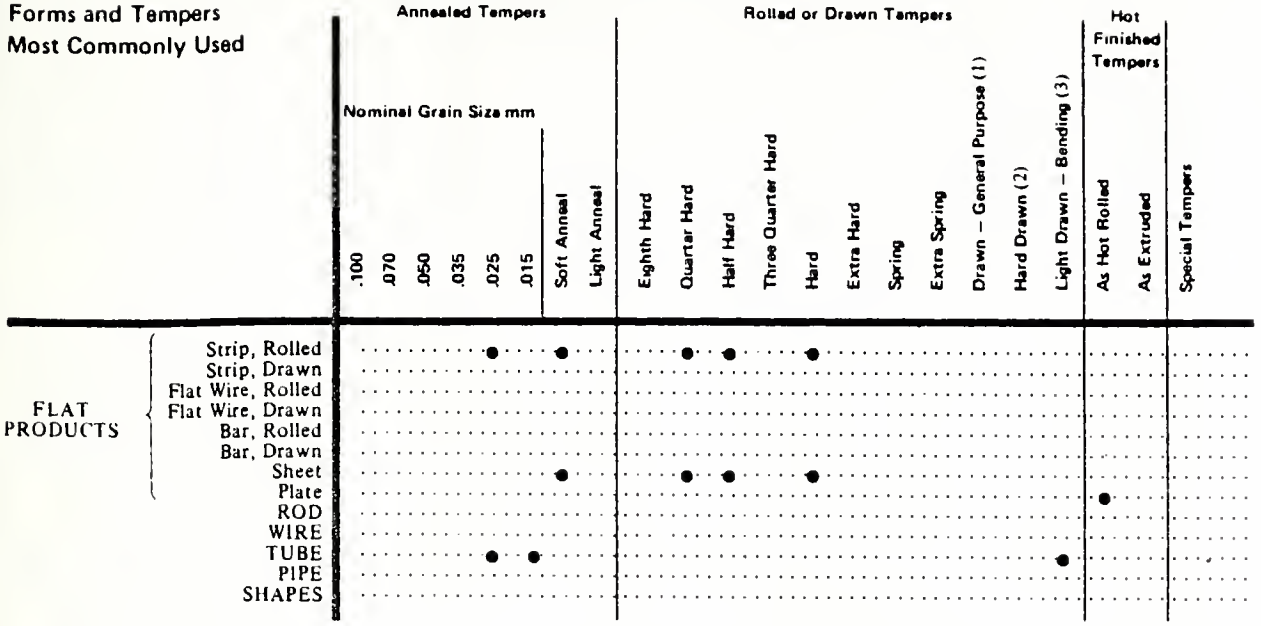

1. DRAWN – GENERAL PURPOSE temper is used for general purpose tube only, usually where there is no real requirement for high strength or hardness on the one hand or for bending qualities on the other.

2. HARD DRAWN temper is used only where there is need for a tube as hard or as strong as is commercially feasible for the size in question.

3. LIGHT DRAWN – BENDING temper is used only where a tube of some stiffness, but yet capable of readily being bent (or otherwise moderately cold worked) is needed.

Mechanical Properties

Form	Size Section in.	Temper	Tensile Strength ksi	Yield Strength (.5% Ext. under Load) ksi	Yield Strength (.2% Offset) ksi	Elongation in 2 in. %	Rockwell Hardness F	Rockwell Hardness B	Rockwell Hardness 30T	Shear Strength ksi	Fatigue Strength ksi	Fatigue Strength Million Cycles
TUBE	1.0 in. OD X .065 in.	.025 mm	44.0	16.0	....	42	65	15	26	....	....	....
		Light Drawn	60.0	57.0	....	10	100	72	70	....	....	....

The values listed above represent reasonable approximations suitable for general engineering use. Due to commercial variations in composition and to manufacturing limitations, they should not be used for specification purposes. See applicable A.S.T.M. specification references.

COPPER ALLOY No. 715 *(COPPER NICKEL, 30%)*

Composition – percent

	Nominal	Minimum	Maximum
Copper	69.5	....	....
Lead	....	....	.05
Iron	.5	.40	.7
Zinc	....	....	1.0
Nickel	30	29.0	33.0
Manganese	....	....	1.0
Copper + Elements with Specific Limits	....	99.5	....

Nearest Applicable A S T M Specifications

Flat Products	B122, B151, B171, B402, B432
Pipe	B466, B467
Rod	B151
Shapes	
Tube	B111, B359, B395, B466, B467, B543, B552
Wire	

Physical Properties

	English Units	C. G. S. Units
Melting Point (Liquidus)	2260 F	1240 C
Melting Point (Solidus)	2140 F	1170 C
Density	.323 lb /cu in @ 68 F	8.94 gm /cu cm @ 20 C.
Specific Gravity	8 94	8.94
Coefficient of Thermal Expansion	per °F from 68 F to 212 F	per °C from 20 C to 100 C
Coefficient of Thermal Expansion	per °F from 68 F to 392 F	per °C from 20 C to 200 C
Coefficient of Thermal Expansion	.0000090 per °F from 68 F to 572 F	.0000162 per °C from 20 C to 300 C
Thermal Conductivity	17 Btu /sq ft /ft /hr /°F @ 68 F	.07 cal /sq cm /cm /sec /° C @ 20 C
Electrical Resistivity (Annealed)	225 Ohms (circ mil /ft) @ 68 F	37.5 Microhm-cm @ 20 C
Electrical Conductivity* (Annealed)	4.6 % IACS @ 68 F	.0267 Megmho-cm @ 20 C
Thermal Capacity (Specific Heat)	.09 Btu /lb °F @ 68 F	.09 cal /gm /° C @ 20 C
Modulus of Elasticity (Tension)	22,000,000 psi	15,500 Kg /sq mm
Modulus of Rigidity	8,300,000 psi	5,800 Kg /sq mm

* Volume Basis

Typical Uses

INDUSTRIAL: condensers, condenser plates distiller tubes, evaporator and heat exchanger tubes, ferrules, salt water piping

Common Fabrication Processes

Forming and bending, welding

Fabrication Properties

Capacity for Being Cold Worked ..... Good
Capacity for Being Hot Formed ..... Good
Hot Forgeability Rating (Forging Brass = 100) .....
Hot Working Temperature .....1700-1900 F or 925-1050 C
Annealing Temperature .....1200-1500 F or 650- 825 C
Machinability Rating (Free Cutting Brass = 100) 20

Suitability for being joined by:
Soldering..... Excellent
Brazing ..... Excellent
Oxyacetylene Welding ..... Good
Gas Shielded Arc Welding ..... Excellent
Coated Metal Arc Welding ..... Excellent
Resistance Welding { Spot ..... Excellent; Seam ..... Excellent; Butt ..... Excellent

The values listed above represent reasonable approximations suitable for general engineering use. Due to commercial variations in composition and to manufacturing limitations they should not be used for specification purposes. See applicable A.S T.M. specification references.

COPPER ALLOY No. 715 *(Continued)*

Forms and Tempers Most Commonly Used

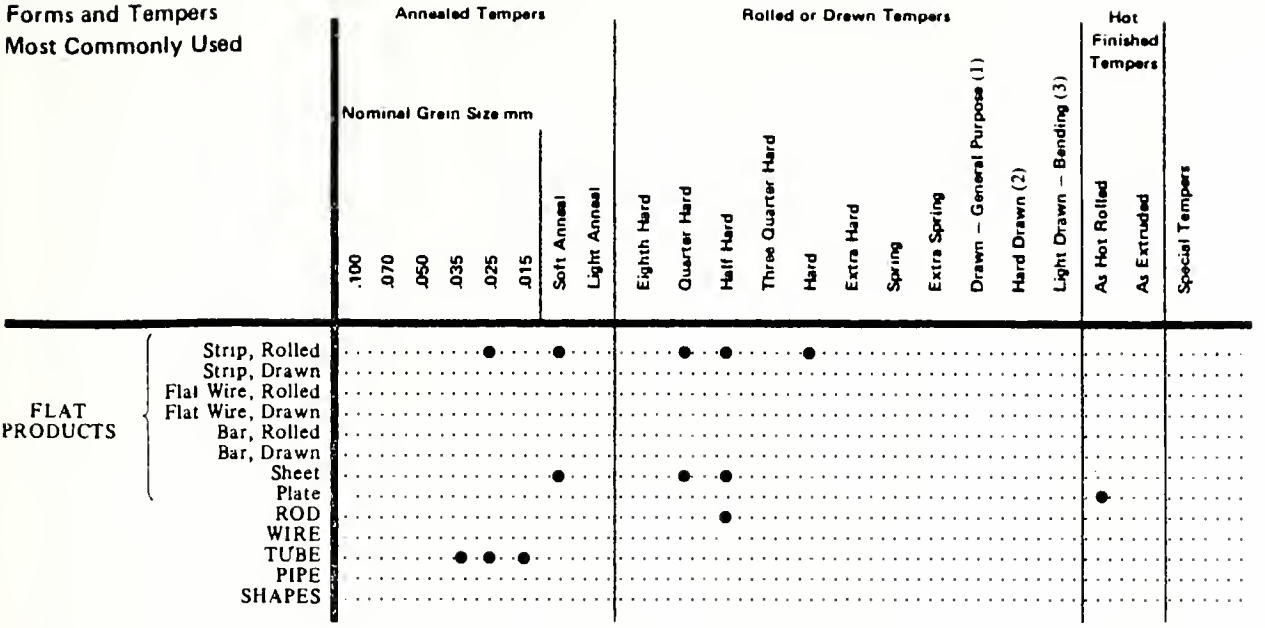

1. DRAWN – GENERAL PURPOSE temper is used for general purpose tube only, usually where there is no real requirement for high strength or hardness on the one hand or for bending qualities on the other.

2. HARD DRAWN temper is used only where there is need for a tube as hard or as strong as is commercially feasible for the size in question.

3. LIGHT DRAWN – BENDING temper is used only where a tube of some stiffness, but yet capable of readily being bent (or otherwise moderately cold worked) is needed.

Mechanical Properties

Form	Size Section in.	Temper	Tensile Strength ksi	Yield Strength (.5% Ext. under Load) ksi	Yield Strength (.2% Offset) ksi	Elongation in 2 in. %	Rockwell Hardness F	Rockwell Hardness B	Rockwell Hardness 30T	Shear Strength ksi	Fatigue Strength ksi	Fatigue Strength Million Cycles
FLAT PRODUCTS	1.0 in.	As Hot Rolled	55.0	20.0	....	45	--	35	–	....	....	..
TUBE	1.0 in. OD X .065 in.	.025 mm	60.0	25.0	....	45	80	45	–	....	....	....
	4.5 in. OD X .109 in.	.035 mm	54.0	....	....	45	77	36	–	....	....	....
ROD	1.0 in.	Half Hard (20%)....	75.0	70.0	....	15	-	80	–	....	....	....

The values listed above represent reasonable approximations suitable for general engineering use. Due to commercial variations in composition and to manufacturing limitations, they should not be used for specification purposes. See applicable A.S.T.M. specification references.

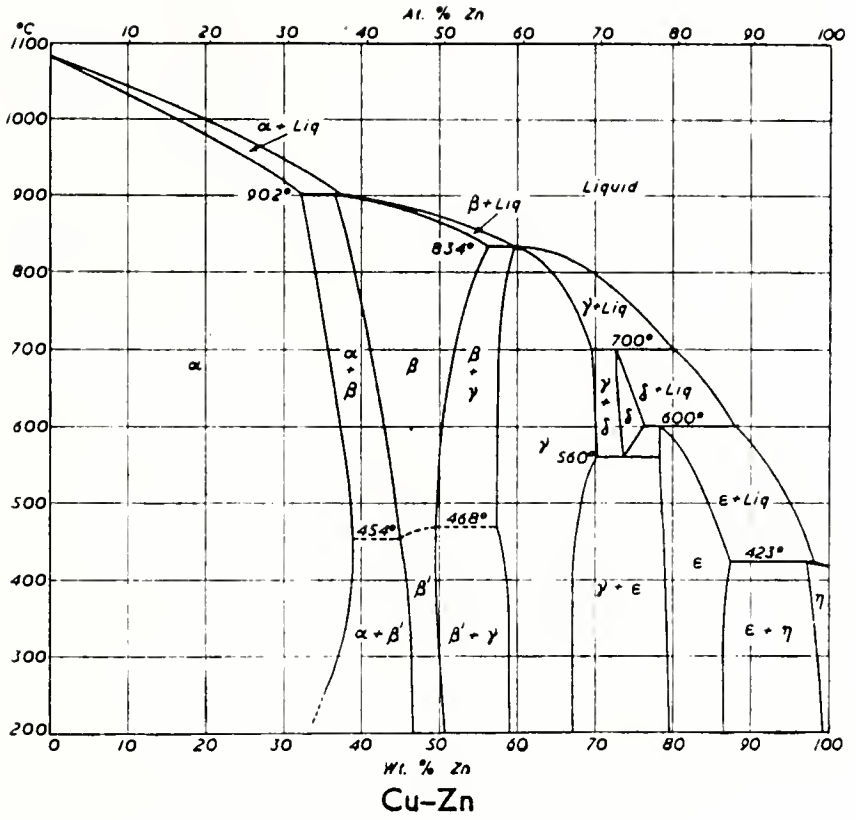

Figure E-1. Phase diagram for the copper-zinc system of alloys.

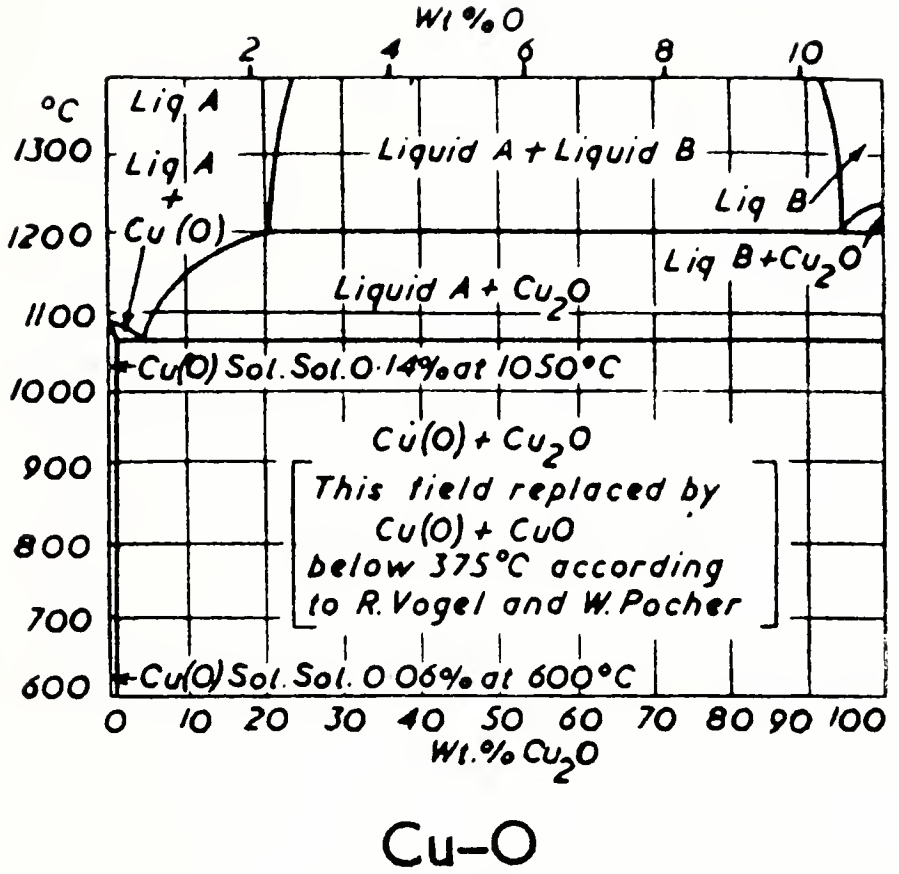

Figure E-2. Phase diagram for the copper-oxygen system.

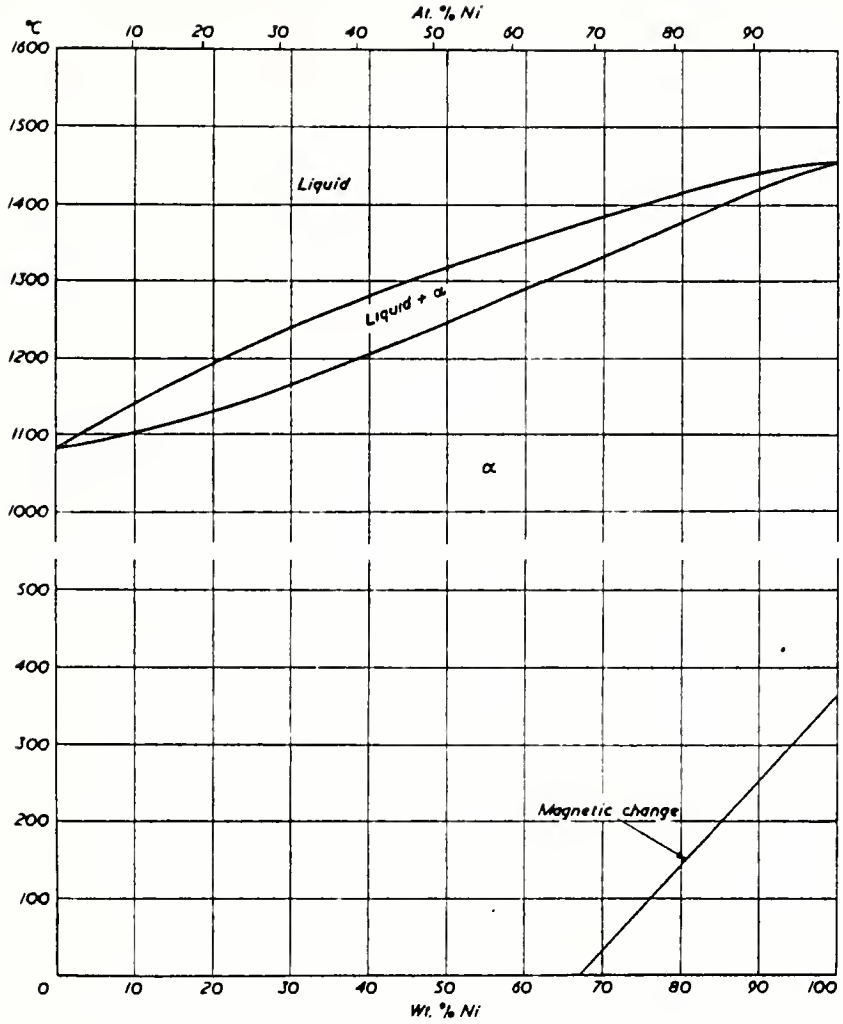

Figure E-3. Phase diagram for the copper-nickel system of alloys.

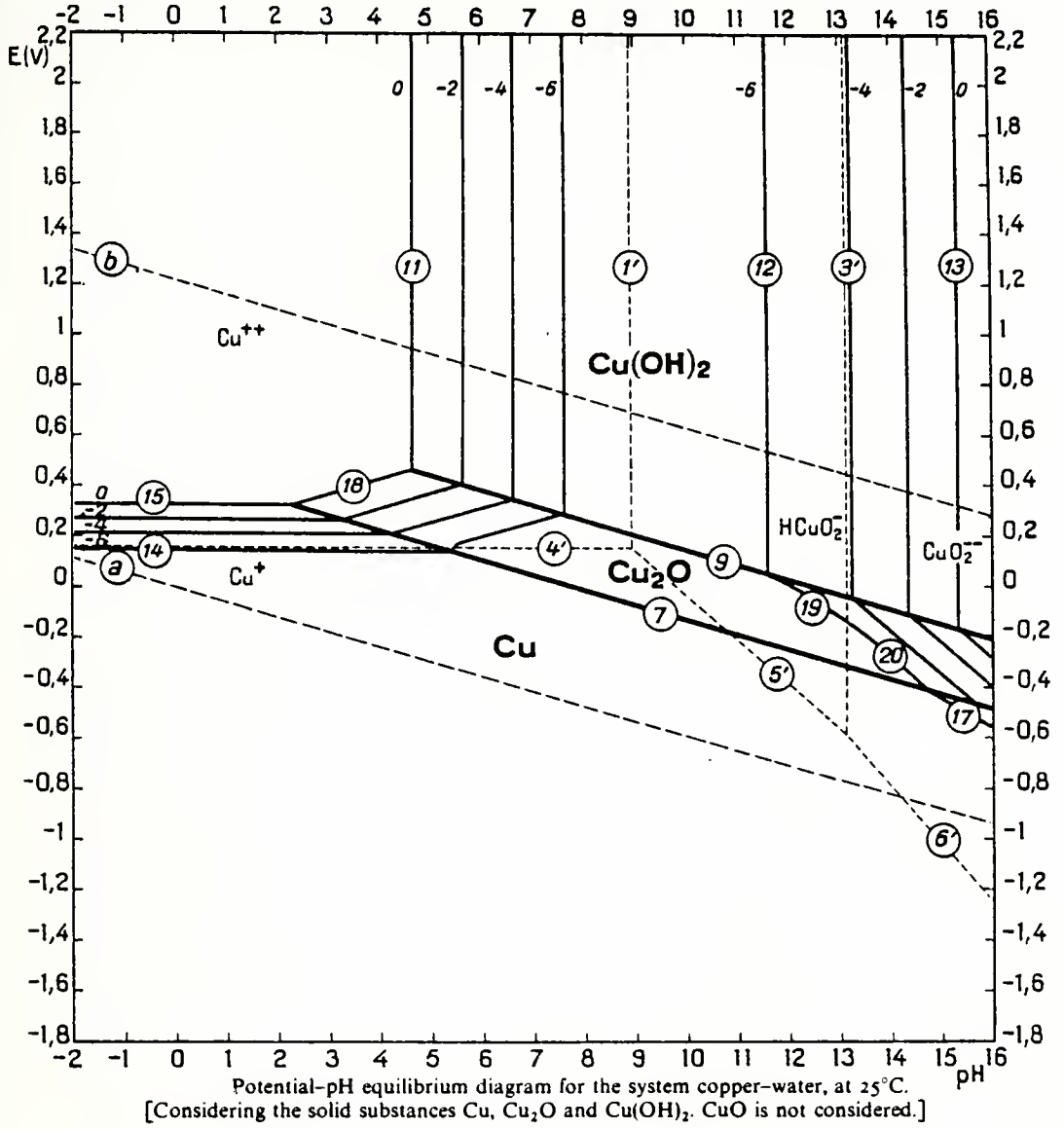

Potential-pH equilibrium diagram for the system copper-water, at 25°C.
[Considering the solid substances Cu, Cu_2O and $Cu(OH)_2$. CuO is not considered.]

Figure E-4. Pourbaix diagram for the system copper-water.
(a) CuO not considered.

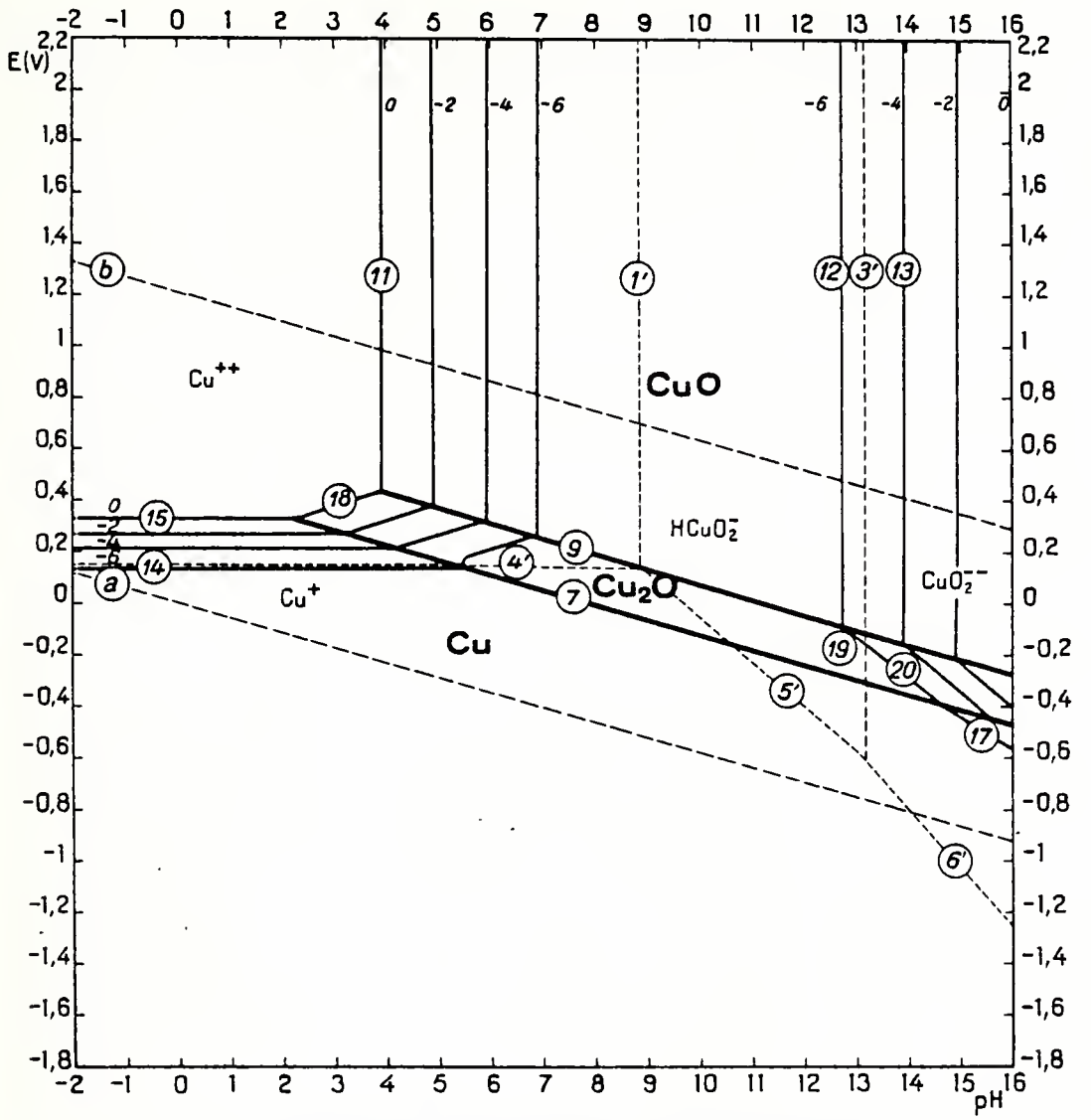

Potential–pH equilibrium diagram for the system copper–water, at 25°C.
[Considering the solid substances Cu, Cu_2O and CuO. $Cu(OH)_2$ is not considered.]

Figure E-4. Pourbaix diagram for the system copper-water. (b) $Cu(OH)_2$ not considered.

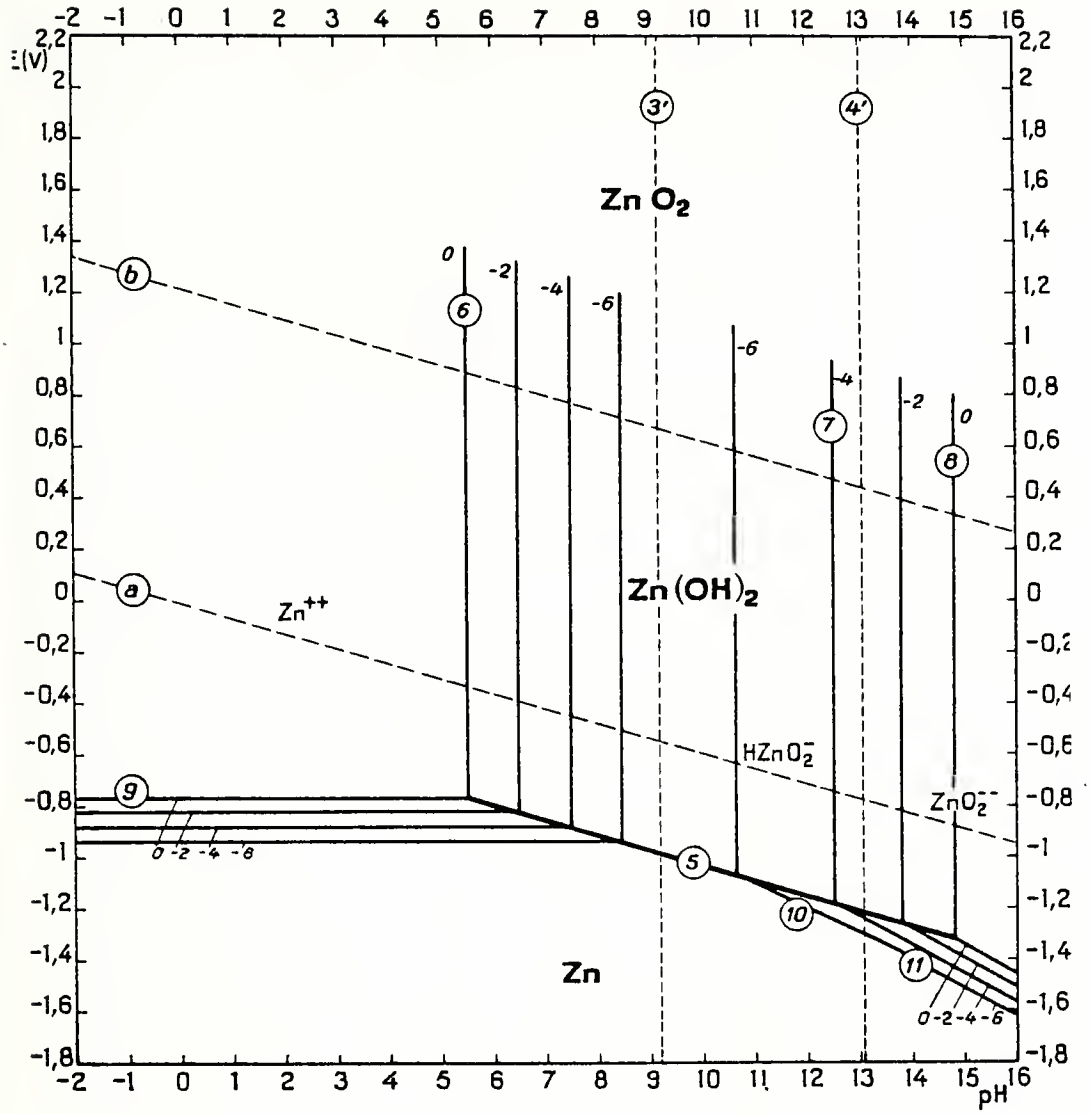

Potential–pH equilibrium diagram for the system zinc–water, at 25°C.
[Established by considering ε-$Zn(OH)_2$.]

Figure E-5. Pourbaix diagram for the system zinc-water.

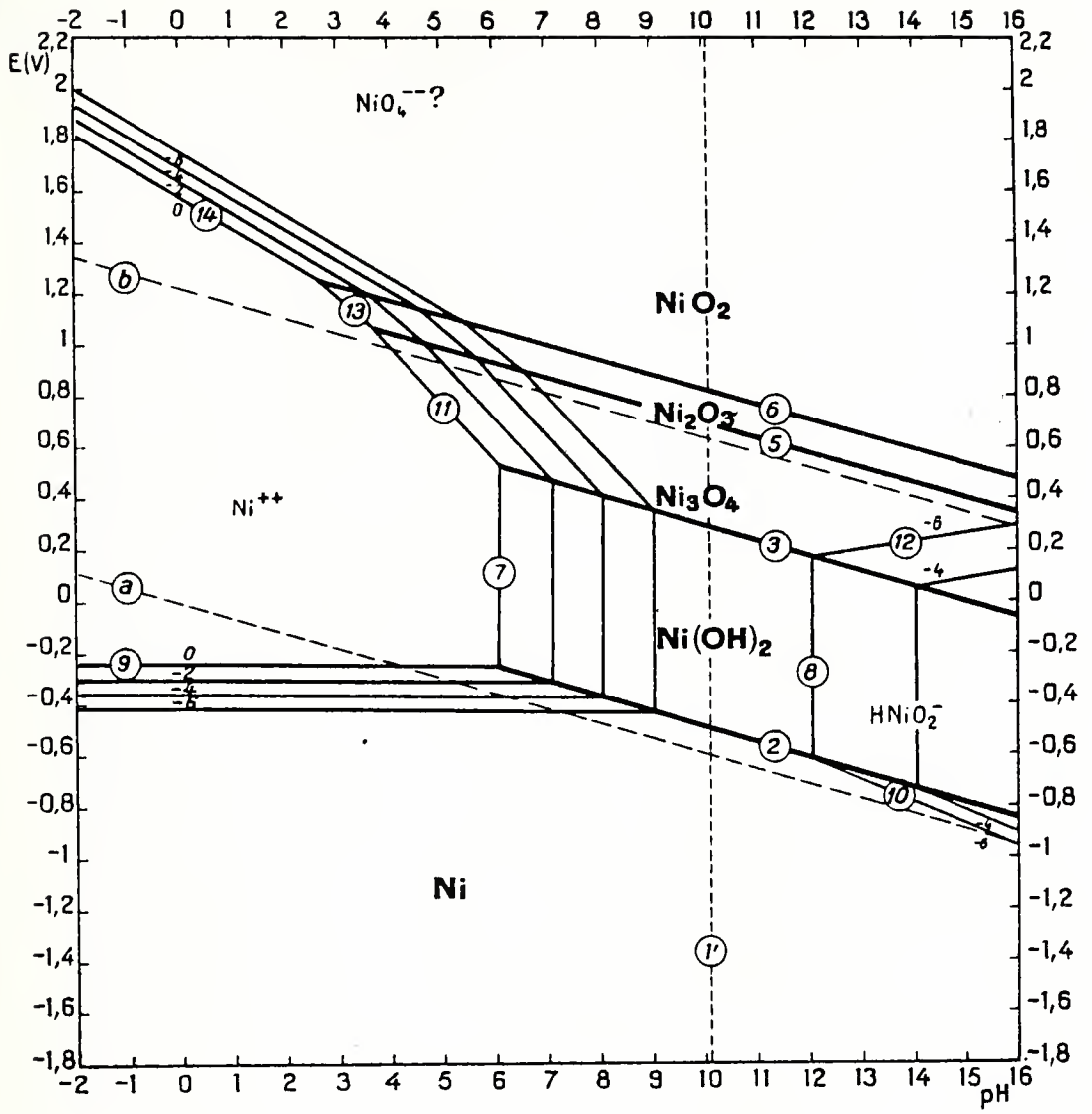

Potential-pH equilibrium diagram for the system nickel-water, at 25°C.

Figure E-6. Pourbaix diagram for the system nickel-water.

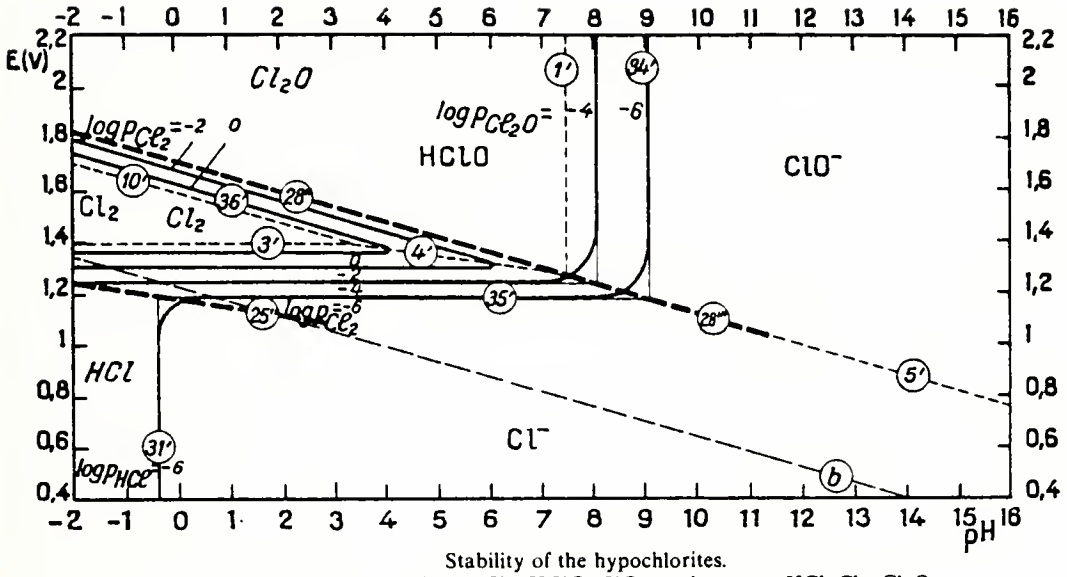

Stability of the hypochlorites.
Equilibria between dissolved Cl^-, Cl_2, HClO, ClO^- and gaseous HCl, Cl_2, Cl_2O.

Potential–pH diagrams for the system chlorine–water, at 25°C.
Metastable equilibria.
(For solutions containing 1 g-at Cl/l.)

Figure E-7. Pourbaix diagram for the system chlorine-water.

TITRATION CALCULATIONS FOR HYPOCHLORITE ION IN SEAWATER.

The amount of hypochlorite ion contained in the electrolyte was measured by withdrawing a 25 ml aliquot from the total volume of 800 ml, adding iodide ion(which was rapidly converted to triiodide ion), and then titrating the liberated triiodide against standard sodium arsenite at pH 7.5-8.0. The flasks had each been initially charged with 200 ppm of sodium hypochlorite (0.1343 meq of ClO^-) and it was desired to return the concentration of hypochlorite ion to this level after the titration. The concentration of the stock sodium hypochlorite solution was known from previous titration against standard arsenite, and was repeatedly checked throughout the 34 day immersion tests. The number of ml of stock sodium hypochlorite to add was calculated as below, and the volume was made up to 25 ml with synthetic seawater, and then replaced in the corrosion flask. Figures B-6 through B-10 show the records of the concentration changes in hypochlorite ion in each flask vs. time. (Note: the "normality" of a solution is found by dividing the "molarity" of the species in question by the number of electrons lost or gained in the half reaction. Thus, the equivalent weight for biiodate is 1/12 of the formula mass, and the equivalent weight for arsenite is 1/2 the molecular weight. Normality is defined as the equivalent weight per unit volume).

$$\text{Volume of } ClO^- \text{ Stock to be added} = \frac{0.1343 \text{ meq} - (\text{Normality} \times \text{volume, arsenite})\frac{(\text{total volume of electrolyte})}{(\text{aliquot volume})}}{(\text{Normality of NaClO stock})}$$

where: $$\text{Normality of arsenite} = \frac{(\text{Normality of standard biiodate})(\text{volume of biiodate})}{(\text{volume of arsenite used in the biiodate reaction})}$$

and $$\text{Normality of NaClO stock} = \frac{(\text{Normality of arsenite})(\text{volume of arsenite})}{(\text{volume of NaClO stock used})}$$

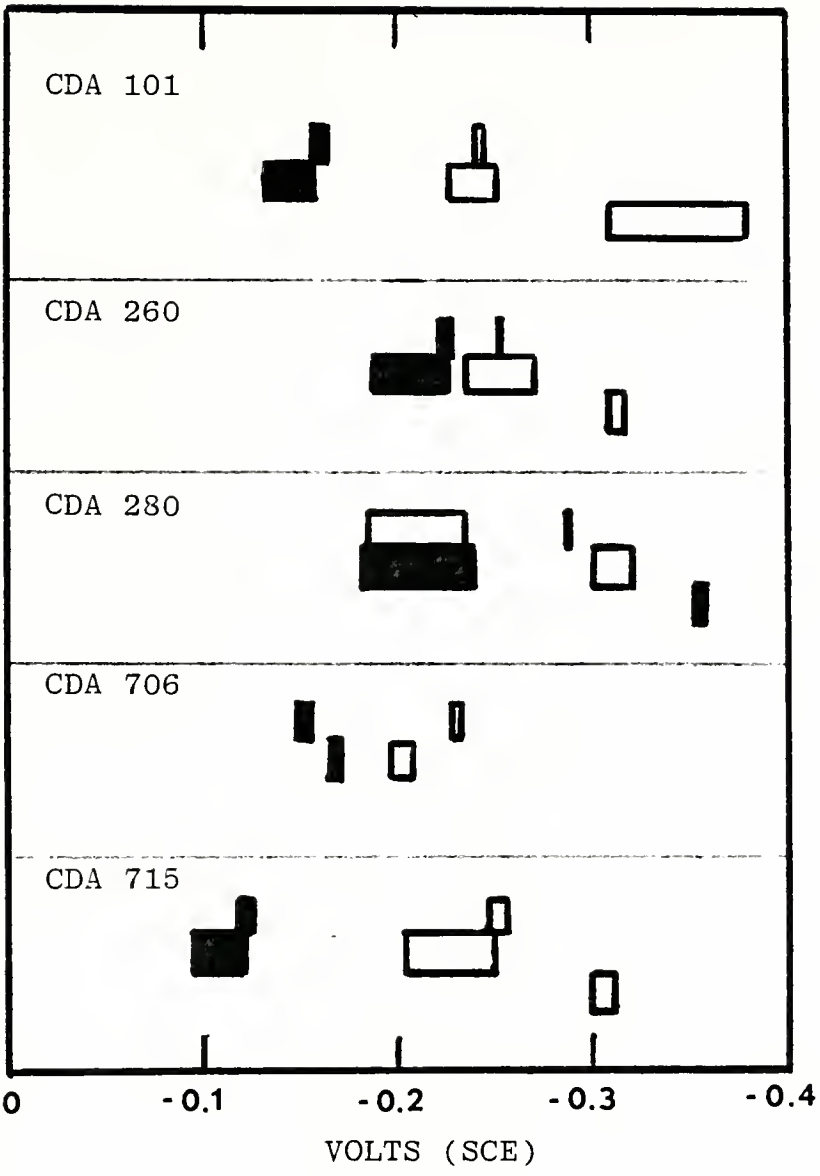

Figure E-7. Experimentally measured corrosion potentials.

Key: Open bars - no added hypochlorite ion

Dark bars - 200 ppm added hypochlorite ion

There are three sets of bars for each material. The upper set is for potential measured by PDP in aerated media. The middle set of bars is for potential measured by PSP in aerated media. The lower set is for potential measured in deaerated media in the PDP experiments.

LIST OF REFERENCES

1. Naval Ship Research and Development Center, David W. Taylor Laboratory, Report PAS-75-29, Marine Fouling of Titanium Heat Exchangers, by W. L. Adamson, p.3, March 1976. (AD-A022-207).

2. Marine Boring and Fouling Organisms, D.L. Ray, editor, University of Washington Press, Seattle, Washington, p. 187, 1959.

3. Kuwabara, R., "Chlorine Tolerance of Mytilus Edulis L.", in Proceedings of the Second International Congress on Marine Corrosion and Fouling, Technical Chamber of Greece, Athens, Greece, p. 413-423, September 1968.

4. Baggs,J., British Patent 2295, 1863.

5. Piggott, W., British Patent 1209, 1866.

6. Edison, T., German Patent 57293, 1891.

7. Frazier, G., U.S. Patent 82015, 1906.

8. Partee, W., U.S. Patent 943357, 1907.

9. Harrison, C., British Patent 1347, 1870.

10. James, J., U.S. Patent 994405, 1911.

11. Delius, G., U.S. Patent 1021734, 1912.

12. Pourbaix, M., Atlas of Electrochemical Equilibria, English Translation, National Association of Corrosion Engineers, Houston, Texas, p. 592, 1974.

13. Fair, G., et. al., Elements of Water Supply and Wastewater Disposal, 2nd edition, J. Wiley and Sons, p. 513 and p. 715, 1971.

14. Ibid., p. 514-517.

15 Adamson, A., et. al., "The Production of Hypochlorite by Direct Electrolysis of Seawater: Electrode Materials and Design of Cells for the Process," in Journal of Applied Chemistry, 13, 483 (1963).

16. Morgenstern,E., "Advances in Antifouling Technology," in Proceedings of the 18th Annual Marine Coating Conference, National Paint and Coatings Association, paper number 9, Monterey, California, March 22-24, 1978.

17. Adamson, W., Naval Ship Research and Development Center, Annapolis, Maryland, private communication.

18. Yoshii, T., et. al., "Antifouling System by Electrolysis of Sea Water," in Proceedings of the ASCE Conference on Civil Engineering in the Oceans, II, Miami Beach, Florida, p. 1045 FF., December 10-12, 1969.

19. Price, J., A Potentiokinetic Determination of Corrosion Rates in Artificial Seawater-Hypochlorite Solutions, M.S. Thesis, Naval Postgraduate School, Monterey, California, June 1976.

20. British Ship Research Association Contract Report W189, An Assessment of the CHLOROPAC Electrolytic Chlorinator, by D. W. Trotman, February 1974.

21. American Society for Testing and Materials, "Preparation, Cleaning and Evaluating Corrosion Test Specimens," ASTM Standard G1-72, in 1975 Annual Book of ASTM Standards, ASTM, Philadelphia, Pennsylvania, Part 10, p.626, 1975.

22. Ibid., p. 660.

23. Kehl, G.L., The Principles of Metallographic Laboratory Practice, 3rd Edition, McGraw-Hill Book Company, New York, 1949.

24. Sutfin, L.V., et. al., "A Comparison of X-ray Analysis Techniques Available for Scanning Electron Microscopes," in IITRI70, Illinois Institute of Technology, Illinois, p. 17-24, 1970.

25. Hannawalt, R., et. al., "Chemical Analysis by X-ray Diffraction," in Industrial and Engineering Chemistry, Analytical Edition, 30, 457 (1938).

26. Joint Committee on Powder Diffraction Standards, Publ. SMH-26, Powder Diffraction File Search Manual, Hannawalt Method, Inorganic, 1976, Park Lane, Pennsylvania, 1976.

27. Washburn, E.W., and E. K. Strachan, Journal of the American Chemical Society, 35, 681 (1913).

28. Roebuck, J., "The Rate of the Reaction Between Arsenious Acid and Iodine in Acid Solution," in Journal of Physical Chemistry, 6, 365 (1902) and 9, 727 (1905).

29. Jamieson, G.S., Volumetric Iodate Methods, Chemical Catalog Company, New York, New York, 1926.

30. Robinson, R.A., and R.H. Stokes, Electrolyte Solutions, 2nd Edition, Butterworths, London; Academic Press, Inc., New York, 1959.

31. American Society for Metals, "Atlas of Microstructures of Industrial Alloys," in Metals Handbook, 8th edition, ASM, Metals Park, Ohio, volume 7, p.287, 1972.

32. Guy, G. and H.Hren, "Quantitative Microscopy" in Elements of Physical Metallurgy,

33. Sinkankas, J., Mineralogy: A First Course, D. Van Nostrand Company, Inc., Princeton, New Jersey, p. 138, 1977.

34. Dana, J.W. and E. S. Dana, The System of Mineralogy, 7th edition, John Wiley and Sons, Inc., New York, volume 1, p.99, 1953.

35. American Society for Metals, op. cit., volume 1.

36. Vermilea, D.A., "What I'd Like to Know About Corrosion," in Proceedings of the First International Congress on Metallic Corrosion, 10-15 April 1961, Butterworths, London, p. 62, 1962.

37. Perkins, J., W. Luebke, K. J. Graham, and J. M. Todd, "Anodic Corrosion of Zinc Alloys in Seawater," in Journal of the Electrochemical Society, 124, 819 (1977).

38. Goudas, J.P., and H.P. Hack, "Sulfide Induced Corrosion of Copper-Nickel Alloys," in Corrosion, National Association of Corrosion Engineers, Katy, Texas, 35, 67 (1979).

39. Venzcel, J., L. Knuttson and G. Wranglen, Corrosion Science, 4, 1 (1964).

40. Asselin, F.J. and F. A. Rohrman, Industrial and Engineering Chemistry, 32, 1015 (1940).

41. Reinhart, F.A., "Corrosion of Copper Alloys in Hydrospace," in ASTM-STP 558, Corrosion in Natural Environments, American Society for Testing and Materials, Philadelphia, Pennsylvania, p.135, 1974.

42. Uhlig, H.H., editor, The Corrosion Handbook, John Wiley and Sons, Inc., New York, 1948.

43. Vajda, O., and T. Zagon, Cukoripar, 12, 69 (1959).

44. Cotton, F. A., and G. Wilkinson, Advanced Inorganic Chemistry, 3rd edition, Interscience Publishers, New York, p.901, 1972.

45. Konaka, R., et. al., "The Mechanism of the Oxidation Reaction with Nickel Peroxide," in Journal of Organic Chemistry, 34, 1334 (1969).

46. Magee, J.S., Canadian Journal of Chemistry, 43, 1234 (1965).

47. Meyerstein, D., Inorganic Chemistry, 10, 638 (1971).

48. Bour, J., and J. Steggerda, Chemical Communications, 85, 1 (1967).

49. Pourbaix, M., CEBELCOR, Rapport Technique RT.100, 1961.

50. Rabald, E., Corrosion Guide, 2nd edition, Elsevier Publishing Co., Amsterdam, p.703, 1968.

51. Gmelin's Handbuch der anorganischen Chemie, Zink, S.N. 32, Verlag Chemie, G.m.b.H., Weinheim, 1956.

52. Leidheiser, H., Jr., The Corrosion of Copper, Tin, and Their Alloys, John Wiley and Sons, Inc., New York, p. 103, 1971.

53. Pohling, G. W. and T. Notoya, "Corrosion Pretreatments for Copper-Zinc Alloys," in Corrosion, National Association of Corrosion Engineers, 39, January 1979.

54. Evans, U.R., The Corrosion and Oxidation of Metals: First Supplementary Volume, St. Martin's Press, London, p. 323, 1968.

55. Pruna, M., et. al., Revue de l'Institut Francaise du Petrole et Annales des combustibles liquides, 6, 145 (1951).

56. Schwabe, K., "Problems of Corrosion Research With Electrochemical Methods," in Journal of Electroanalytical Chemistry, 100, 927 (1979).

57. Stern, M. and A. Geary, "Electrochemical Polarization," in Journal of the Electrochemical Society, 104, 56 (1957).

58. Pye, E.L., "Practical Considerations in Performing Linear Polarization Measurements," Alpha Research, Claremont, California, Report C-10, 1965.

59. Pourbaix, M., "Atlas of Electrochemical Equilibria," loc. cit.

60. Fontana, M. and N. Greene, Corrosion Engineering, McGraw Hill Book Co., New York, p.155, 1971.

61. Cummings, J., Galvanic Aspects of Aluminum Sacrificial Anode Alloys in Seawater, M.S. Thesis, Naval Postgraduate School, Monterey, California, December 1977.

62. Kortüm, G. and J. O'M. Bockris, Textbook of Electrochemistry, Elsevier Publishing Co., Amsterdam, p. 402, 1951.

63. Latimer, W., The Oxidation States of the Elements and Their Potentials in Aqueous Solutions, 2nd edition, Prentice-Hall, Inc., New York, 1952.

64. Kester, D. R., et. al., "Preparation of Artificial Seawater," in Limnology and Oceanography, 12, 176 (1967).

65. Copper Development Agency, Properties of Copper and Its Alloys, volumes 1 - 4, 1975.

66. O'Neal, Cleveland and R. N. Borger, "The Effect of Chlorine on the Performance of Cuprous Metal Corrosion Inhibitors," presented at CORROSION/77, paper 68, National Association of Corrosion Engineers, March 14-18, San Francisco, California, 1977.

INITIAL DISTRIBUTION LIST

		No. copies
1.	Defense Documentation Center Cameron Station Alexandria, Virginia 22314	2
2.	Library, Code 0142 Naval Postgraduate School Monterey, California 93940	2
3.	Department Chairman, Code 61 Department of Physics and Chemistry Naval Postgraduate School Monterey, California 93940	2
4.	Professor R. A. Reinhardt, Code 61Ri Department of Physics and Chemistry Naval Postgraduate School Monterey, California 93940	1
5.	Dr. Melvin H. Miles, Code 38 Research Department Naval Weapons Center China Lake, California 93555	1
6.	Professor A. J. Perkins, Code 69Ps Department of Mechanical Engineering Naval Postgraduate School Monterey, California 93940	1
7.	LCDR Joseph M. Price, USN 808 W. North First Street Shelbyville, Illinois 62565	1
8.	Kenneth J. Graham, Code 3835 Research Department Naval Weapons Center China Lake, California 93555	3

Thesis
G65247
c.1

186605

Graham
Microgalvanic aspects of the seawater corrosion of marine material in the presence of hypochlorite ion fouling inhibitor.